DISSERTATION

CHARACTERIZING BIOLOGICAL SYSTEMS:

QUANTITATIVE METHODS FOR SYNTHETIC GENETIC CIRCUITS IN PLANTS AND INTRACELLULAR MECHANICS

Submitted by

Wenlong Xu

Department of Chemical and Biological Engineering

In partial fulfillment of the requirements

For the Degree of Doctor of Philosophy

Colorado State University

Fort Collins, Colorado

Summer 2018

Doctoral Committee:

Advisor: Ashok Prasad

June I. Medford
Kenneth F. Reardon
Brian E. Munsky

ABSTRACT

CHARACTERIZING BIOLOGICAL SYSTEMS: QUANTITATIVE METHODS FOR SYNTHETIC GENETIC CIRCUITS IN PLANTS AND INTRACELLULAR MECHANICS

This dissertation is a contribution to the development of methods for the characterization of two different types of biological systems – synthetic genetic circuits in plants and the mammalian cytoplasm. This dissertation begins with two reviews on synthetic biology and mechanobiology respectively. In the first part of chapter one, I review the engineering-based methodology developed in synthetic biology, and how this methodology has aided the design, construction and testing of many synthetic networks. I emphasize the assumption of modularity and the challenges to expand the predictive power of synthetic biology into plants. In the second part on mechanobiology, I briefly review the significance of mechanical properties of mammalian cells, the relationship between the mechanical properties and cytoskeleton, and methods developed to measure the cellular mechanical properties. I emphasize the passive and active particle-tracking microrheology (PTMR) and the technical barriers preventing their wider applications.

The assumption of modularity is central to the developments of larger synthetic networks, where the synthetic circuits are assumed to maintain their essential properties characterized in isolation when they are combined into larger networks. In chapter 2, this assumption of modularity was tested with two canonical switches interacting with downstream elements (loads): the mutual-repression based synthetic toggle switch and a positive feedback based switch found widely in nature. We found that adding loads is able to change the dynamics of the

toggle switch, characterized as the time needed to switch the states. The underlying mechanisms were also explored using potential energy landscape. In some scenarios, the loads can actually abrogate its bistability, which is the fundamental functionality of the toggle switch. We also studied naturally-occurring autocatalytic signal transduction switches and showed that their switch-like behaviors can also be undermined and eventually lost when connected to downstream loads. Our work presented in chapter 2 shows that the assumption of modularity has crucial limitations for the two switches. Our study also underscores the necessity to consider the effects of loads in simulating and designing synthetic networks from well-characterized synthetic circuits.

Most studies in synthetic biology were carried out using prokaryotic and single-cell eukaryotic hosts. Due to multifaceted challenges, the predictive powers of synthetic biology have not been extended to plants, among other multicellular and differentiated organisms. Chapter 3 reports our collaborative efforts with Medford lab to complete the engineering-based methodology of synthetic biology for plants. We first utilized mathematical analysis to identify two properties of the synthetic parts required by a functional toggle switch. Two designs of the toggle switch were selected based on these two principles using synthetic parts that we characterized in a previously published work. We then optimized an imaging protocol to quantitatively test the assembled toggle switches. An in-house image processing software was developed to generate quantitative luciferase measurements for shoots and roots of individual plants. The quantitative data enabled us not only to carry out statistical tests but also to devise quantitative modeling to verify that the designed functionalities are achieved. We demonstrated that a functional genetic toggle switch can be constructed in plants using this engineering-based methodology integrating quantitative experiments and computational tools.

A single-cell assay of active and passive intracellular mechanical properties of mammalian cells could give significant insights into cellular processes. Force spectrum microscopy (FSM) is one such technique, which combines the spontaneous motions of probe particles and the mechanical properties of the cytoskeleton measured by active PTMR using optical tweezers to determine the active force spectrum of the cytoskeleton. Though a powerful technique, FSM is instrumentation-demanding and invasive. In chapter 4, we developed an alternative to FSM. To be non-invasive, mitochondria were fluorescently labeled as our endogenous probe particles. To make the FSM less instrumentation-demanding, we replaced the role of active PTMR using passive PTMR in ATP depleted cells. We developed a novel method to identify a range of thermally dominated timescales in the MSDs of ATP depleted cells, so that we can determine the intracellular viscoelasticity using Generalized Stokes-Einstein Relation. We then calculated the force spectrum of active fluctuations by combining the spontaneous fluctuations tracked in control cells and mechanical properties measured in ATP depleted cells. Our results match quantitatively to those obtained by the original FSM. We also studied the roles played by various cytoskeletal components on the active mitochondrial fluctuations to gain insight into the molecular bases of intracellular mechanical properties.

The lack of a general, accessible and reliable delivery method of fluorescent particles into the cytoplasm is a bottleneck for wider applications of PTMR. In chapter five, we demonstrate that a method used for delivering proteins to cells, known as glass bead loading, can deliver fluorescent particles into cells. Using both confocal imaging and particle tracking results under different chemical treatments, we show that glass beads are able to load 100 nm fluorescent particles directly into cytoplasm and probe the mechanical properties of the embedding cytoskeletal network. We also tested the general applicability of bead loading in two more cell

lines. Analysis of the MSD and distribution of directional change provided insights into the complexity of active motion in the cytoplasm. Our observations are consistent with a picture in which the particles are trapped within the actin cytoskeleton, which confines their motion. But due to motor driven fluctuations and cytoskeleton remodeling, the confining cage itself moves over the long timescales. The fluctuations are strongly affected when the actin cytoskeleton is dissolved, and weakly affected by stabilizing it, by inhibiting myosin II or by perturbing the microtubule network. These results suggest that the mechanical microenvironment probed by the glass bead loaded fluorescent particles is strongly dominated by the actin cytoskeleton. Our protocol makes passive and active PTMR more accessible and gives it the potential to become a routine assay of intracellular mechanical properties.

In chapter six, I conclude this dissertation with the most interesting questions, in my viewpoint, that stem out of chapters two to five, and delineate some future directions in order to address these questions.

ACKNOWLEDGEMENTS

I would like to thank my advisor and friend Dr. Ashok Prasad for his support, insights, mentorship and guidance throughout my pursuit of a doctoral degree at CSU. I would like to express my greatest gratitude to Dr. June Medford and other colleagues in the plant synthetic biology project – especially to Dr. Katherine Kiwimagi, Dr. Tessema Kassaw, Dr. Mauricio Antunes, Dr. Christopher Zalewski and Dr. Diane McCarthy – for their help and support. Without the experience working with them, I would not be able to grow into the researcher I am now. I would also like to thank Dr. June Medford, Dr. Brian Munsky, Dr. Kenneth Reardon and Dr. Patrick Shipman for their time and guidance as my current and previous committee members.

I would like to thank all current and previous members of the Prasad lab for their help and supportive discussions, especially to Dr. Elaheh Alizadeh, Dr. Chintan Joshi and Dr. Samanthe Lyons. Working together with them has made my learning experience in the graduate school wonderful. I would like to thank Dr. Keith DeLuca for his help with the confocal microscopy.

I would like to thank my parents for their understanding and support during the seven years I am studying abroad. I would like to thank my lovely and supportive wife, Lei Wang. Working with her in the graduate school to get our doctoral degrees together will be the best years in my life. Finally, I would like to thank my newborn son, Ethan. With all his cries and laughter in the past four months, I found my research and life more meaningful and more complete.

TABLE OF CONTENTS

CHAPTER 1: INTRODUCTION

In last decades, our abilities of manipulation and quantitative measurements of biological systems have seen significant advances, and so have the developments of mathematical theories and computational power. With these advances, scientists and engineers are now endeavoring to characterize biological systems from a more quantitative perspective, and this dissertation finds itself as a part of this trend. This is the overarching theme of the two seemingly very different projects, plant synthetic biology and mechanobiology of mammalian cells, presented in this dissertation. In plant synthetic biology (section 1.1, chapters 2 and 3), I helped develop an engineering-based methodology (as introduced in details in the following section), with associated computational and data analysis tools, which was applied to build a synthetic genetic circuit with designed biological functionalities from quantitatively characterized synthetic parts. In mechanobiology of mammalian cells (section 1.2, chapters 4 and 5), I developed imaging protocols and quantitative methods to characterize the intracellular mechanical properties and to probe the underlying mechanisms on the level of cytoskeleton. In the following parts of this chapter, the two fields, synthetic biology and mechanobiology, are introduced in section 1.1 and section 1.2 respectively.

1.1 Introduction on synthetic biology

Synthetic biology could mean two different fields. One field focuses on developing technologies to synthesize biological macromolecules, including DNA, RNA and protein. The other field generally focuses on the construction of biological systems with pre-designed functionalities through an engineering-based methodology. Throughout the rest of this dissertation, the term “synthetic biology” refers to the latter field unless otherwise indicated. For

the former field, interested readers can refer to the fantastic reviews by Dr. George Church, for example the Ref. [1].

Synthetic biology could trace its roots back to the pioneering work by Monod and Jacob [2], where it was proposed that genetic circuits with virtually any desired property can be constructed from networks of simple regulatory elements [3]. Synthetic biology, as an emerging field, started in 2000 when two papers were published back-to-back in *Nature* reporting constructions of a genetic toggle switch [4] and a genetic oscillator [5] respectively.

1.1.1 Analogy of genetic circuits to electrical circuits

Synthetic biologists seek to advance the field in a way similar to electrical engineers [6,7]. The hierarchical and modular structures found in electrical systems are taken as an analogy to develop synthetic biological systems. On the bottom level in the hierarchy, there are the basic biological components, including DNA, RNA, proteins, and metabolites (e.g., lipids, carbohydrates, amino acids, and nucleotides). Correspondingly, the physical layer of computers includes transistors, capacitors, and resistors. In the device layer, biochemical reactions regulate signal transduction and physical processes, which are analogous to electronic logic gates built on the basis of the physical layer. Both the biochemical reactions and logic gates perform specific computational functions, including sensing and integration of inputs, and delivery of outputs after processing. As modules in computers, biochemical reactions can be assembled into pathways or circuits. A cell can be made of a lot of pathways or circuits, just like a computer is made of numerous modules. On the top of the hierarchy, tissues and cell cultures are comprised of cells connected by cell-cell communications, which are similar to computer networks. Under such an analogy to electrical engineering, the assumption of modularity is pivotal in synthetic biology that aims to rationally design and construct synthetic circuits, cells and tissues with

designed functionality using a bottom-up approach [8]. The assumption of modularity will be discussed in more detail in section 1.1.5.

1.1.2 The engineering-based methodology

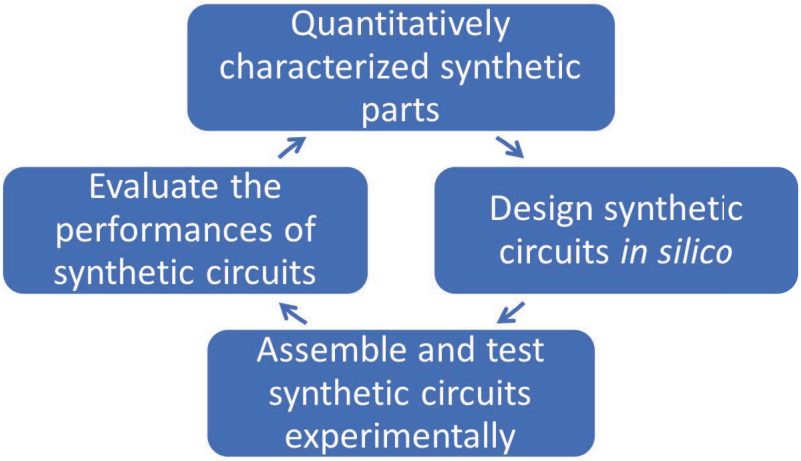

Figure 1.1 The engineering-based methodology is the ideal practice for developing synthetic circuits from quantitatively characterized synthetic parts in synthetic biology.

Following the analogy discussed earlier, it is useful to apply the methodology developed in established engineering fields, like electrical engineering, to synthetic biology (Figure 1.1). Indeed, one important characteristic that distinguishes synthetic biology from the traditional genetic engineering is the integration of mathematical tools and quantitative measurements. The entire workflow of building a functional genetic circuit starts with the design and quantitative characterizations of synthetic parts, including promoters with different expression levels and repressor-promoter pairs [9,10]. In the second step, mathematical models can be formulated, and different combinations of numerical parameters of synthetic parts, characterized in step one, can be fed into the models. The synthetic parts producing desired functionalities *in silico* are then selected to be assembled into synthetic circuits and tested experimentally. If the tested circuit does not satisfy designed functionalities, researchers can either try different combinations of

synthetic parts or change the synthetic parts designs till a functional synthetic circuit is constructed in an iterative manner.

The canonical genetic toggle switch can be taken as a working example to illustrate the workflow. The toggle switch is built from two repressible promoters arranged in a mutually inhibitory network [4]. The workflow started with picking natural repressor-promoter pairs or building synthetic ones, which should be orthogonal to endogenous molecules to reduce undesired interactions [9]. These repressor-promoter combinations were then tested quantitatively, and their operational parameters can be extracted from the experimental data. In the second step, a dimensionless ordinary differential equation (ODE) based model was utilized to help identify the minimum set of conditions on the two repressor-promoter pairs required by a functional toggle switch. Then, the toggle switch design satisfying these conditions was assembled and its functionalities tested. The stability of the two states was tested by removing corresponding inducers and the ability to switch between the two states was also tested. Luckily, the only design of the toggle switch assembled, tested and evaluated in Gardner et al. [4] was reported to be functional as designed. But if this was not the case, the whole workflow can be iterated till a fully functional toggle switch is constructed. In addition to the toggle switch, the repressilator, in which three repressor-promoter combinations are arranged in a ring-shape, was developed following the same workflow [5].

1.1.3 A brief review on synthetic circuit designs

Inspired by the analogy to electrical engineering and networks found in nature, many sophisticated genetic circuits with novel functionalities were designed, constructed and tested in the years following the works of Gardner et al. [4] and Elowitz et al. [5]. The most representative

designs includes logic gates [11], clocks [12], pattern detectors [13], and cell-cell communication modules [14]. In the following, these representative designs of synthetic circuits are reviewed.

Other types of biological molecules can also be incorporated into the circuit designs in addition to transcriptional factors. For example, a gene-metabolic oscillator was designed by integrating metabolite fluxes with a transcriptional network [15]. An oscillation between two inter-convertible metabolite pools was generated through two transcriptionally regulated enzymes [15]. Interestingly, the oscillation is only observed when the glycolytic rate surpasses a preset threshold [15].

Exemplified by the three designs covered so far, early synthetic circuit designs relied only on single cells to realize expected functionalities. Predictable and reliable functionalities can also be realized on the level of cell populations taking advantages of cell-cell communications [7]. The synthetic cell-cell communication module is often based on the quorum sensing machinery found in the bacterium *Vibrio fischeri* [16,17]. Using quorum sensing, a bacterium is able to regulate its own behaviors based on the density of the surrounding population [16,17]. More specifically on the mechanisms, every bacterium in a population secretes acyl-homoserine lactone (AHL), a small signaling molecule that can diffuse across the membranes. When the AHL in the environment reaches a threshold, LuxR, a regulatory protein, can be activated by AHL, binds to the *lux* operator region and activates the expressions of downstream genes [16,17]. As a result of the activation, the bacterium *Vibrio fischeri* becomes luminescent when its population density reaches a threshold [16,17].

By integrating a killer gene at the downstream of the *lux* operator, You et al. constructed a "population control" circuit that can prevent the density of *Escherichia coli (E. coli)* population reaching the limits imposed by the environment [14]. Also using this quorum sensing machinery,

Danino et al. built a genetic clock as an intercellular network of oscillators that enables a growing population of cells to demonstrate synchronized oscillations [12]. Cell-cell communication is also a potential tool for engineering highly sophisticated biological behaviors between heterogeneous cell populations [7].

Besides the transcriptional factors, RNA interference (RNAi), mainly operated by small interfering RNA (siRNA), have also been applied to construct functional synthetic circuits. Interested readers can refer to some excellent reviews on the molecular mechanisms of RNAi, for example, Ref. [18]. Basically, the presence of siRNA prevents the target mRNA from being translated, thus behaving as a NOT gate. By using activating/inhibitory promoters to control the transcriptions of siRNA, it was shown that all the Boolean logic gates can be constructed [11]. Based on this design, a multi-input RNAi-based logic circuit was engineered to identify specific cancer cells [19]. These two sequential studies not only demonstrated the feasibility of RNAi-based circuits but also showcased its potentials for clinical applications.

With the accumulating knowledge on riboswitches and RNA aptamers, scientists and engineers are now able to design RNA aptamers to bind desired metabolites and to cleave mRNA in a directed manner [20]. Combining the knowledge on RNA aptamers and RNA folding, an rationally designed RNA-based scaffold was reported to be able to spatially arrange enzymes into multi-dimensional self-organizing scaffolds [21].

Similar to the RNA scaffold, proteins were also engineered into scaffolds that can spatially recruit metabolic enzymes into a desirable spatial arrangement [22]. This method helps to balance the metabolic flux after the foreign enzymes were incorporated into the metabolic network. A 77-fold increase in product concentration was achieved, along with lower enzyme expression levels and reduced metabolic burden to the host cells [22]. Also using scaffold

proteins, part of the yeast mating MAP kinase pathway was arranged linearly into a unified complex [23]. Such a scaffold not only enables more flexible manipulations of the kinase pathway but also the ability to tune the complex into different functionalities, including ultrasensitive dose response, accelerated or delayed responding dynamics, and tunable adaptation [23].

Promising advancements have been made for protein-based synthetic circuits. There is no photoreceptor in native *E. coli*. A chimeric protein was constructed by combining a cyanobacterial photoreceptor and an *E. coli* intracellular histidine kinase domain, which is able to sense and convert light signals into intracellular chemical signals [24]. As a demonstration, the authors made an *E. coli* film, which expressed light and dark regions accordingly to the inputs on light masks [24]. Following this development, a pattern detector was constructed using an *E. coli* film to detect edges in the light masks [13].

1.1.4 Potential applications of synthetic biology

Despite of being a relatively emerging field, synthetic biology has demonstrated exciting potential to address some of the most urgent global challenges, including healthcare and renewable energy.

Malaria, a mosquito-borne infectious disease, is a major cause of death worldwide, especially in developing countries [25]. It is therefore very important to make anti-malaria drugs affordable to low-income patients living in these developing countries. However, artemisinin, a valuable anti-malaria compound, is isolated from the plant *Artemisia annua*, a herb in Chinese traditional medicine. The market price of artemisinin not only has been high but also has fluctuated widely, making it challenging to control the price of the anti-malaria drug. To address this challenge, a synthetic metabolic pathway to produce artemisinin was successfully engineered

in *E. coli* based on the mevalonate-dependent isoprenoid pathway found in *S. cerevisiae*. Artemisinin can then be produced by the inexpensive fermentation of *E. coli*, potentially a significant progress towards the goal of an affordable anti-malaria drug [26–28].

Cancer is the second leading cause of death in the United States and is a major public health challenge globally [29]. Synthetically engineered *E. coli* strain was reported to be able to hunt solid tumor cells characterized by a combination of hypoxic microenvironment and high populations of certain bacteria [30]. Only when both conditions are satisfied for its AND gate, the *E. coli* cells start secreting invasin to initiate the endocytosis of the tumor cells, thus providing a novel approach for biological therapy [30].

Microalgae-based biofuel holds the potential to replace a significant portion of the fossil fuel consumption and reduce the CO_2 emission globally. However, its production is not yet economically feasible at commercial scales, despite its benefits of high utilization efficiency of sunshine and fast reproduction rate. These benefits are more relevant to optimal laboratory conditions than commercial production conditions. When cultured in the open ponds, which is the most popular and economically viable way, microalgae cell density is very low, accounting for only around 0.1% of the broth. Thus the cost associated to the condensation of the algae biomass is a major bottleneck for algae to become an economically viable option as a future biofuel source [31]. To address this issue, a strain of cyanobacterium was engineered to not only overproduce fatty-acid, an important precursor for the biodiesel production, but also to secrete the fatty-acid into the broth, which has the potential to avoid the costly biomass recovery processes [32]. To further increase the fatty-acid production, this cyanobacterium was incorporated with a Green Recovery strategy to convert the membrane lipids into fatty-acids under CO_2 limitation, which is a signature of termination of the culture [33].

1.1.5 The assumption of modularity and chapter 2

As described in section 1.1.1, the assumption of modularity is central to the development of synthetic biology. In this dissertation, the validity of the assumption of modularity on the circuit level was also studied. We defined modularity as the relative insulation of small subnetworks or circuits inside a larger network from each other [34]. In other words, the synthetic circuits are assumed to maintain their essential properties characterized in isolation when they are combined to form larger synthetic networks. However, recent theoretical and experimental studies suggest that the interactions of synthetic circuits with each other [35–37] and with the host organisms [38,39] may lead to unexpected contextual effects and the invalidity of the assumption of modularity. One of the most interesting example of these unexpected contextual effects is called retroactivity. Synthetic circuits are connected via biochemical interactions with components (loads) from downstream circuits in the larger network, which is unlike electronic circuits connected by insulated wires. These biochemical interactions with loads therefore compete with the interactions inside the synthetic circuits themselves, and incur implicit feedback (retroactivity) between circuits without obvious feedback loops. For example, a recent theoretical analysis has shown that simple binding/unbinding reactions between an oscillator and DNA binding sites (loads) can not only switch the oscillator “on” and “off”, but also be used to tune its oscillating periods [40].

In chapter 2, the effects of loads, and thus the effects of retroactivity, were studied with two types of canonical biochemical switches: the mutual-repression based toggle switch, as described earlier, and a positive feedback based switch found widely in natural signaling pathways. We found that adding loads is able to change the dynamical properties of the toggle switch, characterized as the time needed to switch the states of the toggle switch. Using a novel

computational tool to characterize the potential energy landscape, we also explored the underlying mechanisms of this change in dynamics. In some scenarios, the loads can actually abrogate its bistability, which is the fundamental property of the toggle switch as described in section 1.1.2. Using the same analytical and computational tools, we also studied naturally-occurring autocatalytic signal transduction switches and showed that their switch-like behaviors can also be undermined and eventually lost when connected to downstream loads. Our work presented in chapter 2 underscores the necessity to consider the effects of retroactivity in simulating and designing synthetic networks from well-characterized synthetic circuits, and that retroactivity leads to crucial limitations of the assumption of modularity for synthetic toggle switches and natural signaling switches.

1.1.6 Plant synthetic biology and chapter 3

In the first decade since its emergence as a field, the characteristic techniques and methodology of Synthetic Biology was developed, and more sophisticated synthetic circuits were constructed and reported. Yet these studies were carried out in to prokaryotic and single-cell eukaryotic hosts, including bacterium, yeasts, and cultured mammalian cells, due to their low complexity and ease of genetic manipulation [41]. More recently synthetic circuits have been developed for multi-cellular structures and organoids by programing synthetic intercellular communications [42,43]. Plants were also engineered to sense external ligands and respond in visible color changes, which are potential to serve as sentinel plants [44]. However, the plants, among other multicellular and differentiated organisms, still remain an uncharted territory for synthetic biology's predictive powers from the engineering-based methodology. If similar synthetic circuits, like the toggle switch, could be engineered in plants, both fundamental plant science and various practical applications could benefit significantly [45]. In plant studies, a gene

knock-out could be achieved by simply turning off a synthetic toggle switch controlling that gene, which is particularly valuable to study the lethal mutants of some genes. For practical applications, smart plants can be engineered to carry out novel functions. Genes related to desired plant traits, for example drought resistance or biofuel production, can be controlled more precisely using synthetic circuits rather than being constitutively expressed, thus preventing unnecessary wastes of valuable nutrients among other potential benefits.

The challenges to advance plant synthetic biology are multifaceted, including greater complexity in plant genomes and protein networks, lack of characterized synthetic parts in plants, positional effects of T-DNA insertion, and lack of tools for data analysis and computational, to just name a few [45]. In a close collaboration with Medford lab, we first developed a semi-high-throughput method to design, construct, test and quantitatively characterize synthetic repressor-promoter pairs for plant synthetic biology using transient expression assays [9]. This study is a part of the initial development of methodology to expand the power of synthetic biology to plants [46].

Chapter 3 reports our recent collaborative efforts with Medford lab to complete the engineering-based methodology as described in section 1.1.2 for plant synthetic biology. We first utilized mathematical analysis to identify two properties of the synthetic parts required by a functional toggle switch similar as in Gardner et al. [4]. Two toggle switches were designed based on these two principles using synthetic parts that we characterized using the transient expression assays using protoplasts [9].

We then optimized a quantitative imaging protocol to test the functionalities of assembled toggle switches. We developed an in-house image processing software to measure luciferase expression level quantitatively for shoots and roots of individual plants. The quantitative data

enabled us not only to formulate statistical tests but also to devise quantitative modeling to verify that the designed characteristics are achieved. We developed a Markov Chain Monte Carlo (MCMC) based method to sample the space of good parameter values that fit the plant data to an ODE model of a toggle switch. This ODE model is similar to that in Gardner et al. [4], but different in terms of being dimensional to match the experimental data and including inducible terms to describe the switching dynamics. In the end, these parameter values were used to solve the ODEs numerically to assess the bistability of the toggle switch tested experimentally. We demonstrated that a functional genetic toggle switch can be constructed in plants using this engineering-based methodology integrating quantitative experiments and computational tools.

1.2 Introduction on mechanobiology of mammalian cells

The overall goal of our projects summarized in chapters 4 and 5 is to develop methods for characterizing the intracellular mechanical properties of mammalian cells and to gain deeper insights into the underlying mechanisms.

1.2.1 General introduction on particle tracking microrheology

The classic starting point to understand the general principle used to measure the intracellular mechanical properties, as applied and developed in chapters 4 and 5, is the case of a spherical particle suspended in water. The motion of this particle appears random as a result of random collisions by surrounding water molecules, known as Brownian motion. There are three factors involved in the Brownian motion: the thermal force from the collisions with water molecules, the mechanical property of water, or its viscosity, and the resulting motion of the particle. A relationship between the thermal force, viscosity and random motion is described by the classic Stokes-Einstein relation:

$$\frac{\langle \Delta x^2 \rangle}{4t} = D = \frac{k_B T}{6\pi\eta R}$$

where $\langle \Delta x^2 \rangle$ is the mean square displacement (MSD) which describes the particle motion, $k_B T$ characterizes the level of the thermal force, η is the viscosity of the fluid, R the radius of the particle and D the diffusion coefficient.

Consider now what we would expect to observe when the same particle is embedded in a purely elastic material, such as a piece of rubber. The same thermal force still acts on the particle. As opposed to the response of a fluid, in an elastic material each time the particle is driven into a random direction, it is pushed back by the elastic forces immediately to its original position. The motion of the particle is thus limited to fluctuations in a relatively constant range. Here too there are also three players involved, the motion of the particle, the thermal force and the mechanical property (in this case the elasticity). With the thermal force known, we can also infer the mechanical property of the material by observing the motion of the embedded particle. A particle moving in a larger range indicates that the material has a smaller coefficient of elasticity, and a particle moving in a smaller range indicates a larger coefficient of elasticity.

The cytoplasm of mammalian cells is viscoelastic, exhibiting both viscous and elastic characteristics when undergoing deformation. If we deliver the same spherical particle into the cytoplasm and let the same thermal forces act on the particle, we should be able to infer the viscoelasticity of the cytoplasm based on the motion of this particle following the same strategy introduced earlier. However, the relation between the particle motion and the forces become more complex in this case because a viscoelastic material exhibits a delayed response to a perturbation. The mathematical expression to relate the viscoelasticity and the motion of such a particle is called the generalized Stokes-Einstein relation (GSER) [47], introduced in more detail in section 1.2.6. Although the GSER is mathematically more complex than the classic Stokes-Einstein relation, the basic idea is essentially the same as in the two starting examples. As with

the classic Stokes-Einstein relation, the GSER only works under thermal equilibrium, when thermal force is the only driving force for the particle motion.

In living cells, there are many active forces generated in the expense of cellular energy, mostly in the form of adenosine triphosphate (ATP), in addition to the ubiquitous thermal force. These active forces include the contractile forces generated by myosins, which power our muscles, the forces generated by molecular motor-driven directed motions of vesicles, forces resulting from polymerization and depolymerization the cytoskeleton and so on. Therefore, the particle motion inside the cytoplasm is driven not only by the thermal force but also by these uncharacterized active forces. Although the resulting motion may still seem like a Brownian motion, the previous strategy does not hold any longer [48]. In this case, the active forces are also unknown, as is the viscoelasticity of the cytoplasm, and we are unable to infer two unknowns from one known quantity, the measured particle motion. Force spectrum microscopy (FSM) (3), covered in more details in chapter 4, was proposed to address this challenge to measure the intracellular mechanical properties and extract information on the intracellular active forces as well. The FSM also works by applying the general principle introduced earlier but in two steps. First, in an independent experiment, one particle embedded in the cytoplasm is driven by a known force, applied by an optical tweezer, dominating over the intracellular thermal force and active forces. Combining the known applied force and measurements of the resulting particle motion, the viscoelasticity of the cytoplasm can be determined. In the second step, the total forces combining thermal force and active forces can be determined from the spontaneous particle motion observed in cytoplasm in its native state and the intracellular viscoelasticity measured in the first step. Since the thermal force is essentially known, the information on the active forces can be extracted.

Despite apparent differences in particular theories and techniques, the general principle for the particle-tracking-based measurements of intracellular mechanical properties is the same: only one unknown can be determined from the other two known quantities among the three involving factors of driving force (thermal or active or both or applied), particle motion and intracellular mechanical properties. As introduced in detail in section 1.2.5, this general principle can be generalized to understand many other methods used to measure cellular mechanical properties, despite different technology-specific driving forces and experimentally measurable quantities like the particle motion.

1.2.2 Importance of mechanical properties of mammalian cells

Cellular mechanical properties play significant roles in many physiological activities, for example, cell motility, mitosis and differentiation. Cells with higher motility are generally found to be more pliable than their less motile counterparts [49]. Drastic changes in mechanical properties were characterized as cells progress through different phases in mitosis [50,51] and disruption in cellular mechanical properties could lead to mitotic arrest [51]. Undifferentiated human embryotic stem cells (hESCs) have lower elasticity and viscosity than their differentiated counterparts as measured by a variety of methods [52]. In addition, these intracellular mechanical properties were found to correlate with the degree of differentiation [53]. Deviations from normal cellular mechanical properties were found in tumorigenic and pathogenic processes of significant importance. Cancer cells were shown to be less elastic than normal cells generally and increasing softness appeared to correlate with an increased metastatic potential [54]. Different mechanical properties of the cancer cells are also required at different stages of the metastatic process to successfully form metastasis [55]. Changes in cellular mechanical properties were also reported in pathogenic processes other than cancer, including malaria, sickle

cell anemia and asthma [56]. Mechanical properties of plant cells were also reported to play significant roles in physiological processes, such as the gravisensors [57]. Therefore, better characterizations of cellular mechanical properties may provide more insights into the fundamental cell biology from a mechanical perspective, and could lead to novel medical applications. Thus, cancer diagnosis for example may be aided by mechanical signatures which are essentially label-free [58]. Furthermore, these established mechanical signatures can be used as physical biomarkers to screen and evaluate novel pharmaceutical chemicals targeting cancer metastasis and other pathogenic processes [59].

1.2.3 Cytoskeleton and the mechanical properties

The mechanical properties of mammalian cells are dominantly controlled by the cytoskeleton, which is an interconnected network of filamentous polymers and associated regulatory proteins [60]. There are mainly three types of cytoskeletal polymer: microtubules, actin filaments and various polymers collectively grouped as intermediate filaments.

Microtubules are 24 nm-diameter hollow polymers of heterodimers of α-tubulin and β-tubulin with a persistent length, a measure of filament flexibility that increases with stiffness, of around 3 mm. Microtubules can thus form bundles of rigid fibers that make excellent structural scaffolds, which plays an important role in determining cell shapes. Microtubules also serve as linear tracks for directed movements of organelles and small vesicles, yet microtubules are often found to bend significantly by compressive forces in cytoplasm of cultured mammalian cells [61]. Due to its inherent polarity endowed by α-tubulin and β-tubulin, these linear tracks of microtubules are able to support a two-way traffic. Microtubules are highly dynamic and constantly undergo stable growing and rapidly breaking-up, enabling the cell to respond to subtle

environmental changes promptly. Microtubules also play important roles in the error-proof segregation of chromosomes at mitosis and meiosis.

Filamentous (F) actin is a polymer of two twisting chains of free actin monomers, G-actins (G for globular), with a diameter of 4~7 nm. F-actin assembles into various networks to perform different functions with the help of an array of actin binding proteins, including capping proteins, filament nucleation proteins, cross-linking proteins and severing proteins. These actin binding proteins also enable dynamical and regulated controls of the actin network. The actin network plays important roles in determining cell shape, cellular locomotion, cell division etc.

Intermediate filaments include a diverse group of polymers with intermediate diameters (around 10 nm in average) compared to microtubule and actin. A monomer of an Intermediate filament polymer commonly consists of a central α-helical rod and nonhelical head and tail. Most variation across different monomers happens in the head and tail. The basic building block of intermediate filaments is a tetramer joined by their central α-helical region to form a coiled structure. In the cytoplasm, intermediate filaments tend to form wavy bundles that extend from the nucleus to the cellular membranes. Intermediate filaments are the most stable of the cytoskeletal filaments in terms of dynamics, and the most extensile due to their central α-helical region. Therefore, intermediate filaments are believed to play important roles to maintain cellular integrity.

Interested readers can refer to more detailed coverage on the biophysical and biochemical properties of these cytoskeletal polymers in reviews, such as ref. [62], and cell biology textbooks, like [63]. In summary, the cytoskeleton, as a dynamical network of all three polymers, is able to resist deformations but also respond to externally applied forces and together determine the cellular mechanical properties [60].

1.2.4 Methods to measure cellular mechanical properties

Many methods have been adopted or developed to measure the mechanical properties of mammalian cells. Despite the seeming differences in the underlying theories and enabling technologies, all these methods follow the general principle introduced in section 1.2.1.

Atomic force microscopy (AFM) [64] is one of the most popular techniques to probe the mechanical properties of live cells [65]. AFM probes the cellular mechanical properties from the outside through direct contacts using the cantilever as an indenter. The force applied by the cantilever can be determined by the Hooke's law using its bending (equivalent to the displacement) and stiffness (equivalent to the spring constant). The typical output from AFM is the force-versus-displacement curve (commonly referred as force curve). The cellular elasticity can be quantified with spatial resolution by fitting the force curves to quantitative models. Recently, direct extraction of the viscoelasticity from the force curves was developed [66]. The magnetic twisting cytometry [67,68] measures the rocking motions of tracers adhered to the apical cell surface by applying oscillatory magnetic forces. Both AFM and magnetic twisting cytometry mainly probes the mechanical properties of the cortical actin network underneath the cytoplasm membrane and the probing of intracellular cytoskeleton networks is therefore perturbed [69].

Micropipette aspiration [70,71], microfluidic optical stretching [72] and other microfluidic platforms [73,74] probe global mechanical properties of a suspended cell as a whole object by applying a known force and measuring the resulting deformations. More specifically, a suspended cell can be aspirated by a micropipette with a pre-determined force and the mechanical properties can be determined as a function of the deformation into the micropipette [70,71]. Similarly, optical stretching applies a known force via a pair of optical tweezers and the

deformation of a whole cell can be measured in a high throughput setting [72]. However, most cells in suspension are not in their physiologically relevant conditions. Therefore, the mechanical properties measured by these methods may not be a good representation of the properties of the cells in vivo or even of cultured cells on two-dimensional surfaces.

1.2.5 Particle-tracking microrheology

Compared to the methods described above, particle-tracking microrheology (PTMR) [75,76] has the ability to probe the intracellular mechanical properties without being perturbed by the cortical actin network, to probe local mechanical properties (instead of the global mechanical responses of whole cells) with spatial resolution, and to probe mechanical properties without direct contact with the cell (thus applicable for cells cultured in 3D matrixes as an example) among other benefits [69].

The PTMR can be further classified into passive or active PTMR, depending on whether external forces are applied to drive the probe movements [75]. In passive PTMR, the probe particles are driven purely by thermal forces. Passive PTMR has its roots in the classic works by Einstein [77] and Perrin [78], as introduced in section 1.2.1. However, the classic Stokes-Einstein equation can only be used to determine frequency-independent viscosity, and thus limits its applications to biological materials which are generally better characterized by frequency-dependent viscoelasticity. To tackle this issue, the Stokes-Einstein equation was generalized to determine frequency-dependent viscoelasticity in 1995 [47], which is named the Generalized Stokes-Einstein Relation (GSER) [79].

The application of GSER assumes that [79]: 1) the shear stress relaxation in the locality of the particle is identical to that of the bulk fluid subjected to a perturbing shear strain; 2) the complex fluid under study can be treated as an isotropic, incompressible continuum around a

sphere, and the continuum assumption is valid when the length scales of heterogeneity in the discrete microstructures within the fluid are much smaller than the probe particle; 3) inertia of the particle can be ignored, which only becomes an issue at timescales of microseconds; 4) implicitly Stokes drag for viscous fluids (with no-slip boundary conditions) can be generalized to viscoelastic fluids at all frequency. The last assumption is important and theoretical work has shown that the GSER is valid at best for a range of frequencies, which however may span the physiologically relevant range for cell mechanics measurements [80,81]. In addition, the GSER assumes that the system under study is at thermal equilibrium and that the movements of the probe particles are driven solely by thermal fluctuations, which is same as the Stokes-Einstein equation. When the system satisfies these assumptions, the viscoelasticity across a wide range of frequencies can be determined relatively easily through fluctuation-dissipation theorem (FDT) [47].

The validity of GSER was tested by comparing the results of various complex fluids measured by GSER to well-established mechanical (rheological) measurements on bulk samples [47,79,82,83], which supports the above assumptions phenomenologically. On the numerical side, the accuracy of GSER was initially restricted not only by the limited frequency range of the data used for the calculation, but also by requiring an arbitrary functional form to fit the MSD [47,82]. These limitations were later released by avoiding the numerical transformations and using an algebraic approximation of the MSD in the form of either a first-order [79,84] or a second-order logarithmic time derivatives [83].

After the introduction of GSER, its advantages, requiring only a small volume of sample and covering an extended range of frequencies, quickly drew attentions from the biophysical community to measure cell-free biological samples [79,85]. Quantitative mechanical properties

of live cells (COS7, a kidney epithelial cell line) were also extracted using GSER, in which the movements of single endogenous lipid granules was recorded using laser reflection single-particle tracking [86]. This single-particle tracking was later generalized into video multiple-particle tracking to enable subcellular resolutions on local mechanical properties and thus the ability to evaluate their heterogeneity [87]. Also in this study, carboxylated fluorescent particles were microinjected into the cytoplasm and used as probes, for the first time, rather than the endogenous granules tracked in previous live cell studies [87]. The MSDs measured in the live cells appear to be subdiffusive at short timescales and diffusive at long timescales [87], which resembles that of viscoelastic polymer solutions (flexible polymers that are not permanently cross-linked) [83]. Such behaviors of MSDs were used to determine the viscoelastic properties of the cytoplasm by applying the GSER directly [53,69,86–90].

However, the cytoplasm is an active material driven by chemical energy, mainly in the form of Adenosine Triphosphate (ATP) [91,92]. The Brownian-like motions observed in the control cells are thus driven by both thermal and active forces, specially at long timescales [48,67,93,94]. Therefore, the assumption of thermal equilibrium in GSER is not valid and incorrect cellular viscoelasticity could be determined from MSDs when GSER is applied directly [48,67,95], as in studies previously described [53,69,86–90]. The presence of active forces limits the applications of GSER to either high frequencies in MSDs of control cells [94] or to an extended range of frequencies in ATP depleted cells [96]. The MSDs of the probe particles, in general, still convey important information about the active forces and cytoskeletal dynamics, which can be interpreted on their own [97] or in combinations with other techniques including active PTMR [48] and AFM [98].

In active PTMR, probe particles are driven by constant or oscillatory external forces, often applied by optical or magnetic tweezers [75]. Active PTMR is generally less accessible than passive PTMR with the requirement of specialized instrumentation and expertise to manipulate the probes. One important question is whether active PTMR measures the "true" viscoelasticity as experienced by the particles in cytoplasm in its native state. In particular, optical tweezers used in active PTMR may be strong enough to probe the non-linear responses of the cytoplasm [81,99,100]. Yet previous works have shown excellent consistency between active and passive PTMR [67,94], which lays the experimental foundation to combine the two techniques and obtain more accurate and complete measurements of intracellular mechanical properties. A representative technique following this strategy is the force spectrum microscopy (FSM)[48]. As introduced in section 1.2.1, viscoelastic properties can be first determined by active PTMR, then the spectrum of active forces can be extracted from the spontaneous fluctuations without external forces [48,101–103].

1.2.6 Chapter 4 – simpler and noninvasive alternative to FSM

Though a powerful technique, FSM, as it was originally developed, requires advanced instruments including optical tweezers, microinjectors and confocal microscopes simultaneously [48], which significantly limits its wider application. In addition, microinjecting fluorescent particles into single cells is not only labor-intensive and requiring experienced operators, but also introduces non-physiological disturbance to cells under study. An alternative of FSM that requires fewer instruments and is non-invasive would be of significant importance for wider applications of FSM.

In chapter 4, we developed such an alternative to FSM. To be non-invasive, mitochondria were fluorescently labeled as our probe particles and morphological analysis were carried out to

identify mitochondria that are ideal as endogenous probes for intracellular mechanical properties. The morphological information of each mitochondrion was also used in the later FSM calculations to improve the accuracy. To make the FSM less instrumentation-demanding, we replaced the role of active PTMR by using passive PTMR in ATP depleted cells. This is based on the fact that previous work have shown excellent consistency between active and passive PTMR [67,94]. Furthermore, it has also been shown that the GSER can be applied to an extended range of frequencies in ATP depleted cells in passive PTMR [96]. We developed a method to identify a range of thermally dominated timescales in the MSDs of ATP depleted cells, so that we can determine the intracellular viscoelasticity using GSER. We then calculated the force spectrum of active fluctuations by combining the spontaneous fluctuations tracked in control cells and viscoelasticity measured in ATP depleted cells. Our results match quantitatively to those obtained by the original FSM. Using the developed experimental protocol and tools for data analysis, we studied the roles played by various cytoskeletal components on the active mitochondrial fluctuations to gain insights into the molecular bases of complex mechanical properties.

1.2.7 Chapter 5: bead loading -- a general, robust and simple method to deliver fluorescent particles into the cytoplasm

As discussed in more detail in chapter 4, mitochondria, other endogenous organelles [104,105], and fluorescent particles are probably measuring different aspects of cellular mechanical properties, at different length-scales and dominated by different components of the cytoskeleton. Further work is required to link different aspects of the cellular cytoskeleton together, as measured by fluorescent particles as well as endogenous probes, such as

mitochondria as well as other endogenous organelles [48,104,106]. To achieve this goal, we need to measure the intracellular mechanical properties probed by fluorescent particles.

However, there is a lack of general, robust and simple methods to deliver exogenous probes into the cytoplasm for both passive and active PTMR. The most widely-used techniques for delivering probe particles into cells, used for both passive and active PTMR are microinjection [87] and ballistic injection [69,88]. Microinjection is the most classic and earliest-applied method as mentioned earlier to deliver fluorescent particles into the cytoplasm for PTMR [87]. However, it is tedious, low-throughput and may cause non-physiological trauma to cells under study [69]. Ballistic injection was later optimized to deliver fluorescent particles in a high throughput manner [69,88]. There are also non-physiological perturbations like vacuum and non-sterile conditions in the protocol of ballistic injection [69], similar as microinjection. The ballistic injection also suffers from its own disadvantages, which is the need for extensive optimizations of many operational parameters in the protocol for new cell types [69]. In addition, both techniques require sophisticated instruments and expertise to operate.

In chapter 5, we proposed that an old technique called bead loading [107] could serve as a general, robust and simple delivery method for fluorescent particle into the cytoplasm. Bead loading works by disrupting the cellular membrane mechanically and creating transient channels to allow the fluorescent particles diffuse into the cells [108]. The generality of bead loading was supported by positive results in four different cell lines. Using various cytoskeletal drugs, the bead loaded fluorescent particles were shown to probe the mechanical properties of cytoplasm. In addition, the drug treatment results of bead loaded fluorescent particles indeed support that mitochondria and fluorescent particles are probing different aspects of the cytoskeleton, with

mitochondrial fluctuations influenced by both microtubules and actin, and fluorescent particles dominantly influenced by actomyosin.

REFERENCES

1. Kosuri S, Church GM. Large-scale de novo DNA synthesis: Technologies and applications. *Nat Methods.* 2014;11: 499–507. doi:10.1038/nmeth.2918

2. Medford JI, Prasad A. Towards programmable plant genetic circuits. *Plant J.* 2016;87: 139–148. doi:10.1111/tpj.13235

3. Monod J, Jacob F. Teleonomic mechanisms in cellular metabolism, growth, and differentiation. *Cold Spring Harb Symp Quant Biol.* 1961;26: 389–401.

4. Gardner TS, Cantor CR, Collins JJ. Construction of a genetic toggle switch in Escherichia coli. *Nature*. 2000;403: 339–42. doi:10.1038/35002131

5. Elowitz MB, Leibler S. A synthetic oscillatory network of transcriptional regulators. *Nature*. 2000;403: 335–8. doi:10.1038/35002125

6. Endy D. Foundations for engineering biology. *Nature*. 2005;438: 449–53. doi:10.1038/nature04342

7. Andrianantoandro E, Basu S, Karig DK, Weiss R. Synthetic biology: New engineering rules for an emerging discipline. *Mol Syst Biol.* 2006;2: 1–14. doi:10.1038/msb4100073

8. Cooling MT, Rouilly V, Misirli G, Lawson J, Yu T, Hallinan J, et al. Standard virtual biological parts: a repository of modular modeling components for synthetic biology. *Bioinformatics*. 2010;26: 925–931. doi:10.1093/bioinformatics/btq063

9. Schaumberg KA, Antunes MS, Kassaw TK, Xu W, Zalewski CS, Medford JI, et al. Quantitative characterization of genetic parts and circuits for plant synthetic biology. *Nat Meth.* 2016;13: 94–100. Available: http://dx.doi.org/10.1038/nmeth.3659

10. Ellis T, Wang X, Collins JJ. Diversity-based, model-guided construction of synthetic gene networks with predicted functions. *Nat Biotechnol.* 2009. 27: 465–71. doi:10.1038/nbt.1536

11. Rinaudo K, Bleris L, Maddamsetti R, Subramanian S, Weiss R, Benenson Y. A universal RNAi-based logic evaluator that operates in mammalian cells. *Nat Biotechnol.* 2007;25: 795–801. doi:10.1038/nbt1307

12. Danino T, Mondragón-Palomino O, Tsimring L, Hasty J. A synchronized quorum of genetic clocks. *Nature*. 2010;463: 326–30. doi:10.1038/nature08753

13. Tabor JJ, Salis HM, Simpson ZB, Chevalier A a, Levskaya A, Marcotte EM, et al. A synthetic genetic edge detection program. *Cell*. 2009;137: 1272–81. doi:10.1016/j.cell.2009.04.048

14. You L, Sidney R, Iii C, Weiss R, Arnold FH. Programmed population control by cell – cell communication and regulated killing. *Nature*. 2004;428: 868–871. doi:10.1038/nature02468.1.

15. Fung E, Wong WW, Suen JK, Bulter T, Lee S-G, Liao JC. A synthetic gene – metabolic oscillator. *Nature*. 2005;435: 118–122. doi:10.1038/nature03503.1.

16. Fuqua C, Winans SC, Greenberg EP. CENSUS AND CONSENSUS IN BACTERIAL ECOSYSTEMS: The LuxR-LuxI Family of Quorum-Sensing Transcriptional Regulators. *Annu Rev Microbiol.* 1996;50: 727–751. doi:10.1146/annurev.micro.50.1.727

17. Bassler BL. How bacteria talk to each other: Regulation of gene expression by quorum sensing. *Curr Opin Microbiol.* 1999;2: 582–587. doi:10.1016/S1369-5274(99)00025-9

18. Wilson RC, Doudna JA. Molecular Mechanisms of RNA Interference. *Annu Rev Biophys*. 2013;42: 217–239. doi:10.1146/annurev-biophys-083012-130404

19. Xie Z, Wroblewska L, Prochazka L, Weiss R, Benenson Y. Multi-input RNAi-based logic circuit for identification of specific cancer cells. *Science*. 2011;333: 1307–11. doi:10.1126/science.1205527

20. Isaacs FJ, Dwyer DJ, Collins JJ. RNA synthetic biology. *Nat Biotechnol.* 2006;24: 545–554. doi:10.1038/nbt1208

21. Delebecque CJ, Lindner AB, Silver PA, Aldaye FA. Organization of intracellular reactions with rationally designed RNA assemblies. *Science.* 2011;333: 470–4. doi:10.1126/science.1206938

22. Dueber JE, Wu GC, Malmirchegini GR, Moon TS, Petzold CJ, Ullal A V., et al. Synthetic protein scaffolds provide modular control over metabolic flux. *Nat Biotechnol.* 2009;27: 753–759. doi:10.1038/nbt.1557

23. Bashor CJ, Helman NC, Yan S, Lim WA. Using engineered scaffold interactions to reshape MAP kinase pathway signaling dynamics. *Science.* 2008;319: 1539–43. doi:10.1126/science.1151153

24. Levskaya A, Chevalier AA, Tabor JJ, Simpson ZB, Lavery LA, Levy M, et al. Engineering Escherichia coli to see light. *Nature*. 2005;438: 441–442. doi:10.1038/nature04405

25. Miller LH, Baruch DI, Marsh K, Doumbo OK. The pathogenic basis of malaria. *Nature*. 2002;415: 673–679. doi:10.1038/415673a

26. Martin VJJ, Pitera DJ, Withers ST, Newman JD, Keasling JD. Engineering a mevalonate pathway in Escherichia coli for production of terpenoids. *Nat Biotechnol.* 2003;21: 796–802. doi:10.1038/nbt833

27. Ro DK, Paradise EM, Quellet M, Fisher KJ, Newman KL, Ndungu JM, et al. Production

of the antimalarial drug precursor artemisinic acid in engineered yeast. *Nature*. 2006;440: 940–943. doi:10.1038/nature04640

28. Hale V, Keasling JD, Renninger N, Diagana TT. Microbially derived artemisinin: A biotechnology solution to the global problem of access to affordable antimalarial drugs. *Am J Trop Med Hyg.* 2007;77: 198–202. doi:77/6_Suppl/198 [pii]

29. Siegel RL, Miller KD, Jemal A. Cancer statistics, 2018. *CA Cancer J Clin.* 2018;68: 7–30. doi:10.3322/caac.21442

30. Anderson JC, Clarke EJ, Arkin AP, Voigt CA. Environmentally controlled invasion of cancer cells by engineered bacteria. *J Mol Biol.* 2006;355: 619–627. doi:10.1016/j.jmb.2005.10.076

31. Wang L, Dandy DS. A microfluidic concentrator for cyanobacteria harvesting. *Algal Res.* 2017;26: 481–489. doi:10.1016/j.algal.2017.03.018

32. Liu X, Sheng J, Curtiss III R. Fatty acid production in genetically modified cyanobacteria. *Proc Natl Acad Sci.* 2011;108: 6899–6904. doi:10.1073/pnas.1103014108

33. Liu X, Fallon S, Sheng J, Curtiss R. CO2-limitation-inducible Green Recovery of fatty acids from cyanobacterial biomass. *Proc Natl Acad Sci.* 2011;108: 6905–6908. doi:10.1073/pnas.1103016108

34. Wagner GP, Pavlicev M, Cheverud JM. The road to modularity. *Nat Rev Genet.* 2007;8: 921–931. doi:10.1038/nrg2267

35. Del Vecchio D, Ninfa AJ, Sontag ED. Modular cell biology: retroactivity and insulation. *Mol Syst Biol.* 2008;4: 161. doi:10.1038/msb4100204

36. Ventura AC, Jiang P, Van Wassenhove L, Del Vecchio D, Merajver SD, Ninfa AJ. Signaling properties of a covalent modification cycle are altered by a downstream target. *Proc Natl Acad Sci.* 2010;107: 10032–7. doi:10.1073/pnas.0913815107

37. Jiang P, Ventura AC, Sontag ED, Merajver SD, Ninfa AJ, Del Vecchio D. Load-induced modulation of signal transduction networks. *Sci Signal.* 2011;4: ra67. doi:10.1126/scisignal.2002152

38. Mather WH, Hasty J, Tsimring LS, Williams RJ. Translational Cross Talk in Gene Networks. *Biophys J.* 2013;104: 2564–2572. doi:10.1016/j.bpj.2013.04.049

39. Tan C, Marguet P, You L. Emergent bistability by a growth-modulating positive feedback circuit. *Nat Chem Biol.* 2009;5: 842–848. doi:10.1038/nchembio.218

40. Jayanthi S, Del Vecchio D. Tuning Genetic Clocks Employing DNA Binding Sites. Thattai M, editor. *PLoS One.* 2012;7: e41019. doi:10.1371/journal.pone.0041019

41. Markson JS, Elowitz MB. Synthetic biology of multicellular systems: New platforms and

applications for animal cells and organisms. *ACS Synth Biol.* 2014;3: 875–876. doi:10.1021/sb500358y

42. Morsut L, Roybal KT, Xiong X, Gordley RM, Coyle SM, Thomson M, et al. Engineering Customized Cell Sensing and Response Behaviors Using Synthetic Notch Receptors. *Cell.* 2016;164: 780–791. doi:10.1016/j.cell.2016.01.012

43. Guye P, Ebrahimkhani MR, Kipniss N, Velazquez JJ, Schoenfeld E, Kiani S, et al. Genetically engineering self-organization of human pluripotent stem cells into a liver bud-like tissue using Gata6. *Nat Commun.* 2016;7: 1–12. doi:10.1038/ncomms10243

44. Antunes MS, Morey KJ, Smith JJ, Albrecht KD, Bowen TA, Zdunek JK, et al. Programmable Ligand Detection System in Plants through a Synthetic Signal Transduction Pathway. Fernandez-Fuentes N, editor. *PLoS One.* 2011;6: e16292. doi:10.1371/journal.pone.0016292

45. Medford JI, Prasad A. Plant Science. Plant synthetic biology takes root. *Science*. 2014;346: 162–3. doi:10.1126/science.1261140

46. Kassaw TK, Donayre-Torres AJ, Antunes MS, Morey KJ, Medford JI. Engineering synthetic regulatory circuits in plants. *Plant Sci.* 2018; 0–1. doi:10.1016/j.plantsci.2018.04.005

47. Mason TG, Weitz DA. Optical measurements of frequency-dependent linear viscoelastic moduli of complex fluids. *Phys Rev Lett.* 1995;74: 1250–1253. doi:10.1103/PhysRevLett.74.1250

48. Guo M, Ehrlicher AJ, Jensen MH, Renz M, Moore JR, Goldman RD, et al. Probing the stochastic, motor-driven properties of the cytoplasm using force spectrum microscopy. *Cell*. 2014;158: 822–832. doi:10.1016/j.cell.2014.06.051

49. Luo Q, Kuang D, Zhang B, Song G. Cell stiffness determined by atomic force microscopy and its correlation with cell motility. *Biochim Biophys Acta - Gen Subj*. 2016;1860: 1953–1960. doi:10.1016/j.bbagen.2016.06.010

50. Li M, Dang D, Liu L, Xi N, Wang Y. Atomic force microscopy in characterizing cell mechanics for biomedical applications: A review. *IEEE Trans Nanobioscience.* 2017;16: 523–540. doi:10.1109/TNB.2017.2714462

51. Cattin CJ, Düggelin M, Martinez-Martin D, Gerber C, Müller DJ, Stewart MP. Mechanical control of mitotic progression in single animal cells. *Proc Natl Acad Sci.* 2015;112: 11258–11263. doi:10.1073/pnas.1502029112

52. Earls JK, Jin S, Ye K. Mechanobiology of Human Pluripotent Stem Cells. *Tissue Eng part B.* 2013;19: 420–430. doi:10.1089/ten.teb.2012.0641

53. Daniels BR, Hale CM, Khatau SB, Kusuma S, Dobrowsky TM, Gerecht S, et al. Differences in the Microrheology of Human Embryonic Stem Cells and Human Induced

Pluripotent Stem Cells. *Biophys J.* 2010;99: 3563–3570. doi:10.1016/j.bpj.2010.10.007

54. Alibert C, Goud B, Manneville JB. Are cancer cells really softer than normal cells? *Biol Cell.* 2017;109: 167–189. doi:10.1111/boc.201600078

55. Wirtz D, Konstantopoulos K, Searson PCPPC. The physics of cancer: the role of physical interactions and mechanical forces in metastasis. *Nat Rev Cancer.* 2011;11: 522. doi:10.1038/nrc3080

56. Lee GYH, Lim CT. Biomechanics approaches to studying human diseases. *Trends Biotechnol.* 2007;25: 111–118. doi:10.1016/j.tibtech.2007.01.005

57. Bérut A, Chauvet H, Legué V, Moulia B, Pouliquen O, Forterre Y. Gravisensors in plant cells behave like an active granular liquid. *Proc Natl Acad Sci.* 2018;115: 5123–5128. doi:10.1073/pnas.1801895115

58. Yu W, Sharma S, Gimzewski JK. Nanocytology as a potential biomarker for cancer. *Biomark Med.* 2017;11: 213–216. doi:10.2217/bmm-2017-0019

59. Krishnan R, Park JA, Seow CY, Lee PVS, Stewart AG. Cellular Biomechanics in Drug Screening and Evaluation: Mechanopharmacology. *Trends Pharmacol Sci.* 2016;37: 87–100. doi:10.1016/j.tips.2015.10.005

60. Fletcher DA, Mullins RD. Cell mechanics and the cytoskeleton. *Nature*. 2010. 485–492. doi:10.1038/nature08908

61. Brangwynne CP, MacKintosh FC, Weitz D a. Force fluctuations and polymerization dynamics of intracellular microtubules. *Proc Natl Acad Sci.* 2007;104: 16128–16133. doi:10.1073/pnas.0703094104

62. Huber F, Schnauß J, Rönicke S, Rauch P, Müller K, Fütterer C, et al. Emergent complexity of the cytoskeleton: From single filaments to tissue. *Adv Phys.* 2013;62: 1–112. doi:10.1080/00018732.2013.771509

63. Phillips R, Kondev J, Theriot J, Garcia H. Physical biology of the cell. Garland Science; 2012.

64. Binnig G, Quate CF. Atomic Force Microscope. *Phys Rev Lett.* 1986;56: 930–933. doi:10.1103/PhysRevLett.56.930

65. Kuznetsova TG, Starodubtseva MN, Yegorenkov NI, Chizhik SA, Zhdanov RI. Atomic force microscopy probing of cell elasticity. *Micron.* 2007;38: 824–833. doi:10.1016/j.micron.2007.06.011

66. Efremov YM, Wang WH, Hardy SD, Geahlen RL, Raman A. Measuring nanoscale viscoelastic parameters of cells directly from AFM force-displacement curves. *Sci Rep.* 2017;7: 1–14. doi:10.1038/s41598-017-01784-3

67. Hoffman BD, Massiera G, Van Citters KM, Crocker JC. The consensus mechanics of cultured mammalian cells. *Proc Natl Acad Sci.* 2006;103: 10259–10264. doi:10.1073/pnas.0510348103

68. Fabry B, Maksym GN, Butler JP, Glogauer M, Navajas D, Fredberg JJ. Scaling the microrheology of living cells. *Phys Rev Lett.* 2001;87: 1–4. doi:10.1103/PhysRevLett.87.148102

69. Wu P-H, Hale CM, Chen W-C, Lee JSH, Tseng Y, Wirtz D. High-throughput ballistic injection nanorheology to measure cell mechanics. *Nat Protoc.* 2012;7: 155–170. doi:10.1038/nprot.2011.436

70. Lee LM, Liu AP. The Application of Micropipette Aspiration in Molecular Mechanics of Single Cells. *J Nanotechnol Eng Med.* 2014;5: 040902. doi:10.1115/1.4029936

71. Pachenari M, Seyedpour SM, Janmaleki M, Shayan SB, Taranejoo S, Hosseinkhani H. Mechanical properties of cancer cytoskeleton depend on actin filaments to microtubules content: Investigating different grades of colon cancer cell lines. *J Biomech.* 2014;47: 373–379. doi:10.1016/j.jbiomech.2013.11.020

72. Guck J, Schinkinger S, Lincoln B, Wottawah F, Ebert S, Romeyke M, et al. Optical deformability as an inherent cell marker for testing malignant transformation and metastatic competence. *Biophys J.* 2005;88: 3689–3698. doi:10.1529/biophysj.104.045476

73. Byun S, Son S, Amodei D, Cermak N, Shaw J, Kang JH, et al. Characterizing deformability and surface friction of cancer cells. *Proc Natl Acad Sci.* 2013;110: 7580–7585. doi:10.1073/pnas.1218806110

74. Hou HW, Li QS, Lee GYH, Kumar AP, Ong CN, Lim CT. Deformability study of breast cancer cells using microfluidics. *Biomed Microdevices.* 2009;11: 557–564. doi:10.1007/s10544-008-9262-8

75. Zia RN. Active and Passive Microrheology: Theory and Simulation. *Annu Rev Fluid Mech.* 2018;50: 371–405. doi:10.1146/annurev-fluid-122316-044514

76. Guo M, Ehrlicher AJ, Mahammad S, Fabich H, Jensen MH, Moore JR, et al. The role of vimentin intermediate filaments in cortical and cytoplasmic mechanics. *Biophys J.* 2013;105: 1562–1568. doi:10.1016/j.bpj.2013.08.037

77. Einstein A. On the Motion of Small Particles Suspended in a Stationary Liquid, as Required by the Molecular Kinetic Theory of Heat. *Ann Phys.* 1905;322: 549–560. doi:10.1002/andp.19053220806

78. Perrin JB. Brownian movement and molecular reality. *Ann Chim Phys VIII.* 1909;18: 5–114.

79. Mason T, Ganesan K, van Zanten J, Wirtz D, Kuo S. Particle Tracking Microrheology of

Complex Fluids. *Phys Rev Lett.* 1997;79: 3282–3285. doi:10.1103/PhysRevLett.79.3282

80. Levine AJ, Lubensky TC. One- and two-particle microrheology. *Phys Rev Lett.* 2000;85: 1774–1777. doi:10.1103/PhysRevLett.85.1774

81. Squires TM, Mason TG. Fluid Mechanics of Microrheology. *Annu Rev Fluid Mech.* 2010;42: 413–438. doi:10.1146/annurev-fluid-121108-145608

82. Mason TG, Gang H, Weitz DA. Diffusing-wave-spectroscopy measurements of viscoelasticity of complex fluids. *J Opt Soc Am A.* 1997;14: 139–149.

83. Dasgupta BR, Tee S-Y, Crocker JC, Frisken BJ, Weitz D a. Microrheology of polyethylene oxide using diffusing wave spectroscopy and single scattering. P*hys Rev E Stat Nonlin Soft Matter Phys.* 2002;65: 051505. doi:10.1103/PhysRevE.65.051505

84. Mason TG. Estimating the viscoelastic moduli of complex fluids using the generalized Stokes-Einstein equation. *Rheol Acta.* 2000;39: 371–378. doi:10.1007/s003970000094

85. Gittes F, Schnurr B, Olmsted PD, MacKintosh FC, Schmidt CF. Microscopic Viscoelasticity: Shear Moduli of Soft Materials Determined from Thermal Fluctuations. *Phys Rev Lett.* 1997;79: 3286–3289. doi:10.1103/PhysRevLett.79.3286

86. Yamada S, Wirtz D, Kuo SC. Mechanics of living cells measured by laser tracking microrheology. *Biophys J.* 2000;78: 1736–1747. doi:10.1016/S0006-3495(00)76725-7

87. Tseng Y, Kole TP, Wirtz D. Micromechanical mapping of live cells by multiple-particle-tracking microrheology. *Biophys J.* 2002;83: 3162–3176. doi:10.1016/S0006-3495(02)75319-8

88. Lee JSH, Panorchan P, Hale CM, Khatau SB, Kole TP, Tseng Y, et al. Ballistic intracellular nanorheology reveals ROCK-hard cytoplasmic stiffening response to fluid flow. *J Cell Sci.* 2006;119: 1760–1768. doi:10.1242/jcs.02899

89. Hale CM, Sun SX, Wirtz D. Resolving the role of actoymyosin contractility in cell microrheology. *PLoS One.* 2009;4. doi:10.1371/journal.pone.0007054

90. Wirtz D. Particle-tracking microrheology of living cells: principles and applications. *Annu Rev Biophys.* 2009;38: 301–26. doi:10.1146/annurev.biophys.050708.133724

91. MacKintosh FC, Schmidt CF. Active cellular materials. *Curr Opin Cell Biol.* 2010;22: 29–35. doi:10.1016/j.ceb.2010.01.002

92. Brangwynne CP, Koenderink GH, MacKintosh FC, Weitz DA. Cytoplasmic diffusion: Molecular motors mix it up. *J Cell Biol.* 2008;183: 583–587. doi:10.1083/jcb.200806149

93. Van Citters KM, Hoffman BD, Massiera G, Crocker JC. The role of F-actin and myosin in epithelial cell rheology. *Biophys J.* 2006;91: 3946–3956. doi:10.1529/biophysj.106.091264

94. Gupta SK, Guo M. Equilibrium and out-of-equilibrium mechanics of living mammalian cytoplasm. *J Mech Phys Solids.* 2017;107: 284–293. doi:10.1016/j.jmps.2017.07.007

95. Mizuno D, Tardin C, Schmidt CF, MacKintosh FC. Nonequilibrium mechanics of active cytoskeletal networks. *Science*. 2007;315: 370–373. doi:10.1126/science.1134404

96. Smelser AM, Macosko JC, O'Dell AP, Smyre S, Bonin K, Holzwarth G. Mechanical properties of normal versus cancerous breast cells. *Biomech Model Mechanobiol.* 2015;14: 1335–1347. doi:10.1007/s10237-015-0677-x

97. Gal N, Lechtman-Goldstein D, Weihs D. Particle tracking in living cells: A review of the mean square displacement method and beyond. *Rheol Acta.* 2013;52: 425–443. doi:10.1007/s00397-013-0694-6

98. Agus DB, Alexander JF, Arap W, Ashili S, Aslan JE, Austin RH, et al. A physical sciences network characterization of non-tumorigenic and metastatic cells. *Sci Rep.* 2013;3. doi:10.1038/srep01449

99. DePuit RJ, Khair AS, Squires TM. A theoretical bridge between linear and nonlinear microrheology. *Phys Fluids.* 2011;23. doi:10.1063/1.3598322

100. Puertas AM, Voigtmann T. Microrheology of colloidal systems. *J Phys Condens Matter.* 2014;26. doi:10.1088/0953-8984/26/24/243101

101. Fodor É, Guo M, Gov NS, Visco P, Weitz D a., van Wijland F. Activity-driven fluctuations in living cells. *Europhysics Lett.* 2015;110: 48005. doi:10.1209/0295-5075/110/48005

102. Mizuno D, Tardin C, Schmidt CF, Mackintosh FC. Nonequilibrium mechanics of active cytoskeletal networks. *Science.* 2007;315: 370–3. doi:10.1126/science.1134404

103. Lau AWC, Hoffman BD, Davies A, Crocker JC, Lubensky TC. Microrheology, Stress Fluctuations, and Active Behavior of Living Cells. *Phys Rev Lett.* 2003;91: 198101. doi:10.1103/PhysRevLett.91.198101

104. Goldstein D, Elhanan T, Aronovitch M, Weihs D. Origin of active transport in breast-cancer cells. *Soft Matter.* 2013;9: 7167–7173. doi:10.1039/c3sm50172h

105. Hendricks AG, Holzbaur ELF, Goldman YE. Force measurements on cargoes in living cells reveal collective dynamics of microtubule motors. *Proc Nat Acad Sci.* 2012;109: 18447–52. doi:10.1073/pnas.1215462109

106. Gal N, Weihs D. Intracellular mechanics and activity of breast cancer cells correlate with metastatic potential. *Cell Biochem Biophys.* 2012;63: 199–209. doi:10.1007/s12013-012-9356-z

107. McNeil PL, Warder E. Glass beads load macromolecules into living cells. *J Cell Sci.* 1987;88 (Pt 5): 669–678.

108. Emerson NT, Hsia C-H, Rafalska-Metcalf IU, Yang H. Mechanodelivery of nanoparticles to the cytoplasm of living cells. *Nanoscale.* 2014;6: 4538. doi:10.1039/c3nr06468a

CHAPTER 2: LOADS BIAS GENETIC AND SIGNALING SWITCHES IN SYNTHETIC AND NATURAL SYSTEMS [1]

2.1 Introduction

A longstanding question about signal transduction and gene transcription networks is how modular are they. Here modularity means relative insulation of small subgraphs or motifs of the main network from each other [1]. This question is especially relevant for synthetic biology that aims to build artificial circuits from the bottom up [2]. It is also relevant for molecular biologists that aim to arrive at a quantitative understanding of a cellular decision, by, for example, isolating a crucial network module [3].

For synthetic biologists the challenge is now to move from simple network motifs such as pulse generators [4], genetic switches [5–8], logic gates [9], [10], and oscillators [11–13] to more complicated networks combining multiple motifs and networks in more complex organisms. Novel applications currently being explored include plant biosensors [14], hazardous waste remediation [15], clean fuel technology [16], and numerous medical applications [17–20]. Synthetic biologists hope to utilize biological modules in a manner similar to electrical circuit board components – plugging them together to attain a specific, and novel, function [21]. At the core of the concept of either breaking down complex biological systems into small modules, or

[1] The work presented in this chapter and in Appendix I has been published in PLoS Computational Biology and is reproduced here under the Creative Commons License. Lyons SM, Xu W, Medford J, Prasad A. Loads Bias Genetic and Signaling Switches in Synthetic and Natural Systems. *PLoS Comput Biol.* 2014; 10(3): e1003533. Author contributions: J.M. A.P. conceived and designed the experiments; S.M.L. W.X. A.P. performed the experiments; S.M.L. W.X. A.P. analyzed the data; S.M.L. W.X. J.M. A.P. wrote the paper. I am the co-first author on the publication. This work is being presented in this chapter in its entirety to maintain the intellectual coherence of the project.

even building complex systems from modules, is the belief that these modules will behave predictably in isolation and in connection. Recent theoretical and experimental work however [22-25] suggests that the functioning of modules may not be independent of the downstream components that they are connected to. Adding an additional binding reaction to the output of a gene regulatory network (or loading the network) may decrease system bandwidth [24] and substrate sequestration in covalent modification cycles may result in signaling delay [26]. *In vitro* studies find that there is significant load-induced modulation of the upstream module in an enzymatic signal transduction cascades [24]. Theoretical analysis has also shown that a load can change the fundamental properties of an oscillating circuit [27]. Thus understanding the effects of adding a load to the output of these technologically important network modules is required for a thorough understanding of the challenges of scaling up synthetic networks to higher levels of complexity.

Loads could also have noteworthy unrecognized effects in natural systems. In fact all natural systems have loads in some ways or the other. Motifs in signal transduction networks are connected directly to a transcriptional response, or to downstream proteins that may function as transcription factors or go on to activate transcription factors. Motifs in gene transcription networks have transcriptional outputs with protein domains that bind nonspecifically and specifically to binding sites on the DNA, apart from interacting with other transcription factors.

Circuits that function as switches play an important role in all biological signaling and gene transcription networks because they encode decisions. This change of state can be brought about by an external signal, or an internal accumulation of a protein, which can drive the system to a different steady state. Examples are the regulatory circuits for the cell cycle in yeast [28], mitogen-activated protein kinase cascades in animal cells [29–31], and the lysis-lysogeny switch

in the λ phage [32]. Since many small circuits can show this kind of behavior, switches are among the earliest and most well studied of protein interaction circuits [33]. The genetic toggle switch, which was one of the first two synthetic circuits constructed, is a well-known synthetic example [5]. Given the ubiquity and importance of switch-like motifs, it is important to understand how their function could be affected by binding downstream partners.

These reasons prompted our theoretical study of the behavior of a simple genetic toggle switch [5], a toggle switch with positive feedback as well as a common positive-feedback based switch involving Ras activation in lymphocytes [29, 30] under a load on either one or both of its outputs. These circuits are shown in Fig. 4.1 and described below. The simple toggle switch is a widely studied and emulated synthetic network motif based on the mutual repression of two repressor proteins. However, naturally occurring toggle switches are often found connected to an additional positive autoregulatory component. For example in the competence system in B. subtilis, ComK represses the production of Rok and Rok represses the production of ComK; however ComK also has a strong positive feedback upon its own production [34]. Another example is found in the apoptosis network of many multicellular organisms, including mammals. Within the pathway controlling intrinsic apoptosis is a set of genes with double-negative repression, Casp3 and XIAP, again accompanied by positive autoregulation of Casp3 [35].

The Ras protein is a G-protein found on mammalian cellular membranes that is important in many cellular processes and is an upstream activator of the MAPK pathway. Ras goes from a GDP-bound inactive form to a GTP-bound active form, often in a digital manner [30], and previous studies in lymphocytes have shown that RasGDP is activated to RasGTP via a bistable switch that arises from a positive feedback loop on its own activation via SOS (Son of Sevenless) [30]. However the Ras switch very naturally has an associated load, since to transduce the

cellular signals down along the MAPK/ERK pathway, RasGTP naturally binds to Raf kinase. Thus the Ras switch system contains all the elements we need to study the effects of adding loads to a bistable switch which is based on a positive feedback loop.

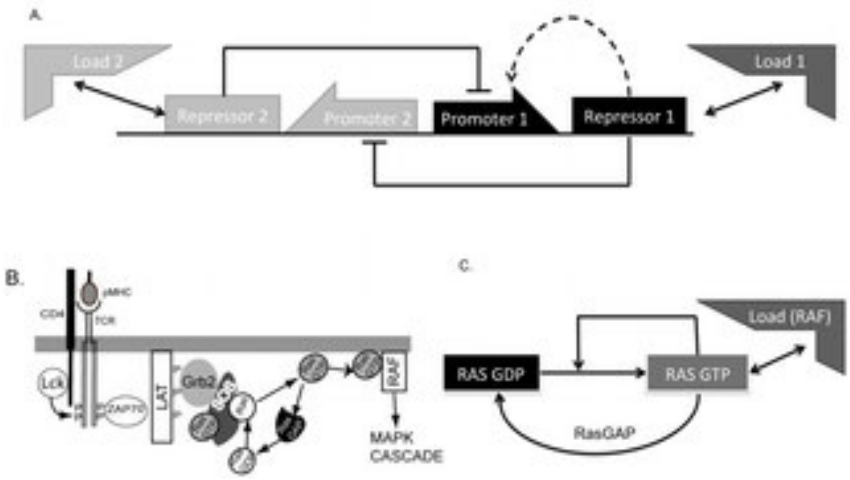

Figure 2.1. Schematic diagram of the circuits studied in this paper.
(A). The basic toggle switch is the network shown without the dotted line. Repressor 1 represses the production of Repressor 2 and vice versa. The dotted line denotes a positive feedback motif found in some natural circuits. (B). A cartoon of part of the MAPK activation pathway in T lymphocytes, adapted from [29], showing the role of Ras activation. Signals from peptide-MHC complexes are received at the TCR and lead to phosphorylation of the cytoplasmic chains of the TCR by the Src kinase, Lck. This recruits the kinase ZAP70 which trans-autoactivates and phosphorylates a scaffold called LAT, which recruits Grb2 and SOS to the plasma membrane. SOS activates Ras as shown. (C) A simplified model of the Ras switch. RasGDP transforms into RasGTP via the enzyme SOS. However the catalytic rate of SOS increases when bound to RasGTP. This sets up an autocatalytic positive feedback. RasGTP is deactivated by enzymes called RasGAP's (among others).

2.2 Methods

2.2.1 Genetic toggle switch

The basic genetic toggle switch consists of two mutually repressing genes as shown in Fig. 2.1 along with an additional system to toggle the states. As shown in previous studies, with the right combination of parameters, the toggle switch will stay in one of two stable states, each characterized by a high concentration of one of the repressor proteins, and strong repression of

the other. The toggle switch can now be induced to switch states using two possible strategies for inducing a transition: decrease the level of highly expressed protein [5], [36] or increase the expression of one of the repressed proteins (Fig. 2.1) using an additional inducible system [36]. For a model which utilizes the latter protocol we obtain a system of four differential equations [36] after including a load. The load may be a protein, a small molecule or a binding site on DNA such that the bound complex prevents the repressor from binding to and repressing its conjugate promoter. In order to make the simplest and the most general model, we have assumed here that the repressors reversibly bind the load only in one copy. We assume that the total load L1T is a constant, L1 is the free load and conservation gives us the bound load as $L_{1T}-L_1$.

$$\frac{du}{d\tau}=\alpha_1+\frac{\beta_1'}{1+v^n}-u-k_{on1}'[L_{1T}]u\ell_1+k_{off1}'[L_{1T}](1-\ell_1) \quad \textbf{(1)}$$

$$\frac{dv}{d\tau}=\alpha_2+\frac{\beta_2'}{1+u^n}-v-k_{on2}'[L_{2T}]v\ell_2+k_{off2}'[L_{2T}](1-\ell_2) \quad \textbf{(2)}$$

$$\frac{d\ell_1}{d\tau}=-k_{on1}'k_1u\ell_1+k_{off1}'k_1(1-\ell_1) \quad \textbf{(3)}$$

$$\frac{d\ell_2}{d\tau}=-k_{on2}'k_2v\ell_2+k_{off2}'k_2(1-\ell_2) \quad \textbf{(4)}$$

These four equations are presented in de-dimensionalized form, with *u*, *v*, l_1, l_2 representing the dimensionless concentrations of Repressor 1, Repressor 2, Load1 and Load2 respectively and τ the de-dimensionalized time. The basal parameter values that we use are as follows: $\alpha_1=\alpha_2=0.2$; $\beta_1'=\beta_2'=4$; $n=3$; $k_{on1}'=k_{on2}'=0.5$; $k_{off1}'=k_{off2}'=0.5$; $k_1=k_2=1$; $[L_{1T}]$ and

[L_{2T}] are variable. Note that Equations (1) and (2) without the last two terms incorporating the load are the standard equations for analyzing the toggle switch that have been widely used in both empirical and theoretical work [5], [36]. These equations are discussed in more detail in Supplementary Text S2.1 Section 1.1. The derivation of this model follows that of Kobayashi et al [33]. All parameters excluding load binding rates were sourced from Kobayashi et al [36]; extensive parameter sensitivity of the load binding rates was performed and are discussed in Appendix I: Supplementary Text S2.1 section 1.4 and Figs. S2.1, S2.2, Table S2.1 and Figs. S2.15 and S2.16. The effect of a load arises from the binding competition between the promoter where the repressor binds and the load. This competition is not directly incorporated into the Hill function, since the binding step with the promoter is not explicitly modeled and is treated in an effective way. In reality however the concentration of the promoter is so small compared to that of the load, that the use of Hill functions is justifiable [37]. There are possibly exceptional cases such as a high copy number of plasmids compared to load concentrations where this assumption does not apply. Note that the Hill function is an effective phenomenological equation describing gene transcription and protein production, and standard Law of Mass Action (LMA) methods to derive the Hill functional form may not apply for many transcription factors that nevertheless show Hill kinetics [38]. Thus it is preferable to use Hill function forms for this analysis.

To calculate transition times, we first start the system in one state, say high Repressor 1. After the system has reached steady-state, we add a constant concentration of the inducer and measure the time taken for Repressor 2 to go from 10% of its maximum value to 90% of its maximum value. This is the “rise time”. Similarly the “decay time” is the time taken for Repressor 1 to go from 90% of its maximum value to 10% of its maximum value. The level of the inducer remains fixed.

In practice the inducer may decay and the transition would depend upon there being inducer present for a sufficiently long time to induce transition. In such cases the amount of inducer required may be of interest. When the inducer is applied as a bolus with a first order decay rate, it appears as an exponentially decaying pulse. We thus included a fifth differential equation governing the amount of Inducer.

$$\frac{dI_1}{d\tau} = -d_I I_1 \tag{5}$$

Here d_I is the ratio of the inducer degradation constant to the repressor degradation constant. We used Eq. 5 only when estimating the amount of inducer required to switch states for different loads and different decay rates of the load (Appendix I: Supplementary Text S2.1 section 1.4 and Supplementary Tables S2.3, S2.4).

A genetic toggle switch can be induced to change states by the alternative method of repressing the highly expressed repressor, and in fact the original toggle switch used this form of induction [5], [33]. We repeated our calculations for the basic model for the case of alternative induction, but found no qualitative differences. The alternative induction model along with the equations is detailed in the Supplementary Text S2.1 section 1.4.

Equations 1–4 assume that the load itself stays in steady state during the switching of the toggle between one state and another. However in reality if the load is another protein, it is also synthetized and degraded by the cell, and therefore its level could be dynamic. We also simulated this situation by incorporating a synthesis and a degradation rate for each load. This resulted in Equations 3 and 4 being replaced by:

$$\frac{d\ell_1}{d\tau} = -k_{on1}{}'k_1\frac{k_{b2}}{k_{d2}}u\ell_1 + k_{off1}{}'k_1\frac{k_{b1}}{k_{d1}}(c_1) + \frac{k_{d1}}{\delta} - \frac{k_{d1}}{\delta}\ell_1$$

(6)

$$\frac{d\ell_2}{d\tau} = -k_{on2}{}'k_2\frac{k_{b2}}{k_{d2}}v\ell_2 + k_{off2}{}'k_2\frac{k_{b2}}{k_{d2}}(c_2) + \frac{k_{d2}}{\delta} - \frac{k_{d2}}{\delta}\ell_2$$

(7)

Here c_1 is the load-repressor complex and k_{b1} and k_{d1} are the synthesis and degradation rates respectively for Repressor 1, and correspondingly for Repressor 2. The parameters are defined in Appendix I: Supplementary Text S2.1, section 1.5. Since the total load is no longer conserved, we need to include additional equations for the load repressor complex.

$$\frac{dc_1}{d\tau} = k_{on1}{}'k_1u\ell_1 - k_{off1}{}'k_1c_1$$

(8)

$$\frac{dc_2}{d\tau} = k_{on2}{}'k_2u\ell_2 - k_{off2}{}'k_2c_2$$

(9)

Our model assumes that when the repressor protein is bound to the load, it is protected from degradation. However it is also possible that even when the protein is bound to the load, it can still degrade. To check the impact of removing the protection assumption, we also consider an additional model where the repressor can still degrade with the same rate constant when bound to the load. The equations for that model are slightly modified versions of the equation above, and are presented in detail in Appendix I: Supplementary Text S2.1, section 3.2.

We conducted parameter sensitivity analysis on models utilizing both forms of induction; these did not show any qualitative change on wide variation of key parameters (Appendix I: Tables S2.1, S2.2, S2.3, S2.4 and Supplementary Text S2.1).

2.2.2 Toggle with positive feedback

A positive feedback was added to the R1 side of the toggle switch as an inducible promoter with a Hill coefficient of 1. We assumed that the positive feedback acted on the same promoter as the repression, resulting in a composite term for production of R1 from promoter 1 where ρ is the strength of positive feedback.

$$\frac{dR_1}{dt} = \alpha_1 + \frac{\rho R_1 + \beta_1}{1 + R_1/k_5 + R_2^{n2}/k_2^{n2}} - d_1 R_1 \quad \textbf{(10)}$$

The derivation of this equation can be found in Appendix I: Supplementary Text S2.1, section 1.6.1. As before, α1 is the leaky production of R1 while α1+β1 represents the activity of the promoter in the absence of repression or positive feedback. We chose k2 and k5=1, d1=0.2, and for the figures in the main paper we chose ρ=3.5. We address other values of the positive feedback in Appendix I: Fig. S2.6 and the Supplementary Text S2.1, section 1.6.2.

2.2.3 Stochastic simulations

We perform stochastic simulations and histogram the concentrations of the repressor proteins to construct their probability distribution. The quasi-potential of the toggle is given by the negative logarithm of this probability distribution [39]. In order to construct the probability distribution we make use of the phenomenon of noise-induced switching. Recent theoretical work has shown that multiplicative noises due to stochastic fluctuations can induce switching [40]–[42]. Experimental results demonstrate bimodal populations that correspond with theoretic predictions arising from noise-induced switching [41].

Stochastic simulations were carried out using a modified Gillespie algorithm using the standard rate expressions for every reaction (Table S2.5). We chose a reaction volume that would correspond to a small number of molecules in the system. Stochastic fluctuations then drive the

system to transition between states rapidly, allowing us to collect sufficient data points. In order to make sure that the system was not being biased by the small volume, we also repeated the calculations for a five times larger volume (and hence molecule number) and found qualitatively similar results (Appendix I: Fig. S2.4).

For the positive feedback toggle switch the same equations were used except for the repressible production of Repressor 1, where we used instead the rate expression given by the right hand side of Eq. 10 in the Monte Carlo simulations.

2.2.4 Ras-kinase system

For our study we adapted the minimal model of the Ras switch proposed by Das et. al. [30] with the addition of a reversibly binding load in the form of the Raf protein (Fig. 2.1C). The model contains three proteins, Ras, which exists as RasGDP or RasGTP, SOS, the guanine exchange factor (GEF) that catalyzes the transformation from RasGDP to RasGTP and a GTPase, RasGAP. SOS on its own has very low GEF activities. However, the activity of the GEF pocket is strongly influenced by the binding state of an allosteric pocket in Cdc25 domain [29], [30]. When the allosteric pocket is bound by RasGDP, the GEF activity is increased by 5 times. If the allosteric pocket is bound by RasGTP, its GEF activity is increased by 75 times. In this way, RasGTP can upregulate its own production rate by binding to SOS, thus constituting a positive feedback loop. RasGTP is deactivated by GTPase's such as RasGAPs that are constitutively present.

After Raf binds RasGTP, the complex catalyzes the phosphorylation of Raf leading to a phosphorylation cascade. For this study we ignore Raf activation and only consider the effects of Raf as a binding partner for RasGTP. The Das paper [30] also models the systems using Michaelis-Menten (MM) forms for the actions of the enzymes which is quite standard for

modeling systems of enzymatic reactions. However since in this model the load competes not with a promoter, as in the toggle switch, but with another protein, it is possible that the quasi-steady state assumption of the MM form could be introducing some inaccuracies in the results. To account for this possibility we wrote the entire model using the Law of Mass Action. We separately simulated the model using the MM functional forms (Supplementary Text S2.1 section 2 and Figs. S2.7 and S2.9). The equations for the MM forms are listed and discussed in detail in the Supplementary Text S2.1. The reactions and rate constants for this model are listed in Table S2.6 and Table S2.7.

We use the following notations for the species involved in the system:

$$x_1 \equiv [SOScat];\ x_2 \equiv [RasGDP];\ x_3 \equiv [RasGTP];$$
$$x_4 \equiv [SOScat(RasGDP)];\ x_5 \equiv [SOScat(RasGTP)];$$
$$x_6 \equiv [SOScat(RasGDP) : RasGDP];$$
$$x_7 \equiv [SOScat(RasGTP) : RasGDP];\ x_8 \equiv [RasGAP];$$
$$x_9 \equiv [RasGAP : RasGTP];\ x_{10} \equiv [Raf];\ x_{11} \equiv [RasGTP : Raf]$$

$$\frac{dx_1}{dt} = -k_{on1}x_1x_2 + k_{off1}x_4 - k_{on2}x_1x_3 + k_{off2}x_5 \tag{11}$$

$$\frac{dx_2}{dt} = -k_{on1}x_1x_2 + k_{off1}x_4 - k_{on3}x_2x_5 + k_{off3}x_7 - k_{on4}x_2x_4 + k_{off4}x_6 + k_{cat5}x_9 \tag{12}$$

$$\frac{dx_3}{dt} = -k_{on2}x_1x_3 + k_{off2}x_5 + k_{cat3}x_7 + k_{cat4}x_6 - k_{on5}x_3x_8 + k_{off5}x_9 - k_{on6}x_3x_{10} + k_{off6}x_{11} \tag{13}$$

$$\frac{dx_4}{dt} = k_{on1}x_1x_2 - k_{off1}x_4 - k_{on4}x_2x_4 + k_{off4}x_6 + k_{cat4}x_6 \tag{14}$$

$$\frac{dx_5}{dt} = k_{on2}x_1x_3 - k_{off2}x_5 - k_{on3}x_2x_5 + k_{off3}x_7 + k_{cat3}x_7 \tag{15}$$

$$\frac{dx_6}{dt} = k_{on4}x_2x_4 - k_{off4}x_6 - k_{cat4}x_6 \tag{16}$$

$$\frac{dx_7}{dt} = k_{on3}x_2x_5 - k_{off3}x_7 - k_{cat3}x_7 \quad \textbf{(17)}$$

$$\frac{dx_8}{dt} = -k_{on5}x_3x_8 + k_{off5}x_9 + k_{cat5}x_9 \quad \textbf{(18)}$$

$$\frac{dx_9}{dt} = k_{on5}x_3x_8 - k_{off5}x_9 - k_{cat5}x_9 \quad \textbf{(19)}$$

$$\frac{dx_{10}}{dt} = -k_{on6}x_3x_{10} + k_{off6}x_{11} \quad \textbf{(20)}$$

$$\frac{dx_{11}}{dt} = k_{on6}x_3x_{10} - k_{off6}x_{11} \quad \textbf{(21)}$$

Moreover, four of the basic protein species along with the complexes they participate in have associated conservation laws. These are as follows:

$$SOS_T = x_1 + x_4 + x_5 + x_6 + x_7 \quad \textbf{(22)}$$

$$Ras_T = x_2 + x_3 + x_4 + x_5 + 2x_6 + 2x_7 + x_9 + x_{11} \quad \textbf{(23)}$$

$$GAP_T = x_8 + x_9 \quad \textbf{(24)}$$

$$Raf_T = x_{10} + x_{11} \quad \textbf{(25)}$$

In the Ras model too we implicitly assume that when RasGTP is bound to Raf, it is protected from de-activation by a RasGAP. We also study the effects of relaxing this assumption on both the LMA and the PSSA models. The modifications to the original model are detailed in Appendix I: Supplementary Text S2.1 section 3.3.1.

We used XPPaut to perform a bifurcation analysis of the Ras switch with changing levels of SOS, with and without a load. The quasi-potential landscape does not provide useful insights into load induced modulation of the Ras switch and hence the probability distributions are not reported.

2.3 Results

2.3.1 The bistability properties of the toggle switch do not change unless the repressor can degrade when bound to the load

The presence of a binding partner for either Repressor 1 or Repressor 2 (which we refer to thereafter as the load) introduces new terms in the differential equations describing the toggle switch, i.e. the last two terms in Eq. 1 and in Eq. 2, as well as two new equations, Eq. 3 and 4, in the dynamical system. However it can be easily seen that in steady state Eq. 3 and 4 are also independently set to zero, and therefore do not affect the bifurcation properties of the switch. Even in the case of a dynamic load, since Eq. S13 and S14 are set to zero to ensure the load-repressor complex is in steady state, the additional terms in Eq. S9 and S10 are also zero. Thus the load makes no difference to either the bistability of the switch or to the parameter values where the bistability is seen.

The exception is when the repressor molecule can degrade even when bound to the load, which may be relevant in some experimental situations. As Fig. 2.2A shows, when a load is added symmetrically to both sides of the toggle switch, the two stable states approach each other and eventually annihilate, leaving a monostable system. Fig. 2.2B shows that when a load is added only to one side, the system again goes from bistable to monostable at some critical value of the load. In effect, the upper stable point vanishes and is no longer accessible due to leakage of the repressor affected by the load.

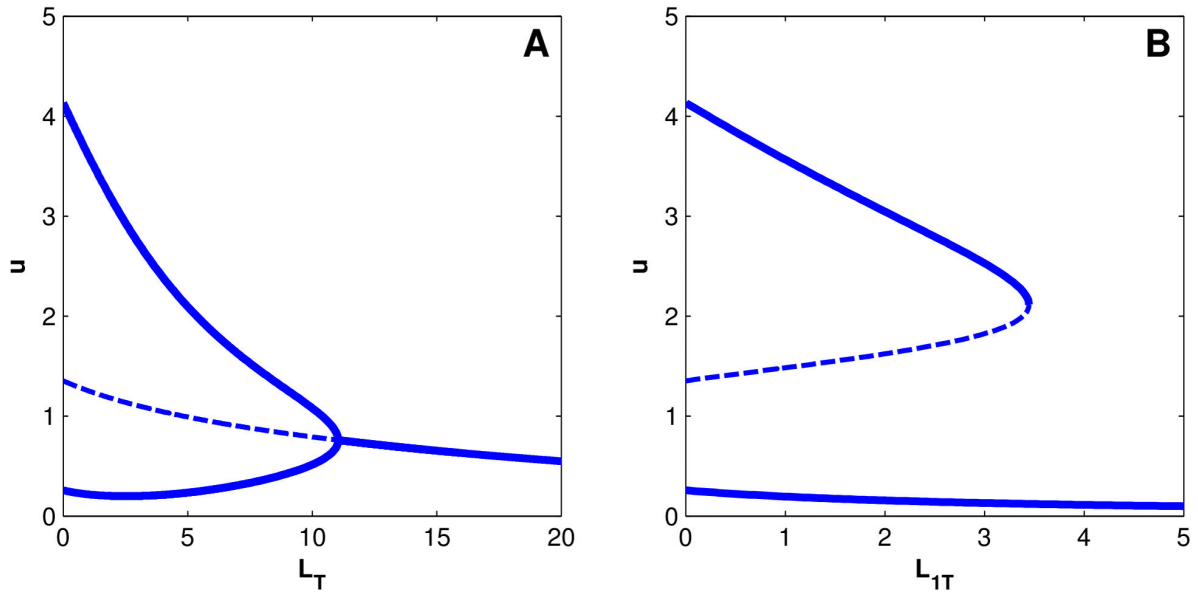

Figure 2.2. Bifurcation diagram of the genetic toggle switch when the repressor can decay from the load-repressor complex.
The thick lines are stable steady states, the dashed lines are unstable steady states. (A). A load is added symmetrically to both sides of the toggle. The stable states of only one Repressor molecule with respect to the load are shown. With zero load the toggle switch is bistable with well separated steady states. As the load increases, the two stable states approach each other and the unstable state, and eventually merge in a bifurcation at a critical value of the load. The system is monostable beyond this critical value. (B) A load is added only to Repressor 1. The high state of Repressor 1 approaches the unstable steady state as the load increases and merges with it at a critical value of the load, leaving only the lower state accessible to the system.

The reason for the change in steady state behavior is made clear on examining the equations of the system. Here we need to incorporate additional reactions that represent the decay of the repressor-load complex into the load alone. This leads to an additional term in the equation for the load and the repressor-load complex (Eq. S44 and S45). However this term does not appear in the equation for the repressors, which continue to be governed by Eq. 1 and Eq. 2. As a consequence in the steady state, the additional terms in Eq. 1 and 2 no longer equal zero and the steady state properties of the switch are influenced by the presence of the load.

As can be seen from an examination of the chemical reaction system, this mechanism of abrogation of bistability arises whenever the load-repressor complex participates in a non-

reversible (from the repressor's point of view) chemical process that leads to an unbalanced leakage of the repressor from its function as a repressor by the presence of the load. A more interesting example of such a process could be provided by a chemical reaction system where the load is an enzyme for one of the repressor molecules, which is transformed by the enzymatic action into a protein no longer capable of repression. The mathematical analysis of this case is exactly the same as the model we are currently discussing hence we do not consider it separately here.

However a load can significantly change the dynamic response of the basic genetic toggle switch as we shall see below. We examined two different measures of dynamic response, response time for state switching and the amount of inducer required for state switching.

2.3.2 The response time for state switching of the toggle switch increases

We measured two response times, the rise time which quantifies the time taken for the concentration of Repressor 2 to increase from its low or zero level in state 1 to its high level in state 2, and the decay time which measures the time taken for Repressor 1 to decay from its high level in state 1 to its low level in state 2, in both cases in response to a constant inducer. Specifically the rise time measured the time to go from 10% to 90% of the steady state maximum, while the decay time measured the time to go from 90% to 10% of the steady state maximum. These measurements were made using the deterministic model in the cases when the load was applied only to one side and to both sides of the switch.

We found that both the rise time and the decay time increase with increasing load concentration. Interestingly, this relationship was approximately linear in all cases (Fig. 2.3A & B). The slope of the linear relationship represents the increase in response time due to unit increase in load. We found that the slope of the line was larger when the load was applied to the

opposite side of the system before the switching rather than the same side (Fig. 2.3A), indicating that it is harder to switch out of a state without a load to a state with a load than the reverse. However when a load was applied to both sides, the slope of the linear fit was higher than when the load was only on the opposite side, suggesting that both the "opposite side" and the "same side" delays are operating.

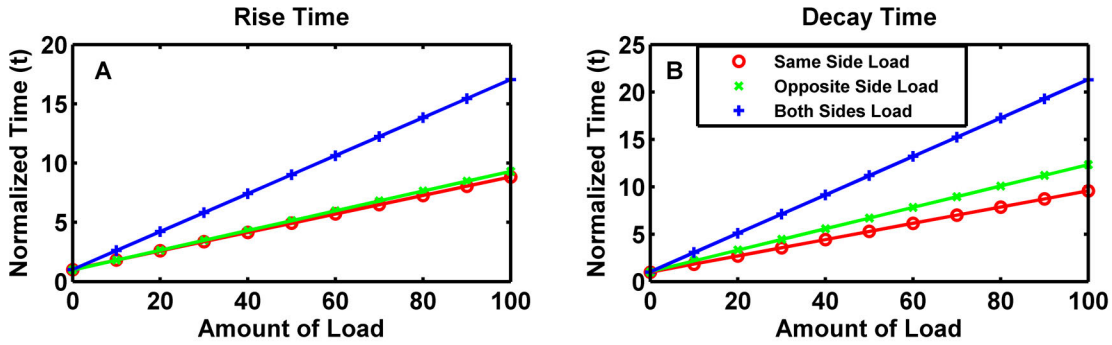

Figure 2.3. Effects of a load on transition times of the basic toggle switch.
(A). The time taken to reach 90% of maximum value for the protein undergoing a low-to-high transition as a function of the Load, normalized by the steady-state amount of Repressor 1. Normalized time is a unit-less number defined by the transition time (rise or decay) of the system at a given loading condition divided by the transition time (rise or decay) of an unloaded system. (B). The time taken for the concentration of the protein undergoing a high-to-low transition to reach 10% of its maximum value. The x- and y- axes are the same as for the previous panel.

While we also found an approximately linear relationship between the decay time and the concentration of the load, there was little difference between the decay times for the state with the load ("same side load") and the state without a load ("opposite side load") at our base parameter values. Thus the load affects rise time and decay time differently. When a load was applied to both sides of the switch, the slope of the decay time linear fit was larger, again indicating the operation of both delays.

We tested these results by changing parameter values for the binding of the load (Appendix I: Table S2.1) and found that in all cases we obtain a good linear fit for the response time. For the rise time, the slope was uniformly larger when the load was applied to the opposite side as

compared to the same side, and it was the largest when loads were applied on both sides. For the decay time, the slope could be larger or smaller when the load was applied to the opposite side of the decaying state compared with the same side, but it was always larger than both when a load was applied on both sides. The slope depended non-monotonically upon the dissociation constant (Kd) of the binding between the repressor protein and the load, with both low Kd and high Kd having a smaller effect that those in between (Appendix I: Fig. S2.1). This was because when the Kd was low, i.e. strong binding, the concentration of the load-repressor complex was unaffected by the state of the switch. However when the Kd was high, the maximum concentration of the load-repressor complex was smaller, thereby having a lesser effect on the system (Appendix I: Fig. S2.2). Thus response times are maximized when the load acts as a dynamic sink, i.e. it takes up newly synthesized repressor when the state changes from the unloaded to the loaded side, and releases the bound repressor when switching from the loaded side to the unloaded side.

Previous studies of response times of biochemical networks with and without a load have also seen monotonic increases in the response time of simple transcriptional circuits [37]. However the extremely consistent approximately linear response we see under wide variation in parameter values is extremely intriguing.

An increase in response time should also imply that the concentration of inducer required to shift states should also be affected, especially when it can decay. In accordance with this expectation we also found that the concentration of inducer required to switch states increased exponentially with increasing load, as seen in Appendix I: Table S2.2. The parameter of the exponential fit was dependent on the inducer decay rate, indicating that the amount of time the inducer remains above a threshold is the key factor governing the switching. We find that this

response to a load is unaffected by the mode of switching the toggle, and induction by repression of the current state yields the same qualitative results (Appendix I: Tables S2.2 & S2.3).

In our analysis so far we have assumed that the total concentration of the load is fixed. We now analyze the case when the load is generated by a constitutively active promoter and can decay at a first order rate. We find that in this case too the qualitative features of the transition time remain the same as the toggle switch with a fixed load, i.e. it was approximately linear in all parameter regimes tested (Appendix I: Supplementary Text S2.1 section 1.5, Fig. S2.3 and Table S2.4). The reason why we do not see a difference from the basic toggle switch is that the transition times ultimately measures time between steady states, and we wait for the system to come quite close to the steady state value (90%). Thus the concentration of the load has also reached a steady state value and the system behaves as it would with a fixed load.

We also tested the response times when the repressor can leak away from the systems after binding with the load. Here we find that (Fig. 2.4) when a load is applied to the same side, the rise time continues to increase monotonically linearly with the load but the decay times decreases monotonically with the load. However when a load is applied to both sides, we find a negative linear relation between the transition times for both rise and decay and the load.

The reasons for the change in behavior is because as we saw previously, when the repressor can leak away from the repressor-load complex, a load has a dramatic effect on the bistability properties of the switch, abrogating bistability very quickly (Fig. 2.1). When only one repressor has a load, the high state of that repressor approaches the unstable state, indicating a decrease in the domain of attraction. Shifting out of that state thus becomes easier with increasing load. When both sides have loads, both stable states approach the unstable state, therefore shifting out of either state becomes easier, and both transition times decrease.

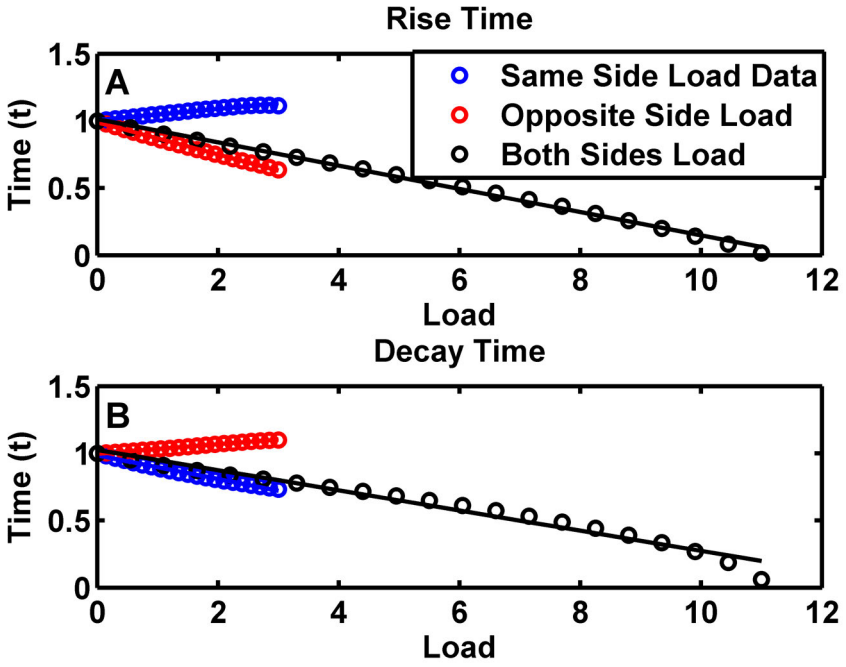

Figure 2.4. Effects of a load on transition times of a toggle switch without the protection assumption.
(A). The time taken to reach 90% of maximum value for the protein undergoing a low-to-high transition as a function of the load. The system is de-dimensionalized as described in Supplementary Text S2.1 section 1.1 and 3.2.1. (B). The time taken for the concentration of the protein undergoing a high-to-low transition to reach 10% of its maximum value. Note that the linear relationship for both-sided load transition times, and same-sided decay time, and opposite-sided rise time has a negative slope. The relationship for same-sided rise time and opposite sided decay time has a very small, but positive slope.

2.3.3 Dramatic changes in the potential energy landscape and probability distributions of the toggle switch

The modulation in the dynamic properties of the basic genetic toggle switch discussed above suggests that the load has altered the potential energy landscape of the toggle switch, making it harder to switch. For two-dimensional and higher systems, such as the toggle switch, analytical methods to construct the potential landscape are not available, but a quasi-potential can be constructed from the probability distribution function of the concentrations of the repressor molecules, where the quasi-potential is given by the negative of the natural logarithm

of the probability distribution [43], [44]. To calculate this we performed Monte Carlo simulations of the toggle switch using a Gillespie type algorithm elaborated in the Methods section. When the toggle switch is symmetrically balanced, both the probability distribution function and the potential energy landscape are completely symmetric. If the system is started in State 1, random fluctuations can drive it into State 2 and vice versa. The probability distribution can then be constructed by counting the frequencies of these random fluctuations. However since the genetic toggle switch can be very stable, a numerical computation of the potential energy landscape requires impractically long simulation times (as we show below). While computational methods to sample rare trajectories in such cases exist, they are very sensitive to choices of parameters [42], [45]. We developed a computational protocol in order to numerically obtain the probability distribution function of both protein concentrations and the transition times. We chose an appropriate volume for the genetic toggle switch such that exactly the same parameters as in the deterministic simulations led to the operation of the toggle switch with only a small number of proteins. The toggle remains bistable in this regime but the small protein numbers vastly increases spontaneous stochastic fluctuations arising out of multiplicative noise in the system and allows the simulation to explore parameter space and collect enough data.

Our simulations showed that the switch switched states a large number of times. In order to account for differences in the time step in different states, the probability density function of the concentrations was constructed using a time trace collected after approximately 1 second intervals. As Fig. 2.5 shows, for a symmetric switch we obtain a symmetric bi-modal probability distribution that corresponds to a double-well potential.

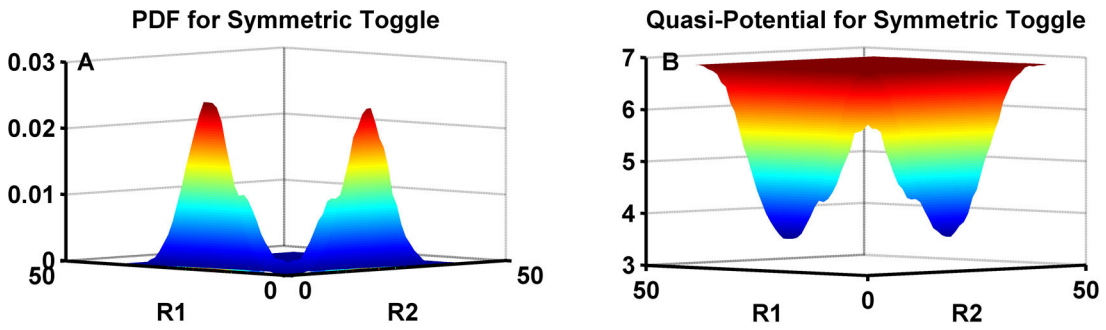

Figure 2.5. The probability distribution function and the quasi-potential of the genetic toggle switch without a load.
(A). The probability distribution function of a toggle switch without a load. The x- and y- axes here represent the number of molecules of Repressor 1 and Repressor 2 respectively, while the z-axis is the frequency of its occurrence. Note that the distribution is symmetric as expected. (B). The quasi-potential of the symmetric toggle switch, showing the symmetric double-well potential constructed by taking the negative logarithm of the probabilities shown in (A). A small offset of 0.001 was added to the probabilities to prevent taking the logarithm of zero. This does not change the shape of the well.

When we add a load to the system asymmetrically, in the form of a binding partner for the Repressor 1, we find that the probability distribution becomes extremely skewed, and the total weight of the probability distribution corresponding to the other side, i.e. Repressor 2, dramatically increases (Fig. 2.6A). This indicates that the underlying double well potential has become skewed and the state 2, corresponding to high Repressor 2, has increased its stability at the cost of State 1 (Fig. 2.6C). When a load is applied to both sides symmetrically, the concentration probability distribution reverts to a symmetric bimodal distribution corresponding to a symmetric double-well potential (Fig. 2.6B & D).

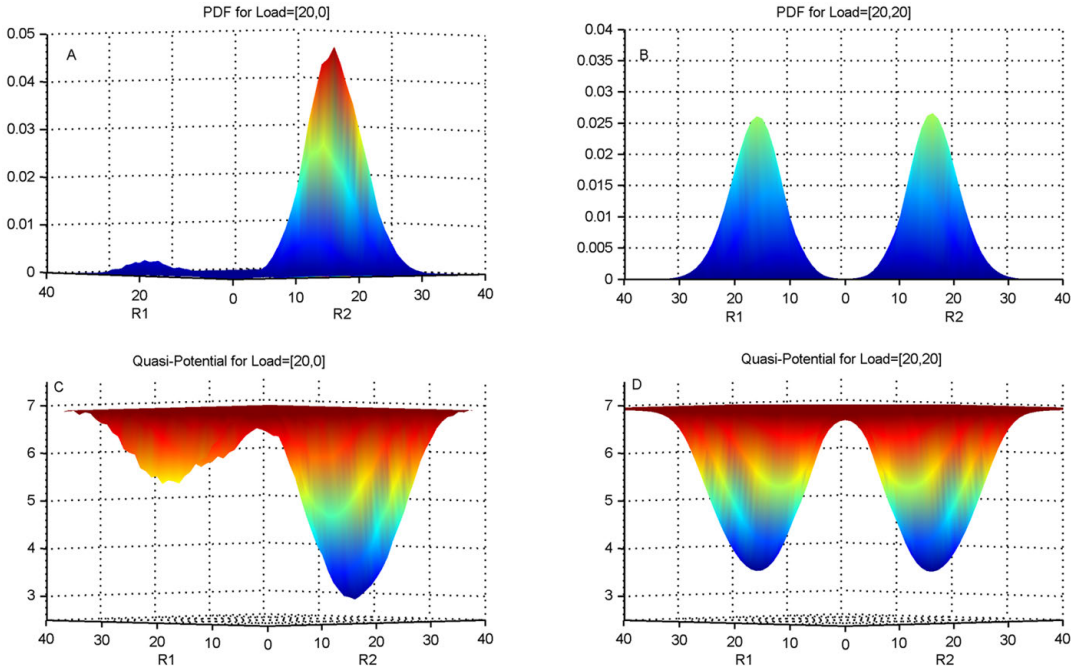

Figure 2.6. The probability distribution function and quasi-potential of a toggle switch with a load.
The 3-dimensional plot is viewed with the xy-plane horizontal for better contrast. The x- and y-axes are numbers of molecules of R1 and R2 while the z-axis is either probabilities or the quasi-potential. (A). The probability distribution function (pdf) of the toggle switch of Fig. 5 but now with a load of 20 molecules on Repressor 1 (R1). (B). The pdf of the toggle switch with a load of 20 molecules on R1 and 20 molecules on R2. (C). The quasi-potential of the toggle with a load of 20 molecules on R1, i.e. corresponding to panel A. (D). The quasi-potential of the toggle with equal loads of 20 molecules on each repressor, i.e. corresponding to panel B.

In order to test this directly we calculated the distribution of lifetimes in state 1 and the lifetimes in state 2. As shown in Fig. 2.7, when the switch is symmetric with no load, the lifetime distribution is exponential, as should be expected for a simple two-state system. However when the load is applied to Repressor 1, the probability distribution of the lifetime in state 2 increases dramatically. The average lifetime of state 1 also increases but only by a very small amount. The time spent in state 2 does not appear to saturate, and continues to increase with increasing load. When loads are applied symmetrically to both sides, the lifetime histogram in Fig. 2.7 indicates that both sides have been stabilized since the system spends significantly longer time in each

state. Note that in an equilibrium system this would have been indicated by the deepening of the potential well. However in non-equilibrium systems the potential well picture does not completely capture the dynamics and there is an additional contribution from a “curl flux” [43], [46] that needs to be taken into account. For our purposes calculating both the distribution of concentrations and the distributions of lifetimes captures the dynamics of the toggle switch.

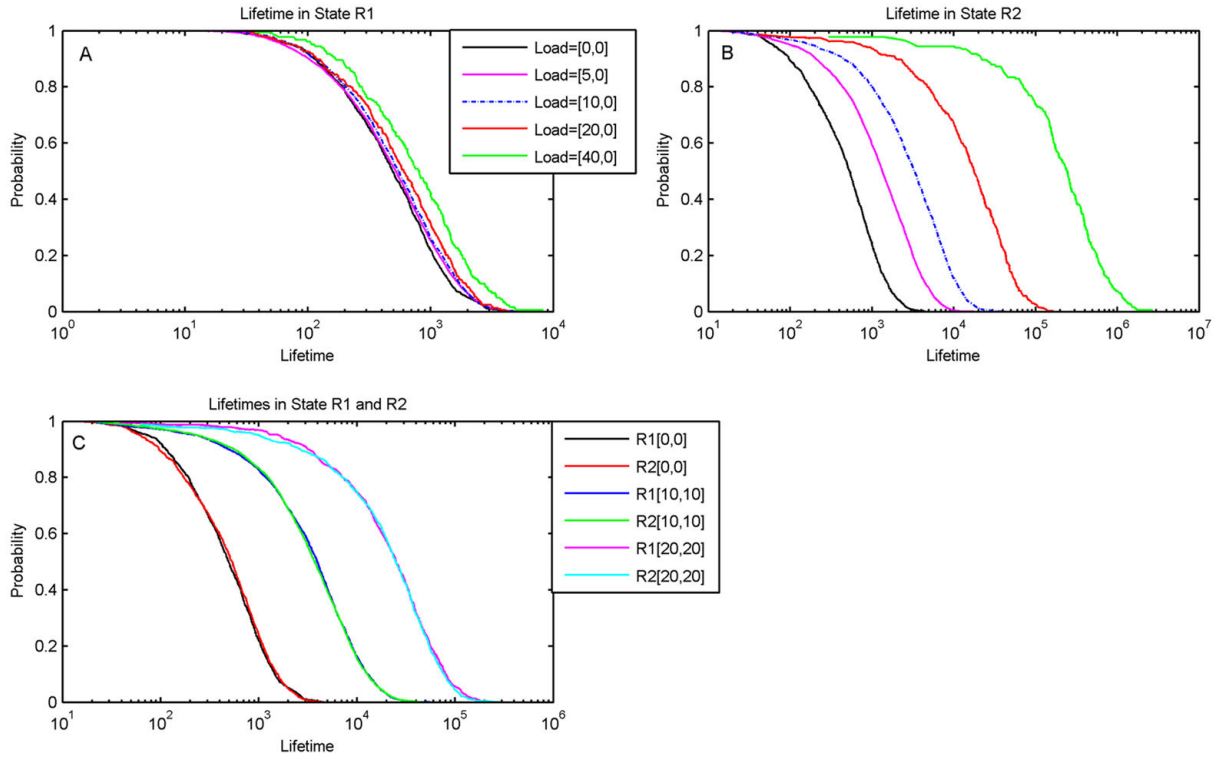

Figure 2.7. Distribution of the lifetimes of the toggle switch with and without loads. The time the system spent in either state R1 or state R2 was calculated from the time trace of the stochastic simulations and a histogram made of the results. The histogram is shown on a semi-log plot to accommodate the data on a single chart. (A). Lifetimes in State R1. The unloaded state is the solid curve that is to the extreme left of the others, showing that the lifetimes in state R1 increase slightly on addition of load on R1 alone due to the “same side effect”. (B) Lifetimes in State R2 when load is on R1. The solid curve on the extreme left is the unloaded state. There is a significant increase in lifetimes due to the “opposite-side effect” of the load on R1. (C). Lifetimes with a balanced load, showing that both the states R1 and R2 get stabilized with a significant increase in lifetimes on addition of a small load on both sides. Note that the distributions for R1 and R2 for equivalent cases coincide as should be expected.

To test whether our results change for higher protein concentrations, we increased protein concentrations about fivefold and recalculated the probability distribution function. We find that our qualitative results remain robust despite the increase in protein concentrations (Appendix I: Supplementary Text S2.1 section 1.3 and Fig. S2.4). Switching between states is rare at these protein numbers, with a mean residence time in state R1 for the unloaded switch being approximately 6×10^5 min against about 700 min for the basal case considered, a difference of almost three orders of magnitude. However as for the basal case, the quasi-potential landscape skews significantly with the addition of a load on the switch.

2.3.4 "Opposite Side effect" dominates the load effect in the basic toggle switch

These results allow us to interpret the dynamic results that we obtained earlier. If the system is in state 2 and there is a load on state 1, a transition requires an increase in Repressor 1 concentration in order to suppress the production of Repressor 2. A load on Repressor 1 however competes with the promoter of Repressor 2 for binding with Repressor 1, and thereby reduces the effective concentration of Repressor 1. This effectively stabilizes state 2. The dynamic analysis shows that state 1 not only remains an attractor state but in fact it takes a longer time, and more inducer, to shift out of state 1 as compared with the no-load situation. This is because the load also acts as a reservoir for Repressor 1, and in fact increases its total concentration. This slows down the transition to state 2. Interestingly this "same side effect" is generally weaker than the "opposite side effect" above. In agreement with this picture, the stochastic simulations show that the distributions of lifetimes in state 1 broaden slightly on addition of a load.

If the load is present symmetrically on both sides, the concentration histograms in Fig. 2.6 and the time histograms in Fig. 2.7 indicate that both states have been stabilized, due to a combination of the 'same side' and the 'opposite side' effect now acting together to stabilize

each state of the switch. In the dynamical simulations this is seen by the increased slope of the response time line for the case of a load on both sides. Results for additional parameter values are shown in Appendix I: Fig S2.15 and Fig S2.16.

2.3.5 Positive feedback moiety makes toggle switch tunable

When a positive feedback moiety is introduced in the toggle switch, we again see a linear relationship between the rise time and the decay time of the two states of the switch and the load (Appendix I: Fig. S2.5). Therefore here too the load appears to be skewing the underlying potential landscape of the switch. Using stochastic simulations we constructed the probability distribution function of this toggle switch as described above. We found that even in the absence of a load, when a positive feedback moiety is introduced on one side of a toggle switch, the probability distribution for the toggle switch, and hence the quasi-potential landscape, becomes extremely skewed in favor of the state with positive feedback as shown in Fig. 2.8A. Even with no load on the system, the switch is biased to State 1 and the lifetime spent in State 1 is much longer than in State 2. If a load is added to R2, the opposite side effect additionally favors State 1. If a load is added to R1 however, the opposite side effect favors State 2 (Fig. 2.8B). It is possible to balance these effects resulting in a more even distribution by adjusting the load on R1 and the strength of positive feedback. As the load on R1 is increased beyond this balance point, the opposite side effect dominates and the probability distribution becomes skewed toward State 2 (Fig. 2.8C). As the opposite side effect increases with increasing load, the lifetime in State 2 also increases in agreement with the findings for the regular toggle switch (Fig. 2.8D). The lifetime in State 1 also increases by a smaller amount, as for the regular toggle switch (Fig. 2.8E).

For the toggle switch with the positive feedback moiety, we can also check the consequences of allowing repressor leakage through the repressor-load complex. As shown in Appendix I: Fig. S2.13, this addition to the system affects the steady state properties of the switch and bistability is abrogated after the load increases beyond a critical value, when load is present for both sides or only one side.

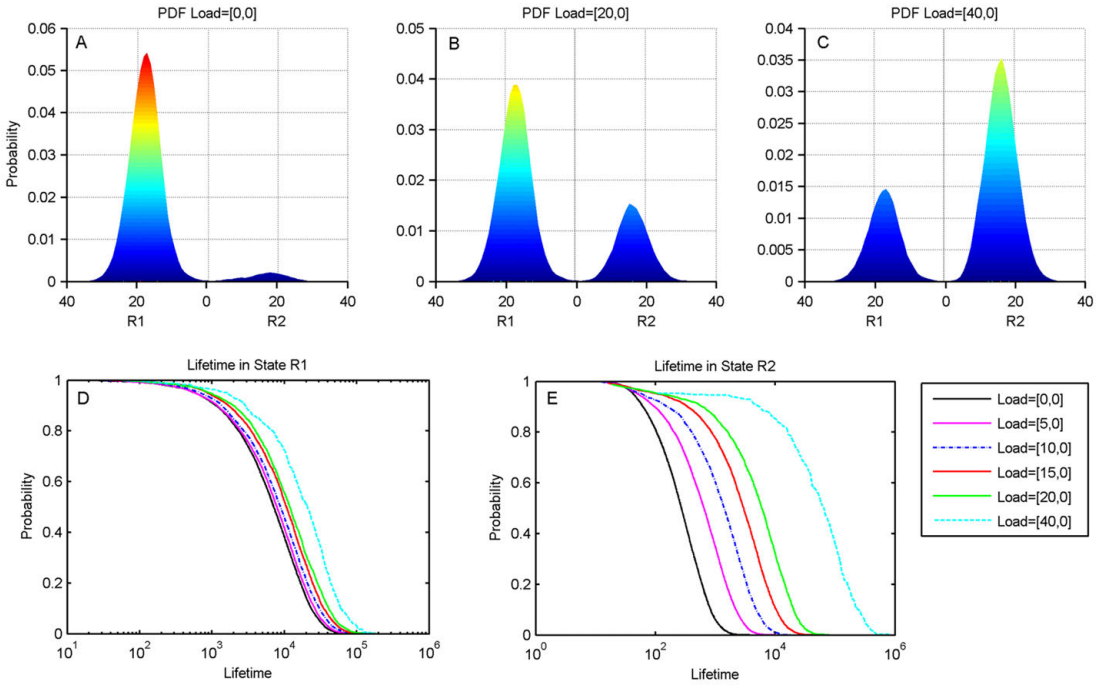

Figure 2.8. The genetic toggle switch with a positive feedback motif on Repressor 1 (R1). (A). The probability distribution function (pdf) with no load. The positive feedback on Repressor 1 leads to a pdf skewed in favor of R1. (B). The pdf with a load of 20 molecules on R1 showing the increase in the weight of R2 due to the "opposite side effect". (C). The pdf with a load of 40 molecules on R1. This load is more than enough to skew the pdf in favor of state R2. (D). Histogram of lifetimes in R1 with varying levels of load on R1. Comparison with panel A shows that the unloaded state has been stabilized by the positive feedback. Note that the lifetimes increase very slightly due to the "same side effect". (E). Histogram of lifetimes in R2 with varying levels of load on R1. The unloaded case is the curve on the extreme left. Note the initial asymmetry in the lifetime distribution due to the positive feedback, as well as the large increase in lifetimes with the inclusion of a load.

2.3.6 Loads fundamentally transform positive feedback based switches in signal transduction

The RasGTP system shows a bistable transition from a low RasGTP state to a high RasGTP state as the activating signal, in our case the number of SOS molecules, are varied. As Fig. 2.9 shows, a system with no Raf shows a classic Z-shaped bifurcation diagram with two bifurcations as SOS is varied. The first bifurcation marks the transition from a monostable low-RasGTP state to a bistable system with a "high" RasGTP state (and an unstable intermediate state). The second bifurcation marks the transition from the bistable state to another monostable state with a high concentration of RasGTP.

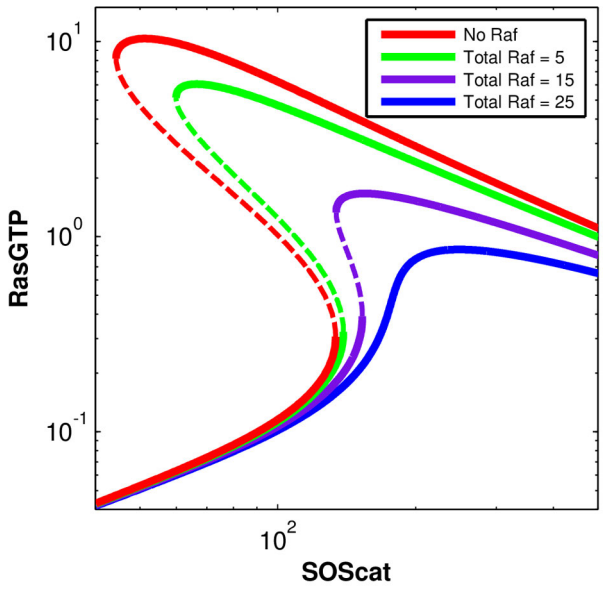

Figure 2.9. Bifurcation diagram of the Ras switch with different levels of Raf (load) on the system.
The total number of SOS in the simulation box is used as the parameter being tuned, which varies from 0 to 1000. For Raf=0, Raf=10 and Raf=30, there are two bifurcations as SOS is increased. In the first bifurcation a new high valued stable steady state appears along with the low valued stable steady state. In the second bifurcation, the low valued stable state disappears leaving behind only the high valued state. The dotted line marks the unstable steady state that also comes into existence in the bistable region. As total Raf increases, the two bifurcations approach each other. When Raf=50, the system has lost both of its bifurcations and is characterized by a single stable steady state at all values of Raf.

When Raf is added to the system, the bifurcation diagram changes and the two bifurcations start approaching each other. This is because the effect of adding Raf is equivalent to sequestering away some of the activated RasGTP in an “inactive” complex. When Raf concentration crosses a threshold, the bifurcations annihilate each other and disappear. This system is now characterized by a single stable point for all concentrations of SOS, and the disappearance of the threshold for Ras activation. While there appears very little free Ras, in reality, even for low SOS concentrations there is a large concentration of the activated RasGTP-Raf complex (since RasGTP in these complexes is also protected from the action of the Ras GTPases).

This can be seen in another way in Appendix I: Fig. S2.8 where the stable state of RasGTP is plotted against the level of total Raf in the system, keeping the level of SOS constant. Again we see that a bistable system is transformed into a monostable system when Raf increases beyond a threshold. These results are exactly the same for the model which assumes Michaelis-Menten kinetics, except for small changes in molecule numbers, as can be seen in Appendix I: Fig. S2.7 and S2.9. Results do not change on changing load-binding parameters (Appendix I: Fig. S2.10, S2.11)

Thus the addition of the Raf scaffold, which is an integral part of the MAPK cascade, fundamentally changes the qualitative behavior of the positive feedback switch. The main reason why the steady state bifurcation properties are affected here in contrast to the basic genetic toggle switch is that for this signaling circuit, as seen in Eq. 22–25, total Raf and Ras are conserved, as is typical for a short timescale signal transduction system. These conservation laws couple Raf concentration to RasGTP concentration even at steady state. Therefore adding Raf to

the system effectively reduces total Ras concentration since Raf sequesters away Ras from the switch.

To see this more generally, consider for example a chemical reaction system comprising of n-species $Y_1,\ldots Y_n$. Let us assume without loss of generality that the species Y_n is coupled to a downstream circuit through a binding reaction with a load, L. The (n+2) differential equations describing this system are:

$$\frac{dY_1}{dt} = f_1(Y_1,\ldots Y_n) \tag{26}$$

$$\frac{dY_n}{dt} = f_n(Y_1,\ldots,Y_n) + k_{on}[Y_nL] - k_{off}[Y_n][L] \tag{27}$$

$$\frac{d[L]}{dt} = k_{off}[Y_nL] - k_{on}[Y_n][L] \tag{28}$$

$$\frac{d[Y_nL]}{dt} = k_{off}[Y_nL] - k_{on}[Y_n][L] \tag{29}$$

Note that for simplicity of notation we have not indicated the dependence of the dynamical system on its own parameter values. Now in the steady state, if the set of equations is complete, the left side uniformly goes to zero and we recover the result that the steady state remains exactly the same with or without a load, as for the genetic toggle switch. However let us now assume that we have an additional conservation law, say,

$$Y_n^{(0)} = Y_n + [Y_nL] \tag{30}$$

This conservation law implies that one equation in our dynamical system is redundant, and we need to drop one equation to make the system linearly independent. We can decide to drop Eq. 19, and substitute $Y_n = Y_n^0 - [Y_nL]$ in Eq. 20 and Eq. 21 and solve the resulting (n+1) equations for the (n+1) unknowns, $Y_1,\ldots,Y_{n-1},Y_nL,L$, obtaining Y_n as a residual from Eq. 22. Thus the steady state solutions of the Y_i's now involve the amount of the load. Clearly, the

existence of the conservation law has led to a change in the steady state properties of the dynamical system. Note that Y_n itself would usually enter (by itself or in the form of other complexes, which then would also need to be accounted for in the conservation law Eq. 22) into one or more of the equations for the remaining species, $Y_1, \ldots Y_{n-1}$. This would result in the equations for those other species explicitly involving, and thus depending upon the level of the load. For the Ras system above, Eq. 16 couples the load, Raf, to the concentration of Ras. However Ras concentration and SOS concentration are also coupled. Thus the load explicitly affects the steady state values of all species concentrations in this system. This leads to a fundamental qualitative change in the bifurcation properties of the system.

2.4 Discussion

It has been pointed out previously that significant sequestration effects can abrogate zero order ultrasensitivity [26], [47], [48], can change the dynamics of simple phosphorylation circuits [23], [24] and change oscillatory behavior in some circuits [27]. We add to this body of work by demonstrating that the addition of a simple binding partner to the output protein of a genetic or signaling switch can have dramatic effects on its properties, and can fundamentally change the operation of the switch.

For a genetic toggle switch with two mutually repressing proteins such as the classic switch built by Gardner et al. [5] we showed that even though the presence of the binding partner does not alter steady state properties of the switch, it can drastically change the dynamic properties. Using a novel potential landscape analysis, we showed that this is because the addition of the binding partner skews the underlying quasi-potential, making one state significantly more stable than the other. In practice therefore, a genetic toggle switch that is significantly skewed towards one side may never properly function as a switch. Thus the

downstream consequences of such loads need to be taken into account when designing larger synthetic circuits with the toggle switch as one of the elements.

On the other hand this phenomenon actually provides a way of making artificial switches tunable. It is possible to engineer a biased switch merely by adding a load on the opposite side of the toggle, which is a useful device when engineering a switch that is designed to be switched on only in special circumstances. A load on both repressor proteins similarly stabilizes both sides of the toggle switch. This could be useful when working with synthetic components with low concentrations in cells, especially those that display stochastic switching. A load on both repressor proteins can significantly increase the stability of such a toggle.

In natural systems, mutually repressing toggle switches are often found with other complexities, such as a positive feedback motif on one side. The positive feedback motif by itself biases the toggle switch by stabilizing the side it is on at the expense of the other side. A load on the same side then stabilizes the opposite side, and can re-establish balance between the two quasi-potential wells. For engineering circuits in multi-cellular organisms, it is worth noting that that feedback between the load on a toggle switch and the strength of the positive feedback may ensure that the switch operates efficiently even in the presence of cell to cell variability in the load. How loads vary between cells and in multi-cellular organisms is an interesting question to explore in future work. The presence of the positive feedback provides a potential target for evolutionary fine-tuning of the switch.

In the above analyses we use novel potential landscape methods that have proved useful and insightful in fields such as protein folding to discuss the fundamental properties of a dynamical system that shows not apparent changes in its stability properties. We demonstrate that these methods, though still relatively underdeveloped for use with non-equilibrium chemical

reaction systems, hold promise for understanding the dynamics of such systems beyond what linear stability analysis can provide. However there are certain conditions when addition of a load changes the stability properties of the genetic toggle switch. One class of such effects happen when the repressor can leak away from the repressor-load complex, as can happen either when the repressor can decay or degrade when bound to the load, or when the load can modify the repressor and make it unable to repress. We show, employing standard bifurcation analysis, that additional loads in this system can abrogate the switch-like properties of the toggle switch entirely.

In switches based on autocatalysis or positive feedback with an enzymatic deactivation, such as is often found in signaling systems, the effects of a load are equally dramatic. We show that in a simple model of Ras activation, adding a small concentration of Raf molecules changes the bifurcation diagram of the signaling circuit and can completely abrogate the bistability in the system. While we have chosen a specific example of Ras activation, our simplified model, with an autocatalytic forward reaction and an enzymatic backward reaction is a minimal model for a many positive feedback switches. The change in the bifurcation diagram arises from the conservation laws that couple the concentration of the load with the concentrations of the proteins in the upstream module. Given the sensitivity of non-linear dynamical systems to initial conditions, it should probably be expected that many, if not all, positive feedback based switches that operate at the short timescales of signal transduction, and therefore must possess these conservation laws, should exhibit this sensitivity to the effect of a load.

Our results throw up an interesting puzzle for quantitative biologists. In many natural signal transduction systems such as the MAPK cascade, the concentration of the output of a bistable switch is quite comparable to the concentration of the load, thus significant changes in

load concentrations could have dramatic effects on the behavior of the switch. However it has also been shown that there is a significant cell to cell variability in protein concentrations [49]. How do cells ensure that positive feedback based switches such as the Ras switch continue to operate robustly in the bistable regime? Additional regulatory mechanisms involving feedback between the load and its partner protein may exist that confer robustness to the qualitative behavior of the biochemical switch. Arguably some of the bells and whistles of natural protein networks that are often disregarded when analyzing the network may in fact be performing this role. In other words, self-assembled switches have to be complex! In this context it is worth mentioning that it has been persuasively argued [50], [51] that some biological circuits maintain robustness of "fold-change' behavior rather than absolute levels of protein concentration. It is possible that additional protein-protein interactions that couple concentrations of loads with output proteins may end up in performing this function. Another significant factor that needs consideration is the role of spatial segregation in producing feedback from the downstream module to the upstream one. In fact it has been shown experimentally that MAPK substrates sequester activated MAPK in the nucleus, and thus protect it from cytoplasmic phosphatases. Changing the concentration of one substrate therefore affects the concentration of activated MAPK [52].

Previous discussions of the effect of loads on the operation of circuits have suggested the use of insulators, that is circuit elements that insulate the upstream module from the downstream module [22]. The initial suggestions for building insulators in Ref. [22] involved incorporating signal amplification along with negative feedback in the upstream circuit. Another way of insulating the circuit is to ensure that the demand of the load for its cognate repressor is never significant compared to the total amount of repressor. For a genetic switch therefore, a possible

insulating mechanism is if the link to the downstream circuit is through a promoter. For example, consider making an AND gate from an output of the toggle switch. This can be done by inserting a constitutively produced protein Y that binds to R1 such that the complex is a transcription factor for another protein, say Z. Thus there is an AND relationship between the two inputs, Y and R1 and the output Z. To offset the effect of load induced modulation of the dynamics of R1, an additional step can be inserted such that R1 first binds to the promoter region of another gene that codes for protein X and activates its transcription, and it is the protein X, rather than R1, that can bind to Y and activate production of Z. The advantage of adding this extra step is that the concentration of the promoter for X is very small compared to the concentration of R1, and therefore load induced modulation of the upstream toggle can be kept at a minimum. Note however that this cannot be done without the additional cost of the time delay required for the transcription and translation of X.

As can be seen, any additional step or series of steps that can amplify a weak signal can act as an insulator. Another standard example of an amplifying circuit is a phosphorylation cascade which is especially relevant when considering Ras activation since it directly leads to the MAPK phosphorylation cascade. Phosphorylation cascades are also very fast, and therefore do not face the additional time delays of an additional transcriptional step. From the point of view of synthetic circuit design, the insulating mechanism here could be constructed by designing a weak binding affinity of Ras (or the synthetic protein that plays that role) for Raf (or the equivalent protein). The bound complex then catalyzes a phosphorylation cascade that ends by connecting to the downstream circuit.

Note that this method of insulation does not have the same time delay costs as the additional transcription steps. However it does come with the metabolic costs of having to

produce large amounts of proteins that are essentially serving no useful physiological purpose for the cell. This cost could be relevant in some synthetic biology applications, and certainly needs to be evaluated during circuit design. It has been shown in the context of phosphorylation cycles that insulation always carries a metabolic cost, and in general better insulation carries a greater metabolic cost [53].

The existence of the MAPK phosphorylation cascade however begs the question whether it serves the purpose of insulation of the upstream Ras circuit from the downstream circuit. While it is not possible to answer this intriguing question without further experiments, it does appear that the Ras-Raf complex is present is quite large numbers on activated cells. This would suggest that insulation is not the function for which the cascade may have evolved. Our own analysis of the genetic toggle switch with the positive feedback motif suggests that Nature may prefer more complicated forms of regulation that balance the different components of the circuit. However there is no reason why both methods cannot be utilized. To our mind this is a very exciting question that requires more attention from experimentalists and theorists alike.

It should also be noted that due to non-specific binding of transcription factors with DNA as well as between proteins, every circuit in the cell, real or synthetic, operates in the presence of a load. Variability in the functioning of circuits that are seen when transferring synthetic circuits between species, or even in different cells, may be a result of not only differences in basic protein concentrations, but also of this undervalued but nevertheless tangible load. Based on this reasoning we predict that some of the host-dependent effects that complicate synthetic biology, i.e. a synthetic circuit that works in one organism not performing well in another, are in fact due to changes in the intrinsic load due to non-specific binding when changing hosts.

Our analysis underscores the importance of incorporating loads when simulating models of switches in natural and synthetic systems. Mathematical analysis of switch-like motifs therefore would do well to at least include a load on their output proteins, in order to incorporate the possible effects of load induced modulation on the circuit.

REFERENCES

1. Wagner GP, Pavlicev M, Cheverud JM. The road to modularity. *Nature reviews Genetics.* 2007; 8: 921–931.

2. Cooling MT, Rouilly V, Misirli G, Lawson J, Yu T, et al. Standard virtual biological parts: a repository of modular modeling components for synthetic biology. *Bioinformatics*. 2010; 26: 925–931.

3. Prasad A. *Computational Modeling of Signal Transduction Networks: A Pedagogical Exposition.* 2012; In: Liu X, Betterton M, editors. *Computational Modeling of Signaling Networks*: Springer.

4. Basu S, Mehreja R, Thiberge S, Chen M-T, Weiss R. Spatiotemporal control of gene expression with pulse-generating networks. *Proc Natl Acad Sci.* 2004;101: 6355–6360.

5. Gardner TS, Cantor CR, Collins JJ. Construction of a genetic toggle switch in Escherichia coli. *Nature*. 2000; 403: 339–342.

6. Chang DE, Leung S, Atkinson MR, Reifler A, Forger D, et al. Building biological memory by linking positive feedback loops. *Proc Natl Acad Sci.* 2010;107: 175–180.

7. Kramer BP, Viretta AU, Daoud-El-Baba M, Aubel D, Weber W, et al. An engineered epigenetic transgene switch in mammalian cells. *Nat Biotechnol.* 2004; 22: 867–870.

8. Ham TS, Lee SK, Keasling JD, Arkin AP. Design and construction of a double inversion recombination switch for heritable sequential genetic memory. *PLoS One.* 2008;3.

9. Anderson JC, Voigt CA, Arkin AP. Environmental signal integration by a modular AND gate. *Mol Syst Biol.* 2007; 3: 133–133.

10. Tamsir A, Tabor JJ, Voigt CA. Robust multicellular computing using genetically encoded NOR gates and chemical ‘wires’. *Nature.* 2011; 469: 212–215.

11. Elowitz MB, Leibler S. A synthetic oscillatory network of transcriptional regulators. *Nature*. 2000; 403: 335–338.

12. Atkinson MR, Savageau MA, Myers JT, Ninfa AJ. Development of genetic circuitry exhibiting toggle switch or oscillatory behavior in Escherichia coli. *Cell.* 2003; 113: 597–607.

13. Stricker J, Cookson S, Bennett MR, Mather WH, Tsimring LS, et al. A fast, robust and tunable synthetic gene oscillator. *Nature*. 2008; 456: 516–519.

14. Morey KJ, Antunes MS, Albrecht KD, Bowen TA, Troupe JF, et al. Developing a synthetic signal transduction system in plants. *Methods Enzymol.* 2011; 497: 581–602.

15. de Lorenzo V. Systems biology approaches to bioremediation. *Current opinion in biotechnology.* 2008; 19: 579–589.

16. Alper H, Stephanopoulos G. Engineering for biofuels: exploiting innate microbial capacity or importing biosynthetic potential? *Nat Rev Microbiol.* 2009; 7: 715–723.

17. Lu TK, Collins JJ. Dispersing biofilms with engineered enzymatic bacteriophage. *Proc Natl Acad Sci.* 2007; 104: 11197–11202.

18. Anderson JC, Clarke EJ, Arkin AP, Voigt CA. Environmentally controlled invasion of cancer cells by engineered bacteria. *J Mol Biol.* 2006; 355: 619–627.

19. Lu TK, Collins JJ. Engineered bacteriophage targeting gene networks as adjuvants for antibiotic therapy. *Proc Natl Acad Sci.* 2009; 106: 4629–4634.

20. Ro D-K, Paradise EM, Ouellet M, Fisher KJ, Newman KL, et al. Production of the antimalarial drug precursor artemisinic acid in engineered yeast. *Nature.* 2006; 440: 940–943.

21. Purnick PE, Weiss R. The second wave of synthetic biology: from modules to systems. *Nature reviews Molecular cell biology.* 2009; 10: 410–422.

22. Del Vecchio D, Ninfa AJ, Sontag ED. Modular cell biology: retroactivity and insulation. *Mol Syst Biol.* 2008; 4: 161.

23. Ventura AC, Jiang P, Van Wassenhove L, Del Vecchio D, Merajver SD, et al. Signaling properties of a covalent modification cycle are altered by a downstream target. *Proc Natl Acad Sci.* 2010; 107: 10032–10037.

24. Jiang P, Ventura AC, Sontag ED, Merajver SD, Ninfa AJ, et al. Load-induced modulation of signal transduction networks. *Sci Signal.* 2011; 4: ra67.

25. Kim KH, Sauro HM. Fan-out in gene regulatory networks. *J Biol Eng.* 2010; 4: 16–30.

26. Bluthgen N, Bruggeman FJ, Legewie S, Herzel H, Westerhoff HV, et al. Effects of sequestration on signal transduction cascades. *The FEBS journal.* 2006; 273: 895–906.

27. Jayanthi S, Del Vecchio D. Tuning genetic clocks employing DNA binding sites. *PLoS One.* 2012; 7: e41019.

28. Pomerening JR, Sontag ED, Ferrell JE Jr. Building a cell cycle oscillator: hysteresis and bistability in the activation of Cdc2. *Nat Cell Biol.* 2003; 5: 346–351.

29. Prasad A, Zikherman J, Das J, Roose JP, Weiss A, et al. Origin of the sharp boundary that discriminates positive and negative selection of thymocytes. *Proc Natl Acad Sci.* 2009; 106: 528–533.

30. Das J, Ho M, Zikherman J, Govern C, Yang M, et al. Digital signaling and hysteresis characterize ras activation in lymphoid cells. *Cell.* 2009; 136: 337–351.

31. Bagowski CP, Ferrell JE Jr. Bistability in the JNK cascade. *Curr Biol.* 2001; 11: 1176–1182.

32. Arkin A, Ross J, McAdams HH. Stochastic kinetic analysis of developmental pathway bifurcation in phage lambda-infected Escherichia coli cells. *Genetics.* 1998; 149: 1633–1648.

33. Ferrell JE Jr. Tripping the switch fantastic: how a protein kinase cascade can convert graded inputs into switch-like outputs. *Trends Biochem Sci.* 1996; 21: 460–466.

34. Maamar H, Dubnau D. Bistability in the Bacillus subtilis K-state (competence) system requires a positive feedback loop. *Molecular microbiology.* 2005; 56: 615–624.

35. Legewie S, Bluthgen N, Herzel H. Mathematical modeling identifies inhibitors of apoptosis as mediators of positive feedback and bistability. *PLoS Comput Biol.* 2006; 2: e120.

36. Kobayashi H, Kaern M, Araki M, Chung K, Gardner TS, et al. Programmable cells: interfacing natural and engineered gene networks. *Proc Natl Acad Sci.* 2004; 101: 8414–8419.

37. Jayanthi S, Nilgiriwala KS, Del Vecchio D. Retroactivity controls the temporal dynamics of gene transcription. *ACS synthetic biology.* 2013; 2: 431–441.

38. Kuhlman T, Zhang Z, Saier MH Jr, Hwa. Combinatorial transcriptional control of the lactose operon of Escherichia coli. *Proc Natl Acad Sci.* 2007; 104: 6043–6048.

39. Kim K-Y, Wang J. Potential energy landscape and robustness of a gene regulatory network: toggle switch. *PLoS Comput Biol.* 2007; 3: e60.

40. Wang J, Zhang J, Yuan Z, Zhou T. Noise-induced switches in network systems of the genetic toggle switch. *BMC Syst Biol.* 2007; 1: 50–50.

41. Tian T, Burrage K. Stochastic models for regulatory networks of the genetic toggle switch. *Proc Natl Acad Sci.* 2006; 103: 8372–8377.

42. Warren PB, ten Wolde PR. Chemical models of genetic toggle switches. *J Phys Chem B.* 2005; 109: 6812–6823.

43. Wang J, Xu L, Wang E, Huang S. The Potential Landscape of Genetic Circuits Imposes the Arrow of Time in Stem Cell Differentiation. *Biophys J.* 2010; 99: 29–39.

44. Strasser M, Theis FJ, Marr C. Stability and multiattractor dynamics of a toggle switch based on a two-stage model of stochastic gene expression. *Biophys J.* 2012; 102: 19–29.

45. Allen RJ, Warren PB, Ten Wolde PR. Sampling rare switching events in biochemical networks. *Phys Rev Lett.* 2005; 94: 018104–018104.

46. Wang J, Xu L, Wang E. Potential landscape and flux framework of nonequilibrium networks: robustness, dissipation, and coherence of biochemical oscillations. *Proc Natl Acad Sci.* 2008; 105: 12271–12276.

47. Buchler NE, Louis M. Molecular titration and ultrasensitivity in regulatory networks. *Journal of molecular biology*. 2008; 384: 1106–1119.

48. Lee TH, Maheshri N. A regulatory role for repeated decoy transcription factor binding sites in target gene expression. *Molecular Systems Biology.* 2012; 8: 576.

49. Raj A, Van Oudenaarden A. Nature, nurture, or chance: stochastic gene expression and its consequences. *Cell.* 2008; 135: 216–226.

50. Shoval O, Goentoro L, Hart Y, Mayo A, Sontag E, et al. Fold-change detection and scalar symmetry of sensory input fields. *Proc Natl Acad Sci.* 2010; 107: 15995–16000.

51. Goentoro L, Shoval O, Kirschner MW, Alon U. The incoherent feedforward loop can provide fold-change detection in gene regulation. *Mol Cell.* 2009; 36: 894–899.

52. Kim Y, Paroush Z, Nairz K, Hafen E, Jimenez G, et al. Substrate-dependent control of MAPK phosphorylation in vivo. *Mol Syst Biol.* 2011; 7: 467.

53. Barton JP, Sontag ED. The energy costs of insulators in biochemical networks. *Biophys J.* 2013; 104: 1380–1390.

CHAPTER 3: A GENETIC TOGGLE SWITCH IN PLANTS[2]

3.1 Main text

Synthetic biology aims to develop programmable traits in organisms that could yield sustainable technologies for human and environmental needs. Previous work established that theoretical and practical design of complex gene networks with programmable functions can be achieved in bacteria. Subsequent studies showed similar programmable functions can be produced in cellular eukaryotic systems such as yeast, cultured mammalian cells and multicellular organoids [1–7]. Here, we expand synthetic biology's predictive abilities to a whole eukaryote organism with functionality maintained through meiosis and in successive generations. Based on quantitatively characterized transfer functions of plant genetic components, we developed in silico predictive models to guide assembly of the first synthetic toggle switch circuit in a plant. Our predictions allow computer selection of specific genetic components that are assembled to form a toggle and tested in transgenic plants. Whole-plant data are quantitatively modeled to verify that the desired behaviors are achieved, and to allow genetic circuit refinement if not achieved. Using this approach, we produced plants that are able to switch states and maintain these states through complex eukaryotic processes. These results

[2] The collaborative work presented in this chapter and in Appendix II is an unpublished manuscript by Tessema K. Kassaw, Wenlong Xu, Christopher S. Zalewski, Katherine A. Kiwimagi, Ron Weiss, Mauricio S. Antunes, Ashok Prasad, June I. Medford. Author contributions: J.I.M. and R.W. conceived the idea, M.S.A. developed the protoplast methodology, K.A.K. and A.P. did the initial data analysis and initial models, A.P. and W.X. developed advanced models, W.X. developed plant imaging automation software, M.S.A., T.K.K., C.S.Z. and J.I.M. designed the synthetic genetic circuits, T.K.K. and C.S.Z. assembled and verified all genetic circuits, T.K.K. and support staff produced all transgenic plants, and all authors aided in data analysis, preparation and writing of the manuscript. I am the co-first author on the manuscript. This work is being presented in this chapter in its entirety to maintain the intellectual coherence of the project.

suggest that synthetic biology's predictive and programmable abilities can be extended to whole organisms, including metazoans and humans, and open the possibility to predictably engineer nature's untapped diversity into sustainable systems.

A genetic toggle switch is a device capable of switching between, and maintaining, two distinct states. The general architecture of our synthetic bistable genetic circuit is based on the topology used for the first genetic toggle switch, described by Gardner et al.[6]. The ability to switch, and maintain, two distinct states is achieved by two constitutively active and repressible promoters that are cross-repressed by their respective repressor proteins (Figure 3.1a). For plant toggle function, our circuits have additional complexity so we can genetically encode the repressor's inducibility, a function not required in the original bacterial circuit (Figure 3.1b, d). The genetic circuit output (readout) is likewise under the control of a repressible promoter and expression levels of the readout (gene of interest) determine the state of the circuit (Fig. 3.1b-e). We define our two states as high and low (HIGH State → high readout expression, LOW State → low readout expression) with the transition between states controlled by a brief chemical induction (Fig. 3.1). Each state is maintained in the absence of the inducer, i.e., it shows memory (Fig. 3.1c, e).

We previously quantitatively characterized the transfer function of synthetic repressible promoters and their cognate transcriptional repressors using a transient expression assay in Arabidopsis protoplasts [7]. We used our models to select, from this pool, quantitatively characterized genetic components with the best predicted ability to produce a genetic toggle switch. However, use of a transient expression system to measure quantitative function left two factors uncharacterized: the actual parameters of the multiplicative noise present in the protoplast system, and positional effects resulting from random stable integration of the genetic circuits (T-

DNA) in transgenic plants. These factors could lead to quantitative variation in parameters ranging from about 0.2 to 2-fold, and thus affect our capacity to use this characterization for predictive fits in synthetic genetic devices. As shown by mathematical analysis (Appendix II: Section 8.4.1), a functional toggle switch requires repressor-promoter pairs with two properties: (i) the input-output functions characterizing the repressibility of a promoter by its repressor must have large Hill coefficients, and (ii) the maximal expression levels of the two promoters must be balanced. We selected the repressor-promoter pairs for our toggle design based on these two principles, and identified two combinations that satisfy these criteria. One combination consists of NOS2xGal4.EAR with two copies of 35S2xLexA.EAR (Toggle 1.0) (Appendix II: Fig. S3.2). The second consists of two copies of 35S4xLexATATA.OFPx and one copy of NOS2xGal4.EAR (Toggle 2.0) (Fig. 3.2). In both cases, the 2:1 combination was chosen to balance the maximal strength of the stronger Gal4-based promoter (see Appendix II: Section 8.2.1 for a detailed discussion of the quantitative characteristics of these components). We generated transgenic plants [8] containing each distinct toggle circuit controlling expression of a quantitative reporter (luciferase). Initial screening of primary transgenic plants in the absence of any inducer showed plants in either the low or high expression states. We focused on plants initially in the low state (no luciferase expression), as plants initially in the high state (strong luciferase expression) could either have a functional toggle or they could simply have constitutive luciferase expression.

We evaluated circuit performance using homozygous plants grown vertically in MS agar plates with or without the chemical inducers, 4-hydroxy-tamoxifen (4-OHT; switching to the high state using the synthetic repressors, LexA.EAR [Toggle 1.0] or LexA.OFPx [Toggle 2.0]) or dexamethasone (DEX; switching to the low state with the synthetic repressor, Gal4.EAR).

The switching time from the low to the high state and from the high to the low state was determined based on the time for the circuit to establish steady-state behavior after a continuous induction with 4-OHT or DEX, as shown in Fig. 3.5. We induced switching of circuit states after four days by moving plants to the opposite induction media (see Section 3.2 Online Methods).

To quantitatively evaluate the bistability of our synthetic toggle switch, we utilized a custom-written image processing algorithm that extracts luciferase data from expression in an image of an entire plant, and can distinguish plant roots from shoots (Appendix II: Section 8.1.2). We devised a novel method to sample all good parameter sets, i.e., parameter sets that fit the plant data to an Ordinary Differential Equation (ODE) model of a toggle switch. The system of ODEs is based on Hill functions to describe the input-output characteristics of each repressible promoter (Appendix II: Section 8.1.4). To sample the space of good parameter values, we used a Markov Chain Monte Carlo (MCMC) method with the Metropolis algorithm [9] to numerically maximize a likelihood function (Appendix II: Section 8.1.4). Parameter values that met the criteria of goodness of fit were used to simulate the ODE model to assess the bistability properties of the system (Appendix II: Section 8.1.4). Figure 3.3a shows fitted ODE simulations (blue lines) versus actual data points (red dots) for plants containing Toggle 1.0. Toggle 1.0 correctly switched from the low state to the high state with 4-OHT induction, producing an average of 21-fold increase in luciferase expression (maximum of 32-fold; Figs. 3.6, 3.7). Similarly, Toggle 1.0 plants in the high state were able to switch back to the low state with DEX induction showing a 25-fold average decrease in luciferase expression (maximum 40-fold; Figs. 3.6, 3.7). However, a hallmark of a bistable toggle switch is memory, i.e., the ability to maintain a stable state even in the absence of the inducer. Toggle 1.0 plants failed to show such a behavior (Figure 3.3a, Fig. 3.8, High Memory), and instead functioned as a monostable “doorbell” switch

that stays in the high state only while the inducer is present. This was confirmed by the quantitative analysis based on ODE simulations (Appendix II: Section 8.2.4).

The Toggle 2.0 genetic circuit is assembled from 35S4xLexATATA and NOS2xGal4 promoters in a 2:1 combination, respectively, and Gal4.EAR and the stronger LexA.OFPx repressor (Fig. 3.2). Toggle 2.0 plants correctly switched from the low to high state in the presence of 4-OHT (Fig. 3.3b, Fig. 3.9b) with an average induction of 80-fold (maximum 96-fold; Fig. 3.10d) in roots. Moreover, unlike Toggle 1.0 plants, Toggle 2.0 plants showed an ability to retain the high state (Fig. 3.3b, Fig. 3.11a, High Memory). However, Toggle 2.0 plants switched poorly from the high state to the low state with DEX induction, demonstrating behavior indistinguishable from the High Memory treatment, where DEX was not added (Fig. 3.3b, High → Low; Figs. 3.9g, 3.10a; Appendix II: Tables S3.6-S3.7). Similar to Toggle 1.0, untreated Toggle 2.0 control plants showed little or no background luciferase expression and remained in the low state throughout our experiments (Fig. 3.3b, Low Memory, and Figs 3.9d, 3.10a). These data suggest that the 35S4xLexATATA promoter is stronger than predicted in silico (Appendix II: Tables S3.10-S3.11), increasing production of the Gal4.EAR repressor that turns off the luciferase output without induction. However, its high cooperativity (Appendix II: Table S3.10), combined with strong repression from LexAOFPx, resulted in a toggle that when switched, produces plants that become trapped in the high state until reset by meiosis, when the plants return to the low state originally selected.

Results from Toggle 1.0 and Toggle 2.0 (Appendix II: Sections 8.2.3-8.2.6, Figs. 3.8, 3.11), indicate that we could produce a fully functional toggle by simply adding a second copy of the DEX-inducible Gal4.EAR repressor to Toggle 2.0 (Fig. 3.2). We assembled this genetic circuit, Toggle 2.1, and produced transgenic plants. Plants containing Toggle 2.1 correctly

switched from the low state to the high state with 4-OHT addition (Figs. 3.3c, 3.4b, 3.12b), producing a 34- and 19-fold increase in luciferase expression in the shoots and roots, respectively (Fig. 3.13c, d), and retained this state (Figs. 3.3c, 3.4d, High Memory). In addition, Toggle 2.1 plants were able to switch back from the high state to the low state and maintain this low memory state (Figs. 3.3c, 3.4a, c). To further quantitatively evaluate bistability shown in Figures 3.3 and 3.4, we used the MCMC scheme to fit the luciferase data from Toggle 2.1 plants. The MCMC analysis shows that for shoots all the parameter sets that met the goodness of fit criterion are bistable, i.e., they displayed two well separated states for a time period much longer than the experimental timescale (see Appendix II: Sections 8.2.7-8.2.8 and Fig. 3.14), whereas roots are bistable but have a smaller number of parameter sets that fit this criterion (Appendix II: Section 8.2.8). Toggle 2.1 is therefore the first bistable genetic toggle switch developed in a plant, and indeed in a complex multicellular organism.

The quantitative difference in our toggle's function between shoots and roots may suggest broader rules for predictive genetic circuits in entire organisms. In plant development, one of the earliest differentiation events is distinction of the root from the shoot [10–13]. When we quantitatively examined switching and memory in shoots and roots, we found differences (Figs. 3.7, 3.10, 3.13). Specifically, for Toggle 2.1, shoots appear to show both higher expression and better memory of the high state than roots (Figs. 3.4b-d, 3.12, 3.13; Appendix II: Tables S3.8, S3.9). One possibility is that tissue specific differences have some scalar effect between roots and shoots, or simply that uptake of the inducers is very likely different in roots than in shoots; shoots could require transport. Another possibility is that positional effects from the random T-DNA integration [14,15] may result in variable accessibility for transcription factors, potential for post-integration modifications, and differences in spatial and temporal regulation of promoter

activity. In support of this, it is notable that the monostable toggle (Toggle 1.0) had higher expression in the roots than the shoots (Figs. 3.3a, 3.6, 3.7).

Nonetheless, our genetic toggle maintains its function through meiosis, cell and tissue differentiation, and distinct life states, suggesting our synthetic circuits have robust abilities. The functional retention through meiosis, with its characteristic chromatin resetting [16], is notable. Hence, our toggle switch extends synthetic biology's programmability to differentiated multicellular organisms. Our quantitative predictions based on transient expression in protoplasts, while still not completely reliable for predictions, can be used to guide the design of synthetic circuits in plants reducing the combinations to test. In support of this, parameter values estimated by the fits to the ODE model in whole plants overlap with those previously estimated for transient expression of the individual genetic parts in protoplasts (Appendix II: Section 8.4.3). The distinct behavior of Toggle 1.0 versus Toggle 2.0 and Toggle 2.1 in roots versus shoots suggests that design of genetic circuits for multicellular organisms could benefit by further quantitative tuning for specific tissues. Because automated genetic design has already been demonstrated in bacteria [17], producing programmable functions in plant platforms may allow us to develop sustainable technologies for food security, material and devices to serve humanity and the environment in the post-industrial period.

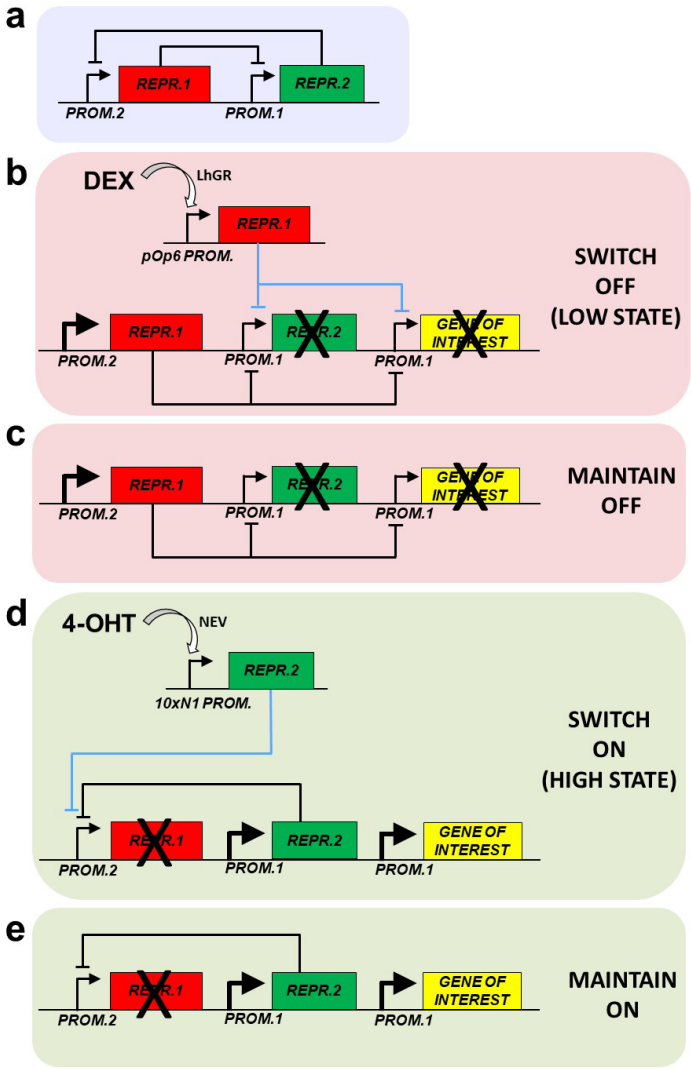

Figure 3.1. General architecture of a plant toggle switch.
a. General structure of toggle where PROM.1 and PROM.2 are mutually repressed by protein repressors (REPR.1 and REPR.2) whose expression is reciprocally directed by each promoter. **b-d**, Design of a synthetic toggle switch. *PROM.1* and *PROM.2* are constitutive and repressible plant promoters that control expression of the orthogonal repressors, *REPR.1* and *REPR.2*. REPR.1 and REPR.2 mutually repress transcription of each other. A second copy of *PROM.1* controls expression of a readout (*GENE OF INTEREST*). The state of the circuit is described by the expression level of the readout (HIGH → high expression, LOW → low expression). Switching states of the toggle circuit is controlled by chemical inducers, DEX (dexamethasone) and 4-OHT (4-hydroxytamoxifen). **a.** DEX induces expression of the second copy of REPR.1 that binds to and represses expression of *PROM.1* (blue lines). This enables the switch to the low state (**b**), and maintenance of this low state without the inducer (**c**). **d**. OHT induces expression of a second copy of *REPR.2* that binds to and represses *PROM.2* (blue line). This enables the switch to the high state (**d**), and maintenance of this high state without the inducer (**e**).

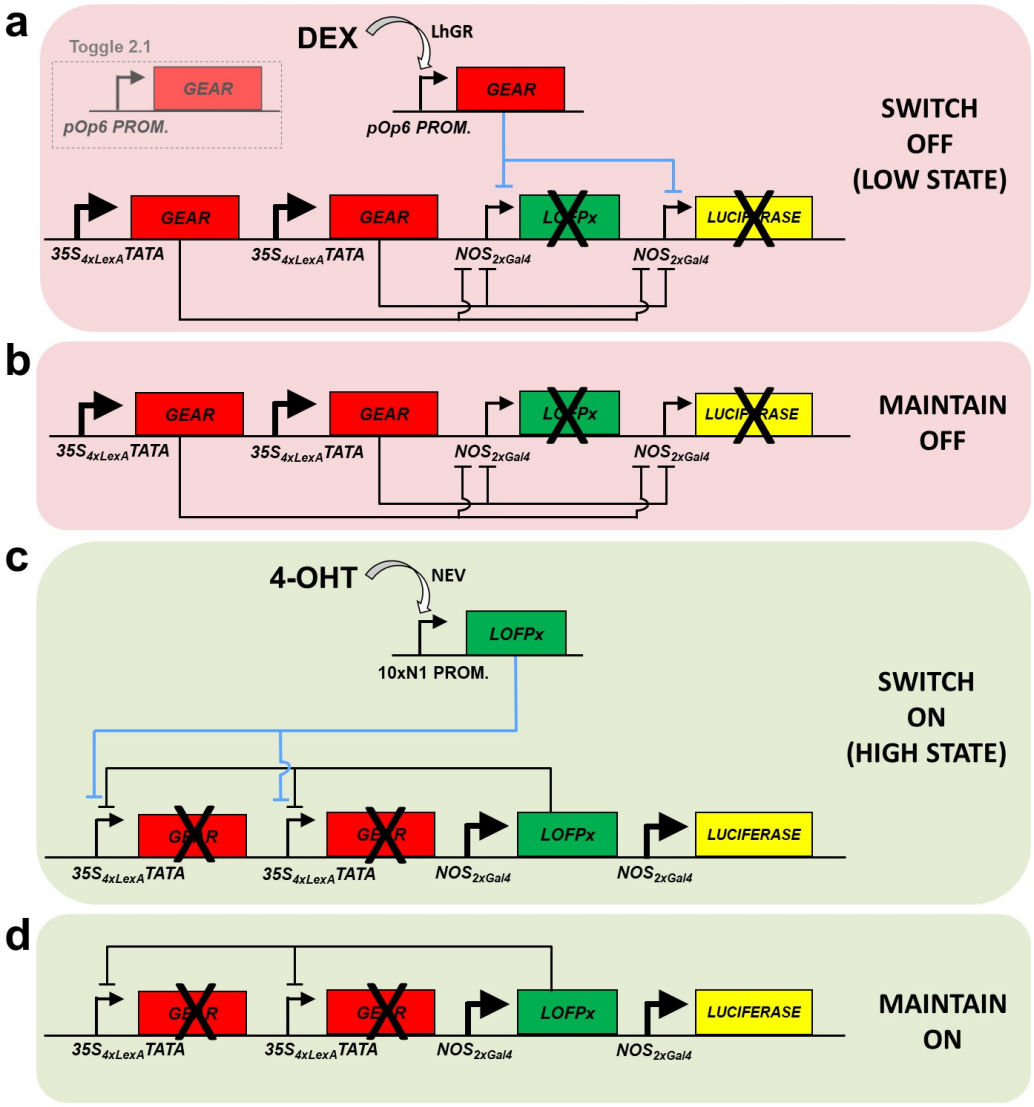

Figure 3.2. Schematic showing assembled components in a plant toggle switch. Repressors *GEAR* (Gal4.EAR) and *LOFPx* (LexA.OFPx) mutually repress expression of each other by binding to the repressible promoters, NOS_{2xGal4} and $35S_{4xLexA}TATA$, respectively. **a-b.** DEX induces a second copy of the *GEAR* repressor that binds to and represses two copies of the promoter, NOS_{2XGal4}, enabling (**a**) the switch to the low state and (**b**) maintenance of the low state without the inducer. **c-d.** OHT induces a copy of the *LOFPx* repressor that binds to and represses two copies of the promoter $35S_{4XLexA}TATA$ enabling (**c**) the switch to the high state and (**d**) maintenance of the high state without the inducer. Firefly luciferase provides a quantitative readout of circuit function. The inset shows a copy of DEX inducible GEAR repressor added in Toggle 2.0 to create Toggle 2.1.

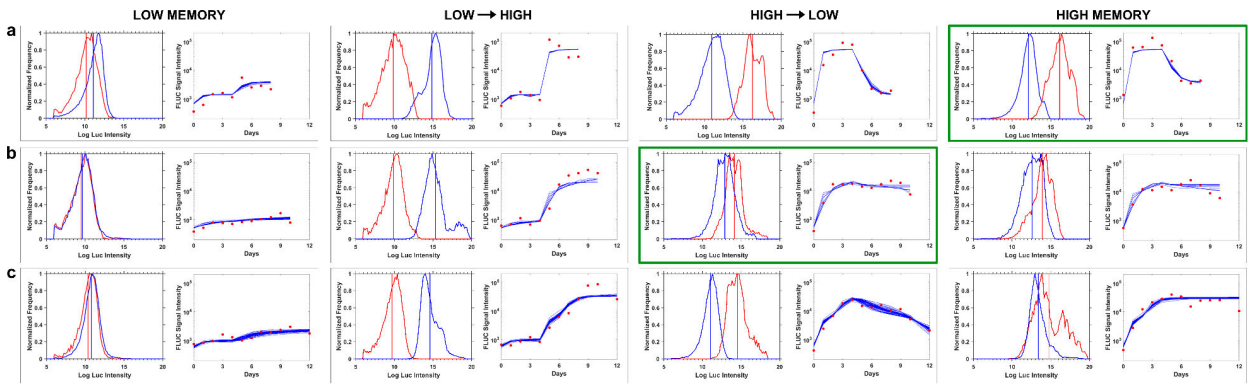

Figure 3.3. Quantitative analysis of bistability of the different toggle circuits in plants. Transgenic plants containing each of the toggle switch circuits were subjected to different inducer conditions (see Section 3.2 Online Methods for sample sizes) to test stability of the low and high states, as well as state transitions. Each box contains a histogram representation of the quantification of luciferase expression in plants, plotted as pixel intensity before (red curves) and after (blue curves) induction of state transition, and an ODE model fit (blue line) to the experimental data collected (red dots). **a,** Toggle 1.0. **b,** Toggle 2.0. **c,** Toggle 2.1. Green boxes in **a** and **b** indicate where the corresponding toggle circuit failed to display the expected behavior. *Low Memory*, plants incubated with DEX inducer for 4 days to establish the low state, then moved to media with no inducer to test for stability (memory) of the low state. *Low → High*, plants incubated with DEX inducer for 4 days to establish the low state, then moved to media with 4-OHT inducer to switch the circuit to the high state. *High → Low*, plants incubated with 4-OHT inducer for 4 days to establish the high state, then moved to media with DEX inducer to switch the circuit to the low state. *High Memory*, plants incubated with 4-OHT inducer for 4 days to establish the high state, then moved to media with no inducer to test for stability (memory) of the high state.

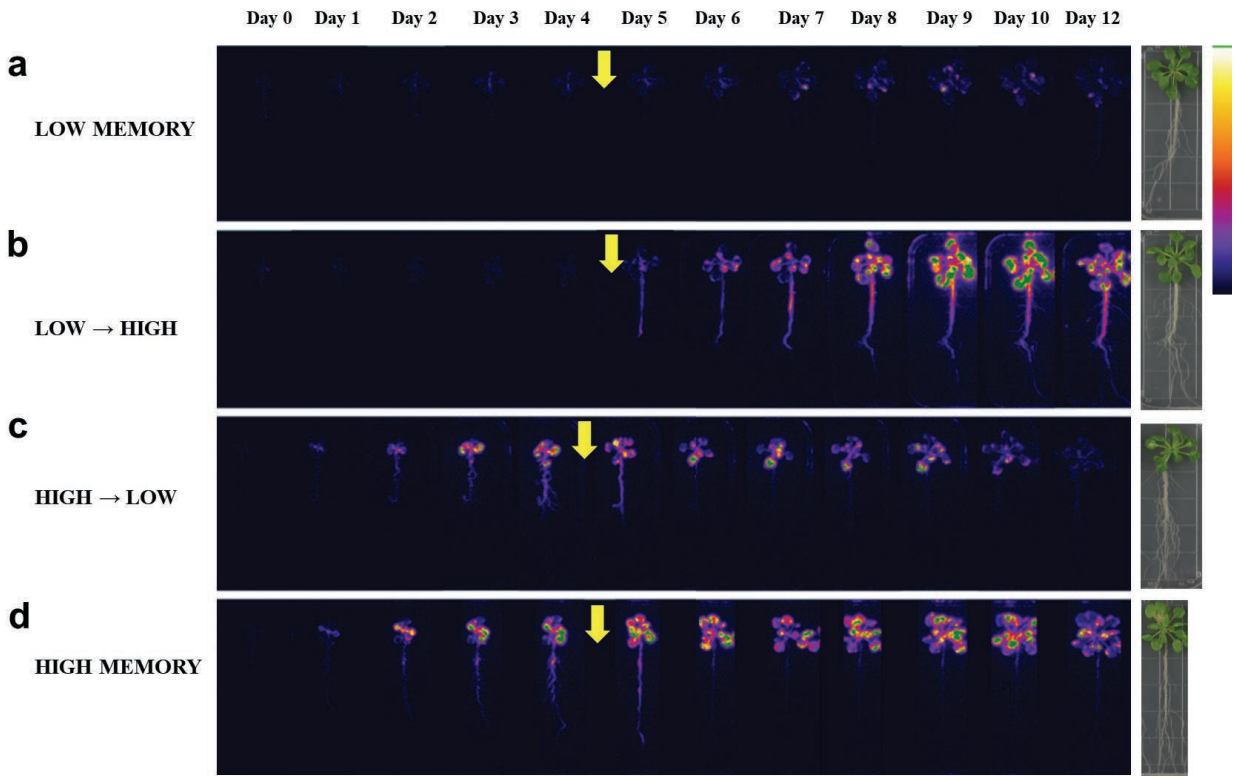

Figure 3.4. Toggle 2.1 function in plants as visualized with false colored luciferase activity. Transgenic plants containing the Toggle 2.1 circuit were incubated under different inducing conditions and imaged for luciferase (readout) activity over 12 days. **a,** *Low Memory*. 3. **b,** *Low → High*. **c,** *High → Low*. **d,** *High Memory*. The states of the plants (**a-d**) are described in Fig. 3. Intensity of luciferase activity is false colored according to the fire scale shown on the right. Arrows indicate when plants were moved to different inducer conditions, as described above. Panels to the right show images of corresponding plants at Day 12.

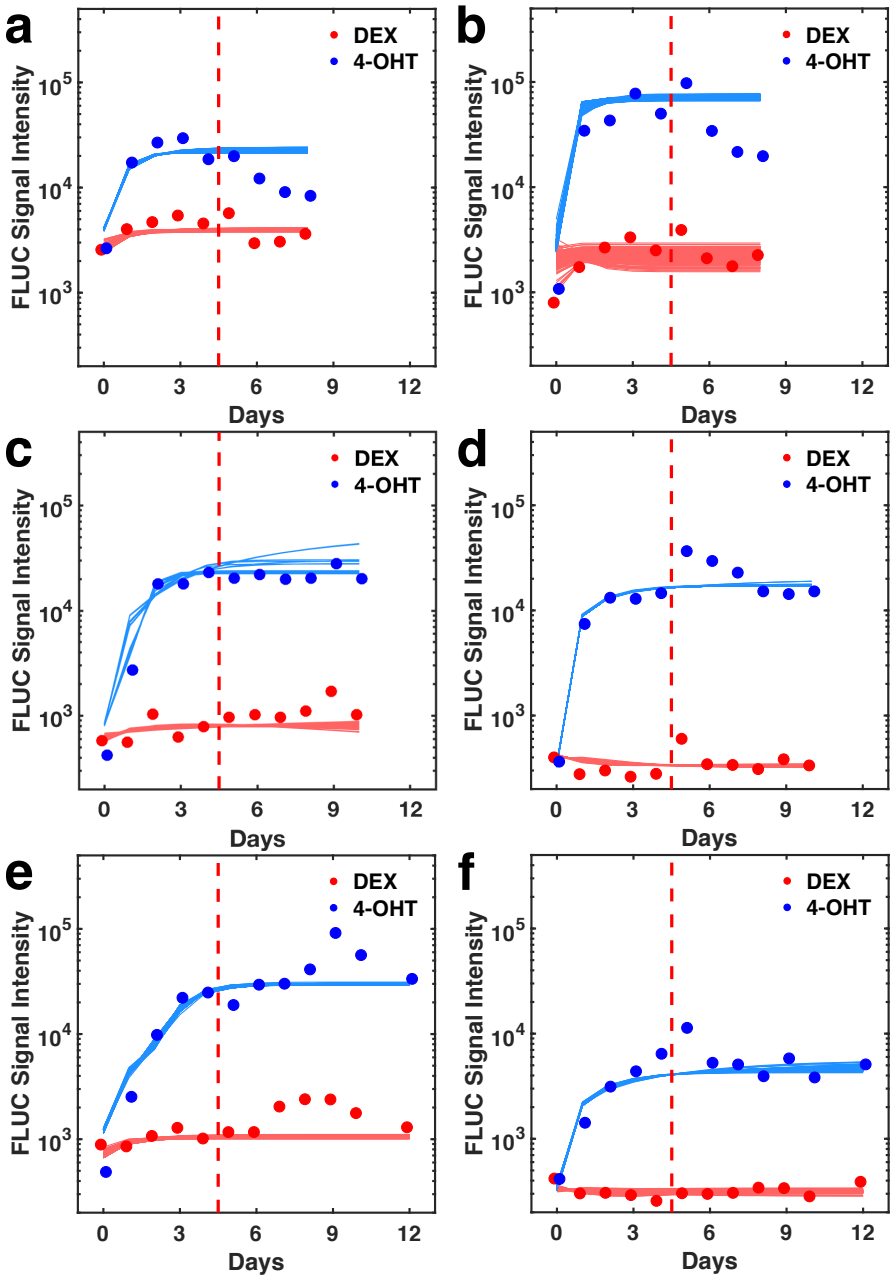

Figure 3.5. Steady state luciferase expression after continuous induction with 4-OHT or DEX.

Shoots (**a**) and roots (**b**) of Toggle 1.0 steady state luciferase expression (*FLUC Signal Intensity*) over eight days of continuous induction. Shoots (**c**) and roots (**d**) of Toggle 2.0 steady state luciferase expression over ten days of continuous induction. Shoots (**e**) and roots (**f**) of Toggle 2.1 steady state luciferase expression over twelve days of continuous induction. Dots represent the experimental data and solid lines of the same color represent the model fitted to the experimental data. Each solid line represents a successful parameter set, as defined in Appendix II: Section 8.1.4. 4-OHT switches the toggle on, to the high state, whereas DEX switches the toggle off, to the low state.

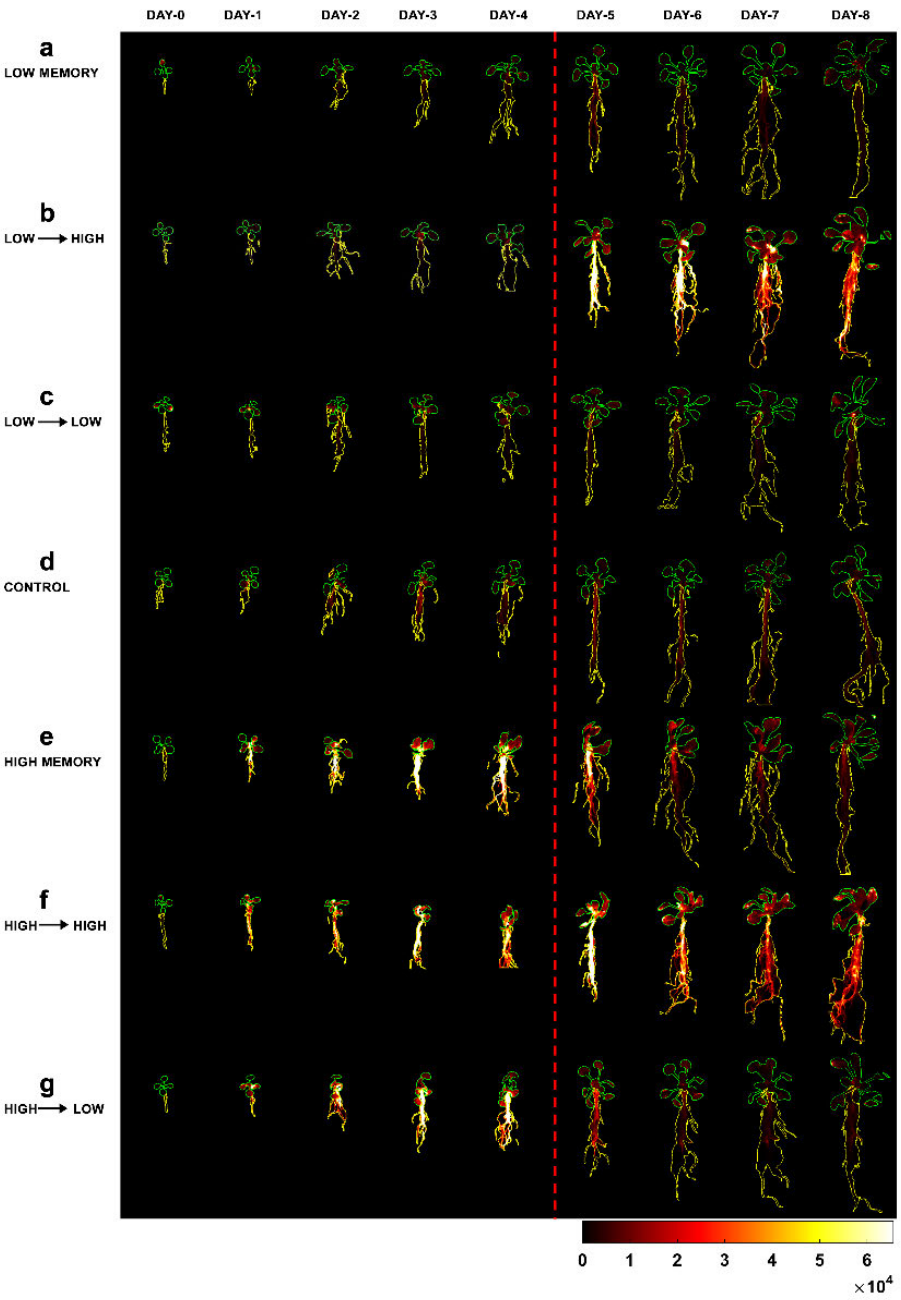

Figure 3.6. Luminescence heat maps (linear scale) of selected plants containing Toggle 1.0 under different treatment conditions.

Regions of Interest (ROI) drawn for the shoots are indicated by green lines, whereas those for the roots are indicated by yellow lines. All images use the same fire scale which false-colors luciferase intensity, with black representing zero and white representing saturation according to the scale shown at the bottom. The colors reflect luminescence intensity changes between different treatments. Inducer conditions were changed after imaging on Day 4, which is indicated by the red dashed line. **a**, ***Low Memory***, plants incubated with DEX inducer for 4 days to establish the low state, then moved to media with no inducer to test for stability (memory) of the low state. **b**, ***Low → High***, plants incubated with DEX inducer for 4 days to establish the low state, then moved to media with 4-OHT inducer to switch the circuit to the high state. **c**, ***Low →***

Low, plants incubated with DEX inducer throughout the experiment (low state). **d**, ***Control***, plants incubated without inducer throughout the experiment. **e**, ***High Memory***, plants incubated with 4-OHT inducer for 4 days to establish the high state, then moved to media with no inducer to test for stability (memory) of the high state. **f**, ***High → High***, plants incubated with 4-OHT throughout the experiment (high state). **g**, ***High → Low***, plants incubated with 4-OHT inducer for 4 days to establish the high state, then moved to media with DEX inducer to switch the circuit to the low state.

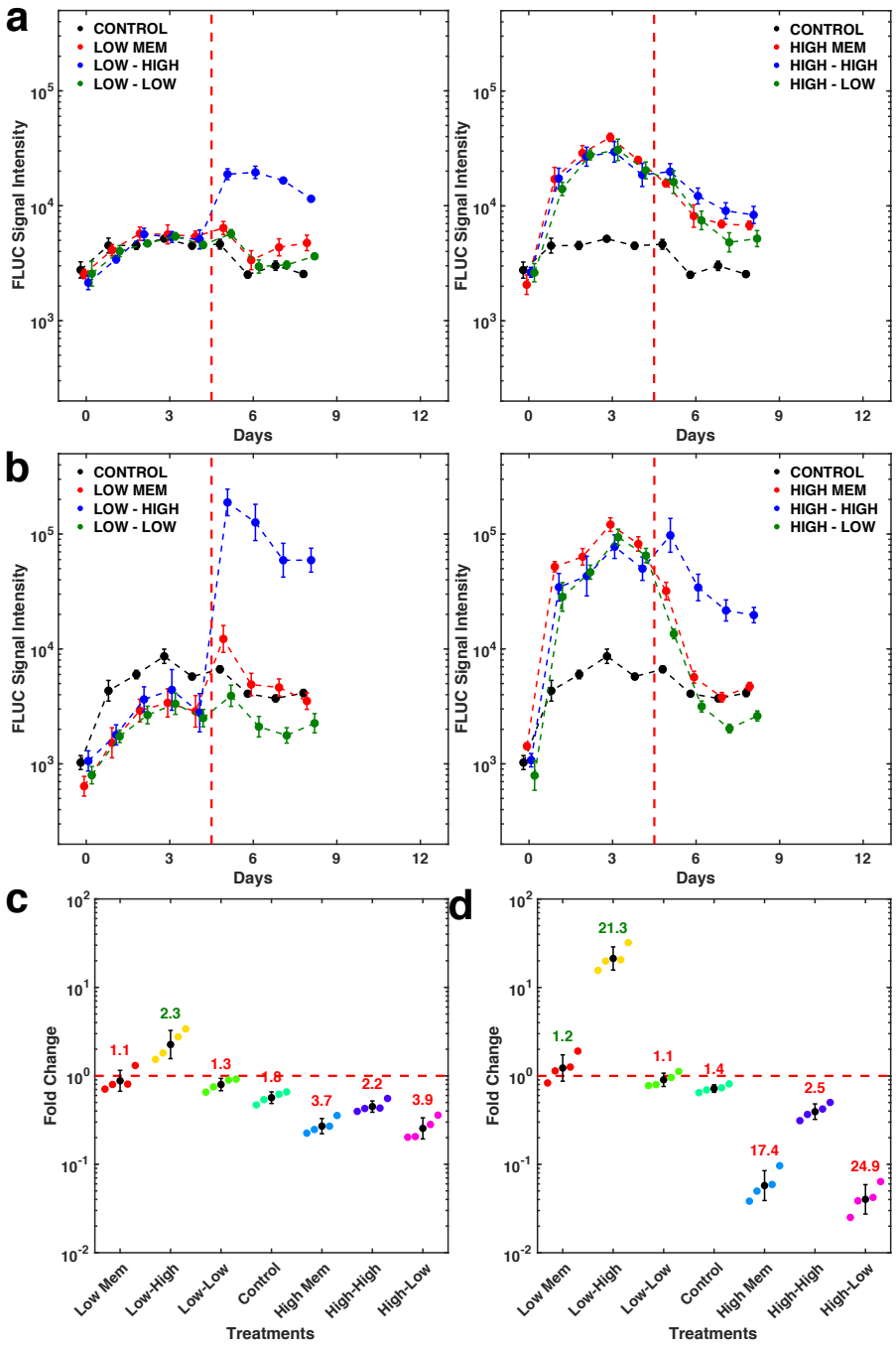

Figure 3.7. Quantitative data analysis of Toggle 1.0 performance.
a-b, Mean temporal luminescence levels of shoots (**a**) and roots (**b**) of plants under different treatments (See Section 3.2 Online Methods for sample sizes). The x-axis shows the number of days on which luminescence data was collected starting from day 0. Data points on a same day are slightly shifted for clearer display. The y-axis shows the luminescence intensity. Error bars indicate standard errors. The red dashed line indicates the time when inducer was changed. **c-d,** Average fold changes in luciferase activity of shoots (**c**) and roots (**d**) under different treatments (See Section 3.2 Online Methods for sample sizes). Closed circles of different colors indicate fold change values of individual plants in corresponding treatment groups. The black closed circles represent the mean fold change and the black bar is the standard deviation. The number above each group of data-points is the average fold change of the corresponding group. Numbers in dark green represent increases in luminescence, while numbers in red indicate a decrease. The red dashed line marks a fold change of one, *i.e.*, no change. All treatments are defined in detail in the Section 3.2 Online Methods and **Fig. 3.6** legend.

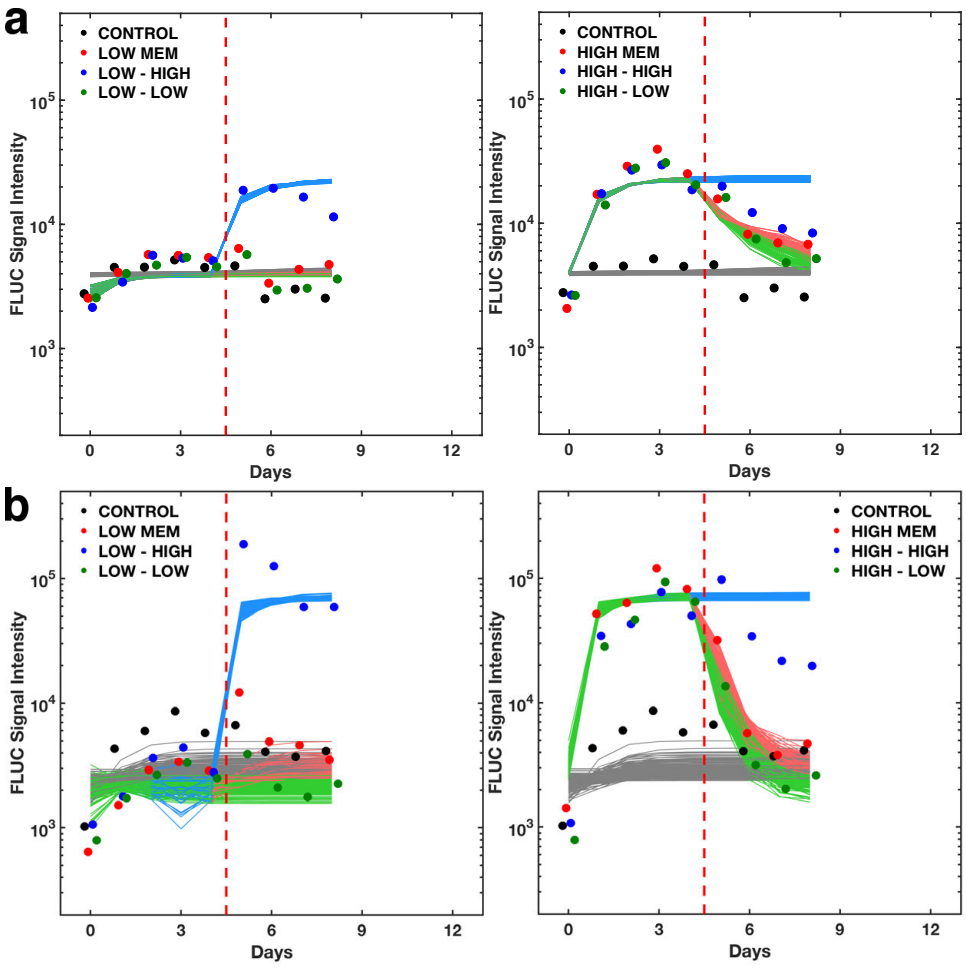

Figure 3.8. Parameter estimation results of Toggle 1.0 using MCMC method.
Closed circles of different colors indicate mean luciferase intensity levels of shoots (**a**) and roots (**b**) of plants under different treatments from the experimental results shown in **Figure 3.7a-b**.

Data points on a same day are shifted a little for clearer display. Each curve represents numerical solutions of ODE using one estimated parameter set. Different colors correspond to different treatment conditions that are described in the legend to **Figure 3.6.** Fits plotted are best parameter sets as defined in Appendix II: Section 8.1.4.

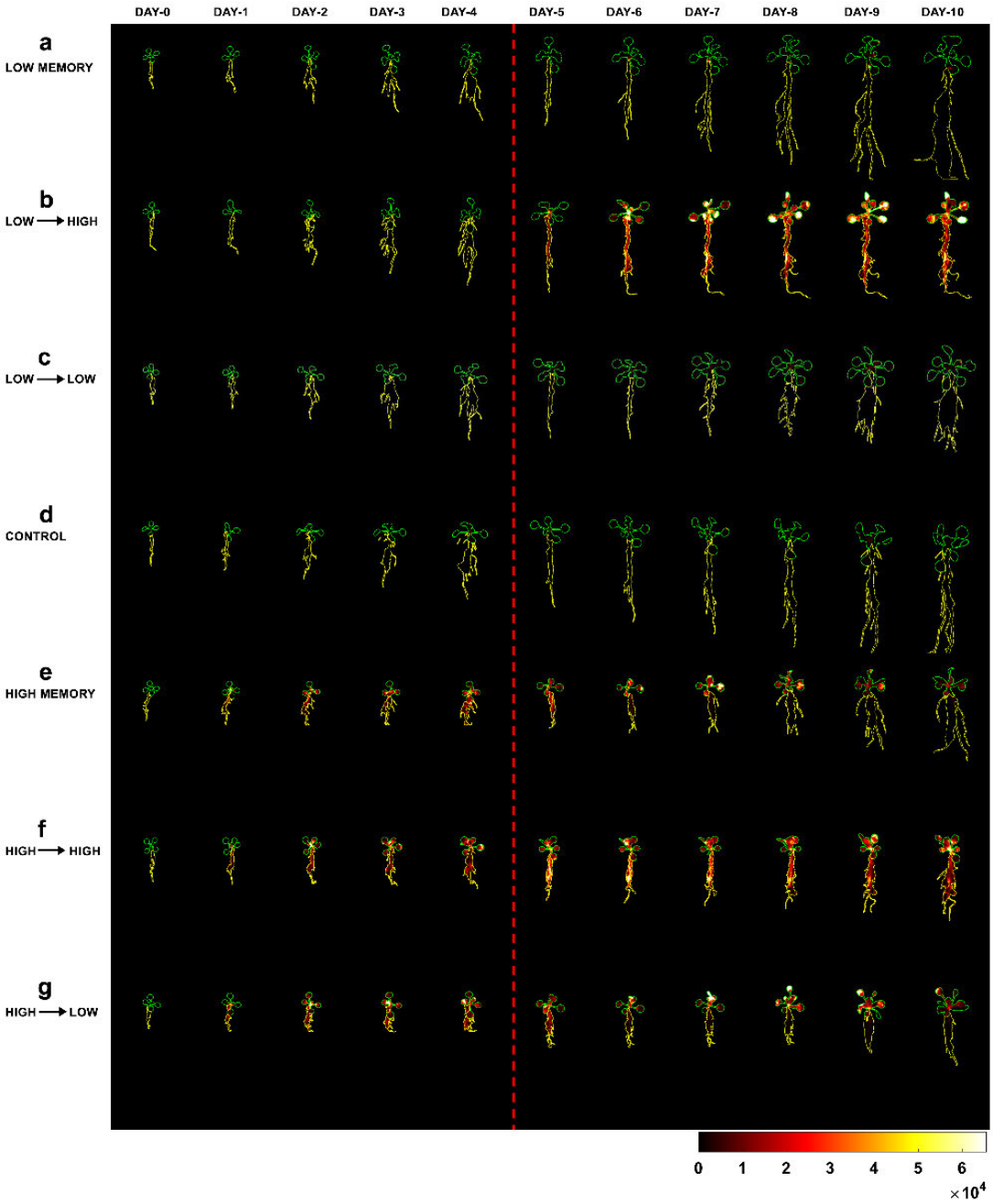

Figure 3.9. Luminescence heat maps (linear scale) of selected plants containing Toggle 2.0 under different treatment conditions.
Green lines indicate ROIs drawn for the shoots, whereas yellow lines indicate those for the roots. All images use the same fire scale to indicate false-colored luciferase intensity, with black

representing zero and white representing saturation according to the scale shown at the bottom. The colors are comparable and reflect luminescence intensity changes between different treatments. Inducer conditions were changed after imaging on Day 4, which is indicated by the red dashed line. **a**, ***Low Memory***, plants incubated with DEX inducer for 4 days to establish the low state, then moved to media with no inducer to test for stability (memory) of the low state. **b**, ***Low → High***, plants incubated with DEX inducer for 4 days to establish the low state, then moved to media with 4-OHT inducer to switch the circuit to the high state. **c**, ***Low → Low***, plants incubated with DEX inducer throughout the experiment (low state). **d**, ***Control***, plants incubated without inducer throughout the experiment. **e**, ***High Memory***, plants incubated with 4-OHT inducer for 4 days to establish the high state, then moved to media with no inducer to test for stability (memory) of the high state. **f**, ***High → High***, plants incubated with 4-OHT throughout the experiment (high state). **g**, ***High → Low***, plants incubated with 4-OHT inducer for 4 days to establish the high state, then moved to media with DEX inducer to switch the circuit to the low state.

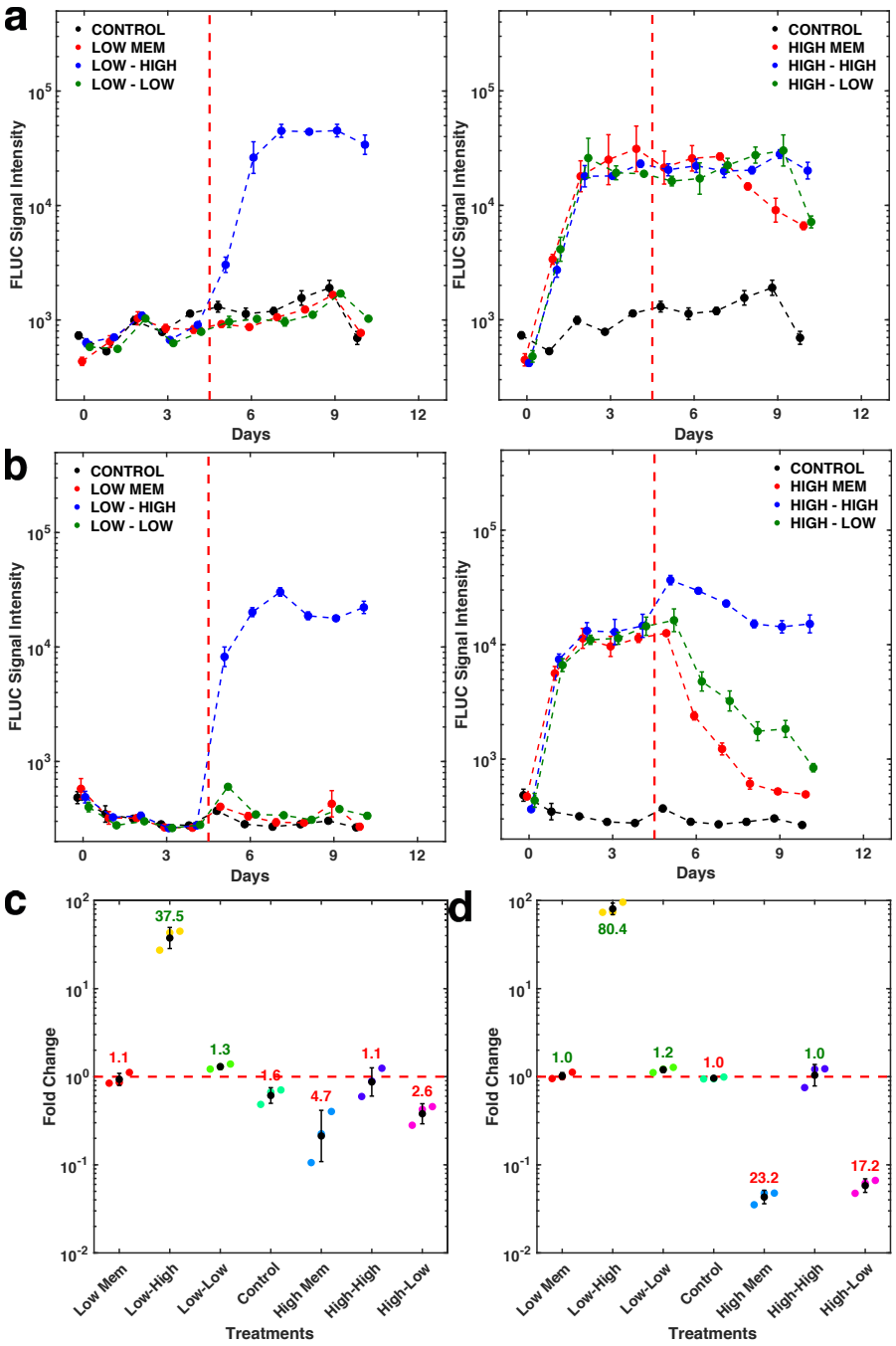

Figure 3.10. Quantitative data analysis of Toggle 2.0 performance.
a-b, Mean temporal luminescence levels of shoots (**a**) and roots (**b**) of plants under different treatments (See Section 3.2 Online Methods for sample sizes). The x-axis shows the number of days on which luminescence data was collected starting from day 0. Data points on a same day are shifted a little for clearer display. The y-axis shows the luminescence intensity. Error bars indicate standard errors. The red dashed line indicates the time when inducer was changed. **c-d,** Average fold changes of shoots (**c**) and roots (**d**) under different treatments (See Section 3.2 Online Methods for sample sizes). Closed circles of different colors indicate fold-change values of individual plants in corresponding treatment groups. The black closed circles represent the mean fold change and the black bar the standard deviation. The number above each group of

data-points is the average fold change of the corresponding group. Numbers in dark green represent increases in luminescence, while numbers in red indicate a decrease. The red dashed line marks a fold change of one, *i.e.*, no change. All treatments are defined in detail in the Section 3.2 Online Methods and **Figure 3.9** legend.

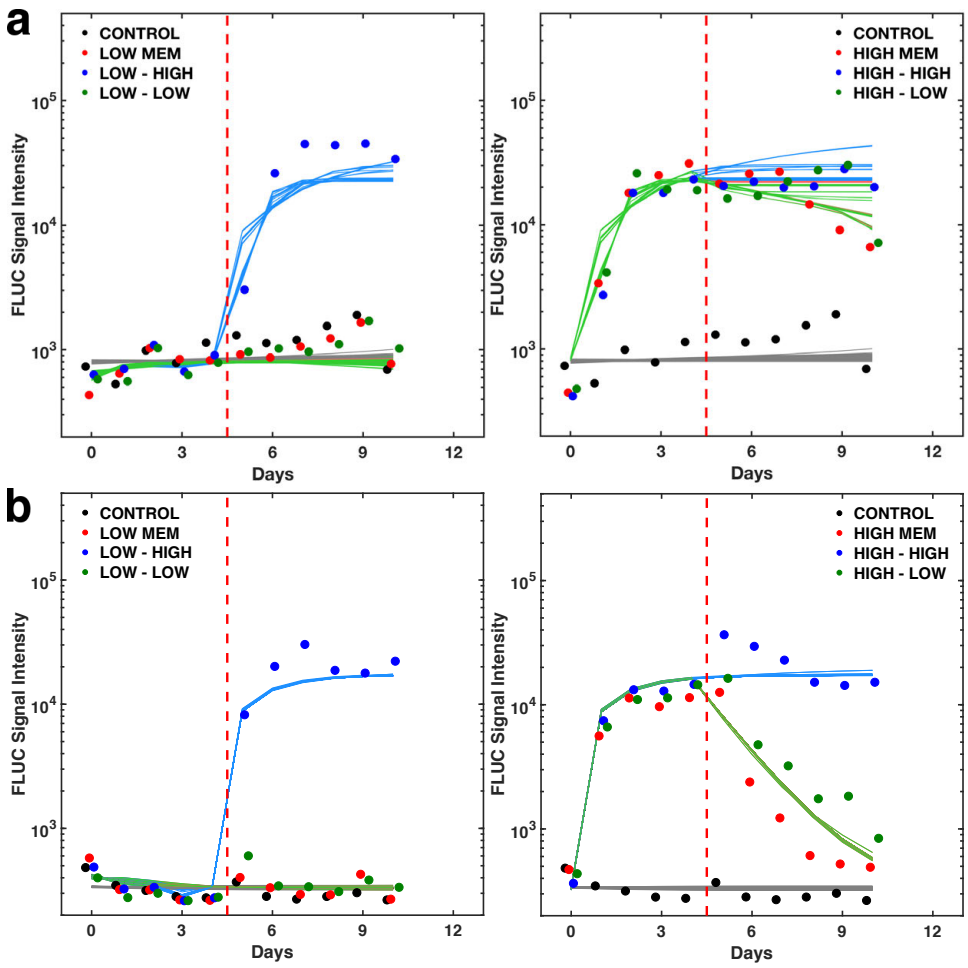

Figure 3.11. Parameter estimation results of Toggle 2.0 using MCMC method.
Closed circles of different colors indicate mean luciferase intensity levels of shoots (**a**) and roots (**b**) of plants under different treatments from the experimental results shown in **Figure 3.10a-b**. Data points on a same day are slightly shifted for clearer display. Each curve represents numerical solutions of ODE using one estimated parameter set. Different colors correspond to different treatment conditions that are described in the legend to **Figure 3.9**. Fits plotted are best parameter sets as defined in Appendix II: Section 8.1.4.

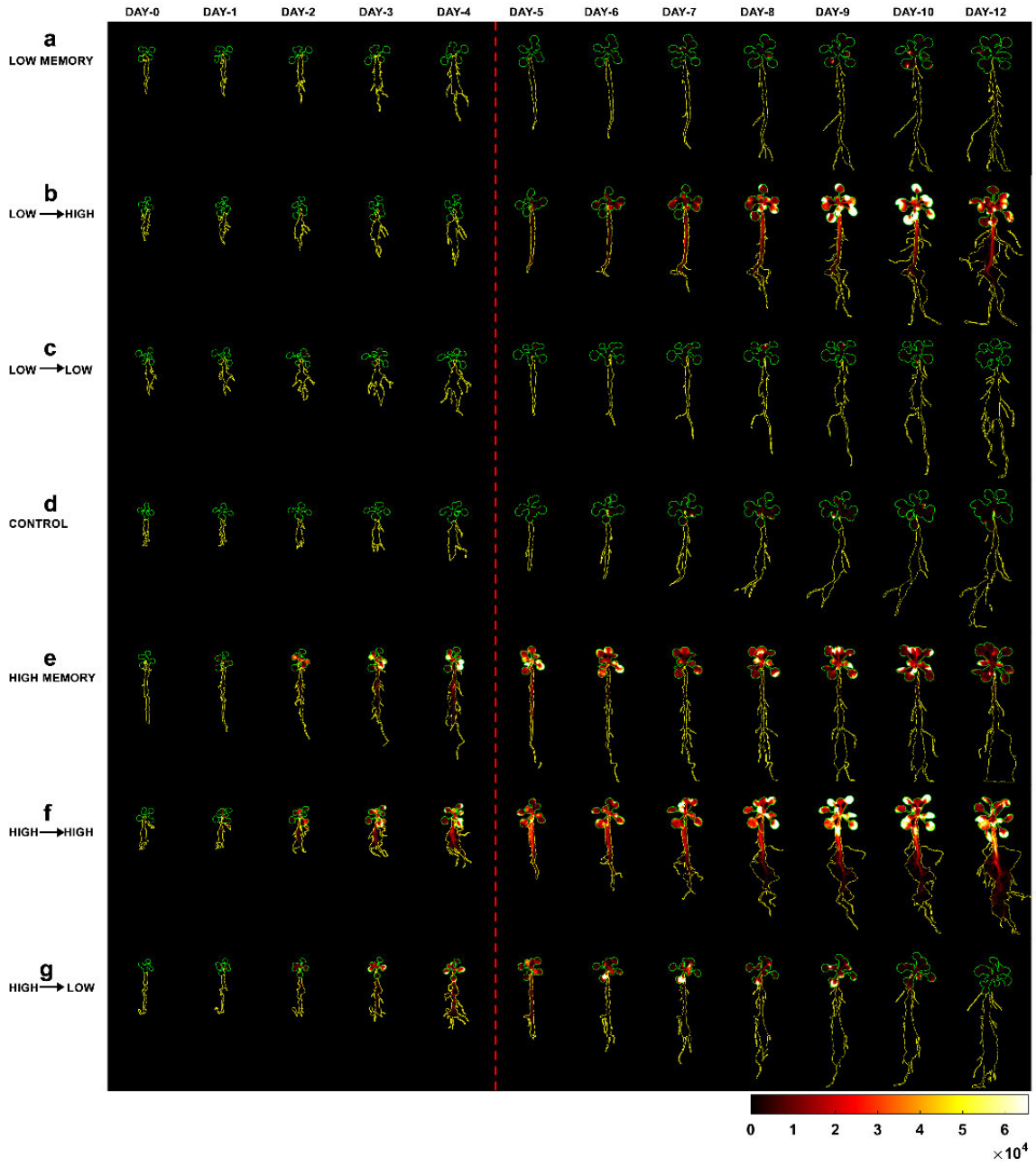

Figure 3.12. Luminescence heat maps (linear scale) of selected plants showing Toggle 2.1 behavior under different treatments.

Green lines indicate ROIs drawn for the shoots, whereas yellow lines indicate those for the roots. All images use the same fire scale to indicate false-colored luciferase intensity, with black representing zero and white representing saturation according to the scale shown at the bottom. The colors reflect luminescence intensity changes between different treatments. Inducer conditions were changed after imaging on Day 4, which is indicated by the red dashed line. **a**, ***Low Memory***, plants incubated with DEX inducer for 4 days to establish the low state, then moved to media with no inducer to test for stability (memory) of the low state. **b**, ***Low → High***, plants incubated with DEX inducer for 4 days to establish the low state, then moved to media

with 4-OHT inducer to switch the circuit to the high state. **c**, ***Low → Low***, plants incubated with DEX inducer throughout the experiment (low state). **d**, ***Control***, plants incubated without inducer throughout the experiment. **e**, ***High Memory***, plants incubated with 4-OHT inducer for 4 days to establish the high state, then moved to media with no inducer to test for stability (memory) of the high state. **f**, ***High → High***, plants incubated with 4-OHT throughout the experiment (high state). **g**, ***High → Low***, plants incubated with 4-OHT inducer for 4 days to establish the high state, then moved to media with DEX inducer to switch the circuit to the low state.

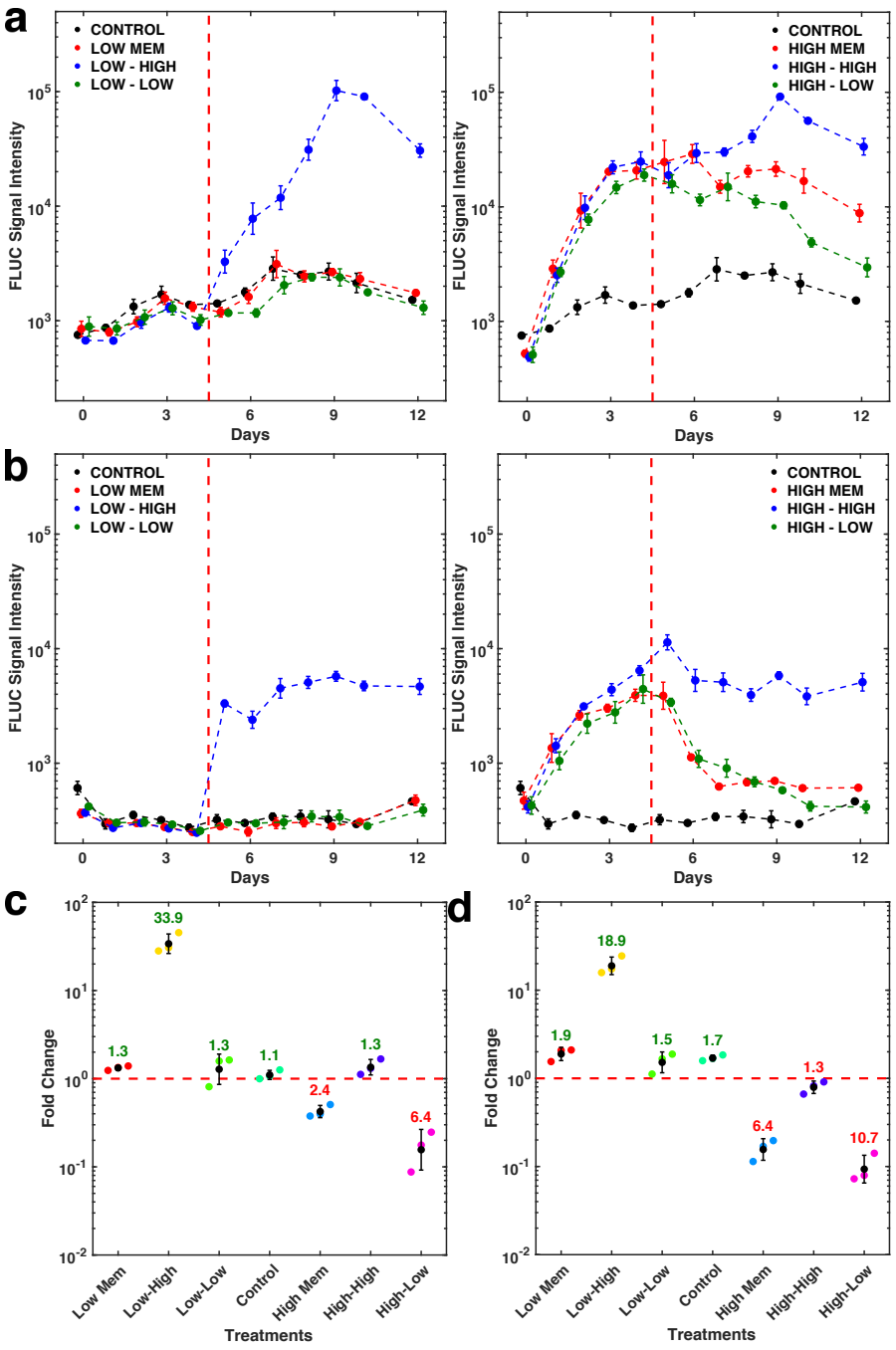

Figure 3.13. Quantitative data analysis of Toggle 2.1 performance.
a-b, Mean temporal luminescence levels of shoots (**a**) and roots (**b**) of plants under different treatments (See Section 3.2 Online Methods for sample sizes). The x-axis shows the number of days in which luminescence data was collected starting from day 0. Data points on a same day are slightly shifted for clearer display. The y-axis shows the luminescence intensity. Error bars indicate standard errors. The red dashed line indicates the time when inducer was changed or media was refreshed. **c-d,** Average fold changes of shoots (**c**) and roots (**d**) under different treatments (See Section 3.2 Online Methods for sample sizes). Closed circles of different colors indicate fold-change values of individual plants under corresponding treatments. The black closed circles indicate the mean fold-change and the black bars indicate the standard deviations. Numbers above the groups are the average fold-change of the corresponding treatment. Numbers in dark green colored number indicates an increase in luminescence level and red colored number a decrease. Red dashed line marks the baseline of one, indicating no change. All treatments were defined in details in the Section 3.2 Online Methods and **Figure 3.12** legend.

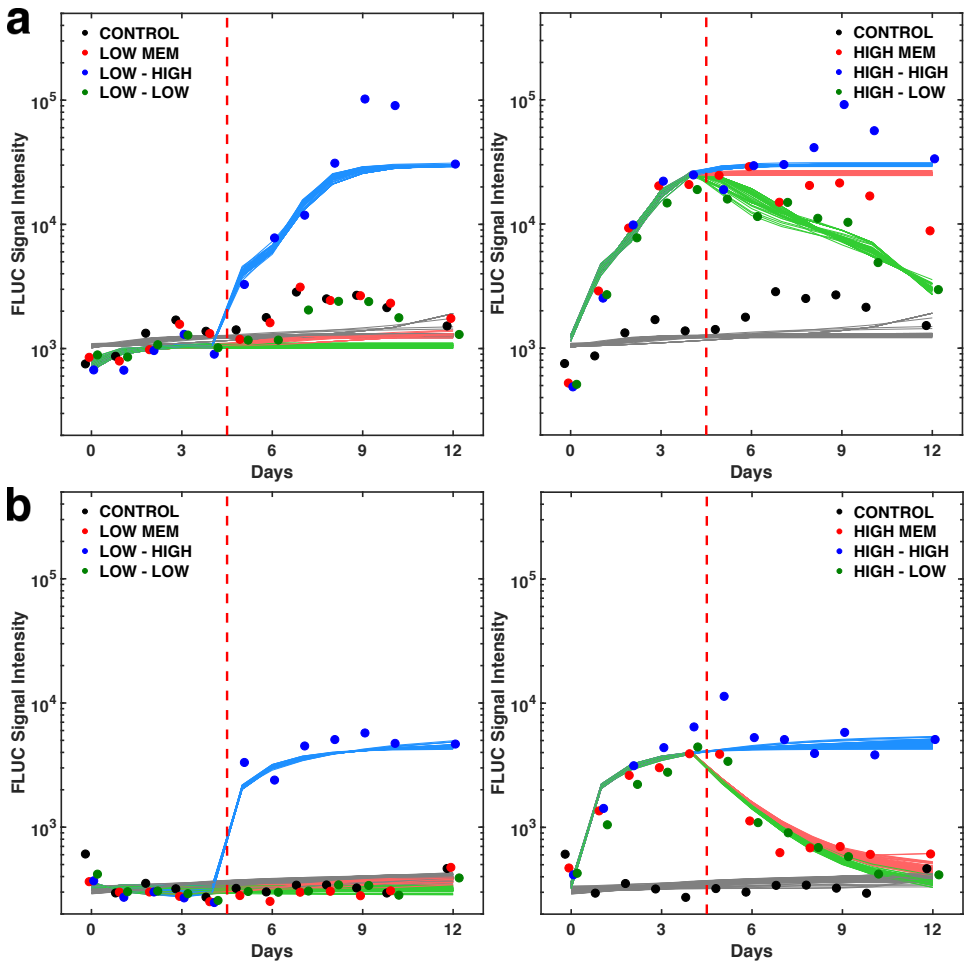

Figure 3.14. Parameter estimation results of Toggle 2.1 using MCMC method.
Parameter values estimated by MCMC method fitted to experimental data of shoots (**a**) and roots (**b**) of plants under different treatments from the experimental results shown in **Figure 3.13a-b**.

Data points on a same day are slightly shifted for clearer display. Each curve represents numerical solutions of ODE using one estimated parameter set. The High to Low (green curve in right panel in (**a**)) shows the improvement in switching dynamics of Toggle 2.1 compared to Toggle 2.0 as shown in **Figure 3.11a**. Different colors correspond to different treatment conditions that are described in the legend to **Figure 3.12**. Fits plotted are best parameter sets as defined in Appendix II: Section 8.1.4.

3.2 Methods

3.2.1 Plasmid Construction

All plasmids were constructed using standard molecular cloning techniques. Two types of plant transformation vectors were used for cloning (Appendix II: Section 8.1.1). The pCambia2300 binary vector was used to assemble the first toggle circuit, Toggle 1.0, in two separate T-DNAs. The pGREENII0229 vector was used to assemble Toggle 2.0 in one T-DNA. An additional DEX-inducible repressor to tune Toggle 2.0 was cloned in pCambia2300 and transformed into plants homozygous for Toggle 2.0 to create Toggle 2.1. The components used in individual toggle switch plasmids are described in Appendix II: Fig. S3.1. To quantify the high/low switching behavior, the plant codon optimized luciferase gene from *Photinus pyralis* (firefly) was placed downstream of one copy of the repressible synthetic promoter, NOS_{2xGal4}, in all three circuits. Nucleotide sequences of individual parts used to assemble the toggle switch circuits are provided in Appendix II: Table S3.1 and/or Schaumberg et al. [7]. The detailed design principles and quantitative characterizations of synthetic transcriptional repressor proteins and cognate repressible promoters were reported in Schaumberg et al. [7]. For the schematic representation of the toggle switch circuits, see Fig. 3.2 and Appendix II: Fig. S3.2.

3.2.2 Plant Materials and Growth Conditions

Arabidopsis thaliana ecotype Columbia (Col-0) was used for all transformations. Plasmids were introduced into *Agrobacterium tumefaciens* GV3101 cells by electroporation. For Toggle 2.0 in the pGREENII0229 vector, the pSOUP helper plasmid was co-transformed. Stable

transgenic plants were generated using the standard Agrobacterium floral dipping method [8]. Primary (T0) transgenic lines were selected on MS [18] media with 100 μg/ml Kanamycin, 34 μg/ml BASTA and 100 μg/ml cefotaxime (Toggle 1.0 and Toggle 2.1), or 34 μg/ml BASTA and 100 μg/ml cefotaxime (Toggle 2.0). Plants were screened initially for luciferase expression by spraying 500 μM d-luciferin solution (Gold Biotechnology, Inc.) containing 0.01% Tween 20 and imaging. Homozygous plants were isolated at T3 (Toggle 1.0) or T2 generations (Toggle 2.0 and 2.1). For the luciferase assay, thirteen-day old homozygous lines were transferred to MS media supplemented with 20 μM 4-OHT or 20 μM DEX for Toggle 1.0, and 5 μM 4-OHT or 50 μM DEX for Toggles 2.0 and 2.1, in 100 mm x 100 mm square plates (Fisher Brand, Cat No FB0875711A). Plants were grown vertically under short-day conditions (10 h light/14 h dark) at 22°C in a growth chamber. All experiments were conducted under seven different treatments conditions including *control*, *Low → Low*, *Low Memory*, *Low → High*, *High → High*, and *High → Low*. ***Control***, plants incubated without inducer throughout the experiment. ***Low → Low***, plants incubated with DEX inducer throughout the experiment (low state). ***Low Memory***, plants incubated with DEX inducer for 4 days to establish the low state, then moved to media with no inducer to test for stability (memory) of the low state. ***Low → High***, plants incubated with DEX inducer for 4 days to establish the low state, then moved to media with 4-OHT inducer to switch the circuit to the high state. ***High → High***, plants incubated with 4-OHT throughout the experiment (high state). ***High → Low***, plants incubated with 4-OHT inducer for 4 days to establish the high state, then moved to media with DEX inducer to switch the circuit to the low state. ***High Memory***, plants incubated with 4-OHT inducer for 4 days to establish the high state, then moved to media with no inducer to test for stability (memory) of the high state. Both 4-OHT and DEX were obtained from Sigma-Aldrich.

3.2.3 Image processing

Luciferase activity was measured using low light imaging with an XR/Mega-10 ICCD camera system (Stanford Photonics, Inc.) and available Piper software (v. 2.6.17) by spraying plants with 500 μM *d*-luciferin solution containing 0.01% Tween 20, and after a minimum of 30 minutes dark adaptation. Five data points, initial (0 hour), 24, 48, 72 and 96 hours were collected before switching inducers. Immediately before switching, plants were rinsed with MS liquid media for two hours by shaking. Four data points for Toggle 1.0 (24, 48, 72 and 96 hours), six for Toggle 2.0 (24, 48, 72, 96, 120 and 144 hours), or seven for Toggle 2.1 (24, 48, 72, 96, 120, 144, 168 and 192 hours) were collected after switching. To obtain proper plant boundaries for quantification purposes, a color high-resolution image was taken with a digital camera (Canon EOS Digital Rebel XTi) and a rough bright-field image was taken with the XR/Mega-10 ICCD camera immediately before measuring luciferase. An in-house image processing software was developed in Matlab (Mathworks). Briefly, masks of Arabidopsis shoots and roots were first generated from the color images using color thresholding. These two masks were then aligned based on the bright-field images to determine the location of plants. The registered plants masks were applied to the low light images of luciferase activities to generate quantitative measurements for shoots and roots of individual plants. More details are in Appendix II: Section 8.1.2.

3.2.4 Data analysis

Similar to that reported in our previous work [7], we found the distributions of pixel intensity of either shoots or roots were better described by log-normal distributions than by Gaussian distributions. Therefore, the mean intensity and standard deviations were calculated in logarithmic scale of base 2 for shoots and roots of an individual plant. Fold changes were

calculated by dividing the mean luciferase intensity on the last day in the experiment by the mean intensity on the day immediately before changing an inducer. We used a two-sample Student's t-test to test whether the logarithmic transformed fold changes of plants under two different treatments are statistically different. P-values smaller than 0.05 were deemed as statistically significant. More details are in Appendix II: Section 8.1.3.

3.2.5 Modeling

In order to quantitatively test whether the observed changes in plant luminescence represented a bistable or a monostable switch, we devised a novel method to fit a simple ODE representation of the toggle switch to the plant data. The ODE representation (details in Appendix II: Section 8.1.4) consists of two Hill functions describing the input-output characteristics of the two repressible promoters. The behaviors of the inducible promoters under different treatments were modeled using a product of a binary term (k_{DEX} and k_{OHT}, with a value of either 0 or 1 based on the absence or presence of inducer, respectively) and a constitutive expression term (α_{DEX} and α_{OHT}, promoter strengths of the inducible promoters) in the ODEs. The values of binary terms were changed to either zero or one based on the inductions applied at that time point.

3.2.6 MCMC parameter fitting

To fit the data to this model, we constructed a log likelihood function as the negative logarithm of the squared distance between the experimental data and numerical values from simulations of the ODE model. The log likelihood function is evaluated as a weighted average of experimental results from the seven different treatments. To estimate the maximum likelihood parameters of the toggle switch tested in plants, we used Markov Chain Monte Carlo (MCMC), specifically the Metropolis MCMC algorithm, where a proposed parameter value is accepted if it

increases the log likelihood (details in Appendix II: Section 8.1.4). The MCMC run was terminated if either the maximum number of runs (10,000) was reached, or convergence was achieved (defined as no significant change in log likelihood for more than 500 steps), or the log likelihood reached a pre-set threshold for a good fit. The latter two instances were treated as success of obtaining parameter values that matched the data. We also added an additional quality control step of eliminating fits with Hill coefficients greater than 6 on the grounds that such high Hill coefficients are not expected to be seen in these genetic circuits. The procedure was repeated 500 times for each of the three toggle switches and the successes recorded. The parameters in each success were then evaluated for bistability.

3.2.7 TAIL-PCR

Shoot and root genomic DNA was extracted from homozygous transgenic lines using the DNeasy plant mini kit (Qiagen) based on the manufacturer's protocol. To identify the T-DNA insertion location in the Arabidopsis genome and the copy number of the transgene, thermal asymmetric interlaced polymerase chain reaction (TAIL-PCR) was employed [19]. Three insertion-specific (nested) primers were designed to anneal to the left T-DNA border of the transgene and used in combination with arbitrary degenerate primers (AD primers) found in the literature (Appendix II: Tables S3.2-S3.3). Three subsequent TAIL-PCR reactions were performed and only the second and third round PCR products were analyzed on 1% agarose gels (Appendix II: Fig. S3.4a). To recover unknown genomic sequences flanking the insertion, gel purified third-round TAIL-PCR products were either directly sequenced or cloned in pJET2.1 vector and sequenced using pJET-specific forward and reverse primers. Flanking sequences were identified by a BLAST search of the *Arabidopsis thaliana* Genome (TAIR10) to find the exact

location of the transgene (Appendix II: Fig. S3.4b). The transgene insertion was further confirmed by PCR amplification using insertion flanking primers.

REFERENCES

1. Ajo-franklin CM, Drubin D a, Eskin J a, Gee EPS, Landgraf D, Phillips I, et al. Rational design of memory in eukaryotic cells service Rational design of memory in eukaryotic cells. *Genes Dev.* 2007;21: 2271–2276. doi:10.1101/gad.1586107

2. Deans TL, Cantor CR, Collins JJ. A Tunable Genetic Switch Based on RNAi and Repressor Proteins for Regulating Gene Expression in Mammalian Cells. *Cell.* 2007;130: 363–372. doi:10.1016/j.cell.2007.05.045

3. Lebar T, Bezeljak U, Golob A, Jerala M, Kadunc L, Pirš B, et al. A bistable genetic switch based on designable DNA-binding domains. *Nat Commun.* 2014;5: 1–13. doi:10.1038/ncomms6007

4. Gander MW, Vrana JD, Voje WE, Carothers JM, Klavins E. Digital logic circuits in yeast with CRISPR-dCas9 NOR gates. *Nat Commun.* 2017;8: 1–11. doi:10.1038/ncomms15459

5. Weinberg BH, Pham NTH, Caraballo LD, Lozanoski T, Engel A, Bhatia S, et al. Large-scale design of robust genetic circuits with multiple inputs and outputs for mammalian cells. *Nat Biotechnol.* 2017;35: 453–462. doi:10.1038/nbt.3805

6. Gardner TS, Cantor CR, Collins JJ. Construction of a genetic toggle switch in Escherichia coli. *Nature.* 2000;403: 339–42. doi:10.1038/35002131

7. Schaumberg KA, Antunes MS, Kassaw TK, Xu W, Zalewski CS, Medford JI, et al. Quantitative characterization of genetic parts and circuits for plant synthetic biology. *Nat Meth.* 2016;13: 94–100. doi: 10.1038/nmeth.3659

8. Clough SJ, Bent AF. Floral dip: A simplified method for Agrobacterium-mediated transformation of *Arabidopsis thaliana*. *Plant J.* 1998;16: 735–743. doi:10.1046/j.1365-313X.1998.00343.x

9. Press, W. H., Teukolsky, S. A., Vetterling, W. T. & Flannery BP. *Numerical Recipes: The Art of Scientific Computing.* 3rd editio. Cambridge University Press; 2007.

10. Benfey PN. *Encyclopedia of Genetics.* Brenner S, Miller JH, editors. Academic Press; 2001.

11. Goldberg RB, de Paiva G, Yadegari R. Plant Embryogenesis: Zygote to Seed. *Science*. 1994;266: 605–614. doi:10.1126/science.266.5185.605

12. Goldberg R. Plants: novel developmental processes. *Science*. 1988;240: 1460–1467. doi:10.1126/science.3287622

13. Laux T. Genetic Regulation of Embryonic Pattern Formation. *Plant Cell.* 2004;16: S190–S202. doi:10.1105/tpc.016014

14. Matzke AJM, Matzke MA. Position effects and epigenetic silencing of plant transgenes. *Curr Opin Plant Biol.* 1998;1: 142–148. doi:10.1016/S1369-5266(98)80016-2

15. Gelvin SB. Integration of *Agrobacterium* T-DNA into the Plant Genome. *Annu Rev Genet.* 2017;51: 195-217 doi:10.1146/annurev-genet-120215-035320

16. She W, Grimanelli D, Rutowicz K, Whitehead MWJ, Puzio M, Kotliński M, et al. Chromatin reprogramming during the somatic-to-reproductive cell fate transition in plants. *Development*. 2013;140: 4008–4019. doi:10.1242/dev.095034

17. Nielsen AAK, Der BS, Shin J, Vaidyanathan P, Paralanov V, Strychalski EA, et al. Genetic circuit design automation. *Science*. 2016;352: aac7341. doi:10.1126/science.aac7341

18. Murashige T, Skoog F. A revised medium for rapid growth and bioassays with tobacco tissue cultures. *Physiol Plant.* 1962;15: 473–497.

19. Singer T, Burke E. *Plant Functional Genomics.* In: Grotewold E, editor. *Methods in Molecular Biology*. Humana Press; 2003. pp. 241–271.

CHAPTER 4: FORCE SPECTRUM MICROSCOPY USING MITOCHONDRIAL FLUCTUATIONS OF CONTROL AND ATP DEPLETED CELLS[3]

4.1 Introduction

The mechanical properties of the cytoskeleton of mammalian cells influence how the cells move, deform, adhere and sense their mechanical environments [1], which are altered in many processes of great significance like tumorigenesis [2–4] and differentiation[5,6]. Therefore, a better understanding of these mechanical properties may not only lead to deeper insights into fundamental cell biology of these processes, but also novel medical applications. Passive particle microrheology, which is based on analysis of the thermal motion of a tracer particle, is one such technique that can probe the mechanical properties of soft materials with relatively little perturbation of the material itself. However, the cellular cytoskeleton is an active mechanical system, being able to convert chemical energy, mainly in the form of adenosine triphosphate (ATP), into mechanical work and motion. At any given instant, in a living cell, there are thousands of processes, involving polymerization and depolymerization, transport, enzymatic reactions and global movements of cell migration or cytoskeletal reorganization, that agitate and liquidize the cytoskeleton and the cytoplasm [7–9]. Thus the spontaneous fluctuations of a particle embedded in the cytoskeleton are determined by the sum of thermal and active forces acting on the material properties of the cytoplasm. A more complete understanding of the

[3] The work presented in this chapter and in Appendix III has been published in Biophysical Journal. Xu W, Alizadeh E, Prasad A. Force spectrum microscopy using mitochondrial fluctuations of control and ATP depleted cells. *Biophy. J.* 2018; 114: 2933–2944. W.X. and A.P. designed the research. W.X. performed the research. W.X. contributed analytic tools. W.X., E.A., and A.P. analyzed the data. W.X. and A.P. wrote the manuscript. I am the co-first author on the publication. This work is being presented in this chapter in its entirety to maintain the intellectual coherence of the project.

mechanical properties of the cytoskeleton thus requires measurements of not only its viscoelastic material properties but also the spectrum of active forces (active mechanical properties)[10] that liquidize the cytoplasm. At thermal equilibrium, the viscoelastic properties can be related to the thermally driven fluctuations through the fluctuation dissipation theorem (FDT). However, it is complicated to disentangle the particle fluctuations driven by thermal agitation from the ones driven by active forces in live cells [11–13]. To tackle this issue, the viscoelastic properties can be first determined by applying a known force and measuring the resulting displacement, then the spectrum of active forces can be extracted from the spontaneous fluctuations [3,13–15]. A representative technique following this strategy is force spectrum microscopy (FSM)[3]. FSM consists of two independent measurements: the viscoelastic properties are measured using active microrheology while spontaneous fluctuations are measured by confocal microscopy. The active force spectrum is calculated using a generalized Hooke's law to combine the two measurements. Though a powerful technique, FSM as it was originally developed, requires access to advanced instruments such as optical tweezers, microinjectors and confocal microscopes at the same time, which significantly limits its wider application. In addition, microinjecting fluorescent particles into single cells is not only tedious but introduces non-physiological disturbance to cells under study. A version of FSM that requires fewer instruments and is non-invasive would be of significant value.

A proposed alternative approach to separate the effects of thermal forces and active forces on the spontaneous fluctuations of intracellular particles is to inhibit general motor, polymerization and other activities by depleting cellular ATP [3,16,17]. If the inhibition level is sufficient, the remaining fluctuations are primarily driven by thermal forces and the viscoelasticity of cytoskeleton can be determined from the mean square displacement (MSD)

using the generalized Stokes-Einstein relationship (GSER)[16]. The results were shown to be similar to measurements made by active microrheology [16,17]. Therefore, applying ATP depletion may remove the requirement for active microrheology measurements. However, this method is controversial. The major criticism is that the treatment with ATP depleting chemicals cannot remove all ATP-dependent processes without significant cellular damage [18]. To deal with this, the convergence of the MSDs of control and ATP depleted cells over short timescales was used to test if the cell damage induced by ATP depletion is significant [3,15,16]. However residual ATP levels and other intracellular energy sources, like guanosine triphosphates (GTPs), may still drive active fluctuations over long timescales, and lead to inaccuracy in the viscoelastic properties measured. Indeed, residual ATP levels of 1-8% of normal were reported after ATP depletion [16], and the viscoelastic modulus and the scaling of the MSD with time were qualitatively different between short and long timescales [16], leading to possibly systematic errors in the determination of the viscoelastic modulus.

Subcellular organelles such as mitochondria have been proposed as an alternative to exogenous fluorescent particles, with the caveat that interpreting measurements may face additional challenges due to hard-to-characterize interactions with other subcellular structures [19]. Mitochondria have been used as probe particles in several studies to measure intracellular mechanical properties of several cell types [3,20]. Mitochondria have the additional benefit that they are abundant in most cell types and can be often found spatially distributed across cells, which enable the probing of intracellular mechanical properties with spatial resolutions [20]. But using mitochondria also poses additional challenges compared to fluorescent particles. Mitochondria are highly dynamic organelles that move, fuse and divide [21,22]. Different activities of fusion and fission (division) result in different mitochondrial morphologies, which

can be roughly classified into three types: short, fragmented (punctate) ones, elongated, highly branched (filamentous) ones and intermediate ones [21–23]. As probe particles, punctate mitochondria are preferable among these three types since they are close to the shape of synthetic fluorescent particles. Even so, due to intrinsic heterogeneity, the morphologies (shapes and sizes) of punctate mitochondria are more variable than commercially available fluorescent particles. In previous studies that use mitochondria as intracellular probe particles, the complexity of their morphology was not addressed explicitly. It is unclear if mitochondrial morphologies are heterogeneous within these studies, if this heterogeneity plays any role in determining the mitochondrial fluctuations, and if this heterogeneity has been considered in the quantification. To make mitochondria function reliably as endogenous probe particles, we need to screen for punctate mitochondria of suitable morphologies, and address their morphological heterogeneity.

In this paper, we develop methods to carry out FSM using fluorescently labeled mitochondria as our probe particles, in which we tackle both issues summarized above. We first use morphological analysis to characterize those mitochondria that can be ideally used as an endogenous probe for intracellular mechanical properties. Using confocal imaging of ideal mitochondria, we calculate their MSD as a function of lag time, as well as the creep compliance and the distribution of directional change. We study the effect of various cytoskeletal drugs on the active mitochondrial motion to gain insights into its driving mechanisms. We analyze the distribution of directional change after ATP depletion and identify a thermally dominated time-scale that we then use for viscoelasticity measurements. We calculate the force spectrum of active fluctuations by combining the spontaneous fluctuations tracked in control cells and viscoelastic properties measured in ATP depleted cells. Our results are quantitatively very

similar to those obtained by others using active microrheology. Visualizing mitochondrial motion therefore may be a non-invasive method, with relatively low requirements for advanced instruments beyond a confocal microscope, for characterizing intracellular mechanical properties.

4.2 Materials and methods

4.2.1 Cell culture

C3H-10T1/2 cells, a murine embryonic mesenchymal cell line, were obtained from the American Type Culture Collection (ATCC, Manassas, VA) and were used at their passages of 5-15. Cells were cultured in Dulbecco's Modified Eagle Medium (DMEM) (Sigma-Aldrich, St Louis, MO) supplemented with 10% fetal bovine serum (FBS, Atlas Biologicals, Fort Collins, CO), 100 Units/ml penicillin and 100 μg/ml streptomycin (Fisher Scientific-Hyclone, Logan, UT) at 37 °C with 5% CO_2. Cells were seeded at 5×10^4 cells/ml the night before experiments in uncoated glass-bottom 35 mm petri dishes (MatTeK, Ashland, MA). Mitochondria were fluorescently labelled with 200 nM MitoTracker Green FM (Molecular Probes, Eugene, OR) or 500 nM MitoTracker Red FM (Molecular Probes, Eugene, OR) in DMEM for 30 min.

4.2.2 Chemical treatments

All chemical treatments (Appendix III: Table S4.1) were carried out right after the MitoTracker staining and incubated for 30 min for cytoskeleton-targeting chemicals or 2 hr for ATP depletion at 37 °C with 5% CO_2. Imaging was completed in 2-3 hours after the treatments. The chemicals were maintained during imaging to prevent recovery. Jasplakinolide and cytochalasin D were purchased from Calbiochem (San Diego, CA), blebbistatin was from Cayman Chemical (Ann Arbor, MI), taxol was from Goldbio (St Louis, MO), nocodazole, NaN_3 and deoxy-glucose were from Sigma-Aldrich (St Louis, MO).

4.2.3 Imaging using confocal microscopy

We optimized a protocol consisting of imaging, image processing, mitochondrial tracking and data analysis (Appendix III: Fig. S4.1 A). Cells were imaged in a 37 °C environmental chamber in CO_2-independent imaging medium which consists of Leibovitz's L-15 media (Gibco, Carlsbad, CA) supplemented with 10% FBS, 7 mM HEPES (Sigma-Aldrich, St Louis, MO) and 4.5 g/l D-glucose (pH 7.0). Random isolated cells were imaged using inverted spinning disk confocal microscope (Nikon Instruments, Inc., Melville, NY) under a 60× oil-immersion objective. SlideBook 6 (Intelligent Imaging Innovations, Inc., Denver, CO) was used to control the hardware. Recording was taken at 10 frames per second (fps) for 100 s using a cascade II EMCCD camera, with a spatial resolution of 167 nm per pixel. The emission filter of 488 nm was used for MitoTracker Green FM and the 580 nm filter for MitoTracker Red FM when blebbistatin was used.

4.2.4 Image processing and Tracking mitochondrial fluctuations

Image processing was carried out by in-house codes programmed in Matlab (Mathworks Inc., Natick, MA), which are available upon request. The time-lapse images of mitochondria were processed using an image processing protocol (details in Appendix III: Supplemental Note 4.1) optimized based on an approach previously described [24,25], including: 1) Histogram matching (Appendix III: Figs. S4.1 B. c-d); 2) Two-dimensional (2D) deconvolution (Appendix III: Figs. S4.1 B. e-f); 3) Bandpass filtering (Appendix III: Figs. S4.1 B. g-h); 4) Grayscale thresholding (Appendix III: Figs. S4.1 B. i-j); 5) Mitochondria spanning the entire imaging period and with no interaction with other mitochondria were selected (Appendix III: Figs. S4.1 B. k-l). The 2D centroid weighted by intensities of each selected mitochondrion was recorded to generate the 2D tracks for further analysis.

4.2.5 Data analysis

From the 2D tracks, the ensemble-averaged, time-averaged MSD was calculated as:

$$\langle \Delta r^2(\tau) \rangle = \langle \big(X(t+\tau) - X(t)\big)^2 + \big(Y(t+\tau) - Y(t)\big)^2 \rangle \quad [1]$$

where τ is lag time and brackets indicate the average over all possible lag times.

At thermal equilibrium, the creep compliance of a material is directly proportional to MSD and characterizes its deformability [19,26]. The creep compliance can be calculated as:

$$\Gamma(t) = \frac{3\pi a}{2k_B T} \langle \Delta r^2(t) \rangle \quad [2]$$

where a is the particle radius, k_B the Boltzmann constant, and T the absolute temperature.

For systems at thermodynamic equilibrium, the frequency-dependent viscoelasticity can be determined based on the GSER [27], which is briefly recapitulated in Appendix III: Supplemental Note 4.2.

To incorporate the irregularities of mitochondrial morphologies, the hydrodynamic radius of a prolate (football-shape) ellipsoid is used in place of a to calculate creep compliance and viscoelasticity:

$$a_h = \frac{\sqrt{m^2 - n^2}}{\ln\left(\frac{m + \sqrt{m^2 - n^2}}{m}\right)} \quad [3]$$

Where a_h indicates the hydrodynamic radius, m and n the major and minor axes of the ellipsoid respectively. Basic morphological measurements were carried out to selected mitochondria in their first frame, where their areas, major and minor axes of minimal enclosing ellipses and convex hull areas were measured. The aspect ratio is defined as the ratio of major axis to minor axis and the solidity as the ratio of convex hull area to mitochondrial area. Both parameters are larger than one.

Directional change was calculated from each set of three points along the trajectory determined by the lag time as defined previously [28]. Then an ensemble-averaged, time-averaged distribution of directional change was obtained as a function of lag times [28]. We have chosen to display the distribution in a [-π, π] window, so that we can emphasize directionally persistent motions. To summarize the rich information contained in the distributions of directional change, an index of directional persistence, P_d, was calculated as the difference between the probabilities of forward and backward motions [18]. If the motion is purely diffusive, the P_d is close to zero at all time scales. Negative P_d values indicate that the anti-persistent motion is dominating. Positive P_d values show that persistent motion is dominating.

4.2.6 Force spectrum

The calculation of force spectrum proposed in [3] is based on the fundamental force-displacement relationship in elastic medium, the Hooke's law, $f = Kx$, where f is the driving force, K the spring constant and x the resulting displacement [3]. To account for the frequency-dependence of the material properties and the stochasticity of the intracellular forces, the Hooke's law is generalized into quadratic form of the averaged quantities in the frequency domain $\langle f^2(\omega)\rangle = |K(\omega)|^2\langle x^2(\omega)\rangle$. The frequency dependent effective spring constant ($K(\omega)$) can be related to the complex shear modulus $G^*(\omega)$ through a generalization of the Stokes relation $|K(\omega)| = 3\pi d|G^*(\omega)|$, where d is the radius of particle. The $\langle x^2(\omega)\rangle$ is obtained as the Fourier Transform of the MSD $\langle \Delta x^2(\tau)\rangle$.

In the two terms to calculate the force spectrum, $\langle \Delta x^2(\tau)\rangle$ comes from spontaneous fluctuations of probe particles and $|K(\omega)|$ comes from the independent measurement of the viscoelasticity. In our system, an equivalent form was developed:

$$\langle f^2(\omega)\rangle = (3\pi)^2|G^*(\omega)|^2(a_h{}^2\langle x^2(\omega)\rangle) \quad [4]$$

$|G^*(\omega)|$ was calculated from the mitochondrial fluctuations in ATP depleted cells and the mitochondrial hydrodynamic radii associated were used rather than fluorescent particles of same sizes in the active microrheology using optical tweezers. ${a_h}^2\langle x^2(\omega)\rangle$ was calculated from spontaneous mitochondrial fluctuations in control cells and the Fourier Transform $\langle x^2(\omega)\rangle$ was multiplied by the square of the corresponding mitochondrial hydrodynamic radius in the control cells. Then, the active force spectrum $\langle f^2(\omega)\rangle$ can be determined.

4.2.7 Statistics

The distribution of MSDs of diffusive particles is not Gaussian [29,30] and our results appear log-normal distributed (Supplemental Note 3) as also observed previously [17]. In this study, the reported means and standard deviations are computed using logarithmic transformed data (Appendix III: Supplemental Note 4.3). The geometric coefficient of variance (GCV) is defined as $\sqrt{e^{s_{ln}^2}-1}$, where s_{ln}^2 is the variance of the logarithmic transformed data.

Wilcoxon rank sum test is a nonparametric alternative of Student's t test on the null hypothesis that the two samples are from continuous distributions with equal means, which does not assume the normality of the data and is generally insensitive to the actual distribution [31,32]. Matlab function ranksum() was used and differences are deemed as statistically significant for p-values less than 0.05.

To minimize the day-to-day variance, all the comparisons were made between control cells and chemical-treated cells imaged on the same day, which may give rise to slightly different results of control cells (Appendix III: Supplemental Note 4.4).

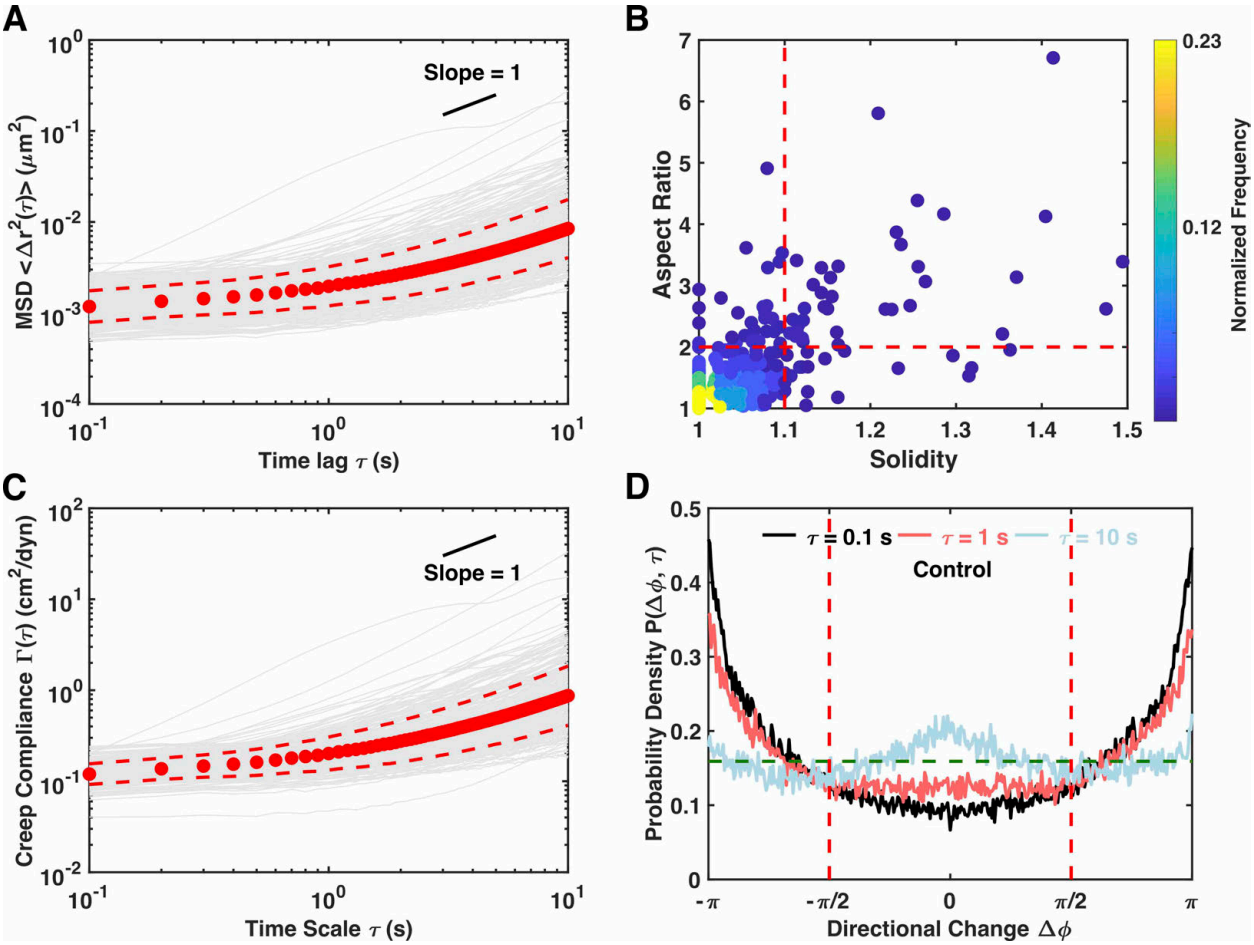

Figure 4.1. Measurements based on mitochondrial fluctuations.
(A, C) Individual and population mean with standard deviations of (A) MSDs (n=211) and (C) creep compliance (n=169). Gray curves are for individual mitochondria and red circles indicate population mean. Red dashed lines are standard deviations. Short black line is a visual guide of slope one. (B) Distribution of mitochondrial morphologies in a 2D space of solidity and aspect ratio. Filled circles are individual mitochondria color-coded with local normalized frequencies in accordance to the colormap. The two dashed red lines represent the morphological filtering criteria of solidity less than 1.1 and aspect ratio less than 2. (D) Distributions of directional change of control cells at different lag times. Green dashed horizontal line indicates a uniform distribution which is characteristic of pure diffusion.

4.3 Results

4.3.1 Normalizing the morphological heterogeneity of punctate mitochondria

In contrast with the relatively tight distribution of sizes of commercially available fluorescent particles, mitochondrial morphologies are very heterogeneous (Figs. 4.1 B and

Appendix III: Fig. S4.1). A plot of the solidity against the aspect ratio shows a wide distribution of 2D projected mitochondrial morphologies, though many mitochondria were located close to the point (1, 1) that corresponds with a round shape (Fig. 4.1 B). For simple diffusion processes, particle size heterogeneity affects the MSD through its effect on the diffusion constant, which scales as 1/a, where a is the particle size, by the Stokes-Einstein relation. The creep compliance, as shown in Eq. 2, scales out the dependence on particle size, and should be able to reduce the variance contributed by morphological heterogeneity in MSD. In Eq. 2, the radius of a spherical particle is incorporated, which is not appropriate for most punctate mitochondria tracked in our cells (Fig. 4.1 B). We generalized the definition of creep compliance by substituting the radius of a spherical particle with the hydrodynamic radius of a prolate (football-like) ellipsoid (Eq. 3). This is analogous to the elegant work of F. Perrin to generalize the Stokes-Einstein equation [33,34]. To make sure that this generalization is appropriate, we filtered the mitochondria close to prolate ellipsoids as being less than 1.1 for solidity and being less than 2 for aspect ratio (Figs. 4.1 B and Appendix III: Fig. S4.1 B. k). At least 70% of all punctate mitochondria tracked pass this morphological filtering criteria in all datasets presented in this study (data not shown). Heterogeneity in the hydrodynamic radii is still present in the filtered mitochondria (Appendix III: Fig. S4.2). Similar to MSDs, the distribution of the hydrodynamic radii is better described by a log-normal distribution than a normal distribution (Appendix III: Fig. S4.2).

The variance in creep compliance reduces significantly after the morphological filtering, especially over the short timescales (Appendix III: Fig. S4.3). To quantify and compare the variances at different levels of population means, GCVs were calculated at every lag time for both MSD and creep compliance. The GCV shows the reductions in variances by the normalization using creep compliances and it shows even more pronounced reduction after

applying the morphological filtering (Appendix III: Fig. S4.4 A). This quantification also supports the conclusions from the visual comparisons made in Appendix III: Fig. S4.3. In all the datasets reported in this study, the morphological filtering and normalization using creep compliance are able to reduce the variances (data not shown). Therefore, creep compliance after morphological filtering is reported rather than MSD in the rest of this study, if not stated otherwise.

4.3.2 Distribution of directional change as a hypothetical signature of mechanisms underlying mitochondrial fluctuations

We observed different power-law scaling at different timescales in the control cells similar to earlier publications [3,14,16,35,36]. Over short timescales (0.5 – 1.5 s), the MSD curves show weak lag-time dependence with a mean power-law scaling factor of 0.35, suggesting that the mitochondrial fluctuations are dominantly subdiffusive (Appendix III: Figs. S4.4 B-C). A stronger lag-time dependence with a mean power-law scaling factor of 0.82 is observed over long timescales (6 – 8 s) (Appendix III: Figs. S4.4 B-C). The high variance observed in the MSDs is also significant in terms of the power-law scaling factors. Interestingly, a significant portion of the power-law scaling factors over the long timescales is larger than one (Appendix III: Fig. S4.4 C). This superdiffusive behavior is consistent with previous studies showing that mitochondria are occasionally directly transported by molecular motors [37], thus suggesting that the mitochondrial fluctuations are also driven by active forces over long timescales, in addition to thermal forces.

It has been shown using simulations that distribution of directional change can provide more information about stochastic processes than MSD, which is essentially a 1D measurement [28]. In addition to the power-law scaling factors, we also calculated distribution of directional

change as a function of lag-time (Fig. 4.1 D). Over short timescales (0.1 s and 1 s), only one peak at $\Delta\phi = \pi$ is present, indicating anti-correlated motion, i.e. a forward step is more likely to be followed by a backward step. This is similar to the distribution of directional change reported for subdiffusive motion in a viscoelastic environment due to caging and escape dynamics [28]. Along with the increase in lag-time, the peak at $\Delta\phi = \pi$ gradually decays, and the peak at $\Delta\phi = 0$ grows and eventually becomes dominant. Thus at the long timescales (10 s), the probability of going forward, i.e. persistent motion, dominates. The combination of "bouncing in a cage" at short timescales and persistent motion at long timescales suggests that the cage itself is drifting, probably driven by directed transport or active cytoskeletal remodeling. In fact the distribution of directional change qualitatively matches that of a particle in a harmonic potential with drift [28]. This trend is also revealed by the index of directional persistence, P_d (Appendix III: Fig. S4.4 D). The P_d of control cells starts with negative values, suggesting anti-persistent motions and in our case the caging effects by cytoskeletal networks. With the increase in lag times, P_d gradually increases to positive values, indicating the increasing dominance of persistent motion at longer times.

Multiple ATP-dependent mechanisms are able to drive the mitochondrial fluctuations and likely to dominate over long timescales, while thermal forces are likely to dominate over short timescales (3, 12, 37, 42, 43). This argument is supported by our results of both power-law scaling factor and distribution of directional change. To further understand the underlying mechanisms of the mitochondrial fluctuations observed in the control cells, we carried out a series of chemical treatments targeting components of the cytoskeleton that may be involved.

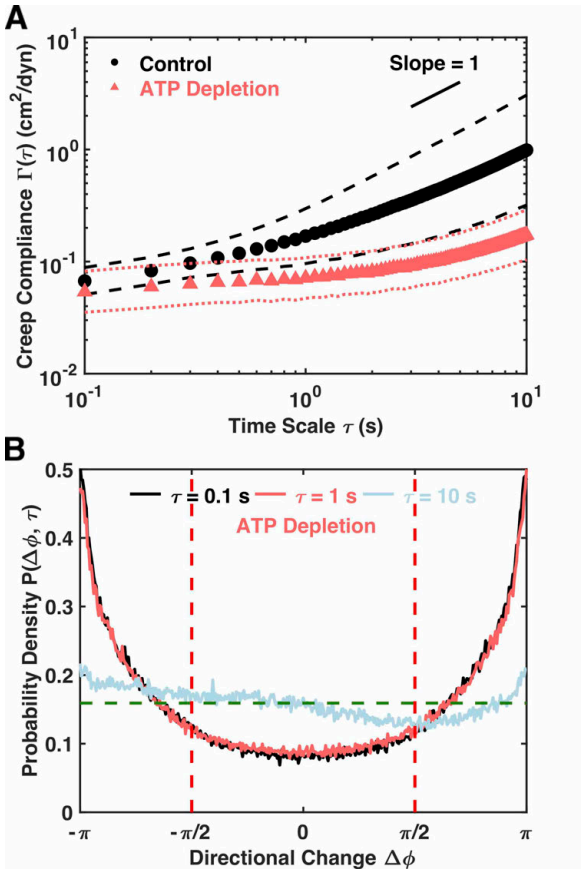

Figure 4.2. Mitochondrial fluctuations are ATP dependent.
(A) Population mean creep compliances with standard deviations of control (n=169) and ATP depleted cells (n=156). Markers of different shapes and colors indicate population means and lines of same colors are standard deviations. Short black line is a visual guide of slope one. (B) Distributions of directional change of ATP depleted cells at different lag times. Green dashed horizontal line indicates a uniform distribution which is characteristic of pure diffusion.

4.3.3 Mitochondrial fluctuations are ATP-dependent over long timescales

We first tested the ATP-dependence of the mitochondrial fluctuations. The C3H-10T1/2 cells were treated with 2 mM NaN_3 and 2 mM deoxy-D-glucose, which inhibits the ATP synthesis in the electron transfer chain and glycolysis respectively [38,39]. Despite an overlap at the shortest timescales, the decrease in the population mean creep compliance of ATP depleted cells is statistically significant over all timescales compared to that of the control cells (Figs. 4.2 A and Appendix III: Fig. S4.5 A), with significant decreases in power-law scaling factor as well

(Appendix III: Figs. S4.5 C-D). The distributions of directional change remain almost the same from 0.1 s till 2 s in lag time, with the anti-persistent motion dominating (Figs. 4.2 B and Appendix III: Fig. S4.6). Along with the increase in lag time, decrease in anti-persistent motions is observed and the motion appears increasingly diffusive (Fig. 4.2 B). More importantly, no preference for persistent motion is observed at any timescales in the ATP-depleted cells. This trend is recapitulated in the P_d curve, which maintains a constant value from 0.1 s till around 2 s and then starts to approach the limit of zero (Appendix III: Fig. S4.5 E).

These results indicate that thermal forces are the dominating mechanism over the short-timescale, and ATP-dependent and thus active processes dominate the longer timescales in control cells. In addition, the distributions of directional change of ATP-depleted cells remain flat at $\Delta ø = 0$ over timescale longer than 2 s (Appendix III: Fig. S4.6). This trend suggests that the increase in creep compliance of ATP-depleted cells over long timescales is likely due to passive escape from local "cages" due to the polymerization-depolymerization dynamics of microtubules that are driven by GTPs which are not depleted by the ATP-depletion treatment. Active yet random motions powered by residual intracellular ATP probably contribute as well. Therefore, the timescales from 0.1 s to 2 s are dominated by thermal forces in ATP depleted cells (Figs. 4.2 B and Appendix III: S4.5 E). The ATP dependence also implies that the creep compliance does not relate directly to the viscoelastic properties of the control cells, since the system is out of thermal equilibrium. However, we will continue using creep compliance to reduce morphological heterogeneity, while placing no interpretation on its physical meaning.

The cellular interior is highly heterogeneous which is reflected in the heterogeneity of the MSD of single mitochondria and the convergence of the cell-wise creep compliance to the population mean (Appendix III: Fig. S4.14 A). The overall heterogeneity in the creep compliance

is dominated by intracellular heterogeneity (Appendix III: Fig. S4.14 B). We saw no evidence of spatial correlation of intracellular mechanical properties (Appendix III: Fig. S4.14 C), possibly because the mitochondria were on average tens of microns away from each other.

We further hypothesized that the microtubule network and actin network may play important roles in forming the local cages for mitochondria. To test this, we carried out chemical treatments targeting these two important players in the cytoskeletal network.

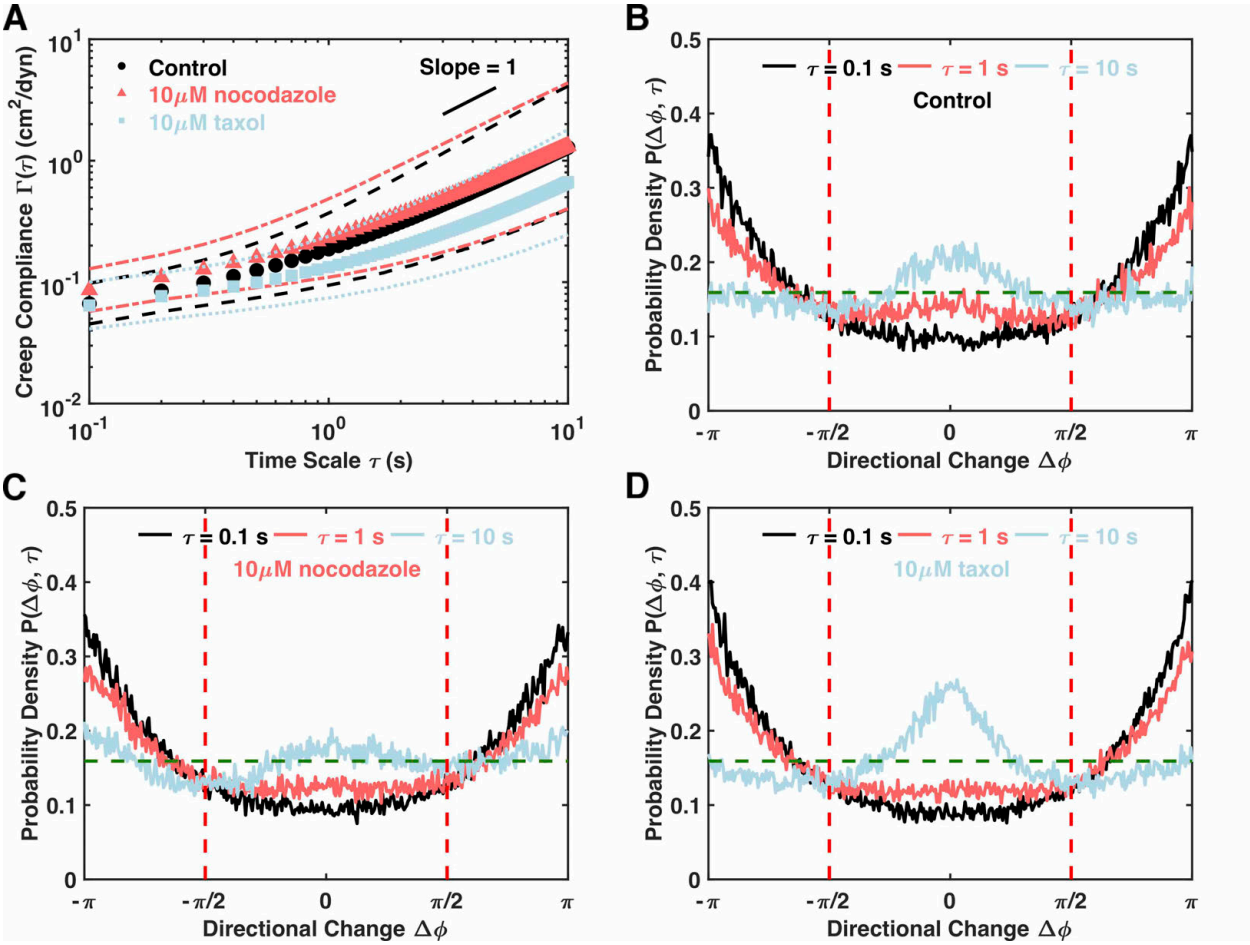

Figure 4.3. Microtubule network plays a significant role in mitochondrial fluctuations. (A) Population mean creep compliances with standard deviations of control cells (n=87), nocodazole treated cells (n=106) and taxol-treated cells (n=131). Markers of different shapes and colors indicate population means and lines of same colors are standard deviations. Short black line is a visual guide of slope one. (B-D) Distributions of directional change at different lag times of control, nocodazole-treated and taxol-treated cells respectively. Green dashed horizontal line indicates a uniform distribution which is characteristic of pure diffusion.

4.3.4 Microtubule network plays a significant role in mitochondrial fluctuations

Two widely-used microtubule-targeting chemicals, nocodazole and taxol (also known as paclitaxel), were applied to C3H-10T1/2 cells. Nocodazole de-stabilizes microtubule polymerization [40]. Destabilizing microtubules by nocodazole statistically significantly increases the creep compliance over the short timescales yet the changes over long timescales are not significant (Fig. 4.3 A and Appendix III: Fig. S4.7 A). The distribution of directional change and the P_d of the nocodazole-treated cells show reduced persistent motions, especially over the longer timescales when compared with control cells (Figs. 4.3 B-C and Appendix III: Fig. S4.7 C). By de-stabilizing microtubules, nocodazole appears to increase the effective cage size, leading to an increase in creep compliance over short times. However nocodazole inhibits the longer time directed motion. Since mitochondria are transported along microtubules, destabilizing microtubules very likely abrogates or impedes the active motion seen in control cells. Taxol inhibits the normal dynamic reorganization of the microtubule network, and leads to the formation of extensive and hyper-stable parallel arrays of microtubules [41–43]. Taxol treatment leads to statistically significant decrease of creep compliance over the long timescales, which becomes insignificant in the limit of short timescales (Fig. 4.3 A). Decrease in directional persistence is observed over timescales shorter than 5 s and an increase thereafter compared to control cells (Figs. 4.3 BD and Appendix III: Fig. S4.7 C). Despite the increase in directional persistence, a two-fold decrease in creep compliance was observed (Appendix III: Fig. S4.7 B). Taxol therefore strengthens the confinement of the mitochondria by the microtubule network, and slows network dynamics, leading to a smaller creep compliance at longer times. However even though the extent of motion is low, directed transport is even more apparent at longer timescales, probably due to the extensive microtubule network.

Taken together, our results show that the microtubule network plays important roles in the mitochondrial fluctuations, probably by a dual-mechanism (Fig. 4.3). Over the short timescales, microtubules confine mitochondria to local “cages”. Over longer timescales, the mitochondria show a persistent drift probably due to a combination of polymerization-depolymerization dynamics and active transport along the microtubule tracks. Destabilizing the cages using nocodazole increases the confinement volume of the mitochondria and thereby increases their creep compliances at short timescales, but decreases the longer time persistent motion. Stabilizing the network using taxol leads to stronger confinement of the mitochondria and makes the longer-time drift slower, and happen much later. These results also support the hypothesis that microtubule dynamics may contribute to the increase in creep compliance of ATP-depleted cells over long timescales. It is also possible that the inhibition of normal dynamics by taxol can result in a decrease in active forces generated by uncorrelated dynamics of microtubule network, and lead to a decrease in the creep compliance. However, the increase in directional persistence after taxol treatment as compared with control cells implies that this mechanism is insignificant (Figs. 4.3 BD and Appendix III: Fig. S4.7 C).

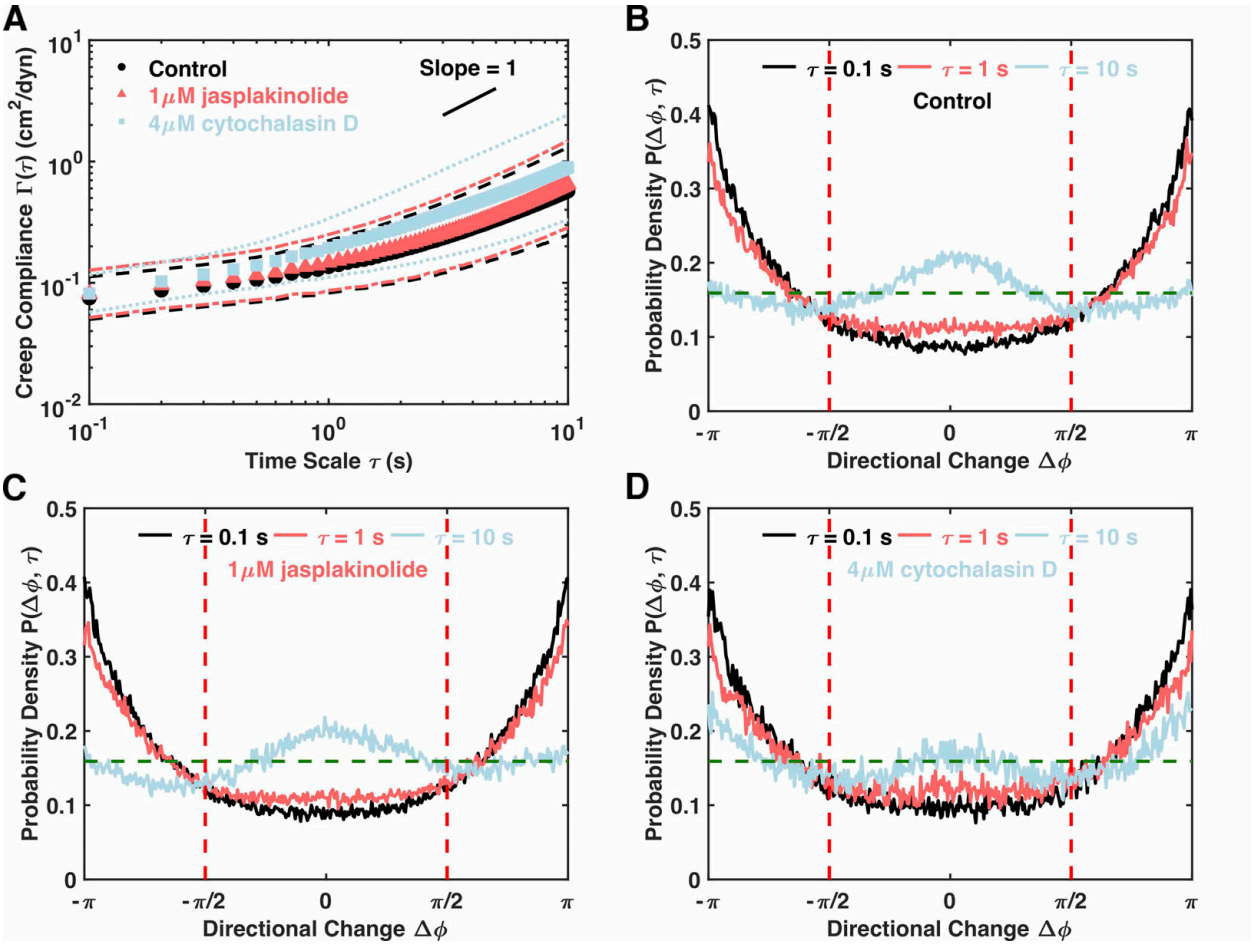

Figure 4.4. Actin network is required for active mitochondrial fluctuations.
(A) Population mean creep compliances with standard deviations of control cells (n=98), jasplakinolide treated cells (n=141) and cytochalasin D treated cells (n=44). Markers of different shapes and colors indicate population means and lines of same colors are standard deviations. Short black line is a visual guide of slope one. (B-D) Distribution of directional change at different lag times of control, jasplakinolide and cytochalasin D treated cells respectively. Green dashed horizontal line indicates a uniform distribution which is characteristic of pure diffusion.

4.3.5 The actin network is required for active mitochondrial fluctuations in a myosin II independent manner

To test the roles played by the actin network on the mitochondrial fluctuations, the C3H-10T1/2 cells were treated with two widely-used actin-targeting chemicals. Jasplakinolide is a potent inducer of actin polymerization and hyper-stabilizes actin filaments [44]. Jasplakinolide can be expected to increase mitochondrial confinement over short timescales and decrease the

escape probability, or reduce active fluctuations, over longer timescales. Our data shows that jasplakinolide leads to no statistically significant change at a high concentration of 1 μM in terms of both creep compliance and directional changes (Figs. 4.4 A-C and Appendix III: Fig. S4.8). Thus stabilizing the actin network had no significant effect on mitochondrial fluctuations.

Cytochalasin D is a widely-used inhibitor of actin dynamics, which binds to the barbed ends of actin filaments and inhibits both actin polymerization and depolymerization [45,46]. Cytochalasin D has been shown to only inhibit the actin dynamics, and the net effects on the stability and density of the actin network depend on other cellular conditions [46]. Therefore, cytochalasin D can specifically affect actin network dynamics as well as active driving forces generated by actin polymerization and depolymerization. Cytochalasin D statistically significantly increases the population mean creep compliance over both short and long timescales (Figs. 4.4 A and Appendix III: Fig. S4.8 A), which suggests a net increase in the confinement volume of the mitochondria, probably due to a reduction in the density of the actin network. However, the distributions of directional change suggest that the cytochalasin D made the confinement of the mitochondria last longer, with a significant peak at $\Delta\phi = \pi$ even at the longest timescale of 10 s (Fig. 4.4 D). In addition, the decrease in persistent motions suggest that the actin network is also involved in active transport (Figs. 4.4 BD). This is consistent with the report that actin network could serve as tracks for active transportation over short length scales [37]. Similar to earlier published studies [47], the microtubule and actin results suggest that the microtubule network is a primary local “cage” and actin network forms a secondary local cage, but both networks appear to be required for the active motion at long timescales.

We also tested the role of non-muscle myosin II, which binds to the actin filaments and generates contractile forces on actin network in an ATP dependent manner. Myosin II had been

shown to play important roles in driving active fluctuations of fluorescent particles in previous studies [3,13–16,35,48]. We treated the C3H-10T1/2 cells with blebbistatin, which specifically binds to myosin II and inhibits its binding to actin filaments [49–51]. However, our results with three different concentrations of blebbistatin show statistically insignificant changes in creep compliance (Appendix III: Fig. S4.9). Although minor decreases can be observed in the distributions of directional change (Appendix III: Fig. S4.9 D), especially in the 10 μM, this effect is small. Thus, in contrast to fluorescent particles that may become trapped in the actin network, the mitochondria are not dominantly affected by the dynamics of myosin II.

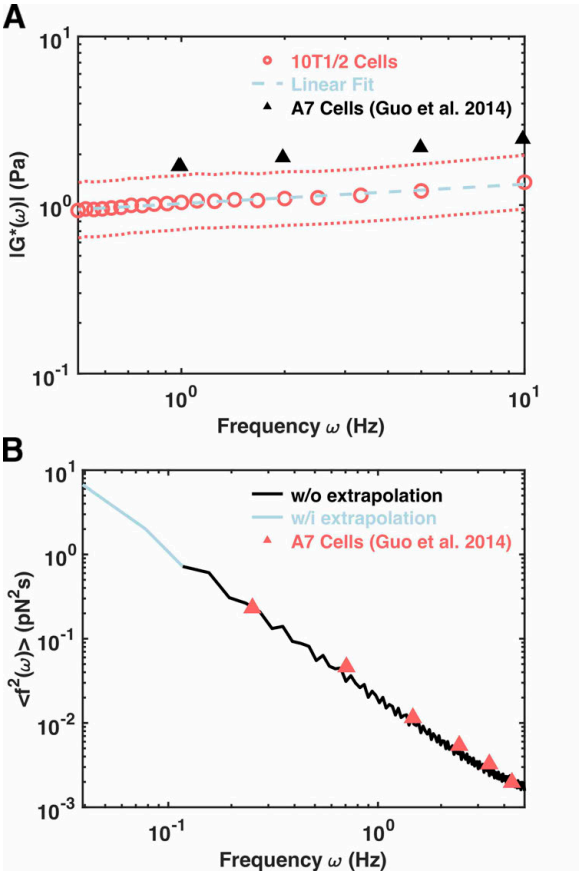

Figure 4.5. Mitochondrial fluctuation based force spectrum calculation.
(A) Population mean complex shear modulus (open red cycles) with standard deviations (red dotted lines) determined from ATP depleted cells. Light blue line is a linear fit to the population mean. Black triangles indicate published measurements made on A7 cells using active microrheology [3]. (B) Force spectrum determined by combining the results from control cells

and ATP depleted cells using Eq. 4. Red triangles indicate published measurement of mitochondria using the original FSM [3].

4.3.6 Force Spectrum Microscopy using the control cells and ATP depleted cells

To improve the accuracy of viscoelastic properties determined from ATP depleted cells, we propose to use the distribution of directional change and P_d to make the selection of the timescales over which thermal forces are dominating. In our results, these two measurements suggest that the relevant thermally dominated timescales are up to 2 s in ATP-depleted cells (Figs. 4.2 B and Appendix III: Figs. S4.5 E and S4.6). In addition, comparing the MSDs and creep compliance of control and ATP-depleted cells shows that the population means converge at the shortest timescale, which is evidence that the ATP depleting treatment has not altered the cytoskeleton structures in any significant way [3,15–17].

The power-law scaling factor over the timescales between 0.1 and 1 s has a mean of 0.15-0.2, which is consistent with reported values [17] and reminiscent of sub-diffusive fluctuations in a nearly elastic medium (Figs. 4.2 A and Appendix III: Fig. S4.5 CD). Similar as in creep compliance, mitochondria after morphological filtering were used to determine the viscoelasticity to make sure the utilization of hydrodynamic radius is appropriate. The viscoelasticity determined using the MSDs of ATP depleted cells under 2 s suggests that the elasticity modulus is indeed more than five times larger than the viscosity modulus (Appendix III: Fig. S4.10). The corresponding amplitude of the complex shear modulus ($|G^*|$) shows a temporal dependence following a power-law form with a scaling factor of 0.12 and a R^2 value of 0.99 (Fig. 4.5 A). To test the validity of our result, we compared our values of $|G^*|$ to those measured for A7 cells using active microrheology (a scaling factor of 0.16 and R^2 value of 0.99) (Fig. 4.5 A) in Ref. [3]. Given the differences in cell lines, the two results are very similar and

within a two-fold difference, which supports the reliability of the alternative method we proposed.

From the MSDs measured in the control cells, we calculated the corresponding Fourier Transform of individual MSDs multiplied by the square of the corresponding mitochondrial hydrodynamic radius as in Eq. 4. Finally, the force spectrum was calculated as the product of the effective spring constant determined from ATP depleted cells and the displacement in control cells in frequency domain (Eq. 4 and Fig. 4.5 B). We first calculated only the force spectrum over the timescales shorter than 2 s selected for ATP depleted cells, as the black curve in Fig. 4.5 B. Since no obvious change in time dependence was observed for the |G*| in the measured frequency range, we assumed linear frequency dependence for the whole frequency range covered in the MSD [3,36] and calculated the force spectrum of the whole range, shown as the light blue curve in Fig. 4.5 B. Again, we compared our force spectrum results to that of mitochondrial fluctuation by the original FSM in Ref. [3]. Surprisingly, our results are almost the same as the original FSM (Fig. 4.5 B), despite the differences between cell types and the differences in viscoelastic parameters.

4.4 Discussion

4.4.1 Spontaneous fluctuations of endogenous particles are valuable probes for measurement of intracellular mechanical properties

We show that a careful treatment of mitochondrial fluctuations along with chemical treatments, especially the ATP depletion, can allow for estimation of intracellular mechanical properties. Our measurements show that the intracellular cytoskeletal network form a weakly elastic microenvironment, and that the |G*| measured is well described by a power-law form with a scaling factor of 0.12 (Fig. 4.5 A). These results are consistent with previous studies in which

spontaneously internalized fluorescent particles and vesicles were tracked [47,52], which are probing similar mechanical microenvironments [53]. Such a weak frequency dependence is also consistent with measurements made by not only active microrheology techniques [3,54] and but also other methods (including optical magnetic twisting cytometry, uniaxial stretching rheometer and atomic force microscopy) [55–57], in spite of different cell types (Table S4.2). The measured |G*| in our ATP depleted cells is approximately 1 Pa, which is similar to the intracellular measurements [3,54] yet orders of magnitudes lower than that measured on the actin cortex [54,55,57]. This supports the argument that the intracellular cytoskeletal network is mechanically distinct from cortical actin networks and is more dilute.

Our results also suggest that the weakly elastic microenvironment is liquidized by ATP-dependent processes. The ATP-dependent processes that exert forces on the mitochondria could arise from polymerization-depolymerization dynamics of microtubules and actin, as well as from motor-driven forces. Our data shows that stabilizing the microtubule or actin network and thus repressing polymerization-depolymerization dynamics had no effect on the short-time fluctuations, but intriguingly different effects at longer times. While stabilizing actin did not significantly affect fluctuations at longer timescales, stabilizing microtubules decreased the extent of fluctuations but increased their persistence. Destabilizing microtubules increased the short-timescale fluctuations but had little effect at longer times, while destabilizing actin had no effect at shorter times but increased the extent of fluctuations at longer times. However for both cases the persistence of long time motion was significantly reduced, which is consistent with the hypothesis that persistent motion is an effect of motor-driven transport on microtubule and actin tracks. Many published results have reported that contractile forces generated by myosin II play important roles in driving active fluctuations of fluorescent particles [3,13–16,35,48]. However,

myosin II was shown not to play a significant role in our study, which is also consistent with studies using spontaneously internalized fluorescent particles and vesicles [47,52].

While mitochondria can be actively transported to regions of the cell where they are required, their positioning at these regions has been shown to be mediated by protein anchors [58] that can tether them to the endoplasmic reticulum as well as the actin and microtubule cytoskeleton. Moreover, stationary mitochondria may also remain attached to the molecular motors responsible for transporting them to the present location in the cell. The tethering may lead to the short timescale confined fluctuations observed in both the creep compliance and the directional persistence. The longer-timescale motion, which we show is ATP-dependent, is probably associated with the movement of the tethers themselves, due to remodeling of the cytoskeleton as well as motor mediated movement, or both. The fact that destabilization of both actin and microtubules does not significantly increase the average creep compliance but decreases persistence, suggests that the confinement probably involves other intracellular structures such as the endoplasmic reticulum, but active motion requires the cytoskeleton.

Active mitochondrial transport has been best studied in neurons, due to its role in neurodegenerative diseases [59]. Kinesin and dynein can move mitochondria toward microtubule plus end and minus end respectively for a long distance. The actin network is more important for short-range transport and anchoring of mitochondria [37,59]. Myosins are responsible to move mitochondria toward actin filament plus end (e.g. myosin V) or minus end (e.g. myosin VI) [59]. Mitochondria can also be completely released of these motor proteins and remain relatively stationary [59]. We therefore hypothesize that the active forces driving mitochondrial fluctuations are generated by motor proteins like dynein, kinesin and myosins other than myosin II, (e.g. myosins V and VI).

The special nature of the confining environment of mitochondria is probably the reason why they are insensitive to suppression of myosin II mediated actomyosin contractility. Passive polyethylene glycol (PEG) coated probe particles may, in many cases, get confined by the actin meshwork and show significant sensitivity to suppression of myosin II. Given the heterogeneity of the cytoskeletal network, mitochondrial fluctuations and fluorescent probe particles are very likely measuring cellular mechanical properties at different length-scales, and possibly somewhat specialized to different components of the cytoskeleton. Future work is required to link the different aspects of the cellular cytoskeleton together, as measured by fluorescent particles as well as endogenous probes such as mitochondria as well as peroxisomes, lysosomes and lipid vesicles [3,52,60].

4.4.2 Limitations of passive microrheology with mitochondria

Microrheology, whether active or passive, cannot provide information on the bulk rheology of the cell as a whole, which would require other assays. However, microrheology does provide an insight into internal and local cytoplasmic properties, including its viscoelastic characteristics that the present study focuses on. The alternative method we propose in this study has the advantages of non-invasiveness and low instrumentation requirements. However, like every technique, it also holds some limitations, some of which are shared by other particle tracking based methods. First of all, we used ensemble averaging measurements, including MSD, creep compliance and distribution of directional change, to characterize the mitochondrial fluctuations in this study. However, different mechanisms may dominate some specific timescales in particle motions, rather than impact uniformly across all timescales, which would be obscured in the ensemble averaging. To gain deeper understanding on the underlying mechanisms, temporal analyses of individual trajectory become necessary. This field has seen

rapid advances recently, including rolling window based methods [61] and hidden Markov Model based methods [62]. Although not included in this current study, these temporal analyses will be incorporated in our future studies.

In this study, mitochondria were chosen as the probe due to its universal presence in different cell types and cellular states, yet the morphological complexity of the mitochondria may limit the applicability of this method in some cell types. As shown previously [23], the morphology of the mitochondrial network is dynamically regulated, mostly due to the important physiological roles played by mitochondria in cell biology. So the punctate mitochondria used in our study may not be abundant in some cell types. However, the fluctuating motion of intermediate and filamentous mitochondria could be included into the analysis to broaden future applications of this method. An automated classification scheme of mitochondrial morphology, like the one developed in [23], could be integrated into the analysis pipeline.

Although ATP depletion enables directly extraction of mechanical properties from passive microrheology measurements, it also poses some unique limitations. Each new cell type requires optimization of the ATP depleting cocktail, and unintended effects may increase when different treatments are combined, for example to measure the mechanical properties of taxol-treated cells. The treatment of ATP depletion may also introduce side-effects to the “true” mechanical properties of the cytoplasm, for example by increasing actin network density [63] and possibly by crosslinking of actin filaments by inactive myosin II motors. To make sure that the side-effect by the ATP depletion is not significant, the convergence on the short timescale was used in our study. Our results also showed that stabilizing the actin network does not affect the MSD of the mitochondria, suggesting that ATP-depletion side-effects should be minimal in our results.

Finally, the use of microrheological techniques in living systems raises many questions that are yet to be settled, and that are the subject of current research. The first overarching assumption is that the cellular cytoplasm can be treated as an isotropic continuous substance at the length scale of the probe particle. Another major assumption of the field is the use of the GSER to calculate the rheological parameters. This is an important assumption and theoretical work has shown that the GSER is valid at best for a range of frequencies, which however may span the physiological relevant range for cell mechanics measurements [64,65]. The use of any type of probe particle also relies on the assumption that boundary conditions at the surface are not perturbing the results. Another important question is whether results from passive microrheology of ATP-depleted cells are equivalent to results from active microrheology. In particular active microrheology using optical tweezers may be probing the non-linear response of the cytoplasm, and theoretical papers have suggested that the non-linear response may be strongly affected by local microstructures [65–67], though previous work has shown excellent consistency between active and passive microrheology [17]. The existence of these debates is proof of the complexity of the cytoplasm, but also an indication of the promise of microrheology in elucidating cytoplasmic properties, including, but not confined to, viscoelastic properties.

4.4.3 Non-invasive Force Spectrum Microscopy

We extract the viscoelastic moduli G' and G" using GSER in ATP depleted cells, by using a statistical test to identify thermally dominated timescales. Based on the distribution of directional change and the probability of persistent motion, P_d, we identify a range of timescales over which thermal forces are dominating in the ATP depleted cells. Even though this results in a smaller range of timescales to determine the viscoelastic properties from the ATP depleted cells, we found that the accuracy is good compared to measurements made by active microrheology

[3]. We could then calculate the force spectrum based on the spontaneous fluctuations of mitochondria in control cells and the complex shear moduli measured in ATP depleted cells. The resulting force spectrum is interestingly almost identical to the force spectrum of mitochondria measured previously [3]. This relatively simple protocol should help expand the use and application of microrheology in living cells, and may facilitate novel applications like measuring mechanics and motor-driven forces within cells in 3D culture, in tissue models and during embryonic development.

REFERENCES

1. Orr AW, Helmke BP, Blackman BR, Schwartz MA. Mechanisms of Mechanotransduction Review. *Dev Cell.* 2006;10: 11–20. doi:10.1016/j.devcel.2005.12.006

2. Cross SE, Jin Y, Rao J, Gimzewski JK. Nanomechanical analysis of cells from cancer patients. *Nat Nanotechnol.* 2007;2: 780–783. doi:10.1038/nnano.2007.388

3. Guo M, Ehrlicher AJ, Jensen MH, Renz M, Moore JR, Goldman RD, et al. Probing the stochastic, motor-driven properties of the cytoplasm using force spectrum microscopy. *Cell.* 2014;158: 822–832. doi:10.1016/j.cell.2014.06.051

4. Spill F, Reynolds DS, Kamm RD, Zaman MH. Impact of the physical microenvironment on tumor progression and metastasis. *Curr Opin Biotechnol.* 2016;40: 41–48. doi:10.1016/j.copbio.2016.02.007

5. Daniels BR, Hale CM, Khatau SB, Kusuma S, Dobrowsky TM, Gerecht S, et al. Differences in the Microrheology of Human Embryonic Stem Cells and Human Induced Pluripotent Stem Cells. *Biophys J.* 2010;99: 3563–3570. doi:10.1016/j.bpj.2010.10.007

6. Earls JK, Jin S, Ye K. Mechanobiology of Human Pluripotent Stem Cells. *Tissue Eng part B.* 2013;19: 420–430. doi:10.1089/ten.teb.2012.0641

7. Brangwynne CP, Koenderink GH, MacKintosh FC, Weitz DA. Cytoplasmic diffusion: Molecular motors mix it up. *J Cell Biol.* 2008;183: 583–587. doi:10.1083/jcb.200806149

8. MacKintosh FC, Schmidt CF. Active cellular materials. *Curr Opin Cell Biol.* 2010;22: 29–35. doi:10.1016/j.ceb.2010.01.002

9. Riedel C, Gabizon R, Wilson CAM, Hamadani K, Tsekouras K, Marqusee S, et al. The heat released during catalytic turnover enhances the diffusion of an enzyme. *Nature.* 2015;517: 227–230. doi:10.1038/nature14043

10. Ahmed WW, Fodor É, Betz T. Active cell mechanics: Measurement and theory. *Biochim Biophys Acta - Mol Cell Res.* 2015;1853: 3083–3094. doi:10.1016/j.bbamcr.2015.05.022

11. Fakhri N, Wessel AD, Willms C, Pasquali M, Klopfenstein DR, MacKintosh FC, et al. High-resolution mapping of intracellular fluctuations using carbon nanotubes. *Science.* 2014;344: 1031–5. doi:10.1126/science.1250170

12. Mizuno D, Head DA, Mackintosh FC, Schmidt CF. Active and Passive Microrheology in Equilibrium and Nonequilibrium Systems. *Macromolecules.* 2008;41: 7194–7202.

13. Lau AWC, Hoffman BD, Davies A, Crocker JC, Lubensky TC. Microrheology, Stress Fluctuations, and Active Behavior of Living Cells. *Phys Rev Lett.* 2003;91: 198101.

doi:10.1103/PhysRevLett.91.198101

14. Fodor É, Guo M, Gov NS, Visco P, Weitz D a., van Wijland F. Activity-driven fluctuations in living cells. *Europhysics Lett.* 2015;110: 48005. doi:10.1209/0295-5075/110/48005

15. Mizuno D, Tardin C, Schmidt CF, Mackintosh FC. Nonequilibrium mechanics of active cytoskeletal networks. *Science.* 2007;315: 370–3. doi:10.1126/science.1134404

16. Smelser AM, Macosko JC, O'Dell AP, Smyre S, Bonin K, Holzwarth G. Mechanical properties of normal versus cancerous breast cells. *Biomech Model Mechanobiol.* 2015;14: 1335–1347. doi:10.1007/s10237-015-0677-x

17. Hoffman BD, Massiera G, Van Citters KM, Crocker JC. The consensus mechanics of cultured mammalian cells. *Proc Natl Acad Sci.* 2006;103: 10259–10264. doi:10.1073/pnas.0510348103

18. Gal N, Lechtman-Goldstein D, Weihs D. Particle tracking in living cells: A review of the mean square displacement method and beyond. *Rheol Acta.* 2013;52: 425–443. doi:10.1007/s00397-013-0694-6

19. Wirtz D. Particle-tracking microrheology of living cells: principles and applications. *Annu Rev Biophys.* 2009;38: 301–26. doi:10.1146/annurev.biophys.050708.133724

20. Mak M, Kamm RD, Zaman MH. Impact of Dimensionality and Network Disruption on Microrheology of Cancer Cells in 3D Environments. *PLoS Comput Biol.* 2014;10: e1003959. doi:10.1371/journal.pcbi.1003959

21. Giampazolias E, Tait SWG. Mitochondria and the hallmarks of cancer. *FEBS J.* 2016;283: 803–814. doi:10.1111/febs.13603

22. Da Silva AF, Mariotti FR, Máximo V, Campello S. Mitochondria dynamism: Of shape, transport and cell migration. *Cell Mol Life Sci.* 2014;71: 2313–2324. doi:10.1007/s00018-014-1557-8

23. Giedt RJ, Fumene Feruglio P, Pathania D, Yang KS, Kilcoyne A, Vinegoni C, et al. Computational imaging reveals mitochondrial morphology as a biomarker of cancer phenotype and drug response. *Sci Rep.* 2016;6: 32985. doi:10.1038/srep32985

24. Kandel J, Chou P, Eckmann DM. Automated detection of whole-cell mitochondrial motility and its dependence on cytoarchitectural integrity. *Biotechnol Bioeng.* 2015;112: 1395–1405. doi:10.1002/bit.25563

25. Giedt RJ, Pfeiffer DR, Matzavinos A, Kao CY, Alevriadou BR. Mitochondrial dynamics and motility inside living vascular endothelial cells: Role of bioenergetics. *Ann Biomed Eng.* 2012;40: 1903–1916. doi:10.1007/s10439-012-0568-6

26. Xu J, Viasnoff V, Wirtz D. Compliance of actin filament networks measured by particle-

tracking microrheology and diffusing wave spectroscopy. *Rheol Acta.* 1998;37: 387–398. doi:10.1007/s003970050125

27. Mason T, Ganesan K, van Zanten J, Wirtz D, Kuo S. Particle Tracking Microrheology of Complex Fluids. *Phys Rev Lett.* 1997;79: 3282–3285. doi:10.1103/PhysRevLett.79.3282

28. Burov S, Tabei SMA, Huynh T, Murrell MP, Philipson LH, Rice SA, et al. Distribution of directional change as a signature of complex dynamics. *Proc Natl Acad Sci.* 2013;110: 19689–19694. doi:10.1073/pnas.1319473110

29. Saxton MJ. Single-Particle Tracking: The Distribution of Diffusion Coefficients. *Biophys J.* 1997;72: 1744–1753.

30. Grebenkov DS. Probability distribution of the time-averaged mean-square displacement of a Gaussian process. *Phys Rev E.* 2011;84. doi:10.1103/PhysRevE.84.031124

31. Gibbons JD, Chakraborti S. Nonparametric statistical inference. Chapman & Hall/Taylor & Francis; 2011.

32. Hollander M, Wolfe DA, Chicken E. Nonparametric statistical methods.

33. Perrin F. Mouvement brownien d'un ellipsoide - I. Dispersion diélectrique pour des molécules ellipsoidales. *J Phys le Radium.*1934;5: 497–511. doi:10.1051/jphysrad:01934005010049700

34. Perrin F. Mouvement Brownien d'un ellipsoide (II). Rotation libre et dépolarisation des fluorescences. Translation et diffusion de molécules ellipsoidales. *J Phys le Radium.* 1936;7: 1–11. doi:10.1051/jphysrad:01936007010100

35. Gallet F, Arcizet D, Bohec P, Richert A. Power spectrum of out-of-equilibrium forces in living cells: amplitude and frequency dependence. *Soft Matter.* 2009;5: 2947–2953. doi:10.1039/b901311c

36. Gupta SK, Guo M. Equilibrium and out-of-equilibrium mechanics of living mammalian cytoplasm. *J Mech Phys Solids.* 2017;107: 284–293. doi:10.1016/j.jmps.2017.07.007

37. MacAskill AF, Kittler JT. Control of mitochondrial transport and localization in neurons. *Trends Cell Biol.* 2010;20: 102–112. doi:10.1016/j.tcb.2009.11.002

38. Ishikawa T, Bao-Li Z, Hitoshi M. Effect of sodium azide on the metabolic activity of cultured fetal cells. *Toxicol Ind Health.* 2006;22: 337–341.

39. Wick AN, Drury DR, Nakada HI, Wolfe JB. Localization of the primary metabolic block produced by 2-deoxyglucose. *J Biol Chem.* 1957;224: 963–969.

40. Vasquez RJ, Howell B, Yvon AM, Wadsworth P, Cassimeris L. Nanomolar concentrations of nocodazole alter microtubule dynamic instability in vivo and in vitro. *Mol Biol Cell.* 1997;8: 973–85.

41. Schiff PB, Fant J, Horwitz SB. Promotion of microtubule assembly in vitro by taxol. *Nature.* 1979;277: 665–667. doi:10.1038/277665a0

42. Horwitz SB. Taxol (paclitaxel): mechanisms of action. *Ann Oncol.* 1994;5 Suppl 6: S3-6.

43. Kingston DGI. Tubulin-interactive natural products as anticancer agents. *Journal of Natural Products.* 2009. pp. 507–515. doi:10.1021/np800568j

44. Spector I, Braet F, Shochet NR, Bubb MR. New anti-actin drugs in the study of the organization and function of the actin cytoskeleton. *Microsc Res Tech.* 1999;47: 18–37. doi:10.1002/(SICI)1097-0029(19991001)47:1<18::AID-JEMT3>3.0.CO;2-E

45. Cooper JA. Effects of cytochalasins and phalloidin on actin. *J Cell Biol.* 1987;105: 1473–1478.

46. Shoji K, Ohashi K, Sampei K, Oikawa M, Mizuno K. Cytochalasin D acts as an inhibitor of the actin-cofilin interaction. *Biochem Biophys Res Commun.* 2012;424: 52–57. doi:10.1016/j.bbrc.2012.06.063

47. Hendricks AG, Holzbaur ELF, Goldman YE. Force measurements on cargoes in living cells reveal collective dynamics of microtubule motors. *Proc Nat Acad Sci.* 2012;109: 18447–52. doi:10.1073/pnas.1215462109

48. Mackintosh FC, Levine AJ. Nonequilibrium mechanics and dynamics of motor-activated gels. *Phys Rev Lett.* 2008;100: 1–4. doi:10.1103/PhysRevLett.100.018104

49. Shu S, Liu X, Korn ED. Blebbistatin and blebbistatin-inactivated myosin II inhibit myosin II-independent processes in Dictyostelium. *Proc Natl Acad Sci*. 2005;102: 1472–1477. doi:10.1073/pnas.0409528102

50. Kovács M, Tóth J, Hetényi C, Málnási-Csizmadia A, Seller JR. Mechanism of blebbistatin inhibition of myosin II. *J Biol Chem.* 2004;279: 35557–35563. doi:10.1074/jbc.M405319200

51. Ramamurthy B, Yengo CM, Straight AF, Mitchison TJ, Sweeney HL. Kinetic mechanism of blebbistatin inhibition of nonmuscle myosin IIB. *Biochemistry.* 2004;43: 14832–14839. doi:10.1021/bi0490284

52. Goldstein D, Elhanan T, Aronovitch M, Weihs D. Origin of active transport in breast-cancer cells. *Soft Matter.* 2013;9: 7167–7173. doi:10.1039/c3sm50172h

53. Wu P-H, Hale CM, Chen W-C, Lee JSH, Tseng Y, Wirtz D. High-throughput ballistic injection nanorheology to measure cell mechanics. *Nat Protoc.* 2012;7: 155–170. doi:10.1038/nprot.2011.436

54. Guo M, Ehrlicher AJ, Mahammad S, Fabich H, Jensen MH, Moore JR, et al. The role of vimentin intermediate filaments in cortical and cytoplasmic mechanics. *Biophys J*. 2013;105: 1562–1568. doi:10.1016/j.bpj.2013.08.037

55. Fabry B, Maksym GN, Butler JP, Glogauer M, Navajas D, Fredberg JJ. Scaling the microrheology of living cells. *Phys Rev Lett.* 2001;87: 1–4. doi:10.1103/PhysRevLett.87.148102

56. Desprat N, Richert A, Simeon J, Asnacios A. Creep function of a single living cell. *Biophys J.* 2005;88: 2224–2233. doi:10.1529/biophysj.104.050278

57. Alcaraz J, Buscemi L, Grabulosa M, Trepat X, Fabry B, Farré R, et al. Microrheology of human lung epithelial cells measured by atomic force microscopy. *Biophys J.* 2003;84: 2071–2079. doi:10.1016/S0006-3495(03)75014-0

58. Kraft LM, Lackner LL. Mitochondrial anchors: Positioning mitochondria and more. *Biochem Biophys Res Commun.* 2017; 1–7. doi:10.1016/j.bbrc.2017.06.193

59. Saxton WM, Hollenbeck PJ. The axonal transport of mitochondria. *J Cell Sci.* 2012;125: 2095–2104. doi:10.1242/jcs.053850

60. Gal N, Weihs D. Intracellular mechanics and activity of breast cancer cells correlate with metastatic potential. *Cell Biochem Biophys.* 2012;63: 199–209. doi:10.1007/s12013-012-9356-z

61. Arcizet D, Meier B, Sackmann E, Rädler JO, Heinrich D. Temporal analysis of active and passive transport in living cells. *Phys Rev Lett.* 2008;101: 1–4. doi:10.1103/PhysRevLett.101.248103

62. Monnier N, Barry Z, Park HY, Su KC, Katz Z, English BP, et al. Inferring transient particle transport dynamics in live cells. *Nat Methods.* 2015;12: 838–840. doi:10.1038/nmeth.3483

63. Atkinson SJ, Hosford MA, Molitoris BA. Mechanism of Actin Polymerization in Cellular ATP Depletion. *J Biol Chem.* 2004;279: 5194–5199. doi:10.1074/jbc.M306973200

64. Levine AJ, Lubensky TC. One- and two-particle microrheology. *Phys Rev Lett.* 2000;85: 1774–1777. doi:10.1103/PhysRevLett.85.1774

65. Squires TM, Mason TG. Fluid Mechanics of Microrheology. *Annu Rev Fluid Mech.* 2010;42: 413–438. doi:10.1146/annurev-fluid-121108-145608

66. DePuit RJ, Khair AS, Squires TM. A theoretical bridge between linear and nonlinear microrheology. *Phys Fluids.* 2011;23. doi:10.1063/1.3598322

67. Puertas AM, Voigtmann T. Microrheology of colloidal systems. J Phys Condens Matter. 2014;26. doi:10.1088/0953-8984/26/24/243101

CHAPTER 5: GLASS BEADS LOAD 100 NM FLUORESCENT PARTICLES INTO LIVE CELLS TO PROBE INTRACELLULAR MECHANICAL PROPERTIES

5.1 Introduction

The mechanical properties of the cytoskeleton of mammalian cells are involved in normal physiological activities of cells to adhere, deform, move and sense their mechanical microenvironments [1], to divide [2], translocate endogenous organelles and protein complexes [3], which are changed in many physiological and pathogenic processes of great significance like differentiation[4–6], tumorigenesis [7,8] and other diseases [9]. Better characterizations and studies of these mechanical properties may not only lead to deeper understandings of the fundamental cell biology of these processes, but also novel applications for medical purposes, including label-free cancer diagnosis [10] and pharmaceutical screening and evaluation [11]. Many methods have been developed or adopted to measure the cellular mechanical properties, including particle-tracking microrheology (PTMR) [12], atomic force microscopy (AFM) [13], micropipette aspiration [14,15], magnetic twisting cytometry [16], optical tweezers[17], microfluidic optical stretching [18] and other microfluidic platforms [19,20]. PTMR gains its popularity due to its ability to probe the intracellular mechanical properties without being perturbed by the cortical actin network, its ability to probe local mechanical properties (as the opposite of global mechanical responses) with spatial resolutions and its ability to probe mechanical properties without requirements on direct contacts among other benefits [21].

The PTMR can be further classified into passive or active PTMR, depending on whether external forces are applied to drive the probe movements [12]. Passive PTMR has its roots in the classic works by Einstein [22] and Perrin [23]. Passive PTMR is able to measure the mechanical

properties of soft materials based on the analysis of the spontaneous Brownian motion of a tracer particle and incur relatively little perturbations to the material under study. This is similar to the viscosity of the solute embedding the probe particles being determined by the spontaneous particles fluctuations via Stokes-Einstein equation. Without the requirement of additional instrumentation to manipulate the probes, passive PTMR is more accessible than its active counterpart. However, the classic Stokes-Einstein equation can only be used to determine frequency-independent viscosity, and this limits its application to biological materials which are better characterized by frequency-dependent viscoelasticity. The Stokes-Einstein equation was generalized to determine frequency-dependent viscoelasticity in 1995 [24], which is called the Generalized Stokes-Einstein Relation (GSER) [25]. As with the Stokes-Einstein equation, the GSER assumes that the system under study is at thermal equilibrium and that the movements of the probe particles are driven solely by thermal fluctuations. When the system satisfies this fundamental assumption, the viscoelasticity across a wide range of frequencies can be determined relatively easily through fluctuation-dissipation theorem (FDT) [24].

However, the cytoplasm is an active material driven by chemical energy, mainly in the form of Adenosine Triphosphate (ATP) [3,26]. The Brownian-like motions observed in the control cells are thus driven by both thermal and active forces, specially at long timescales [27,28]. Therefore, the assumption of thermal equilibrium in GSER is not valid and incorrect cellular viscoelasticity could be estimated from the mean squared displacement (MSD) of probe particles if GSER is applied directly [28–30]. This limits the utility of GSER to high frequencies in MSDs of control cells [31] or to an extended range of high frequencies in ATP depleted cells [32,33]. The MSDs of the probe particles, in general, still conveys important properties of the

active forces and cytoskeletal dynamics, which can be informative on their own [34] or interpreted in combinations with other techniques like active PTMR [29] or AFM [35].

In the passive PTMR, fluorescent particles embedded into the cytoplasm and endogenous organelles are typically used as the tracking probes. However, due to the hard-to-characterize interactions between the organelles and other subcellular structures, the interpretation of the results may be challenging [36]. In contrary, the interactions of fluorescent particles with subcellular structures can be well-controlled by surface coating [37]. Fluorescent particles are also preferred due to its photostability, high signal-to-noise ratio and regular morphology. Multiple methods have been adopted to deliver fluorescent particles into cytoplasm in the field of passive PTMR, including microinjection [17,29], ballistic injection [21,38] and endocytosis [39,40]. Fluorescent particles can be spontaneously engulfed by the cell through endocytosis pathway [39,40]. However, they become trapped inside lipid vesicles without direct contacts with cytoskeletons and may be actively transported by molecular motors [21]. The heterogeneity in the particle-cytoskeleton contacts may further complicate the interpretation of the results, especially the absolute magnitudes [27]. It is thus necessary to circumvent the endocytosis pathway and deliver the fluorescent particles directly into the cytoplasm. This necessity led to the adoption of microinjection and ballistic injection, both of which requires advanced instrumentation and expertise to operate. Microinjection also suffers from being labor-intensive and low-throughput [21]. The lack of a general, accessible and reliable particle delivery method of fluorescent particles directly into cytoplasm is a barrier for passive PTMR to become a routine measurement.

Glass bead loading has been widely used as a simple method to deliver fluorescently labelled proteins into mammalian cells [41–44], by disrupting the cellular membrane

mechanically and creating transient channels to allow the fluorescent particles diffuse into the cells [45]. These disruptions typically reseal very promptly similar to microinjection and ballistic injection, which was shown to happen within 10-120 s depending on the extracellular calcium level [46]. This simple yet elegant technique is drawing increasing attentions due to its simplicity recently. Studies have delivered 34 nm PEG coated quantum dots [45] and 40 nm magnetic nanoparticles [47] into mammalian cells using bead loading. It was also shown that the bead-loaded nanoparticles is able to disperse homogeneously inside the cytoplasm of mammalian cells [45,47]. However, there is no study showing, directly or indirectly, that the bead loading technique is able to deliver fluorescent particles larger than 40 nm.

In this study, we optimized the bead loading protocol into the field of passive PTMR. We tested its general applicability by bead loading 100 nm fluorescent particles in three different cell types. We then tested whether the bead-loaded 100nm fluorescent particles are able to probe the intracellular mechanical properties using pharmaceutical chemicals targeting specific components of cytoskeleton. This study shows that bead loading technique is able to deliver fluorescent particles directly into cytoplasm to measure the mechanical properties of the cytoplasm. Our results further showed that quantitative measurements of MSD and distribution of directional changes could generate deeper insights into the cytoskeletal mechanical properties.

5.2 Materials and Methods

5.2.1 Cell culture

C3H-10T1/2, a murine embryonic mesenchymal cell line was purchased from the American Type Culture Collection (ATCC, Manassas, VA). MCF7 and MDA-MB-231 cells were gifts from Dr. Brian McNaughton at Colorado State University. C3H-10T1/2, MCF7 and MDA-MB-231 cells were cultured in Dulbecco's Modified Eagle Medium (DMEM) (Sigma-

Aldrich, St Louis, MO) supplemented with 10% equaFETAL fetal bovine serum (FBS, Atlas Biologicals, Fort Collins, CO), 100 Units/ml penicillin and 100 μg/ml streptomycin (Fisher Scientific-Hyclone, Logan, UT). C3H-10T1/2 cells at their passages of 5-15 were used in this study. All cells were cultured at standard condition of 37 °C with 5% CO_2 supplemented. Cells were seeded at a concentration of 2.5×10^4 cells/ml the night before imaging in uncoated glass-bottom 35 mm dishes (MatTeK, Ashland, MA) for C3H-10T1/2 and the same dishes coated with fibronectin for the rest of the cell lines. Experiments were carried out after cells spread and attach to the substrate.

5.2.2 Preparation of the PEG-coated fluorescent particles

100 nm fluorescent carboxylate-modified polystyrene spherical particles (Molecular Probes, Eugene, OR) were rendered inert by grafting short amine-terminated poly(ethylene glycol) (PEG, Sigma-Aldrich, St Louis, MO) as described previously [37], in order to reduce nonspecific interactions with intracellular components which may result in directed transportation or entrapping by vesicles [48]. The PEG coated fluorescent particles were separated from unreacted reagents by dialysis in PBS buffer using Biotech cellulose ester membrane with a molecular weight cut-off of 100 kD (Spectrum Laboratories, Inc., Rancho Dominguez, CA). PEG-coated fluorescent particles were stored at 4 °C and used within 4 weeks.

5.2.3 Bead loading

The PEG-coated fluorescent particles were delivered into the cytoplasm of live cells using the bead-loading method [42–44]. The growth medium was aspirated, 4 μl PEG-coated fluorescent particles were added onto the top of the cells, and 106 μm glass beads (Sigma-Aldrich, St Louis, MO) sprinkled. After tapping the dish against the bench four to eight times, glass beads and undelivered fluorescent particles were washed away using 1×PBS and growth

medium was added to the dish. The cells were allowed to recover by incubation at standard growth conditions for 1 hr.

5.2.4 Chemical treatments

An array of chemical treatments were carried out in this study (Table 5.1). ATP depletion was achieved by incubation in PBS with 2 mM NaN3 and 2 mM 2-deoxy-D-glucose for 2 hour. Cytoskeleton-targeting chemicals were added into the film media and cells were incubated for 30 min. The chemicals were maintained in the film media during imaging to prevent recovery. Imaging was typically completed in 2-3 hours after the incubation.

Table 5.1. Chemical treatments

Target	Treatment/Drug name	Concentration	Reference
Actin	Jasplakinolide (Calbiochem)	0.2 μM	[49]
	Cytochalasin D (Calbiochem)	2 μM	[50,51]
Myosin II	Blebbistatin (Cayman Chemical)	10 and 25 μM	[52–54]
Microtubule	Nocodazole (Sigma)	10 μM	[55]
	Taxol (Goldbio)	10 μM	[56–58]
All ATP dependent processes	ATP Depletion	2 mM NaN_3 (Sigma) + 2 mM Deoxy-glucose (Sigma)	[59,60]

5.2.5 Imaging using confocal microscopy

Cells were imaged at 37 °C in CO_2-independent imaging medium made of Leibovitz's L-15 media (Gibco, Carlsbad, CA) supplemented with 10% FBS, 7 mM HEPES (Sigma-Aldrich, St Louis, MO) and 4.5 g/L D-glucose (pH 7.0). Random isolated cells were imaged using inverted spinning disk confocal microscope (Nikon Instruments, Inc., Melville, NY) under a 100× oil-immersion objective (FA ×1.45). NIS Advanced Research software (Nikon Instruments, Inc., Melville, NY) was used to control the hardware. The motions of fluorescent particles were recorded at 10 frames per second (fps) for 200 s using a cooled Andor DU897 X-10679 camera, with a spatial resolution of 140 nm per pixel. A 561 nm laser and the associated filters were used.

5.2.6 Image processing and Tracking mitochondrial fluctuations

The cell shape was traced manually in an in-house Matlab (Mathworks Inc., Natick, MA) and only the fluorescent particles enclosed in the cell boundary was tracked in uTrack [61]. A threshold on fluorescent intensity (1.5e6) is applied to eliminate the particles out of focus from further analysis.

5.2.7 Data analysis

The 2D trajectories of fluorescent particle tracked in the previous step were used to calculate the Mean Squared Displacement (MSD) as a function of lag time:

$$\langle \Delta r^2(\tau) \rangle = \langle \big(X(t+\tau) - X(t)\big)^2 + \big(Y(t+\tau) - Y(t)\big)^2 \rangle \quad [1]$$

where τ is lag time and brackets indicate the ensemble over all time points.

Directional change was calculated from two consecutive steps separated by the lag time for all time points in one trajectory and across all trajectories, which results in an ensemble-averaged, time-averaged distribution of directional change as a function of lag times [62]. The distribution of directional change was displayed in a window of [-π, π] to emphasize directionally persistent motions. An index of directional persistence, Pd, was calculated to summarize the information in the distribution of directional changes, defined as the difference between the probabilities of forward and backward motions [34]. If the motion is purely diffusive, the Pd is close to zero at all timescales. Negative P_d values indicate that the anti-persistent motion is dominating and vice versa.

5.2.8 Statistics

The means and standard deviations reported in this study were calculated by exponentiating the means ($\bar{\mu}_{ln}$) and the standard deviations (s_{ln}) of the logarithmic transformed data.

Wilcoxon rank sum test was used to test the null hypothesis that the two samples are from continuous distributions with equal means. As a nonparametric alternative to Student's t test, Wilcoxon rank sum test does not assume normality and is generally insensitive to actual distributions [63,64]. Wilcoxon rank sum tests, using the Matlab function ranksum, were carried out on the mean MSDs between control and chemical treated cells at all timescales, with p-value smaller than 0.05 deemed as statistically significant.

Control and chemical-treated cells compared in this study were imaged on the same day to minimize the day-to-day variance. Therefore, the mean MSDs of control cells of different days may be slightly different.

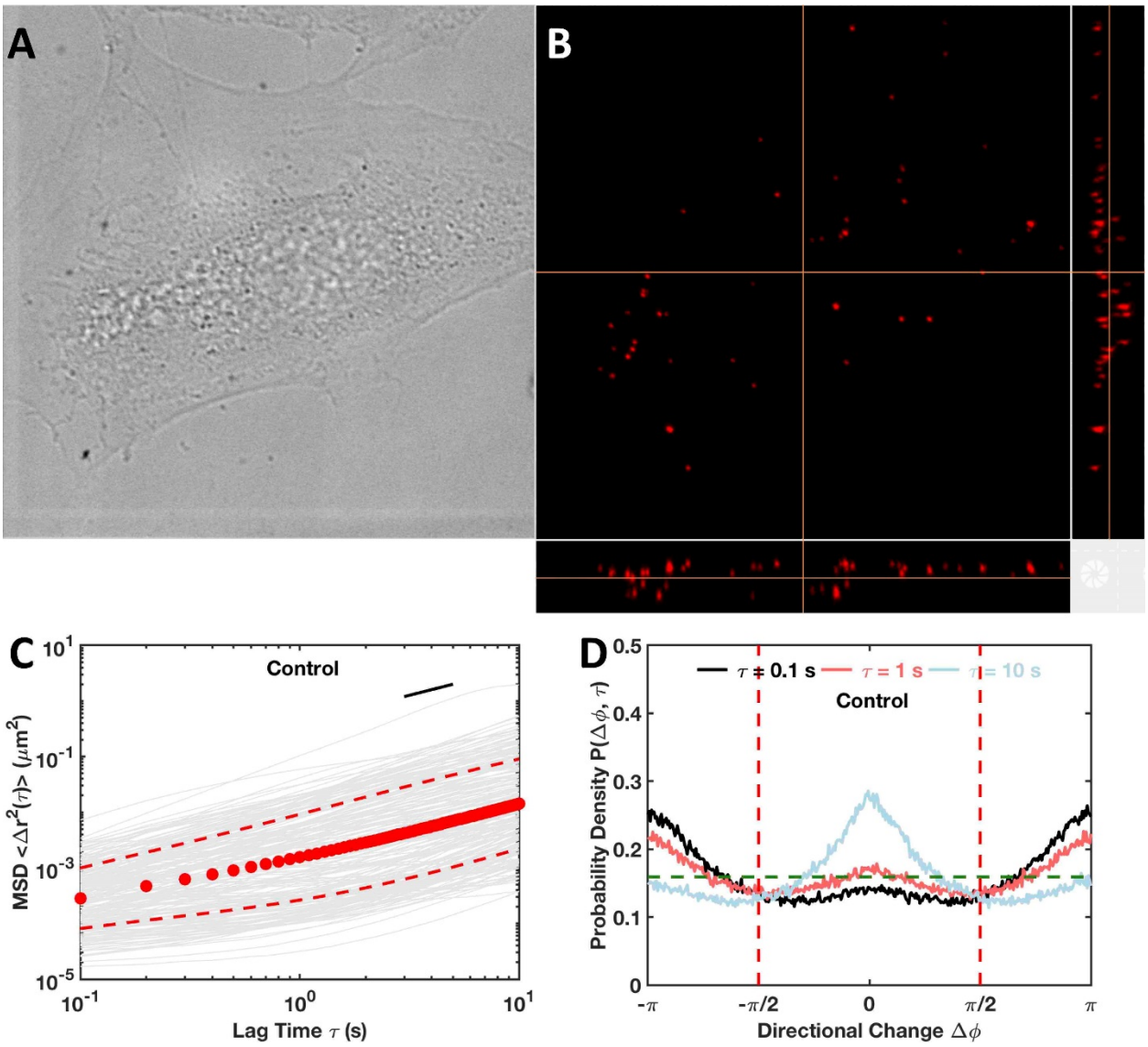

Figure 5.1. Glass beads load 100 nm fluorescent particles in C3H-10T1/2 cells under control condition.

A) Bright-field (DIC channel) and **B)** fluorescent (561 nm) images of C3H-10T1/2 cells bead-loaded with 100nm fluorescent particles respectively. Insets on the right and bottom sides are maximum intensity projection along x and y axes respectively. For the right inset, left side is the bottom of the cell and the right side the top of the cell. For the bottom inset, upper side is the bottom of the cell and the lower side the top of the cell. **C)** Individual and population mean with standard deviation of MSDs (n=217). Blue curves are MSDs of individual mitochondria and red filled circles indicate population mean. Red dashed lines are standard deviations. Black dashed line is a visual guide of slope one. **D)** Distributions of directional change of control cells at different lag times. Green dashed line indicates the uniform distribution which is characteristic of pure diffusion.

5.3 Results

5.3.1 Control cells

The confocal images (Figure 5.1 AB) show uniform dispersions of bead-loaded 100 nm fluorescent particles inside the cell yet well excluded from the nucleus. In contrast, no or very few fluorescent particle inside the cell was observed in the negative control condition with no glass bead added. This drastic difference suggests the efficacy of bead loading to deliver fluorescent particles directly into the cytoplasm. We further tested the general applicability of the bead loading technique using two widely studied breast cancer cell lines, MCF7 and MDA-MB-231, as models for benign tumor cells with low metastatic potential and malignant cancer cells with high metastatic potential respectively [7]. With some minor optimizations on the bead loading protocol, our preliminary results suggest homogeneous distributions of 100 nm fluorescent particles inside the cytoplasm of both cell types (Appendix IV: Figure S5.1).

We then calculated the MSDs based on trajectories of bead-loaded fluorescent particles in control cells. Similar to earlier studies, we observed a wide spread in the MSD results of individual particles (Figure 5.1C). The population mean slope is close to one at both long and short timescales (Appendix IV: Figure S5.2 CD), which is consistent with pure diffusion. However, previous studies suggested that such diffusion-like particle motions can also be driven by ATP-dependent (thus active) yet random intracellular forces [29,65].

To gain more insights into the mechanisms driving the observed motions of bead-loaded fluorescent particles, we calculated the distribution of directional change, which was shown using simulations to summarize more information about stochastic processes than MSD [62]. The distributions of directional change of the control cells at all timescales are not close to uniform distribution (Figure 5.1 D), suggesting that indeed the seemingly diffusive motions

observed in MSD cannot be attributed to just a purely diffusive processes. The distribution of directional change provides additional insights into the underlying mechanism (Figure 5.1 D). There is a dominating anti-persistent peak at $\Delta\phi = \pi$ in the distribution of directional change, i.e. a backward step is more likely to follow a forward step. This is consistent to subdiffusive motion in a viscoelastic microenvironment due to caging and escape dynamics [62]. With the increase in timescales, the anti-persistent peak at $\Delta\phi = \pi$ decreases gradually, and the persistent peak at $\Delta\phi = 0$ becomes dominating at the longest timescale (10 s). The combination of "bouncing in a cage" at short timescales and persistent motion at long timescales suggests that the confinement is moving with the particle, probably driven by actively remodeling cytoskeleton or molecular motor activities. This trend is also revealed by the index of directional persistence, P_d (Appendix IV: Figure S5.2 E). The P_d is negative at the shortest timescales, suggesting that anti-persistent motions and in our cells the confinements formed by cytoskeletal networks. P_d gradually increases to positive values with the increase in timescales, indicating the increasing dominance of persistent motion. These insights provided by the distribution of directional change and the P_d suggest that the mechanisms driving the particle movement, at least in the long timescales, are active in nature.

5.3.2 ATP depletion

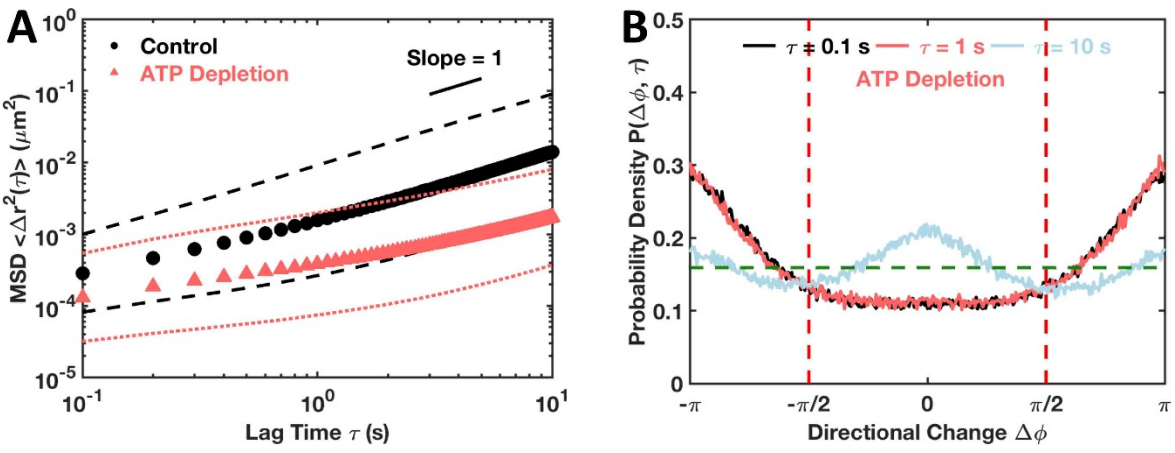

Figure 5.2. Fluctuations of fluorescent particles are ATP-dependent.
A) Population mean MSDs with standard deviations of control (n = 217) and ATP-depleted cells (n = 195). Closed markers indicate population means and dashed lines of the same color are standard deviations. Short black line is a visual guide of slope one. **B)** Distribution of directional change at different lag times of ATP-depleted cells. Green dashed line marks the uniform distribution, indicating no directional preference which is characteristic of pure diffusion.

We directly tested whether active forces are driving the particle movements observed in the control cells by a treatment with NaN_3 and Deoxy-glucose, which inhibit the ATP synthesis through electron transfer chain and glycolysis respectively [59,60]. We observed statistically significant decreases in the magnitudes of MSD in all timescales measured, ranging from 2 folds at the shortest timescale to almost 10 folds at the longest timescale (Figures 5.2 A and Appendix IV: Figure S5.2 AB). The power-law scaling factor at short timescales decreases from 0.8 to 0.5, while a slight recovery can be observed at the long timescales, probably due to incomplete ATP depletion [32] (Appendix IV: Figure S5.2 CD).

The distributions of directional change remain almost the same from 0.1 s till 1 s in lag time, with the anti-persistent motion dominating (Figure 5.2 B). Along with the increase in lag time, decrease in anti-persistent motions and increase in persistent motions are observed (Figure 5.2 B). At the longest timescale of 10 s, persistent motions become dominant but significantly less in magnitudes than the control cells, consistent with the results of local power-law scaling factor (Figure S5.2 CD). The P_d values reveal the same trends.

Therefore, the ATP depletion revealed that the apparently diffusive particle in the control cells are actually embedded in an elastic microenvironment that is liquidized by ATP-dependent forces, same as reported earlier [29,65]. It is thus incorrect to determine the viscoelasticity directly from MSD through GSER since the system is out of thermal equilibrium [24]. As discussed earlier the persistent motions at long timescales may be driven by active forces from

the molecular motors and/or cytoskeletal remodeling. In the rest of the study, we carried out chemical treatments to test different hypothetical contributors to the active forces in the cytoskeletal network.

5.3.3 Myosin II

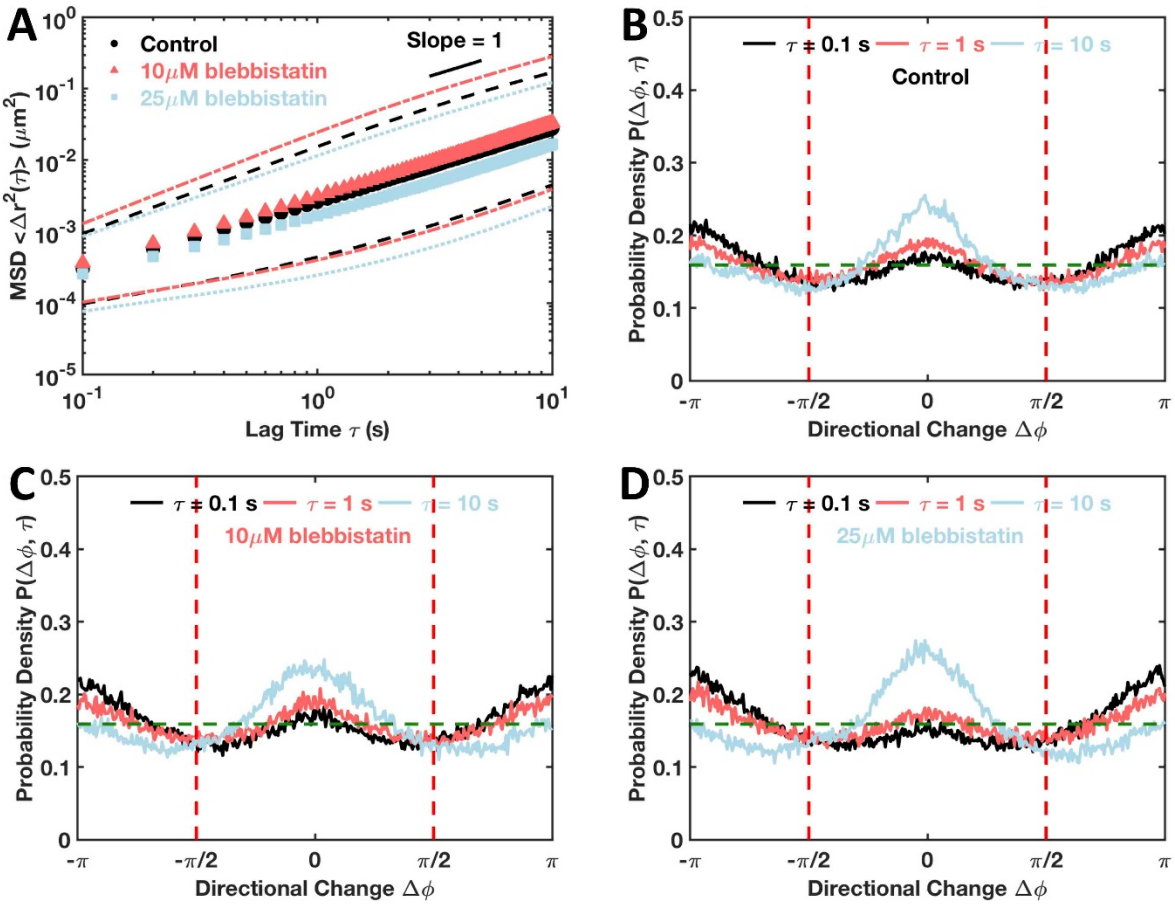

Figure 5.3. Myosin II plays a role in driving fluorescent particle fluctuations.
A) Population mean MSD with standard deviation of control cells (n = 195) and cells treated with 10 μM (n = 144) and 25 μM (n = 142) blebbistatin. Circles indicate population means and dashed lines are standard deviations. Short black dashed line is a visual guide of slope one. **B-D)** Distribution of directional change at different lag times of control cells and cells treated with 10 μM and 25 μM blebbistatin respectively. Green dashed line marks the uniform distribution, indicating no directional preference which is characteristic of pure diffusion.

Contractile forces generated by myosin II were reported to play important roles in driving active fluctuations of intracellular fluorescent particles [29,32,65–69]. To test the roles played by

myosin II in the movements of bead-loaded fluorescent particles, C3H-10T1/2 cells were treated with blebbistatin, a potent anti-cancer drug that binds to myosin II and inhibits its binding with the filamentous actin, leading to its dissociation from the actin network [52–54].

10μM blebbistatin results in no statistically significant difference in the MSDs (Figures 5.3A and Appendix IV: Figure S5.3 A). An increased concentration of 25μM blebbistatin results in a decrease in the MSD in all timescales, which is statistically significant with an approximately 2-fold decrease in timescales longer than 2 seconds (Figures 5.3A and Appendix IV: Figure. S5.3 B). In terms of the directionally persistent motions, neither concentration leads to significant changes in the anti-persistent peak, indicating the local confinement. For the persistent peak, 10 μM blebbistatin does not result in significant difference compared to the control cells, while the higher concentration of 25 μM results in decrease at short timescale of 0.1 and 1 seconds. Interestingly, this reducing effect by 25 μM blebbistatin is reversed at the longest timescale of 10 s. The seemingly contradicting results at different timescale probably are consistent with the two structural roles played by Myosin II, as both an actin cross-linker and molecular motor. At the short timescales, dissociated Myosin II mainly leads to the reduction in driving force. While at the long timescales, the dissociation of Myosin II may reduce the overall crosslinking level in the actin network, and decrease actin density, thereby increasing the active and directionally persistent movement driven by other active mechanisms with characteristic timescales longer than Myosin II, like cytoskeletal remodeling or other molecular motors. Taken together, both MSD and the distribution of directional change support the main role played by the myosin II as one of the driving forces for cytoskeletal fluctuations [29,32,65–69].

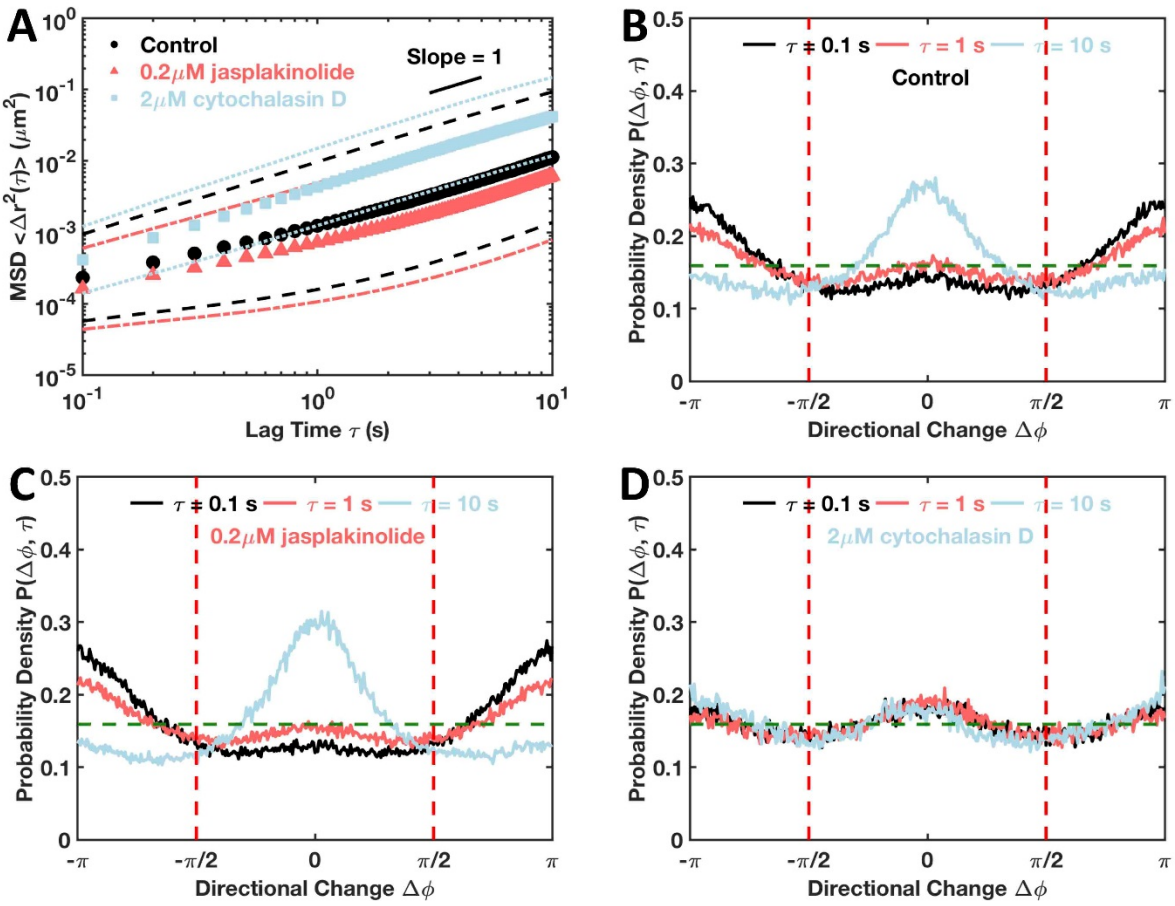

Figure 5.4. Actin network plays a major role in hindering fluctuations of fluorescent particle.
A) Population mean MSD with standard deviation of control cells (n = 194) and cells treated with 0.2 μM jasplakinolide (n = 190) and 2 μM cytochalasin D (n = 110). Circles indicate population means and dashed lines are standard deviations. Short black dashed line is a visual guide of slope one. **B-D)** Distribution of directional change at different lag times of control cells and cells treated with 2 μM cytochalasin D or 0.2 μM jasplakinolide respectively. Green dotted line marks the uniform distribution, indicating no directional preference which is characteristic of pure diffusion.

5.3.4 Actin network

C3H-10T1/2 cells were treated by two widely-used and actin-targeting chemicals to test the roles played by actin network on the fluctuations of bead-loaded fluorescent particles. Jasplakinolide induces actin polymerization and hyper-stabilizes filamentous actin [49]. Cytochalasin D binds to the barbed ends of actin filaments and inhibits the actin dynamics, both

the polymerization and depolymerization [50,51]. Its net effects on the density and stability of the actin network vary with other cellular conditions [51]. Therefore, cytochalasin D is able to specifically inhibit actin network dynamics and the resulting active driving forces.

Jasplakinolide results in statistically significant decreases of around two-fold in the MSD at all timescales (Figure 5.4A and Appendix IV: Figure S5.4 AB). In terms of the distribution of directional change, the treatment of jasplakinolide leads to a slight increase in the anti-persistent peak at all timescales, indicating stronger local confinements by higher concentrations of actin filaments. Interestingly, increase in the persistent peak is also observed at long timescales similar as the results of 25 μM blebbistatin (Figure 5.4C), thus suggesting a similar dual role as well. Hypothetically, actin filaments may serve as tracks for the persistent movement of local actin confinements, similar as its role as tracks for the active transportation of mitochondria in short length scales [33,70].

Cytochalasin D leads to statistically significant increase at every timescales, which is around 2-fold at the shortest timescale and increases to around 4-fold at the longest timescale (Figures 5.4 AB and Appendix IV: Figure S5.4 AB). The MSD results suggest a net increase in the volume of local confinements, probably due to a reduction in the density of the actin network. Surprisingly, the distributions of directional change at all timescales appear to be timescale-independent and close to the uniform distribution (Figure 5.4 D). Therefore, the particle movements after the treatment of cytochalasin D appear to be more diffusive in both measurements of MSD and distribution of directional change. Although both of the persistent and anti-persistent peaks are close to the uniform distribution, small peaks can be observed. This could be attributed to the slow convergence of the distribution of directional change [62] or

weaker confinement by other intracellular structures, like microtubules or endoplasmic reticulum.

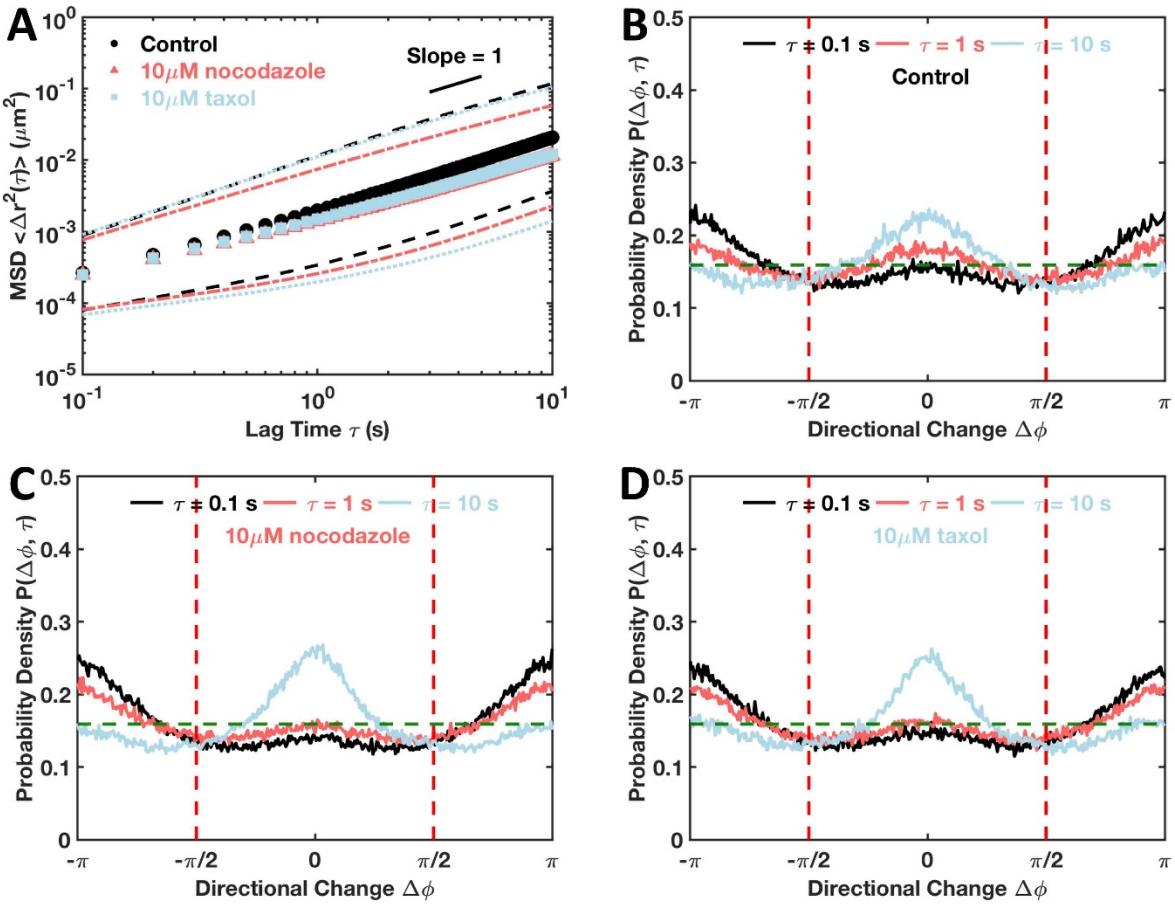

Figure 5.5. Microtubule network plays a minor role in determining fluctuations of fluorescent particle.
A) Population mean MSD with standard deviation of control cells (n = 183) and cells treated with 10 μM nocodazole (n = 251) and 10 μM taxol (n = 205). Circles indicate population means and dashed lines are standard deviations. Short black dashed line is a visual guide of slope one. **B-D)** Distribution of directional change at different lag times of control cells and cells treated with 10 μM nocodazole or 10 μM taxol respectively. Green dashed line marks the uniform distribution, indicating no directional preference which is characteristic of pure diffusion.

5.3.5 Microtubule network

We then tested the role played by the microtubule network. C3H-10T1/2 cells were treated with nocodazole and Taxol (also known as paclitaxel), two widely-used microtubule-targeting

drugs. Nocodazole de-stabilizes microtubule network [55]. Taxol prevents the microtubule network from its normal dynamical reorganization and leads to the formations of extensive and hyper-stable parallel arrays [56–58].

Interestingly, both nocodazole and taxol result in similar responses in both MSD and distribution of directional change, whose magnitudes are both small compared to actin-targeting treatments (Figure 5.5). Both drugs lead to a slight reduction of less than 2-fold in MSD at the longest timescale, which are both statistically significant (Figure 5.5 A and Appendix IV: Figure S5.5 AB). In terms of distributions of directional change, treatments of both chemicals result in decrease in persistent motions at short timescales and enhanced persistent motion at the longest timescale (Figure 5.5 B-D). While these results are interesting, and reflect the complexity of active processes in the cytoplasm, the overall small impacts on the MSDs suggest that the microtubule network serves as a minor contributor to both the confinement at short timescales and the active motion at long timescales.

5.4 Discussion

5.4.1 Glass beads load fluorescent particles directly into the cytoplasm

100 nm fluorescent particle is widely used as exogenous probe to measure intracellular mechanical properties. In this study, we studied whether we could modify the bead-loading procedure to deliver fluorescent particles inside cells, and whether the bead-loaded fluorescent particles probe the mechanical properties of the cytoplasm directly, or get trapped inside endocytosis vesicles. Confocal images across different z-planes of the cell show that the bead-loaded fluorescent particles disperse homogenously inside the cytoplasm (Figure 5.1 AB). However, the confocal images alone are not able to rule out the possibility that the observed

fluorescent particles are enclosed inside endocytosis vesicles and thus are screened from the bulk mechanical properties.

Chemical treatments targeting specific cytoskeletal components provide further tests on the subcellular localization of the bead-loaded fluorescent particles. First of all, earlier studies found that ATP depletion and blebbistatin have no effect on the movements of particles attached to membrane as measured by the magnetic twisting cytometry [27], while ATP depletion and blebbistatin result in significant decreases in the MSD of fluorescent particles microinjected directly into the cytoplasm [29,66]. In our study, the treatments of ATP depletion (Figure 5.2A) and blebbistatin (Figure 5.3A) result in statistically significant decrease in MSDs, which is consistent with the fluorescent particles microinjected directly into the cytoplasm. Secondly, the actin-targeting treatments (Figure 5.4A) lead to more significant changes in the MSDs than the microtubule-targeting treatments (Figure 5.5A). Such a difference in response is opposite from particles endocytosed [40] and endogenous probes [33], which can be actively transported along microtubule tracks. The bead-loaded fluorescent particles are thus not screened by lipid vesicles and are able to probe the mechanical properties of the actin network directly. Combining the confocal imaging and these results, we are able to conclude with confidence that glass beads are able to load 100 nm fluorescent particles directly into cytoplasm and probe the mechanical properties of the embedding cytoskeleton.

5.4.2 Minimize number of factors contributing to the heterogeneity of intracellular mechanical properties

Similar to earlier intracellular particle tracking studies, we also observed a wide-spread distribution of individual MSDs (Figure 5.1A). Although the variance in MSD is informative about the intracellular heterogeneities of the mechanical properties, other factors may also

contribute to the heterogeneity in MSDs and make accurate interpretation of the measurements challenging. Therefore, we tried to minimize these contributing factors, so that the variances in MSDs reflect to the largest extent the heterogeneity in mechanical properties. As an example, a recent study reported that the cell-cell contact influences the organization of actin network in a cell-type specific manner and differences in cellular mechanical properties were found across isolated cells, cells on the periphery of clusters and cells inside clusters [71]. In addition, as cells progress through different phases in the mitosis, cells undergo drastic changes in cytoskeletal organizations and therefore mechanical properties [71]. To minimize these two contributing factors of cell-cell contact and cell cycle, only isolated and well-spread cells were chosen for imaging in our study. Significant heterogeneity in the MSD can also arise from different boundary conditions between the particles contained in lipid vesicles and the cytoskeleton [27]. Glass beads are able to load the PEG-coated fluorescent particles directly into the cytoplasm, thus this issue should be circumvented. In future studies, it would further simplify interpreting the results by minimizing the cell-cell heterogeneity using adhesive micropatterns to standardize the cell morphology [72].

5.4.3 Mechanisms underlying the movement of bead-loaded fluorescent particles

The MSD of bead-loaded fluorescent particles is linear and appears to be diffusive in the control cells. Using treatments of different cytoskeletal drugs, insights into the complexity of the apparently diffusive motion in the cytoplasm was generated by analyzing the MSDs of bead-loaded fluorescent particles. Our results are consistent with a picture [28,29] in which the particles are trapped within the actin cytoskeleton, which confines their motion at short timescales, but due to ATP-dependent processes including molecular motors and cytoskeleton remodeling, the confining cage itself moves at the long timescales. The particle fluctuations are

therefore strongly affected when the ATP is depleted and the actin network is dissolved, and weakly affected by stabilizing the actin network, inhibiting the myosin II activities or by perturbing the microtubule network. Therefore, the particle movements are not as simple as they appeared to be. These results suggest that the mechanical environment of the fluorescent beads is strongly dominated by the actin cytoskeleton. This is different from the local viscoelastic environment around mitochondria, which we showed is dominated by the microtubule network [33]. Such a consistency with previous studies supports that bead-loaded fluorescent particles are probing the intracellular mechanical properties in the same way as microinjected and ballistically injected fluorescent particles [29,31].

In addition to MSD, we also calculated the distribution of directional change as a higher-dimension measurement on the particle trajectories, which indeed brings in deeper understanding into the underlying mechanisms. In control cells, the anti-persistent peak is consistent with the elastic nature of the actin microenvironment embedding the bead-loaded fluorescent particles as discussed. The persistent peak, on the other hand, is characteristic of ATP-dependent active forces. Interestingly, the distributions of directional change suggest that different roles played by myosin II and actin at different timescales, which are otherwise impossible to be revealed by MSD alone. Myosin II behaves as a driving force at short timescales and hypothetically also as an actin crosslinker, which affects random motion at long timescales. This is consistent with its known intracellular functions. Similarly, actin filaments act as local caging structures at short timescales, but support active and persistent movements at long timescales, most probably by serving as tracks for molecular motors. Using a combination of MSD and distribution of directional change, we showed that the movements of bead-loaded fluorescent particles, without

sophisticated techniques like active microrheology, are able to provide insights into the cytoskeletal dynamics.

5.4.5 Conclusion

Based on a combination of confocal imaging and the single particle tracking results under different chemical treatments, we are able to conclude with confidence that glass beads are able to load 100 nm fluorescent particles directly into cytoplasm and probe the mechanical properties of the embedding cytoskeleton, mainly the intracellular actomyosin network. Our preliminary results in MCF7 and MDA-MB-231 cell lines also suggest that bead loading, a mechanical delivery method, is a promising method to serve as a general delivery method of fluorescent particles across different cell types. Due to the simplicity of the technique and no requirements for specialized instrumentation and expertise, the bead loading technique is potentially very useful to make the measurements of intracellular mechanical properties using single particle tracking a routine procedure in more laboratories compared to microinjection and ballistic injection. Furthermore this technique can also be used to introduce quantum dots as well as functionalized beads within cells, which could be useful in many different types of assays [45,47,73].

REFERENCES

1. Orr AW, Helmke BP, Blackman BR, Schwartz MA. Mechanisms of Mechanotransduction Review. *Dev Cell.* 2006;10: 11–20. doi:10.1016/j.devcel.2005.12.006

2. Cattin CJ, Düggelin M, Martinez-Martin D, Gerber C, Müller DJ, Stewart MP. Mechanical control of mitotic progression in single animal cells. *Proc Natl Acad Sci.* 2015;112: 11258–11263. doi:10.1073/pnas.1502029112

3. Brangwynne CP, Koenderink GH, MacKintosh FC, Weitz DA. Cytoplasmic diffusion: Molecular motors mix it up. *J Cell Biol.* 2008;183: 583–587. doi:10.1083/jcb.200806149

4. Daniels BR, Hale CM, Khatau SB, Kusuma S, Dobrowsky TM, Gerecht S, et al. Differences in the Microrheology of Human Embryonic Stem Cells and Human Induced Pluripotent Stem Cells. *Biophys J.* 2010;99: 3563–3570. doi:10.1016/j.bpj.2010.10.007

5. Earls JK, Jin S, Ye K. Mechanobiology of Human Pluripotent Stem Cells. *Tissue Eng part B.* 2013;19: 420–430. doi:10.1089/ten.teb.2012.0641

6. Lv H, Li L, Sun M, Zhang Y, Chen L, Rong Y, et al. Mechanism of regulation of stem cell differentiation by matrix stiffness. *Stem Cell Res Ther.* 2015;6: 103. doi:10.1186/s13287-015-0083-4

7. Alibert C, Goud B, Manneville JB. Are cancer cells really softer than normal cells? *Biol Cell.* 2017;109: 167–189. doi:10.1111/boc.201600078

8. Spill F, Reynolds DS, Kamm RD, Zaman MH. Impact of the physical microenvironment on tumor progression and metastasis. *Curr Opin Biotechnol.* 2016;40: 41–48. doi:10.1016/j.copbio.2016.02.007

9. Lee GYH, Lim CT. Biomechanics approaches to studying human diseases. *Trends Biotechnol.* 2007;25: 111–118. doi:10.1016/j.tibtech.2007.01.005

10. Yu W, Sharma S, Gimzewski JK. Nanocytology as a potential biomarker for cancer. *Biomark Med.* 2017;11: 213–216. doi:10.2217/bmm-2017-0019

11. Krishnan R, Park JA, Seow CY, Lee PVS, Stewart AG. Cellular Biomechanics in Drug Screening and Evaluation: Mechanopharmacology. *Trends Pharmacol Sci.* 2016;37: 87–100. doi:10.1016/j.tips.2015.10.005

12. Zia RN. Active and Passive Microrheology: Theory and Simulation. *Annu Rev Fluid Mech.* 2018;50: 371–405. doi:10.1146/annurev-fluid-122316-044514

13. Binnig G, Quate CF. Atomic Force Microscope. *Phys Rev Lett.* 1986;56: 930–933. doi:10.1103/PhysRevLett.56.930

14. Lee LM, Liu AP. The Application of Micropipette Aspiration in Molecular Mechanics of Single Cells. *J Nanotechnol Eng Med.* 2014;5: 040902. doi:10.1115/1.4029936

15. Pachenari M, Seyedpour SM, Janmaleki M, Shayan SB, Taranejoo S, Hosseinkhani H. Mechanical properties of cancer cytoskeleton depend on actin filaments to microtubules content: Investigating different grades of colon cancer cell lines. *J Biomech.* 2014;47: 373–379. doi:10.1016/j.jbiomech.2013.11.020

16. Fabry B, Maksym GN, Butler JP, Glogauer M, Navajas D, Fredberg JJ. Scaling the microrheology of living cells. *Phys Rev Lett.* 2001;87: 1–4. doi:10.1103/PhysRevLett.87.148102

17. Guo M, Ehrlicher AJ, Mahammad S, Fabich H, Jensen MH, Moore JR, et al. The role of vimentin intermediate filaments in cortical and cytoplasmic mechanics. *Biophys J.* 2013;105: 1562–1568. doi:10.1016/j.bpj.2013.08.037

18. Guck J, Schinkinger S, Lincoln B, Wottawah F, Ebert S, Romeyke M, et al. Optical deformability as an inherent cell marker for testing malignant transformation and metastatic competence. *Biophys J.* 2005;88: 3689–3698. doi:10.1529/biophysj.104.045476

19. Byun S, Son S, Amodei D, Cermak N, Shaw J, Kang JH, et al. Characterizing deformability and surface friction of cancer cells. *Proc Natl Acad Sci.* 2013;110: 7580–7585. doi:10.1073/pnas.1218806110

20. Hou HW, Li QS, Lee GYH, Kumar AP, Ong CN, Lim CT. Deformability study of breast cancer cells using microfluidics. *Biomed Microdevices.* 2009;11: 557–564. doi:10.1007/s10544-008-9262-8

21. Wu P-H, Hale CM, Chen W-C, Lee JSH, Tseng Y, Wirtz D. High-throughput ballistic injection nanorheology to measure cell mechanics. *Nat Protoc.* 2012;7: 155–170. doi:10.1038/nprot.2011.436

22. Einstein A. On the Motion of Small Particles Suspended in a Stationary Liquid, as Required by the Molecular Kinetic Theory of Heat. *Ann Phys.* 1905;322: 549–560. doi:10.1002/andp.19053220806

23. Perrin JB. Brownian movement and molecular reality. *Ann Chim Phys VIII.* 1909;18: 5–114.

24. Mason TG, Weitz DA. Optical measurements of frequency-dependent linear viscoelastic moduli of complex fluids. *Phys Rev Lett.* 1995;74: 1250–1253. doi:10.1103/PhysRevLett.74.1250

25. Mason T, Ganesan K, van Zanten J, Wirtz D, Kuo S. Particle Tracking Microrheology of Complex Fluids. *Phys Rev Lett.* 1997;79: 3282–3285. doi:10.1103/PhysRevLett.79.3282

26. MacKintosh FC, Schmidt CF. Active cellular materials. *Curr Opin Cell Biol.* 2010;22:

29–35. doi:10.1016/j.ceb.2010.01.002

27. Van Citters KM, Hoffman BD, Massiera G, Crocker JC. The role of F-actin and myosin in epithelial cell rheology. *Biophys J.* 2006;91: 3946–3956. doi:10.1529/biophysj.106.091264

28. Hoffman BD, Massiera G, Van Citters KM, Crocker JC. The consensus mechanics of cultured mammalian cells. *Proc Natl Acad Sci.* 2006;103: 10259–10264. doi:10.1073/pnas.0510348103

29. Guo M, Ehrlicher AJ, Jensen MH, Renz M, Moore JR, Goldman RD, et al. Probing the stochastic, motor-driven properties of the cytoplasm using force spectrum microscopy. *Cell.* 2014;158: 822–832. doi:10.1016/j.cell.2014.06.051

30. Mizuno D, Tardin C, Schmidt CF, MacKintosh FC. Nonequilibrium mechanics of active cytoskeletal networks. *Science.* 2007;315: 370–373. doi:10.1126/science.1134404

31. Gupta SK, Guo M. Equilibrium and out-of-equilibrium mechanics of living mammalian cytoplasm. *J Mech Phys Solids.* 2017;107: 284–293. doi:10.1016/j.jmps.2017.07.007

32. Smelser AM, Macosko JC, O'Dell AP, Smyre S, Bonin K, Holzwarth G. Mechanical properties of normal versus cancerous breast cells. *Biomech Model Mechanobiol.* 2015;14: 1335–1347. doi:10.1007/s10237-015-0677-x

33. Xu W, Alizadeh E, Prasad A. Force Spectrum Microscopy Using Mitochondrial Fluctuations of Control and ATP-Depleted Cells. *Biophys J.* 2018;114:2933-2944 doi:10.1016/j.bpj.2018.05.002

34. Gal N, Lechtman-Goldstein D, Weihs D. Particle tracking in living cells: A review of the mean square displacement method and beyond. *Rheol Acta.* 2013;52: 425–443. doi:10.1007/s00397-013-0694-6

35. Agus DB, Alexander JF, Arap W, Ashili S, Aslan JE, Austin RH, et al. A physical sciences network characterization of non-tumorigenic and metastatic cells. *Sci Rep.* 2013;3. doi:10.1038/srep01449

36. Wirtz D. Particle-tracking microrheology of living cells: principles and applications. *Annu Rev Biophys.* 2009;38: 301–26. doi:10.1146/annurev.biophys.050708.133724

37. Valentine MT, Perlman ZE, Gardel ML, Shin JH, Matsudaira P, Mitchison TJ, et al. Colloid Surface Chemistry Critically Affects Multiple Particle Tracking Measurements of Biomaterials. *Biophys J.* 2004;86: 4004–4014. doi:10.1529/biophysj.103.037812

38. Lee JSH, Panorchan P, Hale CM, Khatau SB, Kole TP, Tseng Y, et al. Ballistic intracellular nanorheology reveals ROCK-hard cytoplasmic stiffening response to fluid flow. *J Cell Sci.* 2006;119: 1760–1768. doi:10.1242/jcs.02899

39. Gal N, Weihs D. Intracellular mechanics and activity of breast cancer cells correlate with

metastatic potential. *Cell Biochem Biophys.* 2012;63: 199–209. doi:10.1007/s12013-012-9356-z

40. Goldstein D, Elhanan T, Aronovitch M, Weihs D. Origin of active transport in breast-cancer cells. *Soft Matter.* 2013;9: 7167–7173. doi:10.1039/c3sm50172h

41. Wennmalm S, Simon SM. Studying Individual Events in Biology. *Annu Rev Biochem.* 2007;76: 419–446. doi:10.1146/annurev.biochem.76.062305.094225

42. McNeil PL, Warder E. Glass beads load macromolecules into living cells. *J Cell Sci.* 1987;88 (Pt 5): 669–678.

43. Morisaki T, Lyon K, DeLuca KF, DeLuca JG, English BP, Zhang Z, et al. Real-time quantification of single RNA translation dynamics in living cells. *Science.* 2016;0899: aaf0899. doi:10.1126/science.aaf0899

44. Hayashi-Takanaka Y, Yamagata K, Wakayama T, Stasevich TJ, Kainuma T, Tsurimoto T, et al. Tracking epigenetic histone modifications in single cells using Fab-based live endogenous modification labeling. *Nucleic Acids Res.* 2011;39: 6475–6488. doi:10.1093/nar/gkr343

45. Emerson NT, Hsia C-H, Rafalska-Metcalf IU, Yang H. Mechanodelivery of nanoparticles to the cytoplasm of living cells. *Nanoscale.* 2014;6: 4538. doi:10.1039/c3nr06468a

46. Steinhardt RA, Bi G, Alderton JM. Cell Membrane Resealing by a Vesicular Mechanism Similar to Neurotransmitter Release. *Science.* 1994;263: 390–393.

47. Etoc F, Vicario C, Lisse D, Siaugue J-M, Piehler J, Coppey M, et al. Magnetogenetic Control of Protein Gradients Inside Living Cells with High Spatial and Temporal Resolution. *Nano Lett.* 2015;15: 3487–3494. doi:10.1021/acs.nanolett.5b00851

48. Tseng Y, Kole TP, Wirtz D. Micromechanical Mapping of Live Cells by Multiple-Particle-Tracking Microrheology. *Biophys J.* 2002;83: 3162–3176. doi:10.1016/S0006-3495(02)75319-8

49. Spector I, Braet F, Shochet NR, Bubb MR. New anti-actin drugs in the study of the organization and function of the actin cytoskeleton. *Microsc Res Tech.* 1999;47: 18–37. doi:10.1002/(SICI)1097-0029(19991001)47:1<18::AID-JEMT3>3.0.CO;2-E

50. Cooper JA. Effects of cytochalasins and phalloidin on actin. *J Cell Biol.* 1987;105: 1473–1478.

51. Shoji K, Ohashi K, Sampei K, Oikawa M, Mizuno K. Cytochalasin D acts as an inhibitor of the actin-cofilin interaction. *Biochem Biophys Res Commun.* 2012;424: 52–57. doi:10.1016/j.bbrc.2012.06.063

52. Shu S, Liu X, Korn ED. Blebbistatin and blebbistatin-inactivated myosin II inhibit myosin II-independent processes in Dictyostelium. *Proc Natl Acad Sci.* 2005;102: 1472–

1477. doi:10.1073/pnas.0409528102

53. Kovács M, Tóth J, Hetényi C, Málnási-Csizmadia A, Seller JR. Mechanism of blebbistatin inhibition of myosin II. *J Biol Chem.* 2004;279: 35557–35563. doi:10.1074/jbc.M405319200

54. Ramamurthy B, Yengo CM, Straight AF, Mitchison TJ, Sweeney HL. Kinetic mechanism of blebbistatin inhibition of nonmuscle myosin IIB. *Biochemistry*. 2004;43: 14832–14839. doi:10.1021/bi0490284

55. Vasquez RJ, Howell B, Yvon AM, Wadsworth P, Cassimeris L. Nanomolar concentrations of nocodazole alter microtubule dynamic instability in vivo and in vitro. *Mol Biol Cell.* 1997;8: 973–85.

56. SCHIFF PB, FANT J, HORWITZ SB. Promotion of microtubule assembly in vitro by taxol. *Nature.* 1979;277: 665–667. doi:10.1038/277665a0

57. Horwitz SB. Taxol (paclitaxel): mechanisms of action. *Ann Oncol.* 1994;5 Suppl 6: S3-6.

58. Kingston DGI. Tubulin-interactive natural products as anticancer agents. *Journal of Natural Products.* 2009. pp. 507–515. doi:10.1021/np800568j

59. Ishikawa T, Bao-Li Z, Hitoshi M. Effect of sodium azide on the metabolic activity of cultured fetal cells. *Toxicol Ind Health.* 2006;22: 337–341.

60. Wick AN, Drury DR, Nakada HI, Wolfe JB. Localization of the primary metabolic block produced by 2-deoxyglucose. *J Biol Chem.* 1957;224: 963–969.

61. Jaqaman K, Loerke D, Mettlen M, Kuwata H, Grinstein S, Schmid SL, et al. Robust single-particle tracking in live-cell time-lapse sequences. *Nat Methods.* 2008;5: 695–702. doi:10.1038/nmeth.1237

62. Burov S, Tabei SMA, Huynh T, Murrell MP, Philipson LH, Rice SA, et al. Distribution of directional change as a signature of complex dynamics. *Proc Natl Acad Sci.* 2013;110: 19689–19694. doi:10.1073/pnas.1319473110

63. Gibbons JD, Chakraborti S. Nonparametric statistical inference. Chapman & Hall/Taylor & Francis; 2011.

64. Hollander M, Wolfe DA, Chicken E. Nonparametric statistical methods.

65. Mackintosh FC, Levine AJ. Nonequilibrium mechanics and dynamics of motor-activated gels. *Phys Rev Lett.* 2008;100: 1–4. doi:10.1103/PhysRevLett.100.018104

66. Fodor É, Guo M, Gov NS, Visco P, Weitz D a., van Wijland F. Activity-driven fluctuations in living cells. *Europhysics Lett.* 2015;110: 48005. doi:10.1209/0295-5075/110/48005

67. Gallet F, Arcizet D, Bohec P, Richert A. Power spectrum of out-of-equilibrium forces in living cells: amplitude and frequency dependence. *Soft Matter*. 2009;5: 2947–2953. doi:10.1039/b901311c

68. Lau AWC, Hoffman BD, Davies A, Crocker JC, Lubensky TC. Microrheology, Stress Fluctuations, and Active Behavior of Living Cells. *Phys Rev Lett*. 2003;91: 198101. doi:10.1103/PhysRevLett.91.198101

69. Mizuno D, Tardin C, Schmidt CF, Mackintosh FC. Nonequilibrium mechanics of active cytoskeletal networks. *Science*. 2007;315: 370–3. doi:10.1126/science.1134404

70. Saxton WM, Hollenbeck PJ. The axonal transport of mitochondria. *J Cell Sci*. 2012;125: 2095–2104. doi:10.1242/jcs.053850

71. Li M, Dang D, Liu L, Xi N, Wang Y. Atomic force microscopy in characterizing cell mechanics for biomedical applications: A review. *IEEE Trans Nanobioscience*. 2017;16: 523–540. doi:10.1109/TNB.2017.2714462

72. Slater JH, Culver JC, Long BL, Hu CW, Hu J, Birk TF, et al. Recapitulation and Modulation of the Cellular Architecture of a User-Chosen Cell of Interest Using Cell-Derived, Biomimetic Patterning. *ACS Nano*. 2015;9: 6128–6138. doi:10.1021/acsnano.5b01366

73. Stewart MP, Sharei A, Ding X, Sahay G, Langer R, Jensen KF. In vitro and ex vivo strategies for intracellular delivery. *Nature*. 2016;538: 183–192. doi:10.1038/nature19764

CHAPTER 6: THE CONCLUDING CHAPTER

6.1 Conclusion

In this chapter, I conclude the dissertation with a brief summary of some of the most interesting questions, in my view, that stem out of the studies presented in earlier chapters, and discuss potential future work to address these questions.

6.2 Conclusions from Chapter 2: Loads Bias Genetic and Signaling Switches in Synthetic and Natural Systems

The study presented in Chapter 2 depends heavily on nonlinear ODE models describing the behaviors of the synthetic and natural switches. We used bifurcation analyses and numerical solutions of the ODEs to characterize how loads (retroactivity) are able to impact the properties of the two switches. It would be helpful if we can generalize our methodology to study how loads can change the properties of a broader range of synthetic circuits in terms of number of steady states. Chemical reaction network theory (CRNT) established several theorems that are able tells us the number of steady states of an ODE model when certain conditions are met [1]. We could, in theory, adapt the CRNT to study the effects of loads on the number of steady states of some synthetic circuits satisfying the conditions required by the CRNT. This could help us to reach more general conclusions and designing principles to assemble larger networks from characterized synthetic circuits.

The structures of natural circuits are typically more complex than the synthetic circuits. However, the production of proteins is costly to cells and there should be potential benefits associated with the additional complexity from an evolutionary viewpoint. Implied by our study presented in chapter 2, the additional complexity found in natural networks may hypothetically

play roles in reducing the effects of loads to make the natural networks more robust under various conditions. Further studies are needed to test this hypothesis. If it is true, new design principles may be learnt to construct synthetic circuits that are more robust against the presence of loads among other perturbations.

6.3 Conclusions from Chapter 3: A Genetic Toggle Switch in Plants

6.3.1 Future works on the two factors uncharacterized in the transient expression system

As described in chapter 3, there are two factors uncharacterized in the transient expression system developed to measure quantitative response functions of repressor-promoter pairs in protoplasts [2]: the multiplicative noise in the protoplast system, and the positional effects of random stable genetic integration (T-DNA) of the genetic circuits in plants. A factor ranging from about 0.2 to 2-fold was found in absolute parameter values estimated between the protoplast and stably transgenic plants, as a result of these two factors. Such a factor impairs our ability to quantitatively predict the behaviors of toggle switch designes constructed from these repressor-promoter pairs. Therefore, it is particularly useful to characterize or standardize these two random factors in future work to improve the engineering-based methodology for plant synthetic biology.

The multiplicative noise describes the batch variability (protoplast prepared on different days) as supported by experimental results [2]. We were not able identify the origin of the batch variability. We hypothesized that different compositions of differentiated plant cells in each batch of protoplast preparation may contribute to such a batch variability [2]. In future works, we could attempt to reduce such a variability in protoplast compositions using flow cytometry. We could at first attempt to find the signatures of healthy protoplasts in flow cytometry and take advantage of cell sorting to create populations of pre-determined number of healthy protoplasts

for the original transient-expression assays as described in [2]. This should reduce the variability arising from the number of healthy protoplasts. In addition, we could exploit cell sorting further to create more homogenous protoplast subpopulations in terms of cell types, distinguished by protoplast properties like cell sizes and chlorophyll contents. The relation between the cell types and behaviors of synthetic parts can then be better characterized and understood for future applications. Furthermore, the variability in protoplast compositions could be reduced by defining a standard composition of these homogenous protoplast subpopulations.

Moreover, the next generation of the transient-expression assays [2] may be fully developed on the basis of flow cytometry, which is able to measure single-protoplast behaviors of the repressor-promoter pairs, instead of bulk measurements on the entire population inside one well. This could reduce the variability in the compositions of differentiated plant cells as mentioned earlier. In addition, the distribution of single-protoplast behavior could be informative on the plasmid copy numbers in each protoplast by comparing to the protoplasts prepared from stable transgenic plants as in [2]. However, the dual-luciferase output used in the transient-expression assays is not yet compatible with the flow cytometry. This technical challenge could be overcome by introducing fluorescent proteins into the transient-expression assays as outputs. A major challenge is the strong auto-fluorescence of the chlorophylls in leaf protoplasts, which dwarfs even high expression levels of Green Fluorescent Protein as shown in our unpublished preliminary results and other studies [3,4]. This could be potentially solved by using fluorescent proteins in frequencies that chlorophyll auto-fluorescence is relatively weak. In addition, the amount of chlorophyll could be measured at independent frequencies, its auto-fluorescence in the frequencies of interests calculated using their characterized absorption spectra and subtracted to generate more accurate measurements of the amount of fluorescent proteins. Root protoplasts

could be used as well, which do not have chlorophyll. However, the tissue-specific effects may need to be characterized and taken into account as discussed in chapter 3 and in section 6.3.3.

In general, it is challenging to integrate the transient-expression protoplasts assays with flow cytometry. As suggested by our preliminary results and the literature [3,4], the large amount of debris produced during the protoplast preparation may produce false positives. Efforts are needed to optimize the protoplast preparation protocol and gating strategies to filter the protoplasts from the debris. In addition, protoplasts, plant cells without the protections from cell wall, are very fragile. The configurations of the flow cytometer need to be optimized so that forces acting on the protoplasts are minimized and protoplast bursting during the process can be avoided or reduced. However challenging, the integration of flow cytometry into the transient-expression protoplasts assays may prove fruitful to reduce the variability in the transient-expression protoplasts assays, to gain single protoplast resolutions and to improve the engineering-based methodology for plant synthetic biology.

The positional effects were produced by random integration of the genetic circuits into the plant chromosome using Agrobacterium-mediated transformation to produce transgenic plants [2]. CRISPR/Cas9, a recently developed tool to introduce site-specific double-stranded DNA break, may help us to characterize and standardize the positional effects. A recent study reported that CRISPR/Cas9 is able to integrate a 1.8 kb resistance cassette into the ADH1 locus of *A. thaliana* by homologous recombination [5]. Therefore, it is promising that CRISPR/Cas9 is able to integrate the genetic circuits into a specific pre-determined locus of the plant chromosome. A standard locus can then be chosen for all the integration of genetic circuits and the positional effects can then be characterized and standardized by comparing the parameter estimated from

the transient-expression protoplast assays and protoplasts prepared from stable transgenic plants as in [2].

6.3.2 Future work on the tools developed for plant synthetic biology

In chapter 3, we optimized a quantitative imaging protocol to characterize the behaviors of toggle switches in shoots and leaves of individual plants. The luciferase camera utilized in chapter 3 is able to capture single photons from plants quantitatively. However, a basic limitation is that luminescence images are essentially two-dimensional (2D) but the plant is, of course, a three-dimensional (3D) structure. Plant roots in Arabidopsis are relatively more spread-out in the agar gel and more transparent, therefore, they should be more accurately represented in the 2D imaging than leaves. On the other hand, overlap between leaves are inevitable despite of the delicate leaf arrangements, especially when plants grow larger. Since plant leaves are less transparent, these overlaps may lead to underestimation of the luciferase activities in leaves and thus inaccurate evaluations of the toggle switch tested experimentally. With recent advances in 3D scanning in plant biology [6], it is possible to develop a system for 3D scanning of luciferase activities in plant leaves.

The image processing software developed in chapter 3 is fully supervised visually by the operating researcher at each step to improve the accuracy and minimize the artifacts potentially introduced, making this step relatively time-consuming in the data analysis. With the recent developments in machine learning and computer vision, the image processing could be fully automated with careful validations. Thus, the luciferase data could be processed and analyzed with previous results immediately after the imaging. Prompt adjustments to the ongoing experiments could be made, for example, the experimental duration could be extended if the response is slower than anticipated.

The current version of MCMC, as used in chapter 3, fits to the population mean of the luminescence of the entire tissue, while richer information may be available in the distribution of pixel intensities that is not fully utilized now. As shown in single-cell bacterial or yeast studies, the whole distribution of intensities may convey valuable information about the stochasticity of the synthetic circuits [7], or about the heterogeneity in the host cells in our system. In future work, the MCMC could be improved in this direction. A complication that needs to be overcome is that the sources of the stochasticity in the distribution of pixel intensities are not well understood, and they probably include many other factors apart from intrinsic noise due to stochastic chemical reactions. Some of these factors will be discussed in more details in the following section.

6.3.3 Challenges and opportunities in plant synthetic biology

Using the image processing software developed in chapter 3, we are also able to approximately measure the growth rate of plants under different treatments given the limitation of 2D images as discussed above. We found that the plants with the toggle switch in its HIGH state generally grow slower (data not shown) than the ones in the LOW state. This could be explained by the metabolic burdens associated with the HIGH state, when both the repressor and the luciferase are expressed in large amount [8]. In addition, cellular ATP was converted to luminescence by the luciferase during the imaging. Therefore, significant cellular resources are possibly diverted from normal growth when the toggle switch is in its HIGH state. Mathematically, this leads to a decrease in the effective degradation rate constant (a sum of protein degradation rate and dilutions due to growth, expansion and division). In future works, this could be exploited to design circuits that are more robust when realizing functionalities of interest. Similarly ideas have been tested experimentally in bacterial systems [8].

Plants are multi-cellular differentiated organisms, which have heterogeneity not only on cell level (as discussed in section 6.3.1) but also on tissue levels. In chapter 3, we found that the shoots and roots in same plants generally behave in different manners, which suggests tissue-specific influences on the behaviors of synthetic circuits. We also observed interesting leaf-to-leaf variabilities and even variabilities across different subregions of one leaf in the behaviors of toggle switches. Different leaves may be at different developmental stages and different subregions may correspond to various differentiated tissues. All these variabilities could be understood, in part, by different gene expression profiles in differentiated tissues, which may result in different contextual effects on the same toggle switch designs. There may be differences in terms of transportation and global parameters (like rates of transcription, translation and degradation).

These possible contextual effects on the behaviors of toggle switches brings back the discussion on the limitations of the validity of the assumption of modularity at question. In addition to the effects of retroactivity studied in chapter 2, these observed contextual effects also emphasize the limitations of the useful analogy to electrical engineering (section 1.1.1), especially when we are trying to expand the predictive power of synthetic biology to multi-cellular differentiated organisms.

Although these contextual effects pose additional challenges to construct reliably functional genetic circuits, they may provide more aspects to be engineered for novel functionalities as well. Synthetic circuits with tissue-specific behaviors can be engineered based on accumulating knowledge on these contextual effects. For example, it is more economical to make biofuel production more in shoots and less in roots, which are hard to harvest. In summary, all these complexities associated with multi-cellular differentiated organisms are not only

challenges, but also promising and unique opportunities of plants, compared with other hosts currently used in synthetic biology.

6.4 Conclusions from Chapter 4: Force Spectrum Microscopy Using Mitochondrial Fluctuations of Control and ATP Depleted Cells

In chapter 4, we hypothesized that the active forces driving mitochondrial fluctuations may be generated by motor proteins like dynein, kinesin and myosins (~~e.g.,~~ myosins V and VI, but not myosin II). Furthermore, we can hypothesize that the force spectra of mitochondrial fluctuations carry important information about these molecular motors, for example relative abundances and properties like dragging force. Indeed, the active force spectra in cancer cells with different metastatic potential were reported to be significantly different [9]. This hypothesis can be explored using cell lines with relevant mutants or pharmaceutical drugs targeting these molecular motors.

We also found that the frequency-dependent spectrum of active forces acting on mitochondria in C3H-10T1/2 cells is almost same as the one of A7 cells measured by other researchers [9]. Such a similarity in active force spectra across different cell lines leads to interesting questions. One possibility is that the active force spectra acting on mitochondria are conserved, at least in the same species, which may be necessary for some cellular functionalities under the pressure of evolutionary selection, like the effectiveness in transporting mitochondria around to maintain the energy homeostasis. Furthermore, it is interesting to explore whether these force spectra are organelle-specific, e.g., if the force spectrum of lipid vesicles is different from the one measured for mitochondria. These hypotheses can be tested by applying the method based on mitochondrial fluctuations to more systems and generalize the method to track and study other endogenous organelles, like peroxisomes, lysosomes and lipid vesicles.

6.5 Conclusions from Chapter 5: Glass Beads Load 100 nm Fluorescent Particles into Live Cells to Probe Intracellular Mechanical Properties

6.5.1 Further optimizations of the bead loading protocol

In chapter 5, we reported that glass beads are able to load 100 nm fluorescent particles directly into the cytoplasm. In microrheology, larger fluorescent particles (200 nm, 500 nm or even micron-sized particles) are also widely used. It is therefore valuable to test the upper size limit of the bead loading to deliver fluorescent particles into the cytoplasm.

In chapter 5, we briefly mentioned that the mechanical disruption induced by bead loading on the cellular membrane can reseal promptly depending on the extracellular calcium level [10]. Therefore, it is possible to optimize the calcium level in the growth medium used after the bead loading, so that the resealing of the cellular membranes is facilitated. This may improve the bead loading to deliver larger fluorescent particles in larger quantities.

Comparing to traditional particle delivery methods (i.e., microinjection and ballistic injection), a significant advantage of bead loading is its low requirements on instruments and expertise to operate. However, this introduce additional issues. Mainly the consistency and repeatability of a same researcher or researchers across different groups may be lower than the two traditional methods. Simple and inexpensive devices can be developed in future works to improve this, for example acoustic rocking or magnetic rocking, or even ultrasound-guided bead loading.

6.5.2 The fate of particles loaded into the cytoplasm

Fluorescent particles, even coated with PEG, are foreign to the cytoplasmic environment. The fate of these particles delivered into the cytoplasm is largely unknown. Important questions, like whether they are entirely immune to the exocytosis system, are still left unanswered. If the

answer is no, what's the characteristic timescale of their recognition by the exocytosis system? The particles enclosed in the exocytotic vesicles probe different mechanical properties and thus complicate the interpretation of results. Furthermore, what is the mechanisms leading to the recognition by the exocytosis system? The answer to this question may help us to engineer better surface coating of the fluorescent particle to help them stay free in the cytoplasm for a longer period, which enables long-time tracking across cell generations.

6.6 Common Conclusions from chapters 4 and 5

6.6.1 The trajectory-based analysis

In chapter 4 and 5, we discussed the limitations of ensemble-average and time-average based measurements, including MSD, creep compliance and distribution of directional change, on both mitochondrial fluctuations and particle movements. Interesting information about the trajectory heterogeneities would be obscured by the ensemble averaging. For example, there may be different movement states (the persistent strokes of active forces for example) and the mitochondria/particle may explore different states along one trajectory. Therefore, it would provide deeper understanding on the underlying mechanisms driving the movements if we are able to dissect the temporal trajectory into segments of different movement modes. Such a dissection can potentially be achieved by some advanced methods developed recently, including rolling window based methods [11] and hidden Markov Model (HMM) based methods [12–14]. These methods were developed to mainly separate apart the diffusive motion from directed transportation. In our results, there are also the active yet random fluctuations, whose direction is random with lower persistence when compared to the directed transportation. Our preliminary results (data not shown) showed that these developed methods are not able to separate the active fluctuations accurately yet. This trajectory-based analysis will be part of our future work. We

will try to develop a HMM based method modified to integrate information from multiple timescales, similar to the idea of so called multi-rate or multi-scale HMM [15,16].

6.6.2 The relationship between the mechanical properties measured by mitochondria and fluorescent particles.

Combining the results in chapters 4 and 5, the intracellular cytoskeletal network forms a weakly elastic microenvironment that is liquidized by ATP-dependent processes. The movements of both mitochondria and fluorescent particles are both driven by ATP-dependent processes. This is consistent with the ubiquitous role of the active yet random forces [9,17]. In addition, our results suggest that mitochondria and fluorescent particles may not probe the same aspects of the intracellular mechanical properties. As shown in chapter 4, mitochondrial fluctuations are influenced by both microtubules and actin networks with the microtubule network playing a dominating role. While shown in chapter 5, the movements of fluorescent particles are mainly determined by the intracellular actomyosin network and the microtubule network plays a relatively minor and possibly indirect role. There are also differences in subcellular localizations between the mitochondria and fluorescent particles. The football-like mitochondria tracked in chapter 4 are relatively rare in the subcellular regions close to nuclei and more abundant in cell peripheries. On the other hand, the intracellular fluorescent particles are more located in the peri-nuclei region and are less represented in the peripheries as in our study presented in chapter 5 and other studies [18]. There are also differences between the two kinds of probes in other aspects as discussed in more details in chapter 4. Further work is therefore required to generate a more complete understanding of the cellular cytoskeleton in different subcellular regions, as measured by fluorescent particles and mitochondria as well as other

endogenous organelles including peroxisomes, lysosomes and lipid vesicles. Ideally, both the fluorescent particles and endogenous organelles should be tracked in the same cells.

6.6.3 Better control of the chemical treatments

When we were carrying out different treatments using chemicals and pharmaceutical drugs, there is generally a lack of precise control over these treatments on the single-cell level. All the cells in one petri dish were started with treatment at a same time. They were then imaged in a variable duration of 2~3 hr. The general assumption is that the cells should have reached their new steady state after an initial incubation time (ATP depletion for 2 hour and cytoskeleton-targeting chemicals for 30 min). However, this might not be true since cytoskeletal network is a complex network and multiple characteristic times may exist. Therefore, different cells imaged at different time points may not constitute a uniform population and this may incur extra challenges to interpret the treatment results. It is even more complicated taking into account of the hard-to-characterize side-effects of the drugs and chemicals used. In addition, cell cycles are generally not synchronized.

Multiple tools developed recently may help to improve our capability to control these complex factors, including optogenetic tools and microfluidic devices. Optogenetic control of RhoA was reported to enable real-time and local activations of RhoA on a single-cell level [19]. In Mak et al. [20], a microfluidic chamber was used to culture the cells under study and growth media was exchanged continuously in microfluidic channels. Such a chamber can be paralleled into a 96-well plate format with a drug mixing module integrated. Precise treatments on a single-cell level can then be achieved if we study just one cell per well. Furthermore, such a microfluidic unit can be integrated with single cell culture array reported earlier [21], so that

there is only one cell per well. This would also enable long-term study on single cells with careful indexing of wells and automated stage control.

6.6.4 A potential interface between the mechanobiology and synthetic biology

As discussed earlier, the methodology used in chapters 4 and 5 is mainly top-down. Due to the current limitations in the experimental system as discussed in section 6.6.3, we lack the ability to precisely control the underlying contributing factors. Therefore, it is sometimes challenging to interpret the experimental results, especially since the cytoskeleton consists of hundreds of proteins that interact with each other.

Designed and constructed to perform designed biological functions, synthetic circuits may endow us with more power to manipulate and study intracellular mechanical properties. For example, toggle switches, as the one constructed in chapter 3, can be integrated into mammalian cells to control the expressions of dynein, one of the molecular motors hypothesized to drive the mitochondrial fluctuations. Then, we will be able to measure the force spectra of mitochondria in high or low expression levels of dynein. In addition, we can use fluorescent proteins as a proxy to the expression level of dynein. Such a system would establish a quantitative response function with the expression levels of dynein as the input and the intracellular mechanical properties as the output, thereby yielding deeper mechanistic insight into the mechanical properties of mammalian cells.

REFERENCES

1. Shinar G, Feinberg M. Structural Sources of Robustness in Biochemical Reaction Networks. *Science*. 2010;327: 1389–1391.

2. Schaumberg KA, Antunes MS, Kassaw TK, Xu W, Zalewski CS, Medford JI, et al. Quantitative characterization of genetic parts and circuits for plant synthetic biology. *Nat Meth.* 2016;13: 94–100.

3. Grønlund JT, Eyres A, Kumar S, Buchanan-Wollaston V, Gifford ML. Cell specific analysis of Arabidopsis leaves using fluorescence activated cell sorting. *J Vis Exp*. 2012; 1–7. doi:10.3791/4214

4. Bargmann BOR, Birnbaum KD. Fluorescence activated cell sorting of plant protoplasts. *J Vis Exp*. 2010; 1–5. doi:10.3791/1673

5. Schiml S, Fauser F, Puchta H. The CRISPR/Cas system can be used as nuclease for in planta gene targeting and as paired nickases for directed mutagenesis in Arabidopsis resulting in heritable progeny. *Plant J.* 2014;80: 1139–1150. doi:10.1111/tpj.12704

6. Paulus S, Schumann H, Kuhlmann H, Léon J. High-precision laser scanning system for capturing 3D plant architecture and analysing growth ofcereal plants. *Biosyst Eng.* 2014;121: 1–11. doi:10.1016/j.biosystemseng.2014.01.010

7. Kærn M, Elston TC, Blake WJ, Collins JJ. Stochasticity in gene expression: From theories to phenotypes. *Nat Rev Genet.* 2005;6: 451–464. doi:10.1038/nrg1615

8. Tan C, Marguet P, You L. Emergent bistability by a growth-modulating positive feedback circuit. *Nat Chem Biol.* 2009;5: 842–848. doi:10.1038/nchembio.218

9. Guo M, Ehrlicher AJ, Jensen MH, Renz M, Moore JR, Goldman RD, et al. Probing the stochastic, motor-driven properties of the cytoplasm using force spectrum microscopy. *Cell.* 2014;158: 822–832. doi:10.1016/j.cell.2014.06.051

10. Steinhardt RA, Bi G, Alderton JM. Cell Membrane Resealing by a Vesicular Mechanism Similar to Neurotransmitter Release. *Science.* 1994;263: 390–393.

11. Arcizet D, Meier B, Sackmann E, Rädler JO, Heinrich D. Temporal analysis of active and passive transport in living cells. *Phys Rev Lett.* 2008;101: 1–4. doi:10.1103/PhysRevLett.101.248103

12. Monnier N, Barry Z, Park HY, Su KC, Katz Z, English BP, et al. Inferring transient particle transport dynamics in live cells. *Nat Methods.* 2015;12: 838–840. doi:10.1038/nmeth.3483

13. Das R, Cairo CW, Coombs D. A hidden Markov model for single particle tracks quantifies

dynamic interactions between LFA-1 and the actin cytoskeleton. *PLoS Comput Biol.* 2009;5. doi:10.1371/journal.pcbi.1000556

14. Persson F, Lindén M, Unoson C, Elf J. Extracting intracellular diffusive states and transition rates from single-molecule tracking data. *Nat Methods.* 2013;10: 265–269. doi:10.1038/nmeth.2367

15. Cetin O, Ostendorf M. Multi-rate hidden Markov models and their application to machining tool-wear classification. 2004 IEEE International Conference on Acoustics, Speech, and Signal Processing. IEEE; p. V-837-40. doi:10.1109/ICASSP.2004.1327241

16. Leos-Barajas V, Gangloff E, Adam T, Langrock R, van Beest FM, Nabe-Nielsen J, et al. Multi-scale modeling of animal movement and general behavior data using hidden Markov models with hierarchical structures. 2017; 1–28. doi:10.1007/s13253-017-0282-9

17. Brangwynne CP, Koenderink GH, MacKintosh FC, Weitz DA. Cytoplasmic diffusion: Molecular motors mix it up. *J Cell Biol.* 2008;183: 583–587. doi:10.1083/jcb.200806149

18. Wu P-H, Hale CM, Chen W-C, Lee JSH, Tseng Y, Wirtz D. High-throughput ballistic injection nanorheology to measure cell mechanics. *Nat Protoc.* 2012;7: 155–170. doi:10.1038/nprot.2011.436

19. Oakes PW, Wagner E, Brand CA, Probst D, Linke M, Schwarz US, et al. Optogenetic control of RhoA reveals zyxin-mediated elasticity of stress fibres. *Nat Commun.* 2017;8. doi:10.1038/ncomms15817

20. Mak M, Kamm RD, Zaman MH. Impact of Dimensionality and Network Disruption on Microrheology of Cancer Cells in 3D Environments. *PLoS Comput Biol.* 2014;10: e1003959. doi:10.1371/journal.pcbi.1003959

21. Carlo D Di, Wu LY, Lee LP. Dynamic single cell culture array. *Lab Chip.* 2006;6: 1445. doi:10.1039/b605937f

APPENDIX I: SUPPLEMENTARY INFORMATION FOR CHAPTER 2

7.1 Genetic Toggle Switch

7.1.1 Derivation and Dedimensionalization of Genetic Toggle Switch

Let $[R_1]$, $[R_2]$ be the concentration repressors 1 and 2. Let $[L_{1F}]$ and $[L_{2F}]$ be the concentration of unbound load 1 and 2 with total load concentration $[L_{1T}]$ and $[L_{2T}]$, and which can bind R1 and R2 reversibly. Let $[C_1]$ and $[C_2]$ be the concentration of a load-receptor complex.

$$[R_1]+[L_{1F}] \underset{k_{off\,1}}{\overset{k_{on1}}{\rightleftharpoons}} [C_1]$$
$$[R_2]+[L_{2F}] \underset{k_{off\,2}}{\overset{k_{on2}}{\rightleftharpoons}} [C_2]$$

R_1 is produced at a maximal rate of β_1 and is repressed by R_2. R_2 is produced at a maximal rate of β_2 and repressed by R_1. R_1 and R_2 degrade as a first order process at rate δ. Thus the differential equations governing $[R_1]$ and $[R_2]$ are:

$$\frac{d[R_1]}{dt} = \frac{\beta_1}{1+\left([R_2]/k_2\right)^n} - \delta[R_1] - k_{on1}[R_1][L_{1F}] + k_{off\,1}[C_1]$$
$$\frac{d[R_2]}{dt} = \frac{\beta_2}{1+\left([R_1]/k_1\right)^n} - \delta[R_2] - k_{on2}[R_2][L_{2F}] + k_{off\,2}[C_2]$$

We now de-dimensionalize these equations and define the following parameters. L_{10}, L_{20} are total amount of load 1 and 2 respectively.

$$u = [R_1]/k_1 \qquad v = [R_2]/k_2 \qquad \tau = t\delta$$
$$\ell_1 = [L_{1F}]/[L_{1T}] \qquad [C_1] = [L_{1T}] - [L_{1F}] \qquad C_1' = [L_{1T}](1-\ell_1)$$
$$\ell_2 = [L_{2F}]/[L_{2T}] \qquad [C_2] = [L_{2T}] - [L_{2F}] \qquad C_2' = [L_{2T}](1-\ell_2)$$
$$\frac{d\delta k_1 u}{d\tau} = \frac{\beta_1}{1+v^n} - \delta k_1 u - k_{on1} k_1 u \ell_1 L_{1T} + k_{off\,1} L_{1T}(1-\ell_1)$$
$$\frac{d\delta k_2 v}{d\tau} = \frac{\beta_2}{1+u^n} - \delta k_2 v - k_{on2} k_2 v \ell_2 L_{2T} + k_{off\,2} L_{2T}(1-\ell_2)$$

These equations reduce to:

$$\frac{du}{d\tau} = \frac{\beta_1/\delta k_1}{1+v^n} - u - \frac{k_{on1}\left[L_{1T}\right]}{\delta}u\ell_1 + \frac{k_{off1}\left[L_{1T}\right]}{\delta k_1}\left(1-\ell_1\right)$$

$$\frac{dv}{d\tau} = \frac{\beta_2/\delta k_2}{1+u^n} - v - \frac{k_{on2}\left[L_{2T}\right]}{\delta}v\ell_2 + \frac{k_{off2}\left[L_{2T}\right]}{\delta k_2}\left(1-\ell_2\right)$$

We now redefine several parameters and add a basal production rate of u and v, α_1 and α_2:

$$\beta_1' = \beta_1/\delta k_1 \qquad k_{on1}' = \frac{k_{on1}}{\delta} \qquad k_{off1}' = \frac{k_{off1}}{\delta k_1}$$

$$\beta_2' = \beta_2/\delta k_2 \qquad k_{on2}' = \frac{k_{on2}}{\delta} \qquad k_{off2}' = \frac{k_{off2}}{\delta k_2}$$

The final differential equations are therefore:

$$\frac{du}{d\tau} = \alpha_1 + \frac{\beta_1'}{1+v^n} - u - k_{on1}'\left[L_{1T}\right]u\ell_1 + k_{off1}'\left[L_{1T}\right]\left(1-\ell_1\right) \qquad \text{[S1]}$$

$$\frac{dv}{d\tau} = \alpha_2 + \frac{\beta_2'}{1+u^n} - v - k_{on2}'\left[L_{2T}\right]v\ell_2 + k_{off2}'\left[L_{2T}\right]\left(1-\ell_2\right) \qquad \text{[S2]}$$

$$\frac{d\ell_1}{d\tau} = -k_{on1}'k_1u\ell_1 + k_{off1}'k_1\left(1-\ell_1\right) \qquad \text{[S3]}$$

$$\frac{d\ell_2}{d\tau} = -k_{on2}'k_2v\ell_2 + k_{off2}'k_2\left(1-\ell_2\right) \qquad \text{[S4]}$$

$\alpha_1 = \alpha_2 = 0.2$; $\beta_1' = \beta_2' = 4$; n=3; $k_{on1}' = k_{on2}' = 0.5$; $k_{off1}' = k_{off2}' = 0.5$; $k_1 = k_2 = 1$; $[L_{1T}]$ and $[L_{2T}]$ are variable.

Note that the bifurcation analysis presented later in the Supplementary figures demonstrates that the various models that we study possess at least one stable state, i.e. the Jacobian of the system has eigenvalues with all negative real parts at the fixed points, and hence are asymptotically stable (see for example Theorem 4.6, p121 in "Differential Dynamic Systems" by Meiss). Thus all models discussed can be assumed to show convergence to equilibrium.

7.1.2 The simulation box and concentrations for the stochastic simulations.

We used a volume of 1 μm^3 for the simulation box and the base parameters for simulation of the genetic toggle switch as in the deterministic simulations. This corresponded to small numbers of about 10-20 molecules of the two repressors in the simulation box. The small numbers of molecules led to frequent stochastic events and many spontaneous transitions between the two states. The rate expressions used for the stochastic simulations of the genetic toggle switch are shown in Table S2.5.

7.1.3 Sensitivity to molecule number of the genetic toggle switch

In order to test whether our procedure for constructing the quasi-potential landscape for the genetic toggle switch was robust to larger molecule numbers, we ran the simulation with the average number of molecules in each state about 5 times larger than that reported in the text. As shown in Figure S2.4, the trends are similar to those reported in the main paper. Note that the number of transitions seen in any block of time is much fewer and hence it takes a significantly longer computational time to actually collect enough data for smooth and accurate plots. However there is no qualitative change in the results due to a larger molecule number.

7.1.4 Parameter Sensitivity in Deterministic Simulations and Alternative Induction Method

7.1.4.1 Alternative Induction Method

We considered a second method of induction that utilizes an inducer that directly reduces the level of a repressor. We derived similar a system of four differential equations listed below:

$$\frac{du}{d\tau} = \alpha_1 + \frac{\beta_1'}{1+v^n} - \left(u + \frac{\gamma_3 I_1}{1+I_1}\right) - k_{on1}'\left[L_{1T}\right]u\ell_1 + k_{off1}'\left[L_{1T}\right]\left(1-\ell_1\right) \qquad [S5]$$

$$\frac{dv}{d\tau} = \alpha_2 + \frac{\beta_2'}{1+u^n} - \left(v + \frac{\gamma_4 I_2}{1+I_2}\right) - k_{on2}'\left[L_{2T}\right]v\ell_2 + k_{off2}'\left[L_{2T}\right]\left(1-\ell_2\right) \qquad [S6]$$

$$\frac{d\ell_1}{d\tau} = -k_{on1}'k_1 u\ell_1 + k_{off1}'k_1\left(1-\ell_1\right) \quad [S7]$$

$$\frac{d\ell_2}{d\tau} = -k_{on2}'k_2 v\ell_2 + k_{off2}'k_2\left(1-\ell_2\right) \quad [S8]$$

γ_3 and γ_4 represent the activities of a factor (I_1 or I_2) that degrades R1 or R2, similar to the degradation of λ CI by RecA, modeled as in [1].

Because the qualitative results for both transition time and inducer required to transition did not vary with induction method, we report the results for the second method below in this Supplementary Information.

7.1.4.2 Transition Time

The relationship between amount of load and transition time was found to be linear across a range of parameters and both induction methods. This was true for a range of load binding on rates from K_{on}= 5 to 0.005. Of note is the identification of an optimal K_d for load binding which results in maximal effect on transition time. This can be seen in Figure S2.1. The effects of a low, medium and high K_d is demonstrated in Figure S2.2. We additionally varied β across two orders of magnitude; the relationship between transition time and load was found to be linear as shown in Table S2.1.

7.1.4.3 Inducer Required to Transition

The inducer decay rate, d_{I1}, affects the exponential parameter. As decay rate increases, more inducer is required to transition because the inducer persists in the system for less time. The exponential relationship can actually be written as a function of the decay rate: Inducer=C*exp(k*d_I*Load). This fact shows that the exponential relationship between the amount of inducer required to transition states and the load applied to the system is dependent upon the decay rate of the inducer. This procedure was repeated for both induction methods resulting in similar qualitative results. The results are shown in Tables S2.2 and S2.3.

7.1.5 Effects of a Dynamic Load

We explored the possibility that a load was not present in a constant amount but rather varied as the load was created and degraded. The equations used for a dynamic load are:

$$\frac{du}{d\tau} = \alpha_1 + \frac{\beta_1'}{1+v^n} - u - k_{on1}' \frac{k_{b1}}{k_{d1}} u\ell_1 + k_{off1}' \frac{k_{b1}}{k_{d1}}\left(c_1\right) \quad [S9]$$

$$\frac{dv}{d\tau} = \alpha_2 + \frac{\beta_2'}{1+u^n} - v - k_{on2}' \frac{k_{b2}}{k_{d2}} v\ell_2 + k_{off2}' \frac{k_{b2}}{k_{d2}}\left(c_2\right) \quad [S10]$$

$$\frac{d\ell_1}{d\tau} = -k_{on1}' k_1 \frac{k_{b2}}{k_{d2}} u\ell_1 + k_{off1}' k_1 \frac{k_{b1}}{k_{d1}}\left(c_1\right) + \frac{k_{d1}}{\delta} - \frac{k_{d1}}{\delta}\ell_1 \quad [S11]$$

$$\frac{d\ell_2}{d\tau} = -k_{on2}' k_2 \frac{k_{b2}}{k_{d2}} v\ell_2 + k_{off2}' k_2 \frac{k_{b2}}{k_{d2}}\left(c_2\right) + \frac{k_{d2}}{\delta} - \frac{k_{d2}}{\delta}\ell_2 \quad [S12]$$

$$\frac{dc_1}{d\tau} = k_{on1}' k_1 u\ell_1 - k_{off1}' k_1 c_1 \quad [S13]$$

$$\frac{dc_2}{d\tau} = k_{on2}' k_2 u\ell_2 - k_{off2}' k_2 c_2 \quad [S14]$$

Where k_{b1} is the creation rate of load 1 and k_{d1} is the degradation rate. K_{eq1}, defined as k_{b1}/k_{d1} was chosen as the de-dimensionalization constant (similar to L_{1T}, L_{2T} used above). As a result, the transition times were plotted against K_{eq} rather than L_T. The default parameter values used were: $k_{d1}=k_{d2}=0.5$; $k_1=k_2=1$; $\delta=1$; k_{b1} and k_{b2} were varied from 0.5 to 50 to cover a range of loading conditions. In addition to the default parameters, we tested the effects of k_d, k_1, k_{on} and k_{off} on the relationship between load and transition time. Because the transitions between states are not induced until the system has reached a steady state, there was no qualitative effect on the deterministic results. The relationship between K_{eq} for the load and transition time was found to be linear in all parameter regimes. This is shown for the default parameter conditions in Figure S2.3 and for the other parameter conditions in Table S2.4.

7.1.6 Positive Feedback on the Toggle Switch

7.1.6.1 Derivation of Composite Promoter Term

Let *P* be a constitutively active promoter which produces repressor R_1 at rate β:

$$P \xrightarrow{\beta} P + R_1$$

Let R_1 have positive feedback on *P*:

$$P + R_1 \underset{k_2}{\overset{k_1}{\rightleftharpoons}} PR_1 \xrightarrow{\rho} PR_1 + R_1$$

$$P + R_1 \xleftarrow{k_2} PR_1$$

Let R_1 be a repressor of *P* which binds in n copies:

$$P + nR_2 \underset{k_4}{\overset{k_3}{\rightleftharpoons}} PnR_2$$

We assume quasi-steady state:

$$\frac{d[PR_1]}{dt} = k_1[P][R_1] - k_2[PR_1] = 0$$

$$\frac{d[PR_2]}{dt} = k_3[P][R_2]^n - k_4[PR_2] = 0$$

Therefore:

$$[PR_1] = \frac{k_1}{k_2}[P][R_1]; \quad [PR_2] = \frac{k_3}{k_4}[P][R_2]^n$$

We assume a constant amount of P. From the law of conservation:

$$P_0 = [P] + [PR_1] + [PnR_2]$$

Let $k_1/k_2 = k'$ and $k_3/k_4 = k''$

$$P_0 = [P] + k'[P][R_1] + k''[P][R_2]^n$$

$$[P] = \frac{P_0}{1 + k'[R_1] + k''[R_2]^n}$$

We now solve for the rate of R1:

$$\frac{d[R_1]}{dt} = \rho[PR_1] - k_1[P][R_1] + k_2[PR_1] + \beta P = \rho k'[P][R_1] + \beta P$$

$$\frac{d[R_1]}{dt} = [P]\left(\rho k'[R_1] + \beta\right) = \frac{P_0 \rho k'[R_1] + P_0 \beta}{1 + k'[R_1] + k''[R_2]^n}$$

Let $\rho' = P_0 \rho k'$ and $\beta' = P_0 \beta$

$$\frac{d[R_1]}{dt} = \frac{\rho'[R_1] + \beta'}{1 + k'[R_1] + k''[R_2]^n}$$

This yields the positive feedback term in Eq. 10 in the text.

7.1.6.2 Strength of Positive Feedback

To assess the effects of a positive feedback on repressor 1, we tested various values of parameter ρ, the strength of positive feedback. First note that the positive feedback moiety, even in the presence of the load, does not abrogate bistability, unless ρ is very large, as shown in Figure S2.5. We then tested the probability distribution functions for the toggle with positive feedback without and with a load. The results of this are shown in Figure S2.6. When the positive feedback is 0, the probability distribution function for R1 and R2 is perfectly balanced. As the strength of positive feedback increases from 0 to 5, the pdf is increasingly skewed to R1. When ρ=5, the effects of the positive feedback are so strong that the system never switches stochastically into R2. As shown in the paper, this effect may be overcome by increasing the load on R1.

7.1.6.3 Effect of Positive Feedback on Transition Time

Even in the case of a positive feedback, the relationship between transition time and load remains linear. We explored the effect of transition time when the positive feedback was applied

to the R1 and R2. In all cases, the relationship was linear. This is shown in Supplementary Figure S2.5.

7.2 Motivations of the Ras System Model

7.2.1 Assumptions underlying the Ras Model:

The model we used for the Ras-Kinase system is mainly adopted from the minimal model of the Ras Switch proposed by Das et. al. [1] In the following section, we briefly discuss the underlying assumptions of the minimal model of Ras Switch:

1. SOS: As in [1], only SOS (Son of Sevenless) family of Ras Guanine Nucleotide Exchange Factors (GEFs) is included in the model. The RasGRP (Ras Guanine Nucleotide Release Protein) family (including RasGRP1 and RasGRP2) which are also GEFs are not included. SOS is ubiquitously distributed, while RasGRP family is restricted to the nervous and hematopoietic systems.
2. SOScat: Not all the domains of SOS are taken into consideration in this model. Cdc25 and REM, together named as SOScat, are only two included, which are essential domains for GEF catalytic activities. The domains flanking SOScat, both N-terminal and C-terminal, are shown to be inhibitory to GEF activities. *In vivo,* when SOS is recruited to the plasma membrane, the resulting conformational changes release this inhibition. In this minimal model this inhibiting effect is not modeled. For our purpose of investigating the effects of adding loads to the positive feedback based bistable Ras switch, we also only consider SOScat in our model.
3. SOS basal GEF activity: The original GEF activity of SOS is very low. However, its GEF activity is strongly influenced by the allosteric pocket in REM domain. When RasGDP binds to this pocket a 5-fold increase is observed in its GEF activity, while binding of

RasGTP to this site results in an increase of 75 times. Based on the main aim of the paper, we also choose to neglect the original GEF activity of SOScat. However, we also tested this assumption by including this basal GEF activity in the Ras model, whose behaviors show no qualitative differences with the model we described in the main text (data not shown).

4. Intrinsic GTPase activity of Ras: intrinsic GTPase activity of Ras is relatively low. Proteins we have generically called RasGAPs are constitutively present that promote Ras deactivation from RasGTP into RasGDP. For simplicity the intrinsic GTPase activity of Ras is neglected and the enhanced deactivation of RasGTP by RasGAP is modeled as an enzymatic reaction.
5. Truncated Raf cascade: after RasGTP binds to Raf *in vivo*, Raf will be phosphorylated and activated by the RasGTP:Raf complex. Then the activated Raf proteins activate the RAF-MEK-ERK-CD69 pathway. However, for the purpose of our study here, Raf is simplified into only a binding partner of RasGTP. Thus, the downstream phosphorylation and activation steps are not considered.
6. Since we are interested in the short-term behavior of the system, no synthesis or degradation dynamics is considered in our model, i.e. total amounts of all primary molecules (SOScat, Ras protein, RasGAP, Raf) are conserved. Note that experiments show Ras activation peaking in one or two minutes after activation [1,2].
7. All enzymatic reactions are modeled by sequential reactions of enzyme (E) and substrate (S) firstly bind together to form enzyme:substrate complex (ES) with a reaction rate constant of $k_{on(i)}$, then the complex disassociates reversibly with $k_{off(i)}$ or produces the product (P) irreversibly with $k_{cat(i)}$. These reactions are shown schematically as:

$$E + S \underset{}{\overset{kon(i),koff(i)}{\leftrightarrow}} ES \overset{kcat(i)}{\rightarrow} P$$

7.2.2 Reactions modeled in Ras model

Based on the abovementioned assumptions, all reactions considered in our model are listed in Table S6. In particular, [R1] and [R2] describe the allosteric pocket reactions of binding and unbinding reactions between RasGDP/RasGTP and the allosteric pocket in SOS REM domain. [R3] and [R4] describe the reactions catalyzed by GEF pocket of SOScat with allosteric pocket occupied by RasGTP and RasGDP, indicated by SOS(RasGTP) and SOS(RasGDP) correspondingly. [R5] describes the RasGTP deactivation reaction into RasGDP enhanced by RasGAP. The last but not least, [R6] describes the binding and unbinding of RasGTP and Raf. An underlying assumption here is the protection model, where RasGTP is assumed to be free from deactivation of RasGAP after being bound to Raf. We refer the reader to a later section where this assumption is relaxed.

7.3 ODE formulation

To be more general, we use Law of Mass Action (LMA) to model all the rates of reactions listed in Supplementary Table S2.6. Then, the following set of ODEs is achieved for the changing rate of each of the involving species, which we will call the LMA model. For the following sections, we use the following notations for the species involved in the system:

$$x_1 \equiv [SOScat];\ x_2 \equiv [RasGDP];\ x_3 \equiv [RasGTP];\ x_4 \equiv [SOScat(RasGDP)];$$

$$x_5 \equiv [SOScat(RasGTP)];\ x_6 \equiv [SOScat(RasGDP):RasGDP];$$

$$x_7 \equiv [SOScat(RasGTP):RasGDP];\ x_8 \equiv [RasGAP];\ x_9 \equiv [RasGAP:RasGTP];$$

$$x_{10} \equiv [Raf];\ x_{11} \equiv [RasGTP:Raf]$$

$$\frac{dx_1}{dt} = -k_{on1}x_1x_2 + k_{off1}x_4 - k_{on2}x_1x_3 + k_{off2}x_5 \quad [S15]$$

$$\frac{dx_2}{dt} = -k_{on1}x_1x_2 + k_{off1}x_4 - k_{on3}x_2x_5 + k_{off3}x_7 - k_{on4}x_2x_4 + k_{off4}x_6 + k_{cat5}x_9 \quad [S16]$$

$$\frac{dx_3}{dt} = -k_{on2}x_1x_3 + k_{off2}x_5 + k_{cat3}x_7 + k_{cat4}x_6 - k_{on5}x_3x_8 + k_{off5}x_9 - k_{on6}x_3x_{10} + k_{off6}x_{11} \quad [S17]$$

$$\frac{dx_4}{dt} = k_{on1}x_1x_2 - k_{off1}x_4 - k_{on4}x_2x_4 + k_{off4}x_6 + k_{cat4}x_6 \quad [S18]$$

$$\frac{dx_5}{dt} = k_{on2}x_1x_3 - k_{off2}x_5 - k_{on3}x_2x_5 + k_{off3}x_7 + k_{cat3}x_7 \quad [S19]$$

$$\frac{dx_6}{dt} = k_{on4}x_2x_4 - k_{off4}x_6 - k_{cat4}x_6 \quad [S20]$$

$$\frac{dx_7}{dt} = k_{on3}x_2x_5 - k_{off3}x_7 - k_{cat3}x_7 \quad [S21]$$

$$\frac{dx_8}{dt} = -k_{on5}x_3x_8 + k_{off5}x_9 + k_{cat5}x_9 \quad [S22]$$

$$\frac{dx_9}{dt} = k_{on5}x_3x_8 - k_{off5}x_9 - k_{cat5}x_9 \quad [S23]$$

$$\frac{dx_{10}}{dt} = -k_{on6}x_3x_{10} + k_{off6}x_{11} \quad [S24]$$

$$\frac{dx_{11}}{dt} = k_{on6}x_3x_{10} - k_{off6}x_{11} \quad [S25]$$

The followings are conservation laws for primary molecules (SOS, Ras, GAP and Raf) involved in the system.

$$SOS_T = x_1 + x_4 + x_5 + x_6 + x_7 \quad [S26]$$

$$Ras_T = x_2 + x_3 + x_4 + x_5 + 2x_6 + 2x_7 + x_9 + x_{11} \quad [S27]$$

$$GAP_T = x_8 + x_9 \quad [S28]$$

$$Raf_T = x_{10} + x_{11} \quad [S29]$$

We can recover the equations used in Ref. [1] with: 1) classic Pseudo Steady State Assumption (PSSA) for all the time derivatives of enzyme-substrate complexes; 2) defining Michealis constants as $K_{(i)M} = (k_{off(i)} + K_{cat(i)})/k_{on(i)}$; 3) Approximations of conservation law by ignoring enzyme-substrate complexes under PSSA. Then the enzymatic reaction rates can be simplified into classical Michealis Menten Kinetics and the overall set of ODEs simplified as:

$$x_1 \equiv [SOScat];\ x_2 \equiv [RasGDP];\ x_3 \equiv [RasGTP];\ x_4 \equiv [SOScat(RasGDP)];$$

$$x_5 \equiv [SOScat(RasGTP)];\ x_6 \equiv [SOScat(RasGDP):RasGDP];$$

$$x_7 \equiv [SOScat(RasGTP):RasGDP];\ x_8 \equiv [RasGAP];\ x_9 \equiv [RasGAP:RasGTP];\ x_{10} \equiv [Raf];$$

$$x_{11} \equiv [RasGTP:Raf]$$

$$\frac{dx_1}{dt} = -k_{on1}x_1x_2 + k_{off1}x_4 - k_{on2}x_1x_3 + k_{off2}x_5 \quad [S30]$$

$$\frac{dx_3}{dt} = -k_{on2}x_1x_3 + k_{off2}x_5 + \frac{k_{cat3}x_2x_5}{K_{m3} + x_2} + \frac{k_{cat4}x_2x_4}{K_{m4} + x_2} - \frac{k_{cat5}GAP_Tx_3}{K_{m5} + x_3} - k_{on6}x_3x_{10} + k_{off6}x_{11} \quad [S31]$$

$$\frac{dx_5}{dt} = k_{on2}x_1x_3 - k_{off2}x_5 \quad [S32]$$

$$\frac{dx_{11}}{dt} = k_{on6}x_3x_{10} - k_{off6}x_{11} \quad [S33]$$

The total molecular numbers of SOS, Ras and Raf are conserved in the PSSA system resulting in three additional conservation equations:

$$SOS_T = x_1 + x_4 + x_5 \quad [S34]$$

$$Ras_T = x_2 + x_3 + x_4 + x_5 + x_{11} \quad [S35]$$

$$Raf_T = x_{10} + x_{11} \quad [S36]$$

7.3.1 Simulation box and parameters

A quasi-two dimensional simulation box, similar to the one used by Das et al. [1] was utilized. Our simulation box is a 2μm by 2 μm surface with a height of 1.7 nm. Every molecular species is assumed to be well-mixed in this box.

Reaction rate constants were referenced from [1] and [3]. In our analysis, molecular concentrations were converted to molecular numbers in the simulation box for both deterministic and stochastic analyses. Thus, reaction rate constants need to be converted accordingly. For our simulation box, all the reactions are assumed to happen in the membrane area, which can be considered as two-dimensional. Therefore, the reaction rate constants need conversions not only from concentrations to molecular numbers, but also from 3D to 2D. Based on the simulation box used, a factor of 0.941/4 is used for the conversion from 3D rate constants with unit of (μM^{-1} s^{-1}) to 2D rate constants with unit of ($Molecules^{-1}$ s^{-1}). All the parameters we used in our deterministic and stochastic studies are listed in Supplementary Table 7 with both 3D and 2D values.

For all the following studies, 75 molecules of Ras, 6 molecules of RasGAP were used unless otherwise indicated.

7.3.2 Results for both cases of LMA and PSSA

Results for both the case of LMA and PSSA are shown in Figure 9 (main text) and Figure S7 correspondingly. For the case of LMA, the red line shows the bifurcation analysis results for the Ras system without Raf inside. A bistable regime is observed. While adding more Raf molecules into the system, both limit points are shifting to the right, bistable regime is decreasing and maximal excitable level of RasGTP is decreasing. When more than 21 molecules of Raf are

added, as shown by the curve of “Total Raf = 25”, the bistable regime totally diminishes and for all values of SOScat only one monostable point of the system remains.

Supplementary Figure S2.7 shows the case of PSSA, similar pattern of the changes in bistable region can be observed as shown in Figure 4.9 (main text). The only difference between these two cases is for the case of PSSA slightly more Raf molecules are needed to achieve same effect.

To directly examine the effects of adding different amount of Raf into the Ras activation system for both LMA and PSSA models, we also carried out bifurcation analyses with total number of Raf, i.e. Raf_T as primary parameter, which are shown in Supplementary Figure S2.8 and S2.9 correspondingly. Both Supplementary Figure S2.8 and S2.9 start with bistable region when there is no Raf in the system as we can predict. With the increase of total number of Raf in the system, the values of “high” steady state decrease together with increase in the values of the unstable steady state. This results in vanishing of both steady states and only one monostable region after Raf_T reaches a certain threshold. Again, similar patterns are observed for both cases of LMA and PSSA, and the only difference between them is the scale.

7.3.3 Parameter Sensitivity Analysis (PSA)

For PSA of the Ras Minimal Model, we refer the reader to Das et. al. [1]. For our main purpose of investigating the load to the Ras Switch, we varied the values of k_{on6} and k_{off6} and check their influences on the bistability of the system. We first maintained the same ratio of k_{on6} to k_{off6}, then we changed this ratio and check individual influences.

When keep the ratio between k_{on6} and k_{off6} the same and vary absolute values of k_{on6} and k_{off6}, no difference in bifurcation diagram is noticed (data not shown). This means there are no changes in steady state values if the ratio between these two parameters is maintained.

Then k_{on6} and k_{off6} are varied separately. As shown in Figure S10, increase of k_{off6} results in left shifts of both limit points, increase in bistable regime and increase in maximal RasGTP activation level. Qualitative features of bistability are maintained. Decrease of k_{off6} results in right shift of both limit points, increase in unstable bistable regime and decrease in maximal RasGTP activation level. Qualitative features of bistability are also maintained.

Supplementary Figure S2.11 shows the results of an increase in k_{on6} value. This results in reverse effects as shown in Supplementary Figure S2.10. Noticeably, increase k_{off6} by 10 times has exactly the same effects as decrease k_{on6} by 10 times and *vice versa*. This indicates the key player of k_{on6} and k_{off6} in the Ras system is the value of their ratio and is additional assurance that no changes would be observed when the ratio between these two parameters is maintained.

7.4 Discussion on protection assumption with a toy toggle switch and Ras Model

7.4.1 Assumption of Protection Model

For both the toggle switch and the Ras Switch, we assumed that the output molecule is protected when bound with the Load. For the toggle switch model, we assumed the repressor proteins are free from first order degradation when bound in the repressor-load complex; for the Ras Switch model, we assumed RasGTP is relieved from enhanced GTPase activity by RasGAP in its complex form with Raf. We show the effects of removing this assumption in the main text. Here we report additional data.

The Hill function form of the genetic toggle we have used does not allow for explicit binding of the repressors with the promoters they repress. We also considered the question whether allowing the repressor to decay when bound with the promoter (note, not the load) would have an effect on the system. To elucidate this point, a toy model is proposed to make the lumped processes in the Toggle Switch model more explicit. We present below an LMA based model for the toggle switch which we use to test whether allowing the *decay of the repressor when bound to the promoter it represses* can has any effect on the system.

7.4.2 Toy Toggle Switch model

For this model, we construct a demonstrative classical toggle switch similar to the one discussed in the text, but using LMA. In this model system, two equivalent repressors are expressed by corresponding genes. Inactive repressors monomers then become activated after a trimerization process. Activated repressor trimmers can then bind to corresponding promoters and repress the transcriptions of the other repressor monomer. Without repressor bound to promoters, genes can be transcribed at full rate.

7.4.2.1 Assumptions

1. Several assumptions were made for this model to both meet our purpose and maintain it in an intuitive form.
2. Two sides of the toggle switch are identical, i.e. same reactions involved and same parameters for same reactions.
3. Since we are interested in the steady state behaviors of the model system, transcriptional and translational processes are lumped together into one overall reaction and assumed to happen immediately without delay.

4. Promoter values are approximated as continuous concentrations rather than more appropriate discrete number of sites.
5. "Leaky" transcriptions of the promoters when they are bound by corresponding repressors are ignored.
6. Repressor monomers and trimers are identical in their degrading dynamics, thus same degrading parameters are used.

Reactions included in this toggle switch model were then formulated and listed in Supplementary Table 4.8. Particularly, [P1] and [P8] describe the trimerization reactions of inactive repressor monomers ($R_{(i)}$) into active repressor trimers ($AR_{(i)}$). [P2] and [P9] describe the binding and unbinding reactions of active repressor trimers to corresponding promoters ($Pro_{(i)}$) to form repressor:promoter complex ($AR_{(i)}$: $Pro_{(i)}$). [P3] and [P10] describe the "ON state" of the promoters without being bound by repressor, which directly give birth to repressor monomers. [P4] and [P11] will be used to test the protection model, which describes the degradations of repressor trimers when they are bound to promoters. Degradation rate constants of this reaction will be set to zero for protection assumption as control and set equal to other degradation rate constant for our purpose. [P5], [P6], [P12] and [P13] are degradation reaction of both repressor monomers and trimers. [P7] and [P14] describe binding and unbinding reactions between repressor monomers and load molecules ($L_{(i)}$) to form repressor:load complex ($R_{(i)}$:$L_{(i)}$).

7.4.2.2 ODE model

Following notations are used for the toggle switch model:

$$x_1 \equiv [R_1];\ x_2 \equiv [AR_1];\ x_3 \equiv [Pro_1];\ x_4 \equiv [AR_1 : Pro_1];\ x_5 \equiv [L_1];\ x_6 \equiv [R_1 : L_1]$$

$$x_7 \equiv [R_2];\ x_8 \equiv [AR_2];\ x_9 \equiv [Pro_2];\ x_{10} \equiv [AR_2 : Pro_2];\ x_{11} \equiv [L_2];\ x_{12} \equiv [R_2 : L_2]$$

We use Law of Mass Action to formulate all the reaction rates and achieve the following time dependent ODEs for each species:

$$\frac{dx_1}{dt} = -3k_1x_1^3 + 3k_2x_2 + \alpha_1x_9 - k_7x_1 - k_{on1}x_1x_5 + k_{off1}x_6 \quad [S37]$$

$$\frac{dx_2}{dt} = k_1x_1^3 - k_2x_2 - k_3x_2x_3 + k_4x_4 - k_6x_2 \quad [S38]$$

$$\frac{dx_3}{dt} = -k_3x_2x_3 + k_4x_4 + k_5x_4 \quad [S39]$$

$$\frac{dx_4}{dt} = k_3x_2x_3 - k_4x_4 - k_5x_4 \quad [S40]$$

$$\frac{dx_5}{dt} = -k_{on1}x_1x_5 + k_{off1}x_6 \quad [S41]$$

$$\frac{dx_6}{dt} = k_{on1}x_1x_5 - k_{off1}x_6 \quad [S42]$$

Since the toggle switch is symmetric, ODEs for the other side are identical except for indexes of variables and parameters thus not presented here. Also governing this system is the conservation of molecule numbers of promoters:

$$Pro_{1T} = x_3 + x_4 \quad [S43]$$

To generate Figure S12, following parameter values are used:

$k_1 = k_8 = 0.3$, $k_2 = k_9 = 10$, $k_3 = k_{10} = 0.6$, $k_4 = k_{11} = 1$, $k_5 = k_{12} = 0.1$, $k_6 = k_{13} = 0.1$, $k_7 = k_{14} = 0.1$, $k_{on} = 0.5$, $k_{off} = 0.2$.

7.4.2.3 Results

Supplementary Figure S2.12 shows the differences between the system with protection of repressor molecules from degradation when bound to promoter (note: not the load) and the one without. If the protection is not included, a very minor increase in the bistable region can be observed with right shift of upper limit point and left shift of lower limit point.

7.4.3 Toggle Switch without and with Positive Feedback Motif

7.4.3.1 Modifications to original models

If the protection assumption is released for the toggle switch model, two more reactions should be added into the reaction system.

$$C_1 \xrightarrow{\delta} L_{1F}$$
$$C_2 \xrightarrow{\delta} L_{2F}$$

Corresponding changes to de-dimensionalized ODEs should also be made:

$$\frac{dl_1}{dt} = -k_{on1}{}' k_1 u l_1 + k_{off1}{}' k_1 \left(1 - l_1\right) + \left(1 - l_1\right) \qquad [S44]$$

$$\frac{dl_2}{dt} = -k_{on2}{}' k_2 v l_2 + k_{off2}{}' k_2 \left(1 - l_2\right) + \left(1 - l_2\right) \qquad [S45]$$

When assuming steady state for the entire system, all the terms introduced by load molecules cannot be cancelled out as in the case of protection model. Thus, influences to steady-state behaviors by adding load molecules to the Toggle Switch system should be expected.

7.4.3.2 Results

Figure 4.2A shows the steady-state effects of adding increasing number of load molecules to both sides of the original genetic toggle switch. Without load molecule, the system is bistable with two stable steady states and one unstable steady state as predicted. With the increase of number of load molecules, all these three steady state become closer and finally meet together at certain level of L_T. Then two steady states vanish and only one stable steady state left. Figure 4.2B shows the steady-state effects of adding increasing number of load molecules to R1 side (L_{1T}) of the original genetic toggle switch. Without any load molecule in the system, the toggle switch is bistable with two stable steady states and one unstable steady state as predicted. Adding increasing number of load molecules results in becoming closer between the upper stable steady

state and the unstable steady state. At certain threshold of L_{1T} these two steady states meet and vanish, with only the lower stable steady state left.

Supplementary Figure S2.13 shows effects of adding load molecules to the toggle switch with positive feedback on one side when the protection assumption is released. Interestingly, adding same amount of load molecules to different sides also cause different responses from the system. Adding load to R1 side results in increase of bistable regime and adding to R2 side results in decrease of bistable regime. When equal amount of loads added into both sides, the bistable regime is increased but to an extent smaller than adding to R1 side along. Increase in R1 level is much faster in this case than in Figure 2 due to the positive feedback loop.

7.4.3.3 Transition times in the absence of protection

The relationship between transition times and load is altered when the protection of a lower or absent decay rate of the repressor from the load complex. As predicted from Figure 2, the system with a one-sided load loses bistability with a load of 3.4; with a both sided load the system loses bistability with a load of 11. Thus we tested the transition times of the system within this regime. As shown in Figure 4, when a load is applied to the same side, there is a positive linear relationship between rise time and load, but a negative linear relationship with decay time. Conversely, a load applied to the opposite side results in a negative linear relationship between rise time and load, but a positive linear relationship with decay time. A load applied to both sides result in a negative linear relationship for both rise time and decay time. This result is discussed in the main text.

7.4.4 Ras Model

For Ras model, protection model is also assumed implicitly, since RasGTP is free from GTPase activities after binding to Raf. In this section, we examine potential influences caused by

this assumption. For the Ras Switch, we modified the original set of ODE's by including the RasGTP:Raf complexes as an equivalent substrate of RasGAP.

7.4.4.1 Modifications to original model

If RasGTP can still be deactivated into RasGDP by RasGAP in the complex form with Raf, one more reaction should be included into the Ras System:

$$\text{RasGAP+RasGTP:Raf} \xleftrightarrow[koff5]{kon5} \text{RasGAP:RasGTP:Raf} \xrightarrow{kcat5} \text{RasGAP+RasGDP+Raf}$$

$$\text{RasGAP} + \text{RasGTP} : \text{Raf} \overset{\text{kon5,koff5}}{\leftrightarrow} \text{RasGAP} : \text{RasGTP} : \text{Raf} \overset{\text{kcat5}}{\rightarrow} \text{RasGAP} + \text{RasGDP} + \text{Raf}$$

$$\text{RasGAP} + \text{RasGTP} : \text{Raf} \overset{\text{kon5,koff5}}{\leftrightarrow} \text{RasGAP} : \text{RasGTP} : \text{Raf} \overset{\text{kcat5}}{\rightarrow} \text{RasGAP} + \text{RasGDP} + \text{Raf}$$

The same reaction rate constants are assumed for the new reaction as free RasGTP de-activation. One more species is introduced into this system, i.e. $x_{12} \equiv \left[RasGAP : RasGTP : Raf \right]$. Based on this new reaction, several modifications should also be made for the ODEs system including adding more terms into x_2, x_8, x_{10} and x_{11} equations and add a new equation of x_{12}.

$$\frac{dx_2}{dt} = -k_{on1}x_1x_2 + k_{off1}x_4 - k_{on3}x_2x_5 + k_{off3}x_7 - k_{on4}x_2x_4 + k_{off4}x_6 + k_{cat5}x_9 + k_{cat5}x_{12} \qquad [S46]$$

$$\frac{dx_8}{dt} = \dagger - k_{on5}x_3x_8 + k_{off5}x_9 + k_{cat5}x_9 - k_{on5}x_8x_{11} + k_{off5}x_{12} + k_{cat5}x_{12} \qquad [S47]$$

$$\frac{dx_{10}}{dt} = -k_{on6}x_3x_{10} + k_{off6}x_{11} + k_{cat5}x_{12} \qquad [S48]$$

$$\frac{dx_{11}}{dt} = k_{on6}x_3x_{10} - k_{off6}x_{11} - k_{on5}x_8x_{11} + k_{off5}x_{12} \qquad [S49]$$

$$\frac{dx_{12}}{dt} = k_{on5}x_8x_{11} - k_{off5}x_{12} - k_{cat5}x_{12} \qquad [S50]$$

Modifications are also needed for conservation laws:

$$Ras_T = x_2 + x_3 + x_4 + x_5 + 2x_6 + 2x_7 + x_9 + x_{11} + x_{12} \qquad [S51]$$

$$GAP_T = x_8 + x_9 + x_{12} \quad [S52]$$

$$Raf_T = x_{10} + x_{11} + x_{12} \quad [S53]$$

7.4.4.2 Results

Figure S2.14 shows the changes of bifurcation curve with different numbers of Raf molecules (5, 15, 25 and 200) added into the system in logarithmic scale respectively. A similar pattern of decreases in bistable region and finally elimination of the bistable region as reported in the Figure 9 in main text is still observed but with a more complicated dynamics. Differences between the case without protection model and the one in main text as with protection model will be discussed as follows.

As shown in Figure 4.9 in the main text, where the protection model is included, maximal activation level of RasGTP is always decreasing with increase in Raf molecules added into the system. While in Supplementary Figure S2.14 reported here, maximal activation level of RasGTP first increase (as for the case of “Total Raf=5”) and then decrease (comparing the case of “Total Raf=25” to “Total Raf = 15”) with adding more Raf molecules.

Elimination of bistable region happens with much more Raf molecules. Even though the bistable region already decreased a lot after adding 25 molecules, the left bistable region needs much more Raf molecules to eliminate. Even with 150 Raf molecules, a tiny bistable region still exists. After around 200 molecules of Ras added, the bistability is abrogated.

Decrease in bistable region in Figure 4.9 in the main text is a result of right shifts of both fixed points with a faster rate of shift for the upper fixed points. While the decrease in Supplementary Figure S2.14 is a result of the leftward shift of both fixed points with a faster shift rate for the lower fixed point.

7.5 Supplemental figures

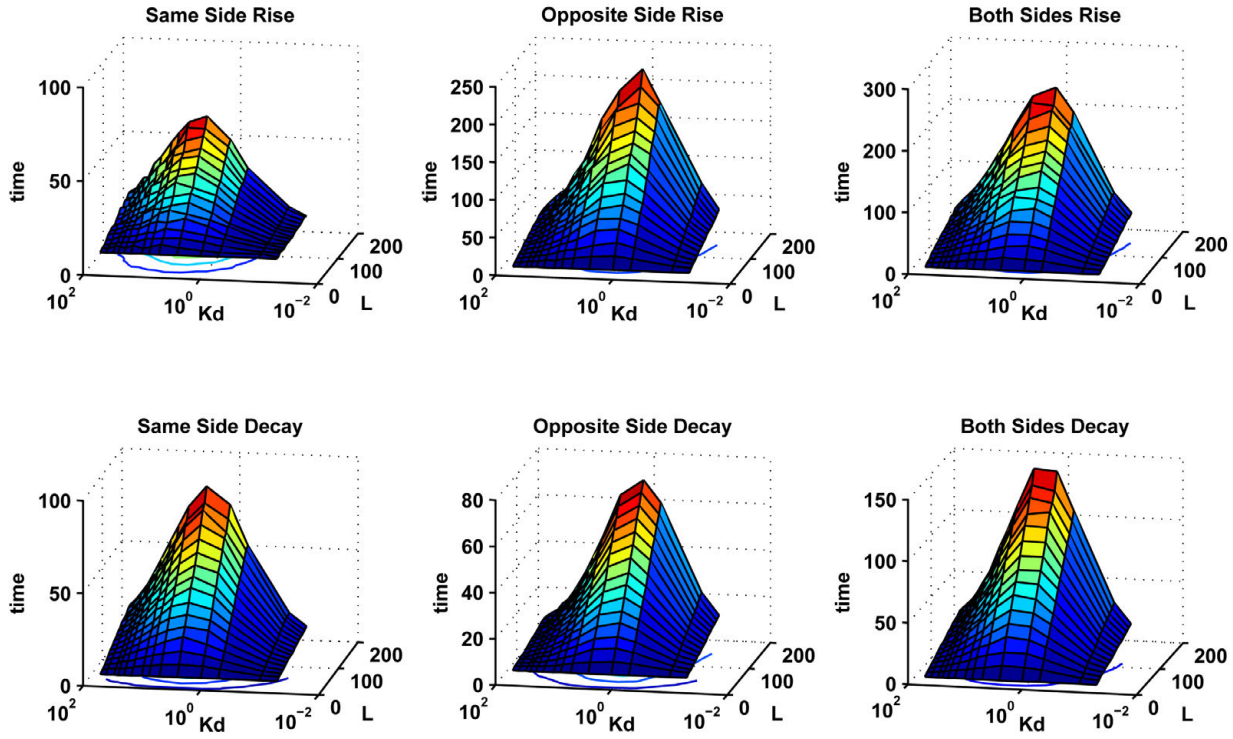

Figure S2.1. Surface plots showing response times of the simple genetic toggle switch with changes in load (L) and changes in the dissociation constant (Kd) of binding with load. The units of L and Kd are (molecules/µm3). The z-axis measures the response time indicated in the title. "Same Side Rise" and "Same Side Decay" refers to the rise time and decay time when the load is on the same side as the repressor whose concentration is increasing. "Opposite Side Rise" and "Opposite Side Decay" refers to the rise time and the decay time when the load is on the other side of the repressor whose concentration is increasing. "Both Sides Rise" or decay refer to the rise and decay times when a load is present on both sides (symmetrically). The plot shows that at every Kd, the relation between the response time and load is approximately linear. The response time is largest for the case of "Both Sides Rise" followed by "Opposite Side Rise". The response time is also non-monotonic with respect to the Kd for a given load, and is maximized at intermediate values of Kd.

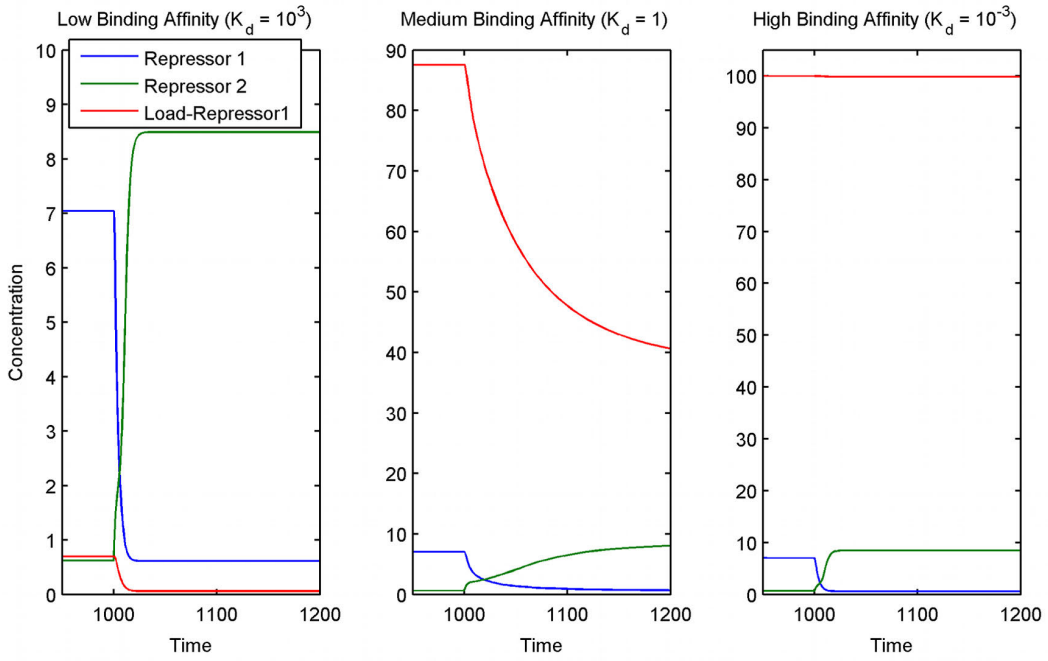

Figure S2.2. Time plot of switching of the simple toggle switch with a load on Repressor 1, at three different values of the dissociation constant.
In all three cases the system is switched by providing 150 molecules/µm3 of an inducer at 1000 minutes. The inducer stays constant at that value and is not shown in the plots. The left panel has a very high dissociation constant (Kd=1000 molecules/µm3) of binding between the load and the repressor, due to which the load has a minimal effect on the system. The middle panel has an intermediate value (Kd=1 molecules/µm3) because of which the load acts as a dynamic sink by releasing Repressor 1 and slowing the switching. The right panel shows the effect of a small dissociation constant (Kd=10−3molecules/µm3). At such strong binding affinities, all of the load is always bound to Repressor 1. Thus the load has minimal effect on the switching dynamics. In all cases total load concentration is 100 molecules/µm3.

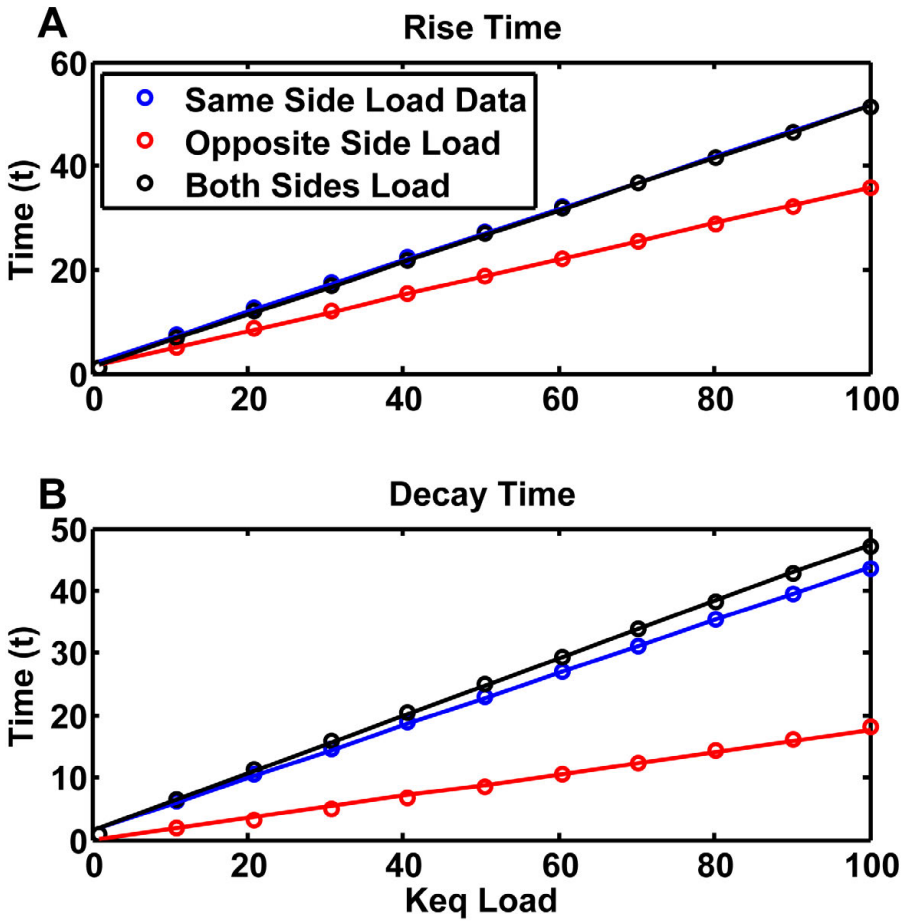

Figure S2.3. Effects of a dynamic load on dynamics of a symmetric toggle switch.
(A). The time taken to reach 90% of maximum value for the protein undergoing a low-to-high transition as a function of the equilibrium constant of a dynamic load. Normalized time is a unit-less number defined by the transition time (rise or decay) of the system at a given loading condition divided by the transition time (rise or decay) of an unloaded system. (B). The time taken for the concentration of the protein undergoing a high-to-low transition to reach 10% of its maximum value.

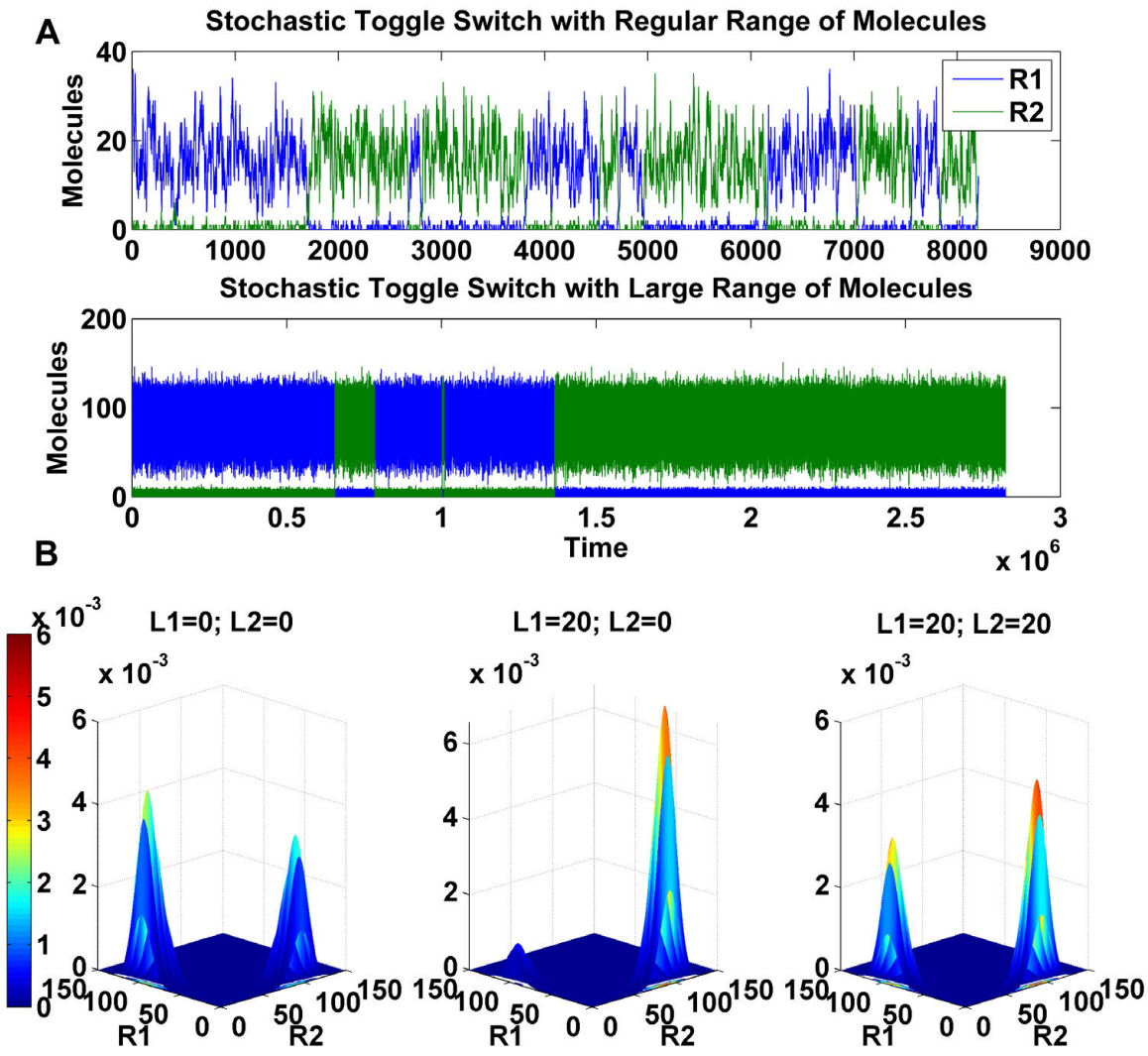

Figure S2.4. Stochastic time trace and the probability distribution function of repressor concentrations for the large volume simulations.
(A). Comparison of time traces of the stochastic simulations of the simple toggle switch with basal parameters (top panel) and a larger volume (bottom panel). The average molecule number is about 5 times greater, and the number of transitions are significantly fewer. (B). The probability distribution function of the genetic toggle switch with the larger molecular number without (left) and with (right) a load. The effect of a load on R1 is qualitatively the same for this system as for the smaller system. Since transitions are slower the data are more uneven for this simulation.

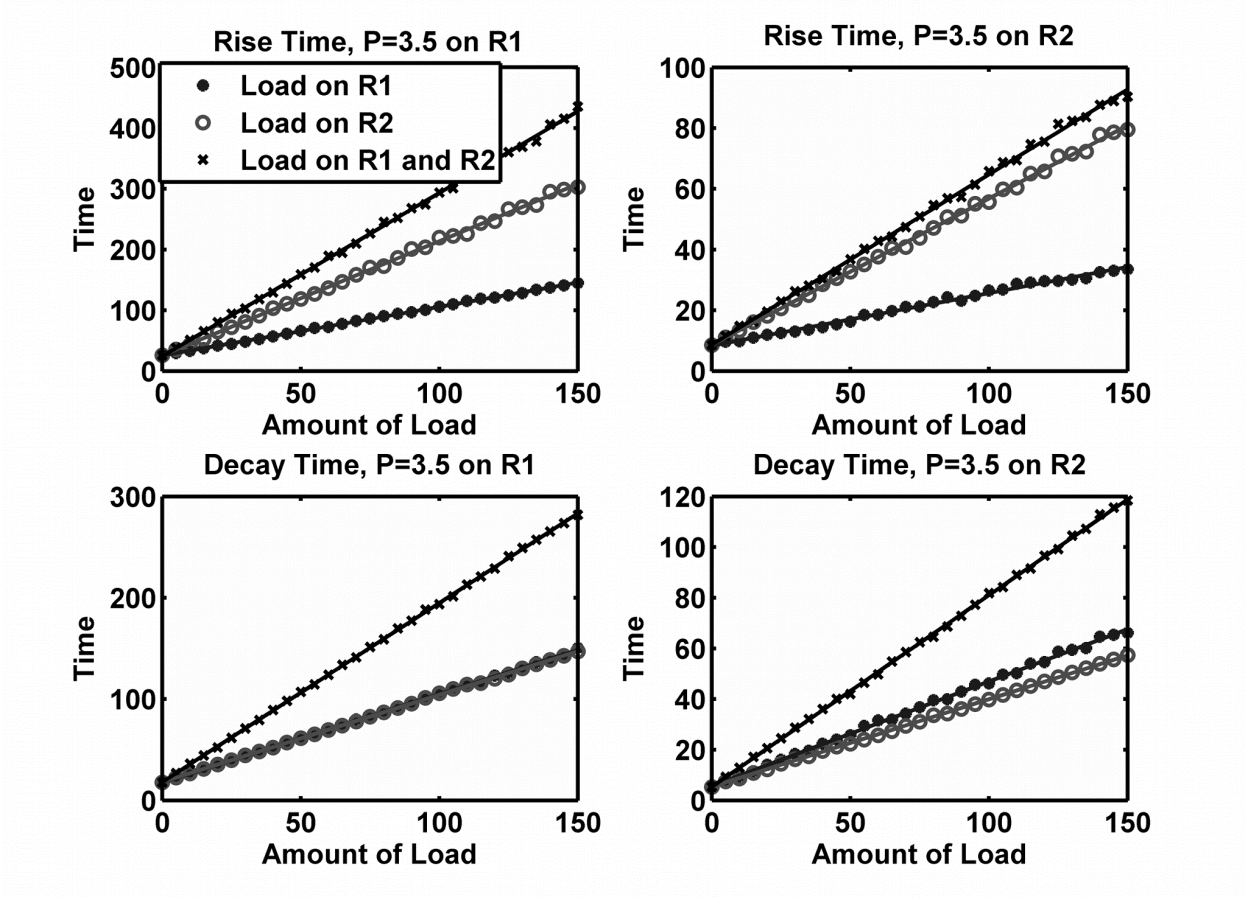

Figure S2.5. Transition times in a genetic toggle switch with a positive feedback moiety. In all cases the strength of the positive feedback (denoted here by P instead of ρ) is 3.5 on either Repressor 1 (R1) or Repressor 2 (R2). Top Left: Rise time - time to transition INTO state R1 with the positive feedback on R1. Note that the rise time is larger at nonzero loads when the load is on R2 or when the load is on both sides, in agreement with the simple toggle switch. Top Right: Rise time - time to transition INTO state R1 with the positive feedback on R2. Bottom Left: Decay time - time to transition OUT OF state R1 with the positive feedback on R1. Bottom Right: Decay time - time to transition OUT OF state R1 with the positive feedback on R2.

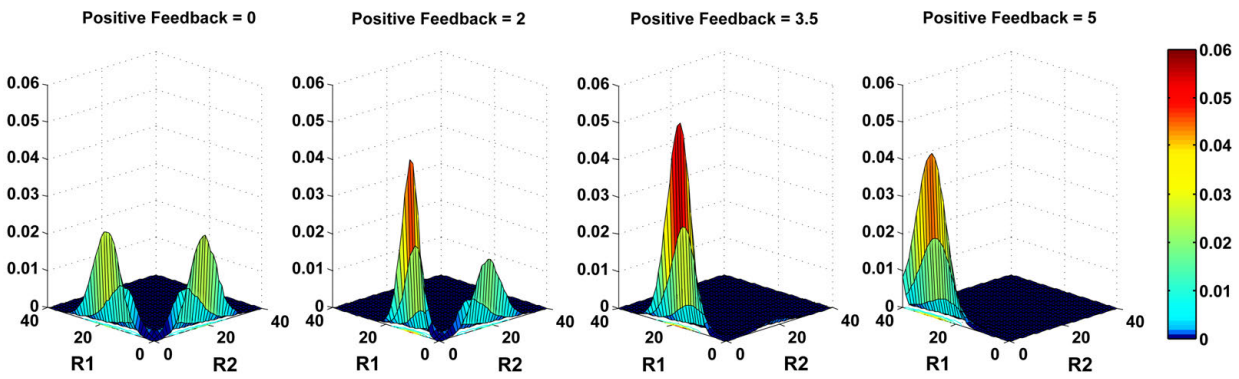

Figure S2.6. Probability distribution functions of repressor concentrations for the toggle with a positive feedback moiety.
The left panel shows that when ρ=0, the switch is balanced evenly. As ρ increases, the side of the switch with the positive feedback becomes more and more prominent, at the expense of the other side. When ρ=5, the system spends most of its time in one state.

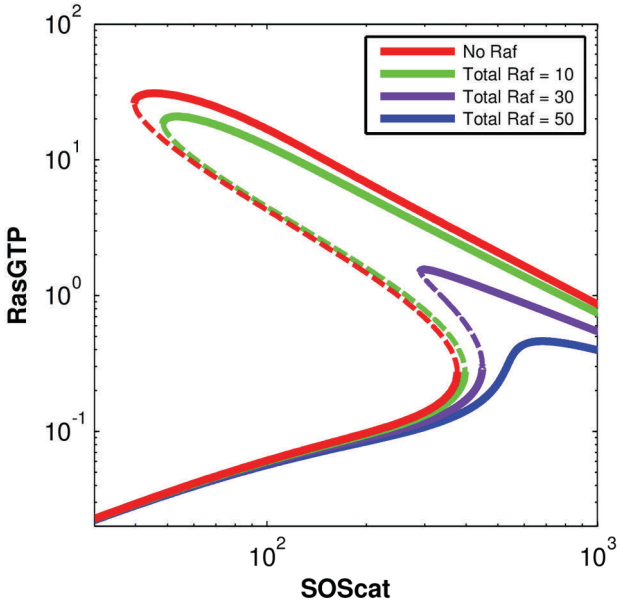

Figure S2.7. Bifurcation diagram of the Ras switch with different levels of Raf (load) on the system for the model with Pseudo Steady State Assumption (PSSA).
The total number of SOS in the simulation box is used as the parameter being tuned, which varies from 0 to 1000. For Raf=0, Raf=10 and Raf=30, there are two bifurcations points as SOS is increased. In the first bifurcation a new high valued stable steady state appears along with the low valued stable steady state. In the second bifurcation, the low valued stable state disappears leaving behind only the high valued state. The dotted line marks the unstable steady state that also comes into existence in the bistable region. As total Raf increases, the two bifurcations approach each other. When Raf=50, the system has lost both of its bifurcations and is characterized by a single stable steady state at all values of Raf.

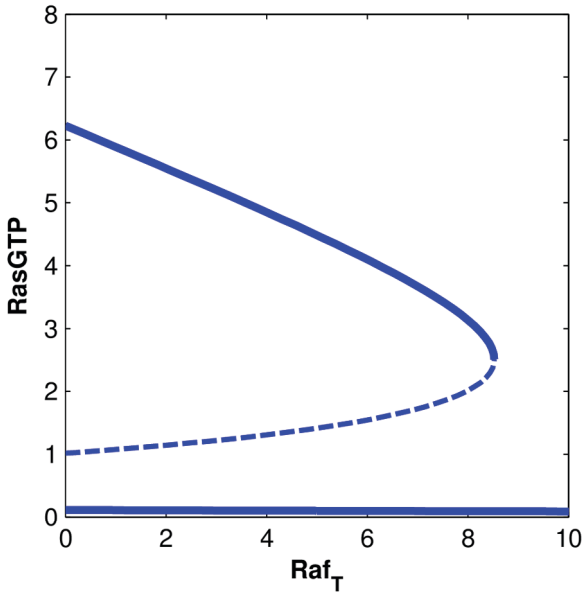

Figure S2.8. Bifurcation diagram of the Ras activation model based on Law of Mass Action (LMA).
Here the total number of Raf molecules (RafT) is the primary parameter being varied. Without Raf, the Ras activation system is bistable as reported. With increasing RafT, the "high" stable steady state branch comes closer with the unstable steady state branch and both are eliminated after a threshold of RafT. A monostable region is maintained beyond the threshold.

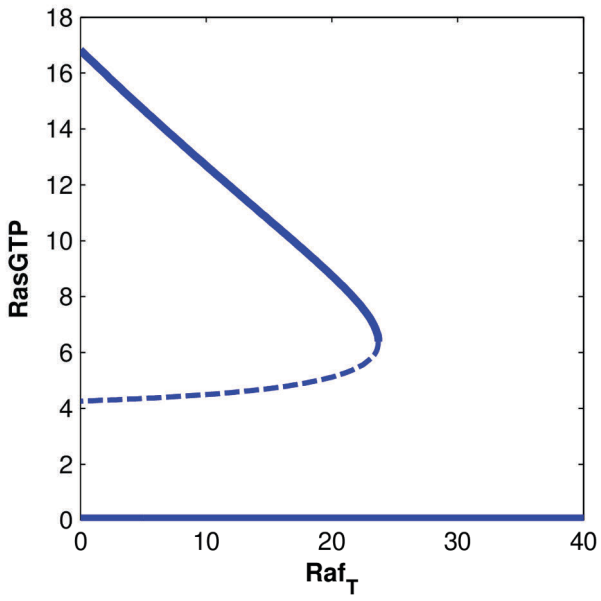

Figure S2.9. Bifurcation diagram of the Ras activation PSSA model with total number of Raf molecules (RafT) as the primary parameter.
Without Raf, the Ras activation system is bistable as reported. With increasing RafT, the "high" stable steady state branch comes closer with the unstable steady state branch and both are eliminated after a threshold of RafT. A monostable region is maintained beyond the threshold.

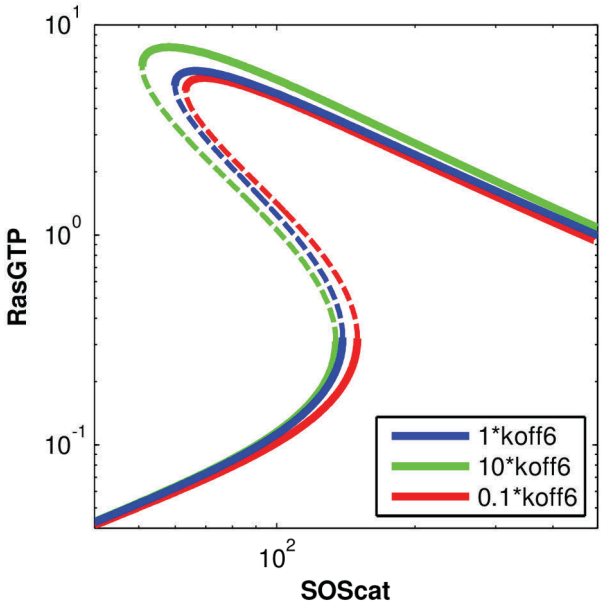

Figure S2.10. Parameter sensitivity of the bistability of Ras switch to changes in koff6. Increase of koff6results in leftward shifts of both stable fixed points, increase in the bistable regime and increase in maximal RasGTP activation level (Green Line) when compared to baseline with original value (Blue Line). Decrease of koff6 (Red Line) results in right shift of both limit points, increase in unstable bistable regime and decrease in maximal RasGTP activation level. Qualitative features of bistability are maintained.

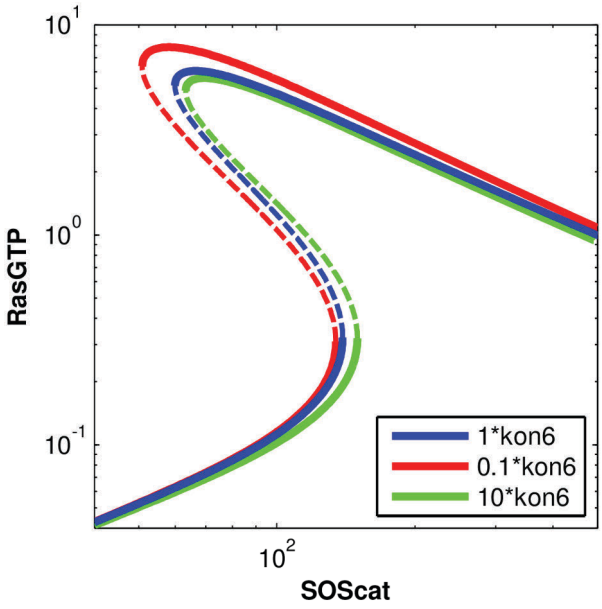

Figure S2.11. Parameter sensitivity of the bistability of Ras switch to changes in kon6. Increase of kon6(Green Line) results in right shift of both limit points, increase in unstable bistable regime and decrease in maximal RasGTP activation level when compared to baseline original value (Blue Line). Decrease of kon6 (Red Line) results in left shifts of both limit points, increase in bistable regime and increase in maximal RasGTP activation level. Qualitative features of bistability are maintained.

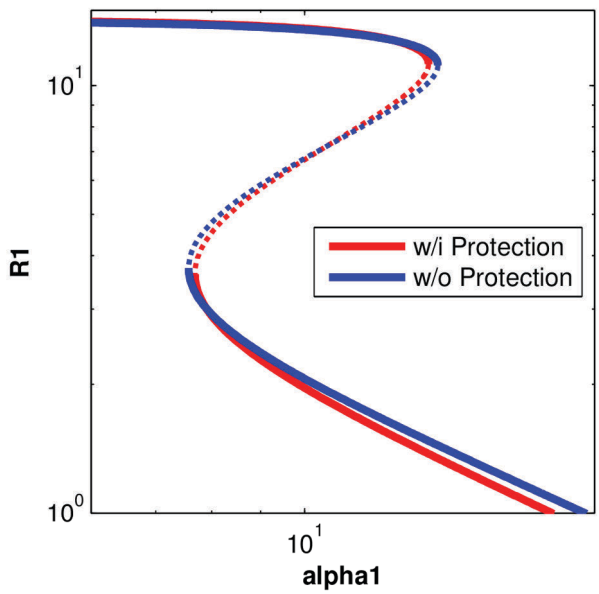

Figure S2.12. Comparison between bifurcation diagrams of toy genetic toggle switch with and without protection of repressor degradation when bound with promoters.
If the protection is not included (Blue Line), a minor increase in the bistable region can be observed with right shift of upper limit point and left shift of lower limit point compared to the case with protection assumed (Red Line). Note that this is not the same as degradation after being bound with the load.

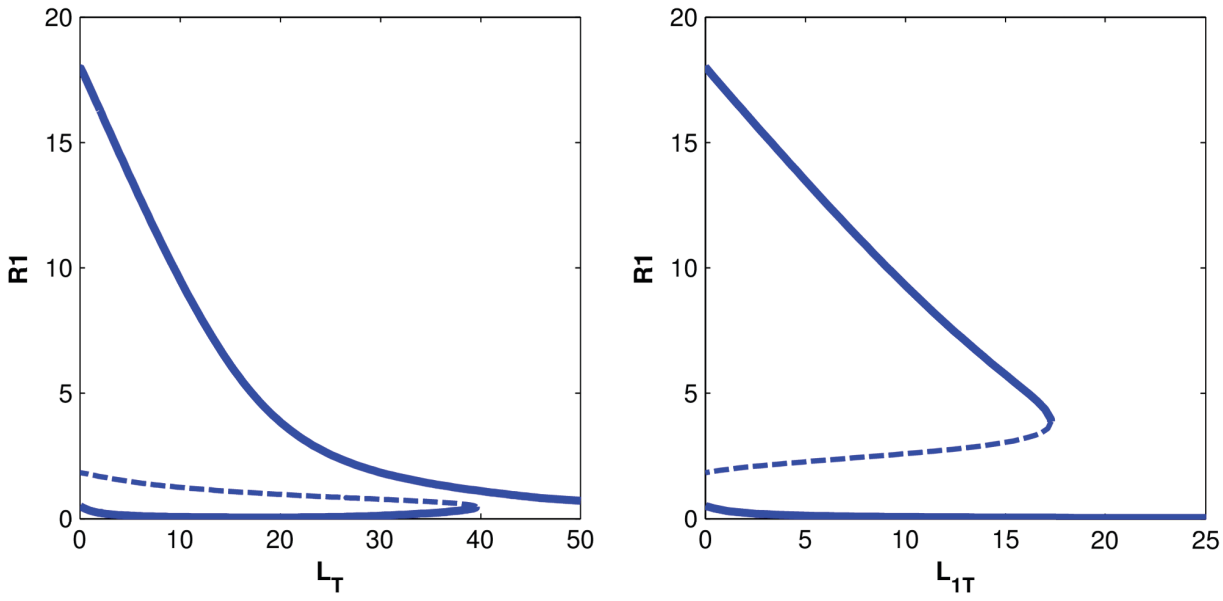

Figure S2.13. Bifurcation diagram of the genetic toggle switch with positive feedback loop on one side after removal of the protection assumption.
The left panel shows the bifurcation diagram when the load is added symmetrically to both sides. Without load molecule, the toggle switch is bistable as predicted. With the increase in LT, the unstable steady state and the "low" stable steady state come closer and meet at certain threshold. The value of "high" stable steady state decreases with increase in LT. Beyond the threshold, the toggle switch becomes monostable. The right panel shows the effect of just adding a load to R1. In this case the high state of R1 approaches the unstable steady state, and annihilates itself. The system jumps to the low stable state, which is equivalent to the "high" state of the other repressor.

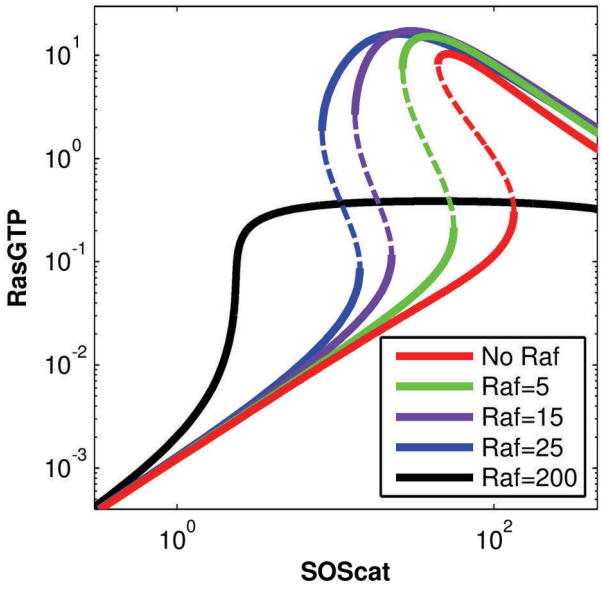

Figure S2.14. Bifurcation diagram of the Ras activation model when Ras can degrade when bound with Raf.
As the number of Raf molecules increase, the bistable region decreases. However unlike the case with no protection, the curve moves to the left. When Raf molecules increase by a large amount, bistability is abrogated.

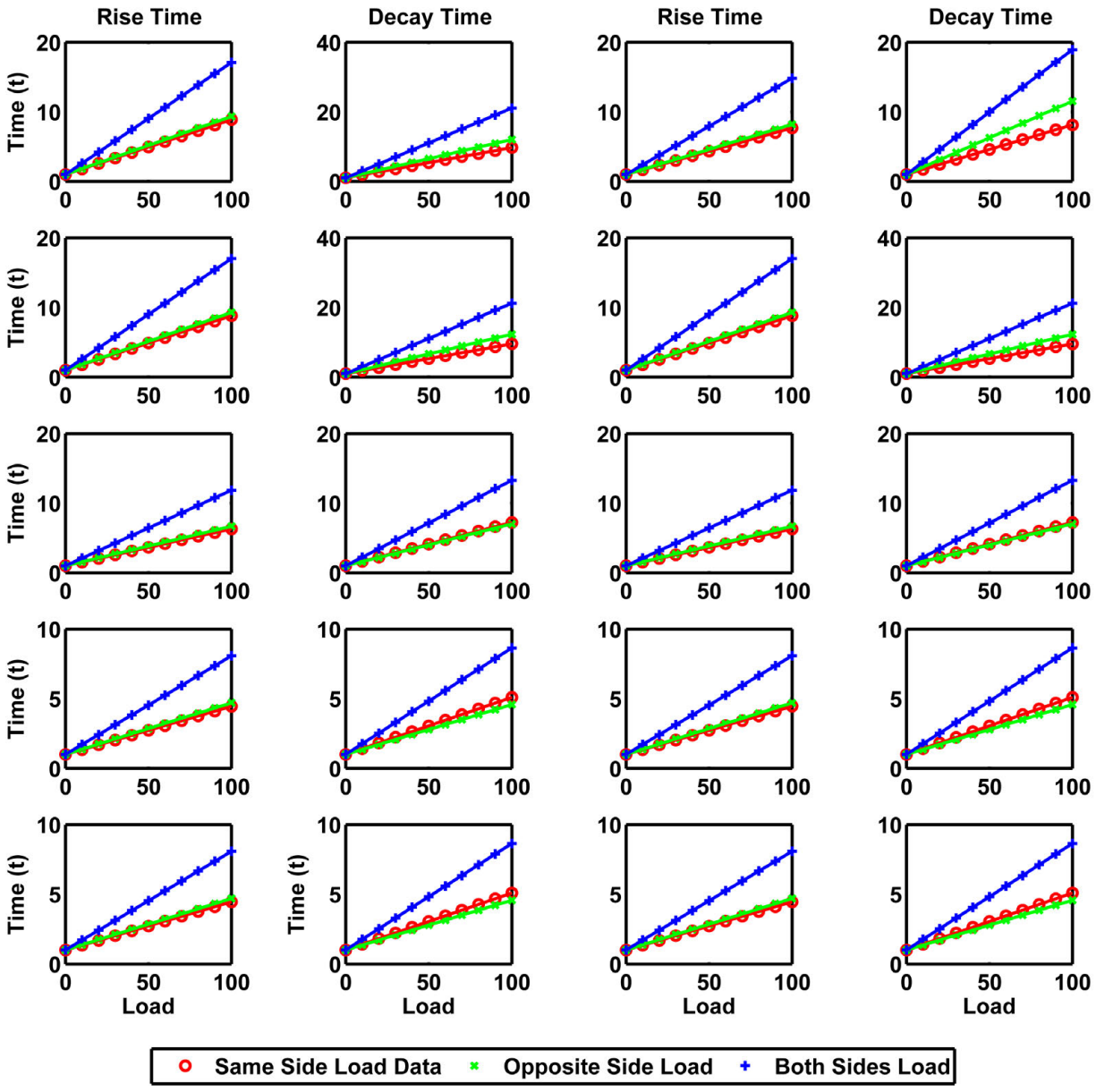

Figure S2.15. Transition times for various k′on and k′off values plotted as a function of load for the basic toggle switch.

Even if the binding-unbinding rates are slower or much faster than protein decay rates, the load-transition time relationship stays linear. A, C, E, G, I, K, M, O, Q and S show the rise time. B, D, F, H, J, L, N, P, R, and T show decay time. (A,B) k′on=4, k′off=0.5, Kd=0.125. (C,D) k′on=10, k′off=0.5, Kd=0.05. (E,F) k′on=4, k′off=4, Kd=1. (G,H) k′on=10, k′off=10, Kd=1. (I,J) k′on=4, k′off=20, Kd=5. (K,L) k′on=10, k′off=50, Kd=5. (M,N) k′on=4, k′off=40, Kd=10. (O,P) k′on=10, k′off=100, Kd=10. (Q,R) k′on=40, k′off=400, Kd=10. (S,T) k′on=100, k′off=1000, Kd=10.

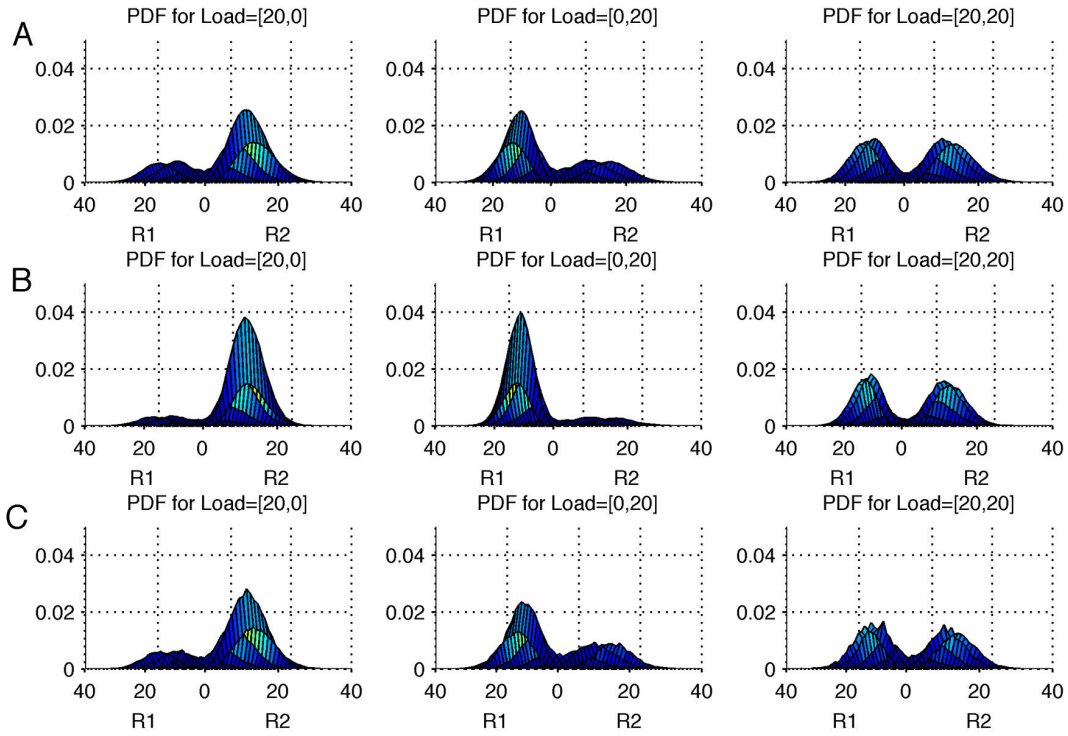

Figure S2.16. Probability distributions of repressor concentrations for various values of k′on and k′offfor the basic toggle switch.
Even when the binding-unbinding with the load is several times faster than protein decay rates, the basic phenomena discussed in the paper remains unchanged. (A) k′on=50, k′off=500 (B) k′on=500 k′off=500 (C) k′on=500 k′off=5000.

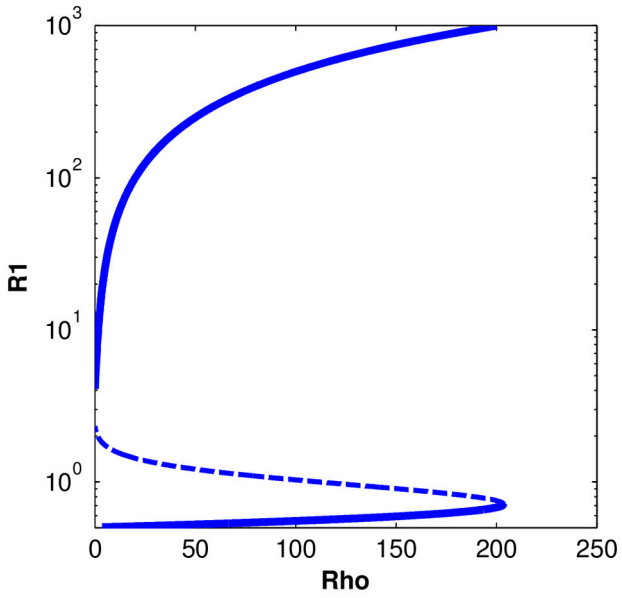

Figure S2.17. Bistability of the toggle switch with positive feedback.
A bifurcation diagram of the simple toggle switch with a positive feedback moiety on one side, with respect to the parameter ρ that measures the strength of the positive feedback. Only the concentration of R1 is shown for simplicity. The switch remains bistable till ρ becomes larger than a little over 200.

7.6 Supplemental tables

Table S2.1. Slopes of linear fits to rise and decay time with various values of Koff, Kon and β.

The first column reports the values of the dissociation constant (Kd=Koff/Kon) and the kinetic constants of the binding of Repressor 1, 2 or the value for β, which represents promoter strength. The other columns report the slopes of the linear fits of the various rise times and decay times. In all cases the fits have high R-squared values (>0.95). Intercept is 1, as the slopes are normalized to the un-loaded transition time. For Kd we change the parameters by two orders of magnitude in both directions to show that the linear relation is robust despite these changes. Note that the relation between rise time or decay time and the binding constant is non-monotonic. Units are as reported in the text.

	Rise Time			Decay Time		
	Same-Sided	Opposite Side	Both Sides	Same-Sided	Opposite Side	Both Sides
Koff=0.005; Kon=0.5; Kd= 0.01	4.59E-03	2.12E-03	6.72E-03	1.76E-03	1.01E-02	1.19E-02
Koff=0.05; Kon=0.5; Kd= 0.1	2.46E-02	2.75E-02	5.19E-02	2.50E-02	4.47E-02	7.10E-02
Koff=0.5; Kon=0.5; Kd= 1	7.80E-02	8.32E-02	1.60E-01	8.59E-02	1.13E-01	2.03E-01
Koff=5; Kon=0.5; Kd= 10	3.46E-02	3.71E-02	7.08E-02	4.11E-02	3.57E-02	7.66E-02
Koff=50; Kon=0.5; Kd= 100	4.68E-03	4.98E-03	9.62E-03	5.51E-03	4.25E-03	9.72E-03
Koff=0.5; Kon=50; Kd= 0.01	2.50E-04	3.93E-04	6.44E-04	3.34E-04	4.68E-04	8.01E-04
Koff=0.5; Kon=5; Kd= 0.1	2.83E-03	3.31E-03	6.14E-03	3.05E-03	5.36E-03	8.41E-03
Koff=0.5; Kon=0.5; Kd= 1	7.80E-02	8.32E-02	1.60E-01	8.59E-02	1.13E-01	2.03E-01
Koff=0.5; Kon=0.05; Kd= 10	3.45E-02	3.80E-02	7.15E-02	4.28E-02	3.47E-02	7.77E-02
Koff=0.5; Kon=0.005; Kd= 100	5.29E-03	5.24E-03	1.07E-02	5.89E-03	4.12E-03	1.03E-02
β1= β2 = 0.4	7.22E-02	1.48E-02	1.42E-01	2.08E-01	3.76E-02	2.46E-01
β1= β2 = 4	3.69E-03	1.62E-01	1.50E-01	5.29E-03	8.70E-02	9.76E-02
β1= β2 = 40	-	2.09E-01	2.02E-01	3.68E-05	9.20E-02	9.23E-02

Table S2.2. Exponential Fits of the amount of inducer required to transition states as a function of load.

The basic genetic toggle switch switch was toggled to its other state by production of the other repressor protein by an inducer, given here as a bolus with a decay rate as shown. The size of the bolus was increased until the state changed. This was repeated at different levels of load and the minimum size of the bolus required was fit by an exponential function of the load. The fits are shown here, along with their R-squared values. "Load applied to the opposite side" means switching from a state without a load to a state with a load. "Load applied to the same side" means switching from a state with a load to a state without a load.

Inducer Decay Rate (1/min)	Equation	R^2 Value
	Load Applied to both sides	
0.5	Inducer = 18.44*exp(0.305*Load)	0.99971
0.1	Inducer = 2.41*exp(0.0629*Load)	0.99627
0.05	Inducer = 2.00*exp(0.0308*Load)	0.99995
0.01	Inducer = 1.69*exp(0.006147*Load)	0.99271
0.005	Inducer = 2.23*exp(0.00294*Load)	0.99204
	Load Applied to the "opposite side"	
0.5	Inducer = 16.80*exp(0.108*Load)	0.999188
0.1	Inducer = 1.94*exp(0.0224*Load)	0.994335
0.05	Inducer = 1.54*exp(0.0111*Load)	0.993154
0.01	Inducer = 1.05*exp(0.00233*Load)	0.998114
0.005	Inducer = 0.972*exp(0.00116*Load)	0.996343
	Load Applied to the "same side"	
0.5	Inducer = 17.7*exp(0.219*Load)	0.999907
0.1	Inducer = 2.34*exp(0.0484*Load)	0.996021
0.05	Inducer = 1.91*exp(0.0239*Load)	0.997584
0.01	Inducer = 1.45*exp(0.00496*Load)	0.992406
0.005	Inducer = 1.46*exp(0.00245*Load)	0.991991

Table S2.3. Exponential Fits of the amount of inducer required to transition states as a function of load, in the case of induction by repression.
The switch was toggled to its other state by repression of the current state by an external molecule, given to the system as a bolus with a decay rate as shown. The size of the bolus was increased until the state changed. This was repeated at different levels of load and the minimum size of the bolus required was fit by an exponential function of the load. The fits are shown here, along with their R-squared value. Thus the inducer required depends exponentially on the load in both the methods of induction. "Load applied to the opposite side" means switching from a state without a load to a state with a load. "Load applied to the same side" means switching from a state with a load to a state without a load.

Inducer Decay Rate	Equation	R^2 Value
	Load Applied to Both Sides	
0.5	Inducer = 43.56*exp(0.506*Load)	0.999911
0.1	Inducer = 5.61*exp(0.111*Load)	0.998743
0.05	Inducer = 3.90*exp(0.0586*Load)	0.993461
0.01	Inducer = 3.08*exp(0.0117*Load)	0.991054
0.005	Inducer = 3.07*exp(0.00580*Load)	0.991298
	Load Applied to Opposite Side	
0.5	Inducer = 45.13*exp(0.0700 *Load)	0.999526
0.1	Inducer = 5.12*exp(0.0127*Load)	0.999407
0.05	Inducer = 3.42*exp(0.00663*Load)	0.996845
0.01	Inducer = 2.68*exp(0.00130*Load)	0.99715
0.005	Inducer = 2.49*exp(0.000665*Load)	0.994754
	Load Applied to Same Side	
0.5	Inducer = 47.01*exp(0.413*Load)	0.999474
0.1	Inducer = 8.35*exp(0.0839*Load)	0.993501
0.05	Inducer = 5.35*exp(0.0450*Load)	0.995209
0.01	Inducer = 4.98*exp(0.00881*Load)	0.995697
0.005	Inducer = 4.54*exp(0.00450*Load)	0.993970

Table S2.4. Slopes of linear fits to rise and decay time with a dynamic load, with varying values of load decay rate Kd, load binding rates Kon and Koff, and constant K1.
The first four columns report the values of the various parameters. The other columns report the slopes of the linear fits of the various rise times and decay times. In most cases the fits have high R-squared values (>0.95). The two exceptions are >0.90 and starred. Intercept is 1, as the slopes are normalized to the un-loaded transition time. Note that for all cases, the relationship between load (expressed here as Keq=Kb/Kd) and transition time is a positive linear relationship.

				Rise Time			Decay Time		
Kd	K1	Kon	Koff	Same	Opposite	Both	Same	Opposite	Both
0.5	1	0.5	0.5	0.498	0.345	0.502	0.423	0.179	0.460
0.5	**5**	0.5	0.5	1.333	0.518	0.340	0.463	0.773	0.435
0.5	**0.5**	0.5	0.5	0.264	0.224	0.343	0.308	0.089	0.337
0.05	1	0.5	0.5	0.044	0.483	0.547	0.622	0.058	0.628
5	1	0.5	0.5	0.357	0.332	0.437	0.393	0.187	0.427
0.5	1	**5**	0.5	4.367	0.540	0.520	0.535	1.767	0.578
0.5	1	**0.05**	0.5	0.062	0.059	0.100	0.093	0.014	0.105
0.5	1	0.5	**5**	0.057	0.055	0.093	0.084	0.017	0.093
0.5	1	0.5	**0.05**	4.538	0.582	0.506	0.578	1.835	0.625

Table S2.5. Rate expressions used for the stochastic simulations of the genetic toggle switch.
The rate expressions used for the stochastic simulation of the toggle switch along with the description of the reaction are listed.

Rxn	Rate Expression	h_i	Description of rate
1	h_1*R1	α_1*V	Basal production promoter 1
2	h_2*R1	β_1/(1+R2/V)^n_1)	Repressed production promoter 1
3	-h_3*R1	D*R1	Degradation
4	h_4*R1-h_4[R1:L1]	k_{off}*[R1:L1]	Unbinding from load
5	-h_5*R1+h_5[R1:L1]	k_{on}*R1	Binding to load
6	h_6*R2	α_2*V	Basal production promoter 2
7	h_7*R2	β_2/(1+R2/V)^n_2)	Repressed production promoter 2
8	-h_8*R2	D*R2	Degradation
9	h_9*R2-h_9[R2:L2]	k_{off2}*[R2:L2]	Unbinding from load
10	-h_{10}*R2+h_{10}[R2:L2]	k_{on2}*R2	Binding to load

Table S2.6. List of reactions in the minimal model of Ras activation.
The reactions in the minimal model of Ras activation, along with the labels of the corresponding rate constants are shown. Parameters used in the simulations are given in Table S2.7.

$Reactions$
$SOScat + RasGDP \overset{kon\,1,koff\,1}{\longleftrightarrow} SOScat(RasGDP)$
$SOScat + RasGTP \overset{kon\,2,koff\,2}{\longleftrightarrow} SOScat(RasGTP)$
$(RasGTP) + RasGDP \overset{kon\,3,koff\,3}{\longleftrightarrow} SOScat(RasGTP){:}\,RasGDP \xrightarrow{kcat\,3} SOScat(RasG$ $+ RasGTP$
$(RasGDP) + RasGDP \overset{kon\,4,koff\,4}{\longleftrightarrow} SOScat(RasGDP){:}\,RasGDP \xrightarrow{kcat\,4} SOScat(RasG$ $+ RasGTP$
$RasGAP + RasGTP \overset{kon\,5,koff\,5}{\longleftrightarrow} RasGAP{:}\,RasGTP \xrightarrow{kcat\,5} RasGAP + RasGDP$
$RasGTP + Raf \overset{kon\,6,koff\,6}{\longleftrightarrow} RasGTP{:}\,Raf$

Table S2.7. Kinetic rate parameters used for the simulations of the Ras model.
Here the numbers in the subscript of the rate constants in the "Constant" column refer to the reactions shown in the corresponding row of Supplementary Table S2.6. The meaning of the rate constants are as follows: kon refers to the on-rate, koff is the off rate and kcat is the catalytic rate. The sources for the rates are as shown in the last column.

Rxn	Constant	3D Rate Values	Units	2D Rate Values	Units	Reference
1	k_{on1}	0.12	$\mu M^{-1}\ s^{-1}$	0.028	$Molecules^{-1}\ s^{-1}$	[2]
1	k_{off1}	3.0	s^{-1}	3.0	s^{-1}	[2]
2	k_{on2}	0.11	$\mu M^{-1}\ s^{-1}$	0.026	$Molecules^{-1}\ s^{-1}$	[2]
2	k_{off2}	0.4	s^{-1}	0.4	s^{-1}	[2]
3	k_{on3}	0.05	$\mu M^{-1}\ s^{-1}$	0.0118	$Molecules^{-1}\ s^{-1}$	[2]
3	k_{off3}	0.1	s^{-1}	0.1	s^{-1}	[2]
3	k_{cat3}	0.038	s^{-1}	0.038	s^{-1}	[2]
4	k_{on4}	0.07	$\mu M^{-1}\ s^{-1}$	0.0165	$Molecules^{-1}\ s^{-1}$	[2]
4	k_{off4}	1.0	s^{-1}	1.0	s^{-1}	[2]
4	k_{cat4}	0.003	s^{-1}	0.003	s^{-1}	[2]
5	k_{on5}	1.74	$\mu M^{-1}\ s^{-1}$	0.41	$Molecules^{-1}\ s^{-1}$	[2]
5	k_{off5}	0.2	s^{-1}	0.2	s^{-1}	[2]
5	k_{cat5}	0.1	s^{-1}	0.1	s^{-1}	[2]
6	k_{on6}	29.6e6	$M^{-1}\ s^{-1}$	6.96	$Molecules^{-1}\ s^{-1}$	[3]
6	k_{off6}	5.22	s^{-1}	5.22	s^{-1}	[3]

Table S2.8. List of reactions in the toy model of genetic toggle switch.
The reactions in the toy model of the genetic toggle switch, discussed in Supplementary Text S2.1 are listed. The description of the various chemical species in the reactions are also provided in the Supplementary Text S2.1.

Reactions	*Index*
AR_1 *Module*	
$R_1 + R_1 + R_1 \underset{k_2}{\overset{k_1}{\rightleftharpoons}} AR_1$	*P1*
$AR_1 + Pro_1 \underset{k_4}{\overset{k_3}{\rightleftharpoons}} AR_1 : Pro_1$	*P2*
$Pro_1 \xrightarrow{\alpha_2} Pro_1 + R_2$	*P3*
$AR_1 : Pro_1 \xrightarrow{k_5} Pro_1$	*P4*
$AR_1 \xrightarrow{k_6} \varnothing$	*P5*
$R_1 \xrightarrow{k_7} \varnothing$	*P6*
$R_1 + L_1 \underset{k_{off\,1}}{\overset{k_{on1}}{\rightleftharpoons}} R_1 : L_1$	*P7*
AR_2 *Module*	
$R_2 + R_2 + R_2 \underset{k_9}{\overset{k_8}{\rightleftharpoons}} AR_2$	*P8*
$AR_2 + Pro_2 \underset{k_{11}}{\overset{k_{10}}{\rightleftharpoons}} AR_2 : Pro_2$	*P9*
$Pro_2 \xrightarrow{\alpha_1} Pro_2 + R_1$	*P10*
$AR_2 : Pro_2 \xrightarrow{k_{12}} Pro_2$	*P11*
$AR_2 \xrightarrow{k_{13}} \varnothing$	*P12*
$R_2 \xrightarrow{k_{14}} \varnothing$	*P13*
$R_2 + L_2 \underset{k_{off\,2}}{\overset{k_{on2}}{\rightleftharpoons}} R_2 : L_2$	*P14*

REFERENCES

1. Das J, Ho M, Zikherman J, Govern C, Yang M, et al. Digital signaling and hysteresis characterize ras activation in lymphoid cells. *Cell*. 2009; 136: 337-351.

2. Prasad A, Zikherman J, Das J, Roose JP, Weiss A, et al. Origin of the sharp boundary that discriminates positive and negative selection of thymocytes. *Proc Natl Acad Sci.* 2009; 106: 528-533.

3. Kiel C, Serrano L. Cell type-specific importance of ras-c-raf complex association rate constants for MAPK signaling. *Science Signaling.* 2009; 2: ra38.

APPENDIX II: SUPPLEMENTARY INFORMATION FOR CHAPTER 3

8.1 Supplementary Methods

8.1.1 Plasmid constructions and schematic diagrams

All plant toggle switch plasmids were assembled following standard molecular cloning techniques. Primers and gBlocks were ordered from Integrated DNA technologies (IDT) and PCR reactions were performed with Herculase II (Agilent) or Phusion DNA polymerase (New England BioLabs) according to manufacturers' protocols. In order to prevent transcription read-through among the genetic components, consecutive transcriptional units were insulated by transcription blocks [1]. All the genetic components used to assemble the necessary plasmids are listed in **Table S3.1**. Plasmids were verified by DNA sequencing before using for plant transformation. DNA sequencing was provided by the Colorado State University Proteomics and Metabolomics Facility. Stable co-transformation of plants with TKK121 and TKK109 binary plasmids resulted in Toggle 1.0 (**Fig. S3.1a & b**). Toggle 2.0 contains all the toggle switch components in a single T-DNA (TKK489, in a pGREENII0229 vector backbone) (**Fig. S3.1c**). Stable co-transformation of plants with TKK489 and TKK663 plasmids resulted in Toggle 2.1 (**Fig. S3.1c & d**). TKK121 plasmid is in a modified pCambia2300 vector backbone (PAB2300) where the kanamycin resistance nptII gene is replaced by the Basta resistance BAR gene. TKK109 and TKK663 plasmids are in the kanamycin resistant pCAMBIA2300 binary vector backbone. TKK489 is in the Basta resistant pGREENII0229 vector backbone.

The schematic for the mutual repression arrangement of Toggle 1.0 is depicted in **Fig. S3.2**. The circuit is composed of two transcriptional repressors, two constitutive and repressible promoters, two inducible promoters and one reporter gene (Luciferase) as readout to quantify the

ON/OFF switch behaviors. Toggle 1.0 is based on $35S_{2xLexA}$ and NOS_{2xGal4} promoters in a 2:1 combination, respectively (**Fig. S3.2**). Similar to the original toggle switch circuit[2], two possible stable states are expected without applying external input signals. When $35S_{2xLexA}$ promoter transcribes the GEAR repressor, the circuit is set in the low state (low luciferase expression levels). Alternatively, when the NOS_{2xGal4} promoter transcribes the LEAR repressor, the circuit is set in the high state (high luciferase expression levels). To switch between stable states, expression of an extra copy of the genes encoding the repressors is placed under control of chemical inducible systems, dexamethasone (DEX) and 4-hydroxytamoxifen (4-OHT). In Toggle 1.0, 4-OHT induces switching to the high state, *i.e.*, the production of LEAR repressor, which results in luciferase expression (**Fig. S3.2c**). On the other hand, DEX induces the production of GEAR, which represses luciferase expression (low state) (**Fig. S3.2a**). A bistable toggle switch maintains its high (**Fig. S3.2d**) or low (**Fig. S3.2b**) states in the absence of an inducer.

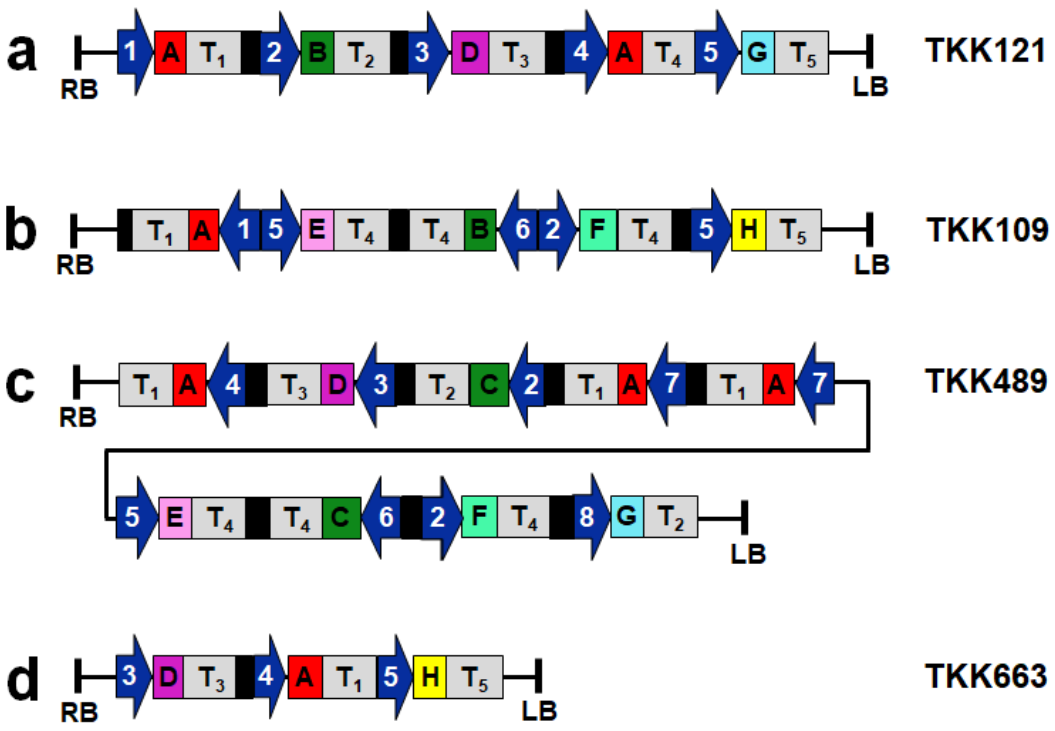

Figure S3.1. **T-DNA regions of the toggle switch plasmids used for plant transformation.** **a**, Schematic diagram of the T-DNA region of Basta (glufosinate ammonium) resistant TKK121 plasmid. **b**, Schematic diagram of the T-DNA region of Kanamycin resistant TKK109 plasmid. Plants co-transformed with binary plasmid **a** and **b** resulted in Toggle 1.0. **c**, Toggle 2.0 components in a single plasmid (TKK489). **d**, The additional DEX inducible Gal4EAR repressor in TKK663 plasmid. Plants co-transformed with binary plasmids in **c** and **d** resulted in Toggle 2.1. Promoters are indicated by blue solid arrow heads and numbered from 1 to 8 (1, $35S_{2xLexA}$; 2, NOS_{2xGal4}; 3, FMV; 4, pOp6; 5, 35S; 6, 10xN1; 7, $35S_{4xLexA}$TATA; 8, NOS). The green and red solid boxes represent synthetic repressors and are labeled as A, B and C (A, Gal4EAR; B, LexAEAR; C, LexAOFPx). D and E are transcription factors for DEX (LhGR2) and 4-OHT (NEV) inducible promoters, respectively. Gray solid boxes labeled T_1 to T_5 are terminators. T_1, OCS terminator; T_2, NOS terminator; T_3, Pea3A terminator; T_4, E9 terminator; T_5, CaMV35S terminator. Transcription blocks are denoted by solid black rectangles. F, Firefly luciferase; G, BAR gene; H, nptII gene; LB, left border; RB, right border.

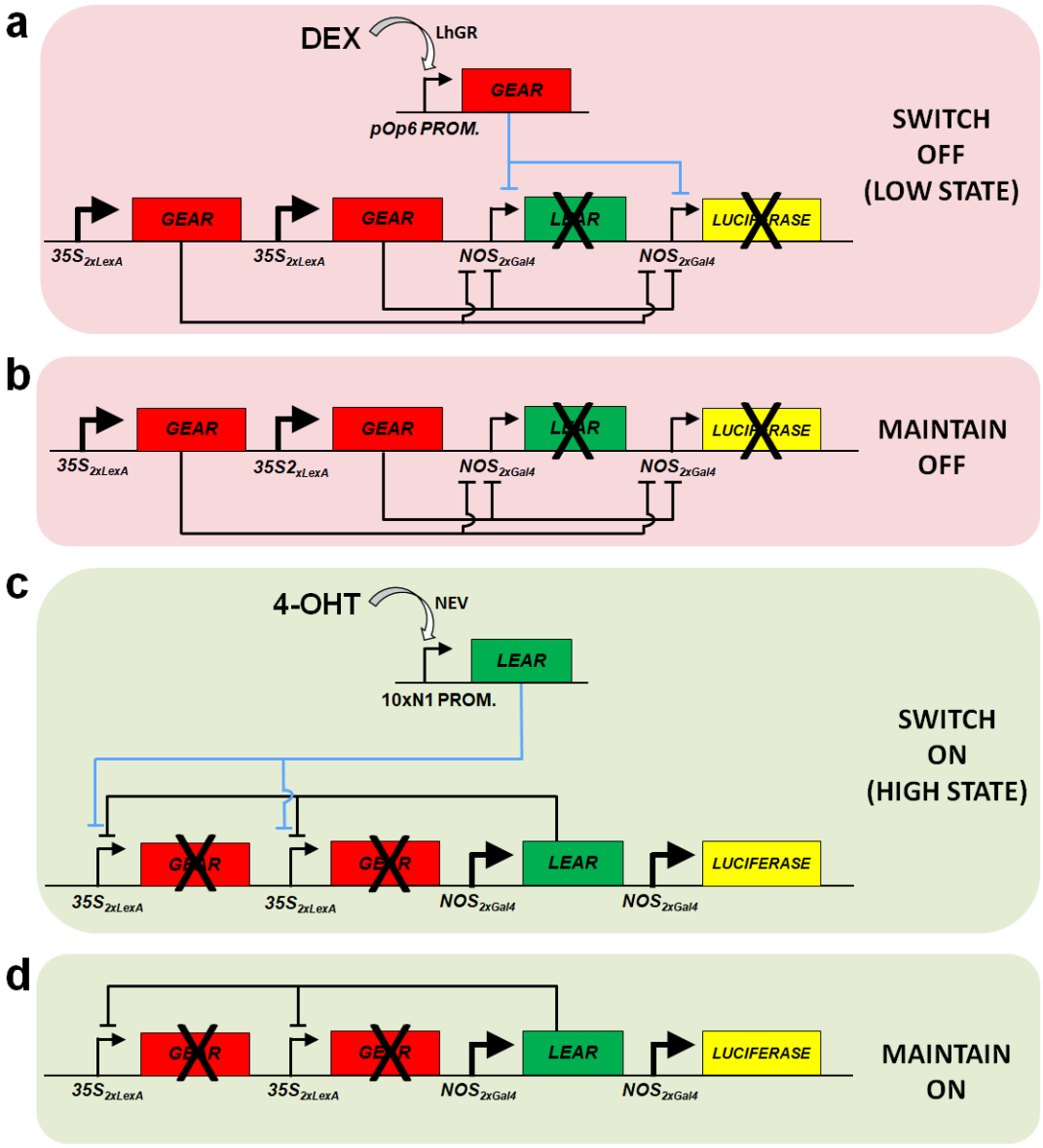

Figure S3.2. Schematic representations of Toggle 1.0.
Repressors GEAR (Gal4EAR) and LEAR (LexAEAR) mutually repress expression of each other by binding to the repressible promoters, NOS_{2xGal4} and $35S_{2xLexA}$, respectively. **a-b**, DEX induces expression of an additional copy of GEAR repressor that binds to and represses two copies of the promoter NOS_{2XGal4}, enabling (**a**) the switch to the low state and (**b**) maintenance of the low state without the inducer. **c-d,** OHT induces expression of an additional copy of LEAR repressor that binds to and represses two copies of the promoter $35S_{2xLexA}$, enabling (**c**) the switch to the high state and (**d**) maintenance of the high state without the inducer. Firefly luciferase provides a quantitative readout of circuit function.

8.1.2 Image Processing

To quantify the performance of the different toggle switch circuits in transgenic plants and make comparable quantifications across different time points and treatments, image-processing software was developed with the ability to distinguish the luminescence signals emitted from shoots and roots (**Fig. S3.3**). The software combines a series of image-processing steps into a workflow. To ensure accuracy of the image processing and reduce possible artifacts, each step in the workflow is fully supervised by the user. The software first loads a high resolution digital color image of the plants and identifies the regions of interest (ROIs) in shoots and roots separately through user-supervised color thresholding (**Fig. S3.3a)**. During this step, ROIs corresponding to different plants are also separated and indexed for further image processing. An image registration step is then carried out between the high resolution and the bright-field images obtained by the luciferase camera by user defined control points ($n \geq 2$) **(Fig. S3.3b)**. This step provides the necessary information about the orientation, spatial shift and scaling to properly align the ROIs to the bright-field image. After the alignment, the ROIs are grouped by the user into individual plants. As shown in **Fig. S3.3c-d**, leaf ROIs 1, 2 and 3 were assigned to plants indexed as 1, 2 and 3, respectively. Similarly, root ROIs 1 and 2 were assigned to plant 1, ROI 3 to plant 2, and ROIs 4 and 5 to plant 3. In the next step, the ROIs of shoots and roots of individual plants are applied to the luciferase luminescence images and several pixel-based measurements are carried out and recorded for further analysis (**Fig. S3.3e-f)**. These measurements of leaf and root ROIs include area in pixels, total intensity levels and a list of intensity levels per pixel.

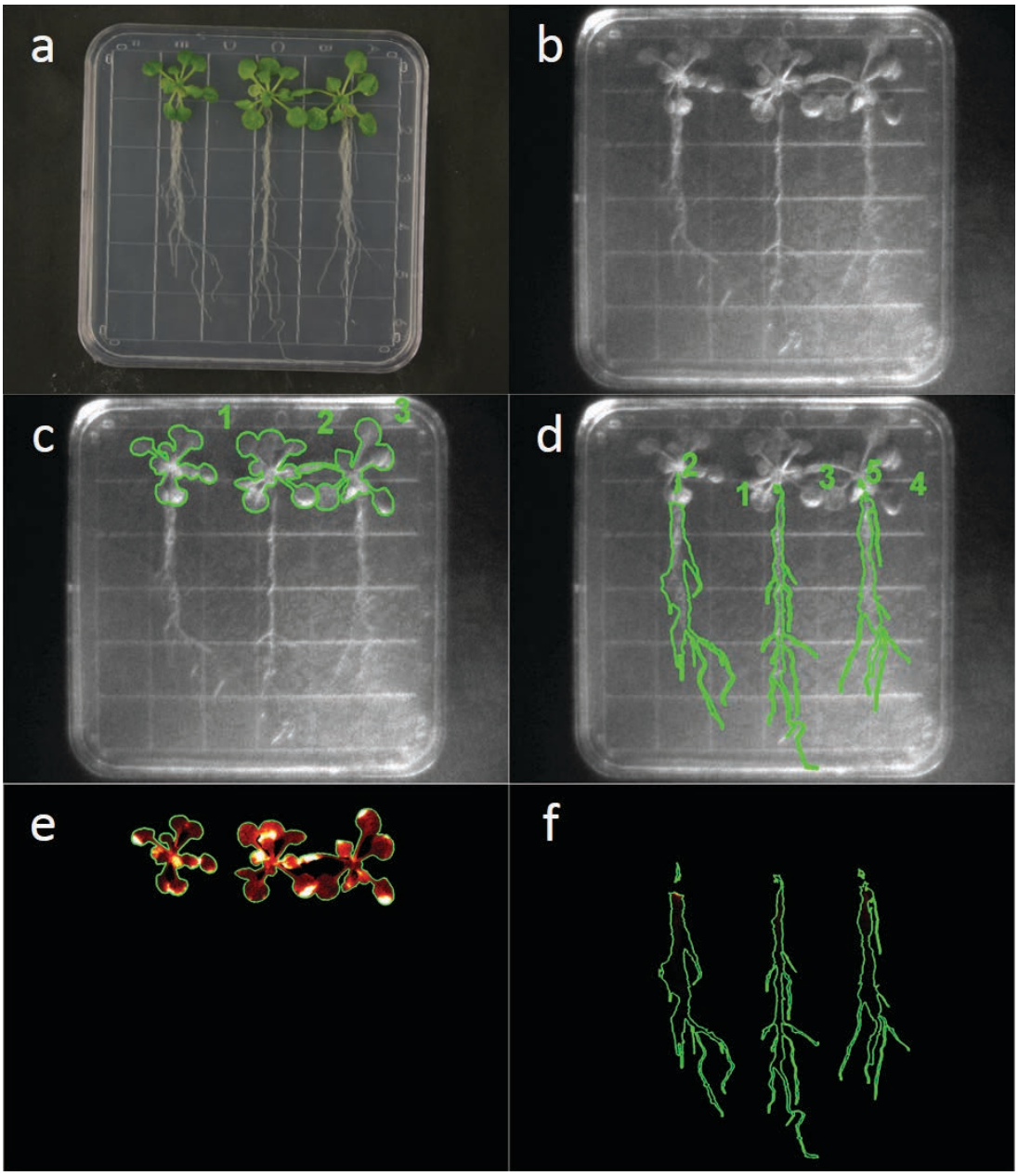

Figure S3.3. Whole plant image processing.
a, High resolution color image collected using a regular digital camera under well controlled lighting conditions prior to the luciferase imaging, which was used for color thresholding and identifying the regions of interest (ROIs) of shoots and roots for individual plants. **b**, Bright-field image collected *in situ* under the luciferase camera, which was used to align the ROIs obtained from **a**). It should be noted that there are differences in resolution, orientation and lighting conditions between **a)** and **b**). **c-d**, ROIs of shoots (**c**) and roots (**d**) aligned with the bright-field image with ROIs indexed spatially. **e-f**, ROIs of shoots (**e**) and roots (**f**) applied to the luminescence images.

8.1.3 Data Analysis and Fold Change Calculation

As we reported in a previous study [2], the distribution of luciferase luminescence per tissue of an individual plant was found to be well described by a lognormal distribution (*i.e.*, a Gaussian distribution after a logarithmic transformation). The sample mean and standard deviations were therefore calculated on a logarithmic scale, for increased accuracy.

Fold changes were calculated by dividing the mean luciferase data on the last day in the experiment by the mean data on the day immediately before changing an inducer. A fold change of one means there is no change. The mean and standard deviation of fold change were first calculated on a logarithmic scale, and then converted back to linear scale. A 2-sample two-sided t-test was used to test whether the differences between fold changes of two different treatments are statistically significant. The test was done on the fold change of individual plants in logarithmic scale. A p-value smaller than 0.05 was deemed as statistically significant.

8.1.4 MCMC Parameter Fitting and Estimation of Bistability

In order to quantitatively test whether the whole-plant luminescence data indicated a bistable or a monostable switch, we devised a novel method to fit the ODE representation (**Equation S3.1**) of the toggle switch to the whole-plant luminescence data. Similar to the ODE models used in **Section 8.4.1**, the main part of the ODE representation consists of two Hill functions describing the input-output characteristics of the two mutually repressible promoters and first-order degradation terms. Two additional terms were introduced in **Equation S3.1** to better model the toggle switches tested in plants. First, as shown in **Fig. 3.1** in the chapter 3, the plant toggle switch was switched between the two different states (LOW and HIGH) using two inducible promoters (DEX and 4-OHT). The behavior of the inducible promoters was modeled using a product of a binary term (k_{DEX} and k_{OHT}, with a value of either 0 or 1 based on the

absence or presence of inducer, respectively) and a constitutive expression term (α_{DEX} and α_{OHT}, promoter strengths of the inducible promoters) in the ODEs. Secondly, leaky expression terms (α_x and α_y, basal expression levels of the promoters producing X and Y repressors, respectively) were also added to the Hill functions to better describe the behaviors of the repressible promoters, and address the increase in the complexity of the system.

$$\frac{dX}{dT} = k_{OHT}\alpha_{OHT} + \alpha_x + \frac{b_x}{1 + \left(\frac{Y}{K_x}\right)^{n_x}} - d_x X$$

$$\frac{dY}{dT} = k_{DEX}\alpha_{DEX} + \alpha_y + \frac{b_y}{1 + \left(\frac{X}{K_y}\right)^{n_y}} - d_y Y \qquad \textbf{Eqn. S3.1}$$

To reduce the number of free parameters and the dimensionality of the problem, we assumed the two degradation rate constants of the repressors to be the same. To fit this model to the whole plant luminescence data, we defined a log likelihood function as the negative logarithm of the squared distances between the experimental data and numerical solutions of **Equation S3.1**. The log likelihood function is evaluated as a weighted average of all seven different treatments, namely Low to Low, Low Memory, Low to High, Control, High to Low, High Memory and High to High. We used Markov Chain Monte Carlo (MCMC) to estimate the maximum-likelihood parameter values of the toggle switch tested in plants. The model parameters were initialized as a uniformly distributed random variable inside the parameter space. At each iteration, a Gaussian displacement was proposed for each parameter sequentially and the log likelihood function evaluated for every new set of parameter values. The proposed parameter set was accepted according to typical Metropolis criteria, where a proposed parameter value was either always accepted if it increased the log likelihood, or occasionally accepted (*i.e.*, accepted with a probability) if it decreased the log likelihood [3]. The MCMC run was

terminated if either the maximum number of iterations (10,000) was reached, or convergence was achieved, defined as no significant change in log likelihood for more than 500 iterations. The last instance was treated as a successful MCMC run, and the parameters obtained were stored. These parameters were then filtered using an additional quality control criterion: eliminate fits with Hill coefficients greater than 6 on the grounds that such high Hill coefficients are not expected in these constructs. The goodness of fit as measured by the value of the log likelihood function was bimodal in most cases, with a distinct population that clustered with the optimal fit and another population with lower values of the log likelihood that also clustered together. Parameter sets estimated by successful MCMC runs and that passed the quality control criterion were deemed as good parameter sets and retained for further analysis. Parameter sets that clustered around the optimal value obtained from the goodness of fit were deemed best parameter sets, and were also analyzed separately in some cases. Note that the best parameter sets are a subset of the good parameter sets. The fitting procedure was repeated at least 1,000 times (and up to 10,000 times) for the three toggle switch circuits to sample the entire parameter space.

The good parameter sets acquired in the MCMC were then evaluated for the bistability of a specific toggle design. For this evaluation, the inducible terms ($k_{OHT}\alpha_{OHT}$ and $k_{DEX}\alpha_{DEX}$) in the ODE model presented in the **Equation S3.1** were removed, since only the bistability of the repressible pairs is relevant, and the ODE model was simulated with the remaining parameter values. The ODEs were simulated numerically, starting from two different initial conditions (high in one state and low in the other one), and the results checked for bistability. We found that the numerical solutions fell in three classes: monostable, bistable or “indistinguishable from bistable”.

A parameter set was bistable if two different steady state values were achieved at the end of the solution, and deemed as monostable if the same steady state was achieved for both instances. A parameter set that is indistinguishable from bistable was defined as one that produced two trajectories that remained separate and relatively stable for a time longer than the experimental timescale of 15 days. In addition, "relatively stable" was defined numerically as a relative daily change (absolute difference over the average level of a day) smaller than 10% within the given state. The bistable and "indistinguishable from bistable" parameter sets were together classified as "bistable for the duration of the experiment".

Our data showed qualitative differences in the behavior of the circuit in the roots versus the shoots of the plants. We quantitatively evaluated these differences by performing the MCMC fitting procedure separately for the two tissues. We repeated the fitting procedure using the data from the plant experiment in two different ways: (i) We fitted the mean of all the technical replicates for each data point for each experimental condition, for both roots and shoots; (ii) We fitted the root or shoot data of each technical replicate separately, by adding a random selection step where the algorithm arbitrarily chooses a technical replicate before fitting. This is equivalent to fitting each technical replicate separately and pooling the data.

We report results of each fitting procedure separately, and report the results of the selected technical replicates whose luminescence heatmap images are shown in the main text. Note that each technical replicate involves seven experimental conditions, each performed with a different plant, that are genetically identical in the composition of the toggle circuit. Detailed analysis of transgene insertion indicates normal events (**Section 8.2.9**) The technical replicates are, with the abbreviations used in parenthesis, (i) Control, (ii) Low state memory (Low Mem), (iii) Low state treated with the switching-on inducer (Low-High), (iv) Low state treated with the switching-off

inducer (Low-Low), (v) High state treated with the switching-on inducer (High-High), (vi) High state memory (High Mem), (vii) High state treated with the switching-off inducer (High-Low). Thus, fitting the data of a technical replicate involves fitting a single ODE model to all the time-course data from a genetically identical toggle circuit in seven independent plants under seven different conditions.

8.2 Supplementary Data

8.2.1 Design of Toggle 1.0 and Toggle 2.0

Building a toggle switch in plants requires genetic parts that produce bistable behavior when combined in the appropriate circuit topology. For the double repressor circuit topology, we can describe bistable bounds for the parameters of the transfer function of the two repressor-promoter pairs by two principles, as follows (previously identified in Gardner et al. [4], and described in **Section 8.4.1** in more detail). A successful bistable toggle switch requires 1) a sigmoidal repressor response with a high Hill coefficient, and 2) High expression levels, from each promoter, that are balanced and mathematically made dimensionless. The latter is explicitly defined below in **Equation S3.3** (below)

We have previously published our methods for construction and characterization of a library of repressor-promoter pairs [2], briefly summarized in **Section 8.4.2**. Comparison of quantitative parameters estimated from transient expression of components in protoplasts with those estimated from stable expression in plants yielded parameters that were approximately within a factor of two of each other, with the discrepancies most likely due to effects arising from the random integration of the synthetic circuit in the plant genome. This level of possible discrepancies led us to conclude that while quantitative predictions based on these parameters were likely to be subject to significant error, we could still use the two bistability criteria defined

above to design a mutual repression-based toggle switch. The first putative combination to satisfy the required criteria very early on was the combination consisting of NOS_{2xGal4}.EAR and $35S_{2xLexA}$.EAR, which had Hill coefficients above 3 and 2, respectively (**Table S3.10**). However, the Gal4-based repressible promoter was found to have a higher maximal expression, and to balance the promoter strengths we combined two copies of the LexA-based promoter with one copy of the Gal4-based promoter (**Table S3.10**). This construct is described as Toggle 1.0 in the text. Given the time requirements for production of plants with stable integration of synthetic genetic circuits, we began to assemble this construct in plants while we continued testing many other promoter-repressor pairs. After testing about 120 such genetic circuits, the high sigmoidality criteria led to identification of three promoter-repressor pairs where at least one experimental replicate was fit by a Hill function with a Hill coefficient, n, greater than 3 ($35S_{4xLexA}$TATA.OFPx, $_{2xGal4}$NOS.EAR and NOS_{2xGal4}.EAR). Of these three, the combination consisting of two copies of $35S_{4xLexA}$TATA.OFPx and one copy of NOS_{2xGal4}.EAR paired the best in terms of balanced dimensionless maximum expression levels, since here too the Gal4-based promoter was found to be stronger (**Table S3.10**). This genetic circuit was assembled and is labeled as Toggle 2.0 in the text.

8.2.2 Time to reach a steady state

In addition to bistability, efficient switching between two stable states (High or Low) by temporary induction is a requirement for a genetic switch. To determine the switching time of the toggle circuits from the high to low state and from the low to the high state, we first probed steady state behavior by continuous induction with either 4-OHT or DEX. All three toggle circuits reached and maintained steady state levels of protein production around 96 hours (4

days) after induction (**Fig. 3.5**), with slight variations. Hence, we chose 4 days after induction to switch between states, or to assess the memory of the state.

8.2.3 Data Analysis of Toggle 1.0

Luminescence heat maps of whole plants carrying Toggle 1.0 are shown in **Fig. 3.6.** The plots were reconstructed using the raw luciferase luminescence images and the ROIs acquired from the image processing as described in the **Section 8.1.2**. One plant in each treatment is shown as an example, whereas data are collected from a minimum of three genetically identical plants per treatment. From analysis of the data such as that shown in the heat maps, the Low and High states were well established and the switching behaviors between the two steady states were as expected. However, the High Memory state did not show stability, with no obvious differences from the High to Low treatment. Interestingly, the roots seemed to perform better than shoots in terms of luminescence intensity and switching behavior.

These observations were supported by quantitative data showing the temporal luminescence intensity profiles (**Fig. 3.7a & b**) and population mean fold change (**Fig. 3.7c & d**). **Fig. 3.7a & b** shows the intensity profile of shoots and roots, respectively, as extracted from the heatmaps (**Fig. 3.6)**. The behavior of the toggle switch showed some significant quantitative differences between shoots and roots. The mean fold change of Low to High was 21.3-fold for roots compared to 2.3-fold for shoots. For High to Low, the mean fold change of roots was 24.9-fold, and 3.9-fold for shoots. However, both shoots and roots failed to establish a stable High State as predicted for a toggle switch, as the differences between the High Memory and High to Low are not statistically significant from the 2-sample t-test.

8.2.4 MCMC Parameter Estimation Results for Toggle 1.0

Shoots: (i) Fits to the means: 239 parameter sets met the criteria for good parameter sets (discussed in the **Section 8.1**), of which 2 were bistable and an additional 3 were indistinguishable from bistable. Thus, about 2.1% of parameter sets showed bistability for the duration of the experiment. Of these 239 parameter sets, 90 were classified as best parameter sets and they included all 5 parameter sets that showed bistability for the duration of the experiment (5.56%).

(ii) Pooled fits to each technical replicate: 167 parameter sets met the criteria for good parameter sets, of which 6 were bistable and 2 were indistinguishable from bistable (for a total of 4.8%). When using this random sampling of replicates method, we only report results of all the good parameter sets.

(iii) Fits to the data of **Fig. 3.6**: We obtained 141 good parameter sets of which 0 were bistable.

Roots: (i) Fits to the means: We found 325 good parameter sets of which 0 were bistable.

(ii) Pooled fits to each technical replicate: Of 100 good parameter sets, 3 were bistable and none were indistinguishable from bistable.

(iii) Fits to the data of **Fig. 3.6**: We found 244 good parameter sets of which 0 were bistable.

Based on these results we classified Toggle 1.0 as a monostable system.

8.2.5 Data Analysis of Toggle 2.0

The intensity plots shown in **Fig. 3.9c & f**, shows that the Low and High states of Toggle 2.0 were well established. The High state of shoots was maintained even after the 4-OHT inducer was removed, as expected for a functional toggle switch (**Fig. 3.9e**). However, the addition of

DEX inducer to switch from the High to the Low state (**Fig. 3.9g**) did not produce an effective switch, and in fact the luminescence on the final day was not statistically significantly different from the High Memory (**Fig. 3.9e**). Interestingly, and distinct from Toggle 1.0, the shoots had some performance which was better in Toggle 2.0 than in Toggle 1.0, with a mean fold change of 37.5 (compared to a fold-change of 2.3 in Toggle 1.0), as shown in **Fig. 3.10c**. On the other hand, the roots of Toggle 2.0 performed similarly to Toggle 1.0. It is noteworthy that the Low to High change in luminescence was almost two orders of magnitude, a fold-change of 80 (**Fig. 3.10d)**.

8.2.6 MCMC Parameter Estimation Results for Toggle 2.0

Shoots: (i) Fits to the means: We obtained 1,141 good parameter sets (after running the MCMC algorithm 10,000 times), of which 278 were bistable and 822 were indistinguishable from bistable (totaling 96.4%). Out of these, 1,079 were best parameter sets, of which 260 were bistable and 812 indistinguishable from bistable (totaling 99.4%).

(ii) Pooled fits to each technical replicate: Of 111 good parameter sets, 22 were bistable and 84 were indistinguishable from bistable, totaling 95.5%.

(iii) Fits to data of **Fig. 3.9**: Almost all the good parameter sets here were also best (142/146). Of the 146 good sets, 21 were bistable and 121 were indistinguishable from bistable (in total 97%).

Roots: (i) Fits to the means: 134 parameter sets were good (and also best); of these none were bistable.

(ii) Pooled fits to each technical replicate: 134 parameter sets were good (and best), and none of these was bistable.

(iii) Fits to the data of **Fig. 3.9**: Almost all the parameter sets were best (129/132). Out of 132 good parameter sets, 1 was bistable and 1 indistinguishable from bistable.

The MCMC fits therefore suggest that the Toggle 2.0 circuit is behaving like a bistable toggle switch in the shoots and a monostable system in the roots. However, since the luminescence change from High to Low in the leaves was not statistically significant, we surmised that the inducible promoter driving expression of the GEAR repressor is not sufficiently strong (our data do not distinguish whether it is the promoter or the GEAR repressor). Toggle 2.1 therefore was constructed with two copies of this inducible promoter driving expression of the GEAR repressor as detailed in **Section 8.1.1**.

8.2.7 Data Analysis of Toggle 2.1

The circuit design with Toggle 2.0 along with a second copy of the DEX-inducible Gal4EAR repressor is referred to as Toggle 2.1. From the intensity plots shown in **Fig. 3.12**, the Low and High states are again clearly distinguishable in Toggle 2.1. In accordance with the modeling predictions, the stability of the High state was maintained, and the switching behavior from High to Low was improved in shoots with a fold change of 6.4 compared to 2.6 in Toggle 2.0 (**Fig. 3.13c**). This difference is statistically significant (**Table S3.8**).

The roots still performed similarly to Toggle 2.0 (**Fig. 3.13a & b**). The fold change of Low to High was 18.9 and the fold change of High to Low was 10.7 (**Fig. 3.13d**).

8.2.8 MCMC Parameter Estimation Results for Toggle 2.1

Shoots: (i) Fits to the means: Out of 321 good parameter sets, 113 were bistable and 206 were indistinguishable from bistable (totaling 99.4%). Of the good fits, 70 parameter sets met the definition of best parameter sets, and 58 of these were bistable and 12 indistinguishable from bistable (totaling 100%).

(ii) Pooled fits to each technical replicate: Out of 148 good parameter sets, 54 were bistable and 85 indistinguishable from bistable (totaling 94%).

(iii) Fits to the data in **Fig. 3.12**: Out of 150 good parameter sets, 68 were bistable and 82 indistinguishable from bistable (totaling 100%). Of these 150, we found 71 best parameter fits, of which 41 were bistable and 30 were indistinguishable from bistable (totaling 100%).

Roots: (i) Fits to the means: We found 133 good parameter sets out of which 17 were bistable and 4 were indistinguishable from bistable (totaling 15.8%). Of these 133, 86 were best parameter sets and they included the 21 parameters that were bistable for the duration of the experiment (24%).

(ii) Pooled fits to each technical replicate: We ran the MCMC procedure 1,700 times and found 354 good parameter sets. Out of these 87 were bistable and 25 indistinguishable from bistable (totaling 31.6%).

(ii) Fits to the data in **Fig. 3.12**: 155 out of 310 good parameters were bistable and 11 were indistinguishable from bistable (totaling 53.6%). However, 201 of these 310 were best parameters, and of these, 152 were bistable and 10 were indistinguishable from bistable, or a total of 80.6% were bistable for the duration of the experiment.

The data strongly suggest that shoots containing Toggle 2.1 have bistability. The behavior of the circuit in the roots is more ambiguous (see Chapter 3 for discussion).

8.2.9 Transgene Insertion and Copy Number Estimation

Thermal asymmetric interlaced polymerase chain reaction (TAIL-PCR) has been used to retrieve sequences flanking insertion sites and estimate the number of insertions in plant chromosomes [5]. Here, we followed standard TAIL-PCR protocol as reported in Singer and Burke [5]. In brief, three subsequent rounds of TAIL-PCR were performed using arbitrary

degenerate (AD) primers (**Table S3.2**) and nested insertion-specific primers (**Table S3.3**). We used published arbitrary degenerate primers from *Arabidopsis thaliana* [5]. The nested insertion-specific primers were designed targeting the BAR gene (selection marker) in the pGREENII0229 binary vector. Both shoot and root genomic DNAs extracted from Toggle 2.0 homozygous lines were used as a template. Only secondary and tertiary TAIL-PCR products were analyzed on gel. The result showed a single band shifting between secondary and tertiary products in shoot as well as root DNA, suggesting a single copy of the transgene (**Fig. S3.4a**). Subsequently, the gel-purified tertiary TAIL-PCR products were cloned in the pJET vector and sequenced. The results show that all the sequenced products contained the inserted T-DNA and its flanking genomic sequences of the Arabidopsis genome (**Fig. S3.4b**). The transgene inserted in Chromosome 5, in the intergenic region between AT5G39980 and AT5G39990. Generation of clean DNA sequence products from TAIL PCR off the insert's left border is consistent with one intact T-DNA in these plants.

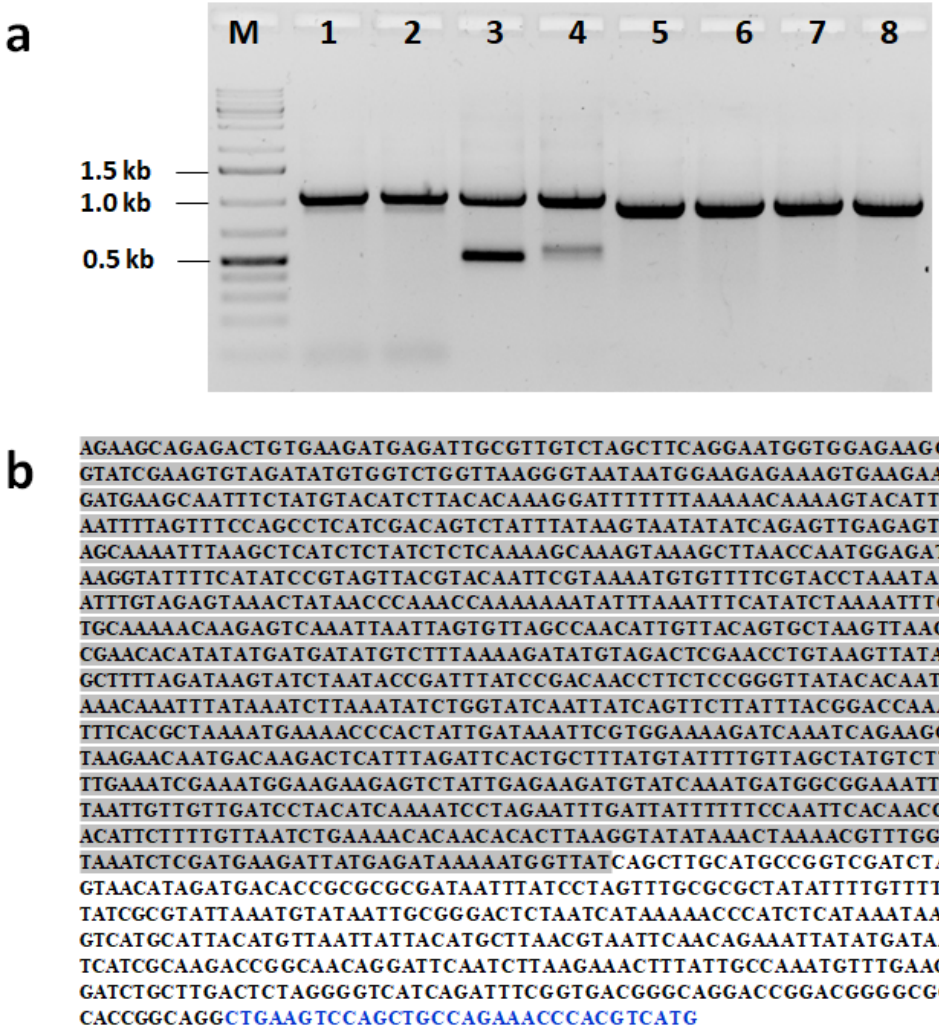

Figure S3.4. Determining chromosomal location and copy number estimation of the transgene.

a, Secondary and tertiary TAIL-PCR products of Toggle 2.0 resolved in a 1% agarose gel stained with ethidium bromide. PCR was performed using genomic DNA isolated from both shoot (Lanes 1, 2, 5 & 6) and root (Lanes 3, 4, 7 & 8) tissues. Samples 1-4 are secondary and samples 5-8 are tertiary TAIL-PCR products. The expected slight decrease in size of tertiary TAIL-PCR products is due to the use of nested primers. M, marker (GeneRuler 1-kb plus ladder, Thermo Scientific). **b**, DNA sequence of Toggle 2.0 tertiary TAIL-PCR product cloned in the pJET vector. T-DNA insertion was found in Chromosome 5 in the intergenic between AT5G39980 and AT5G39990. Gray shaded region is from Arabidopsis chromosome 5, the unshaded sequence is part of the T-DNA border and T-NOS, and nucleotides in blue are the LB1 primer.

8.3 Supplementary Tables

8.3.1 Parts used and their respective sequences

Table S3.1. Sequence information of all the parts used to construct the toggle circuits.

Name	Type	DNA sequence
35S	Promoter	CATGGAGTCAAAGATTCAAATAGAGGACCTAACAGAACTCG CCGTAAAGACTGGCGAACAGTTCATACAGAGTCTCTTACGA CTCAATGACAAGAAGAAAATCTTCGTCAACATGGTGGAGCA CGACACACTTGTCTACTCCAAAAATATCAAAGATACAGTCT CAGAAGACCAAAGGGCAATTGAGACTTTTCAACAAAGGGTA ATATCCGGAAACCTCCTCGGATTCCATTGCCCAGCTATCTGT CACTTTATTGTGAAGATAGTGGAAAAGGAAGGTGGCTCCTA CAAATGCCATCATTGCGATAAAGGAAAGGCCATCGTTGAAG ATGCCTCTGCCGACAGTGGTCCCAAAGATGGACCCCCACCC ACGAGGAGCATCGTGGAAAAAGAAGACGTTCCAACCACGT CTTCAAAGCAAGTGGATTGATGTGATATCTCCACTGACGTA AGGGATGACGCACAATCCCACTATCCTTCGCAAGACCCTTC CTCTATATAAGGAAGTTCATTTCATTTGGAGAGAACACGGG GGACTCTCC
FMV	Promoter	GGCCGCAGGATTTAGCAGCATTCCAGATTGGGTTCAATCAA CAAGGTACGAGCCATATCACTTTATTCAAATTGGTATCGCCA AAACCAAGAAGGAACTCCCATCCTCAAAGGTTTGTAAGGAA GAATTCTCAGTCCAAAGCCTCAACAAGGTCAGGGTACAGAG TCTCCAAACCATTAGCCAAAAGCTACAGGAGATCAATGAAG AATCTTCAATCAAAGTAAACTACTGTTCCAGCACATGCATC ATGGTCAGTAAGTTTCAGAAAAAGACATCCACCGAAGACTT AAAGTTAGTGGGCATCTTTGAAAGTAATCTTGTCAACATCG AGCAGCTGGCTTGTGGGGACCAGACAAAAAAGGAATGGTG CAGAATTGTTAGGCGCACCTACCAAAAGCATCTTTGCCTTTA TTGCAAAGATAAAGCAGATTCCTCTAGTACAAGTGGGGAAC AAAATAACGTGGAAAAGAGCTGTCCTGACAGCCCACTCACT AATGCGTATGACGAACGCAGTGACGACCACAAAAGAATTCC CTCTATATAAGAAGGCATTCATTCCCATTTGAAGGATCATCA GATACTCAACC
$35S_{2xLexA}$	Synthetic promoter	TGAGACTTTTCAACAAAGGGTAATATCGGGAAACCTCCTCG GATTCCATTGCCCAGCTATCTGTCACTTCATCAAAAGGACAG TAGAAAAGGAAGGTGGCACCTACAAATGCCATCATTGCGAT AAAGGAAAGGCTATCGTTCAAGATGCCTCTGCCGACAGTGG TCCCAAAGATGGACCCCCACCCACGAGGAGCATCGTGGAAA AAGAAGACGTTCCAACCACGTCTTCAAAGCAAGTGGATTGA TGTGATATCTCCACTGACGTAAGGGATGACGCACAATCCCA CTATCCTTCGCAAGACCCTTCCTCTATATAAGGAAGTTCATT TCATTTGGAGAGGAACGCGTACTGTACATATAACCACTGGT TTTATATACAGCAGT

$35S_{4xLexA}$TATA	Synthetic promoter	TGAGACTTTTCAACAAAGGGTAATATCGGGAAACCTCCTCG GATTCCATTGCCCAGCTATCTGTCACTTCATCAAAAGGACAG TAGAAAAGGAAGGTGGCACCTACAAATGCCATCATTGCGAT AAAGGAAAGGCTATCGTTCAAGATGCCTCTGCCGACAGTGG TCCCAAAGATGGACCCCCACCCACGAGGAGCATCGTGGAAA AAGAAGACGTTCCAACCACGTCTTCAAAGCAAGTGGATTGA TGTGATATCTCCACTGACGTAAGGGATGACGCACAATCCCA CTATCCTTCGCAAGACCCTTCCTCACTGTACATATAACCACT GGTTTTATATACAGCAGTACTGTACATATAACCACTGGTTTT ATATACAGCAGTTATATAAGGAAGTTCATTTCATTTGGAGA GGA
NOS_{2xGal4}	Synthetic promoter	AGGCGGGAAACGACAATCTGATCATGAGCGGAGAATTAAG GGAGTCACGTTATGACCCCCGCCGATGACGCGGGACAAGCC GTTTTACGTTTGGAACTGACAGAACCGCAACGATTGAAGGA GCCACTCAGCCGCGGGTTTCTGGAGTTTAATGAGCTAAGCA CATACGTCAGAAACCATTATTGCGCGTTCAAAAGTCGCCTA AGGTCACTATCAGCTAGCAAATATTTCTTGTCAAAAATGCTC CACTGACGTTCCATAAATTCCCCTCGGTATCCAATTAGAGTC TCATATTCACTCTCAATCCAAATAATCTGCACCGACGCGTCG GAAGACTCTCCTCCGAGCGGAAGACTCTCCTCCG
Gal4EAR	Synthetic Repressor	ATGAAGTTGTTAAGTTCTATTGAACAGGCTTGTGATATTTGT AGATTGAAGAAGCTCAAGTGTAGTAAAGAGAAACCTAAGT GCGCTAAGTGTCTTAAAAATAACTGGGAGTGCAGATATTCT CCTAAGACTAAGAGATCACCTCTTACTAGGGCTCATCTCAC AGAGGTGGAGTCTAGGCTTGAGAGATTGGAGCAGTTGTTCC TTTTGATTTTTCCAAGAGAAGATCTTGATATGATTCTTAAGA TGGATTCTCTTCAAGATATTAAGGCTCTTCTTACTGGTTTATT CGTTCAAGATAATGTGAATAAGGATGCAGTGACTGATAGAC TTGCATCAGTTGAAACTGATATGCCTCTTACATTAAGACAAC ACAGGATTTCTGCTACTTCAAGTTCTGAAGAAAGTTCTAATA AGGGTCAAAGGCAATTAACCGTTTCTCTTGATTTGGACCTCG AGCTTCGTTTGGGATTCGCTTGA
LexAEAR	Synthetic Repressor	ATGAAAGCTCTTACTGCTAGACAACAAGAAGTTTTTGATTTG ATTAGGGATCATATTTCTCAGACAGGTATGCCTCCTACTAGA GCTGAGATCGCTCAGAGACTCGGTTTCAGATCTCCTAACGCT GCTGAAGAGCATCTTAAGGCTCTTGCTAGAAAGGGAGTTAT TGAGATTGTGAGTGGAGCATCAAGAGGTATTAGGTTGCTTC AAGAGGAAGAAGAGGGACTTCCTCTTGTTGGTAGAGTTGCA GCTGGTGAGCCTCTTGATTTGGACCTCGAGCTTCGTTTGGGA TTCGCTTGA
LexAOFPX	Synthetic Repressor	ATGAAAGCTCTTACTGCTAGACAACAAGAAGTTTTTGATTTG ATTAGGGATCATATTTCTCAGACAGGTATGCCTCCTACTAGA GCTGAGATCGCTCAGAGACTCGGTTTCAGATCTCCTAACGCT GCTGAAGAGCATCTTAAGGCTCTTGCTAGAAAGGGAGTTAT TGAGATTGTGAGTGGAGCATCAAGAGGTATTAGGTTGCTTC AAGAGGAAGAAGAGGGACTTCCTCTTGTTGGTAGAGTTGCA GCTGGTGAGCCTAGCTTGGCGGTGGTGAAGAAGTCGGTGGA TCCAAACAAAGATTTCAGGGAATCAATGGTGGAGATGATAG CAGAGAACAAGATAAGAGCATCAAATGACCTAGAAGAGCT TCTTGCTTGCTACCTTTCGTTAAATCCAAAGGAATATCACGA

		TCTTATTATCAAAGTGTTCGAACAAATCTGGCTTGAACTGAT AAACCCA
NOST	Terminator	CGTTCAAACATTTGGCAATAAAGTTTCTTAAGATTGAATCCT GTTGCCGGTCTTGCGATGATTATCATATAATTTCTGTTGAAT TACGTTAAGCATGTAATAATTAACATGTAATGCATGACGTT ATTTATGAGATGGGTTTTTATGATTAGAGTCCCGCAATTATA CATTTAATACGCGATAGAAAACAAAATATAGCGCGCAAACT AGGATAAATTATCGCGCGCGGTGTCATCTATGTTACTAGATC GGGCGGG
OCST	Terminator	GGAGCTGCTTTAATGAGATATGCGAGACGCCTATGATCGCA TGATATTTGCTTTCAATTCTGTTGTGCACGTTGTAAAAAACC TGAGCATGTGTAGCTCAGATCCTTACCGCCGGTTTCGGTTCA TTCTAATGAATATATCACCCGTTACTATCGTATTTTTATGAA TAATATTCTCCGTTCAATTTACTGATTGTACCCTACTACTTAT ATGTACAATATTAAAATGAAAACAATATATTGTGCTGAATA GGTTTATAGCGACATCTATGATAGAGCGCCACAATAACAAA CAATTGCGTTTTATTATTACAAATCCAATTTTAAAAAAAGCG GCAGAACCGGTCAAACCTAAAAGACTGATTACATAAATCTT ATTCAAATTTCAAAAGGCCCCAGGGGCTAGTATCTACGACA CACCGAGCGGCGAACTAATAACGTTCACTGAAGGGAACTCC GGTTCCCCGCCGGCGCGCATGGGTGAGATTCCTTGAAGTTG AGTATTGGCCGTCCGCTCTACCGAAAGTTACGGGCACCATT CAACCCGGTCCAGCACGGCGGCCGGGTAACCGACTTGCTGC CCCGAGAATTATGCAGCATTTTTTTGGTGTATGT
Pea3AT	Terminator	GCTTCGGGCCTCCCAGCTTTCGTCCGTATCATCGGTTTCGAC AACGTTCGTCAAGTTCAATGCATCAGTTTCATTGCCCACACA CCAGAATCCTACTAAGTTTGAGTATTATGGCATTGGAAAAG CTGTTTTCTTCTATCATTTGTTCTGCTTGTAATTTACTGTGTT CTTTCAGTTTTTGTTTTCGGACATCAAAATGCAAATGGATGG ATAAGAGTTAATAAATGATATGGTCCTTTTGTTCATTCTCAA ATTATTATTATCTGTTGTTTTTACTTTAATGGGTTGAATTTAA GTAAGAAAGGAACTAACAGTGTGATATTAAGGTGCAATGTT AGACATATAAAACAGTCTTTCACCTCTCTTTGGTTATGTCTT GAATTGGTTTGTTTCTTCACTTATCTGTGTAATCAAGTTTACT ATGAGTCTATGATCAAGTAATTATGCAATCAAGTTAAGTAC AGTATAGGCTTT
E9T	Terminator	ATTATGGCATTGGGAAAACTGTTTTTCTTGTACCATTTGTTG TGCTTGTAATTTACTGTGTTTTTTATTCGGTTTTCGCTATCGA ACTGTGAAATGGAAATGGATGGAGAAGAGTTAATGAATGAT ATGGTCCTTTTGTTCATTCTCAAATTAATATTATTTGTTTTTT CTCTTATTTGTTGTGTGTTGAATTTGAAATTATAAGAGATAT GCAAACATTTTGTTTTGAGTAAAAATGTGTCAAATCGTGGCC TCTAATGACCGAAGTTAATATGAGGAGTAAAACATCCCAAA C

TB	Transcription block	AATAAAATATCTTTATTTTCATTACATCTGTGTGTTGGTTTTT TGTGTGAATCGATAGTACTAACATACGCTCTCCATCAAAAC AAAACGAAACAAAACAAACTAGCAAAATAGGCTGTCCCCA GTGCAAGTGCAGGTGCCAGAACATTTCTCT
F-LUC	Gene	ATGGAAGACGCCAAAAACATAAAGAAAGGCCCGGCGCCAT TCTATCCTCTAGAGGATGGAACCGCTGGAGAGCAACTGCAT AAGGCTATGAAGAGATACGCCCTGGTTCCTGGAACAATTGC TTTTACAGATGCACATATCGAGGTGAACATCACGTACGCGG AATACTTCGAAATGTCCGTTCGGTTGGCAGAAGCTATGAAA CGATATGGGCTGAATACAAATCACAGAATCGTCGTATGCAG TGAAAACTCTCTTCAATTCTTTATGCCGGTGTTGGGCGCGTT ATTTATCGGAGTTGCAGTTGCGCCCGCGAACGACATTTATA ATGAACGTGAATTGCTCAACAGTATGAACATTTCGCAGCCT ACCGTAGTGTTTGTTTCCAAAAAGGGGTTGCAAAAAATTTT GAACGTGCAAAAAAAATTACCAATAATCCAGAAAATTATTA TCATGGATTCTAAAACGGATTACCAGGGATTTCAGTCGATG TACACGTTCGTCACATCTCATCTACCTCCCGGTTTTAATGAA TACGATTTTGTACCAGAGTCCTTTGATCGTGACAAAACAATT GCACTGATAATGAATTCCTCTGGATCTACTGGGTTACCTAAG GGTGTGGCCCTTCCGCATAGAACTGCCTGCGTCAGATTCTCG CATGCCAGAGATCCTATTTTTGGCAATCAAATCATTCCGGAT ACTGCGATTTTAAGTGTTGTTCCATTCCATCACGGTTTTGGA ATGTTTACTACACTCGGATATTTGATATGTGGATTTCGAGTC GTCTTAATGTATAGATTTGAAGAAGAGCTGTTTTTACGATCC CTTCAGGATTACAAAATTCAAAGTGCGTTGCTAGTACCAAC CCTATTTTCATTCTTCGCCAAAAGCACTCTGATTGACAAATA CGATTTATCTAATTTACACGAAATTGCTTCTGGGGGCGCACC TCTTTCGAAAGAAGTCGGGGAAGCGGTTGCAAAACGCTTCC ATCTTCCAGGGATACGACAAGGATATGGGCTCACTGAGACT ACATCAGCTATTCTGATTACACCCGAGGGGGATGATAAACC GGGCGCGGTCGGTAAAGTTGTTCCATTTTTTGAAGCGAAGG TTGTGGATCTGGATACCGGGAAAACGCTGGGCGTTAATCAG AGAGGCGAATTATGTGTCAGAGGACCTATGATTATGTCCGG TTATGTAAACAATCCGGAAGCGACCAACGCCTTGATTGACA AGGATGGATGGCTACATTCTGGAGACATAGCTTACTGGGAC GAAGACGAACACTTCTTCATAGTTGACCGCTTGAAGTCTTTA ATTAAATACAAAGGATATCAGGTGGCCCCCGCTGAATTGGA ATCGATATTGTTACAACACCCCAACATCTTCGACGCGGGCG TGGCAGGTCTTCCCGACGATGACGCCGGTGAACTTCCCGCC GCCGTTGTTGTTTTGGAGCACGGAAAGACGATGACGGAAAA AGAGATCGTGGATTACGTCGCCAGTCAAGTAACAACCGCGA AAAAGTTGCGCGGAGGAGTTGTGTTTGTGGACGAAGTACCG AAAGGTCTTACCGGAAAACTCGACGCAAGAAAAATCAGAG AGATCCTCATAAAGGCCAAGAAGGGCGGAAAGTCCAAATT GTAA
10xN1	4-OHT Inducible Promoter	GGGGTAGAAAAAGGGGTAGAAAACCAAGGGGTAGAAAAAG GGGTAGAAAACCAAGGGGTAGAAAAAGGGGTAGAAAACCA AGGGGTAGAAAAAGGGGTAGAAAACCAAGGGGTAGAAAAA GGGGTAGAAGCAAGACCCTTCCTCTATATAAGGAAGTTCAT TTCATTTGGAGAGG

pOp6	DEX Inducible promoter	AATTGTGAGCGCTCACAATTCTTTCTCTTCCCTTTCTTCTTTC TAGTCTTTCAATTGTGAGCGCTCACAATTCTTTCTCTTCCCTT TCTTCTTTCTAGTCTTTCAATTGTGAGCGCTCACAATTCTTTC TCTTCCCTTTCTTCTTTCTTTCAATTGTGAGCGCTCACAATTC TTTCTCTTCCCTTTCTTCTTTCTAGTCTTTCAATTGTGAGCGC TCACAATTCTTTCTCTTCCCTTTCTTCTTTCTAGTCTTTCAATT GTGAGCGCTCACAATTCTTTCTCTTCCCTTTCTTCTTTCTAGT GGATCGATCTTCGCAAGACCCTTCCTCTATATAAGGAAGTTC ATTTCATTTGGAGAGGA
NEV	Transcription Factor	ATGGCCCAGGCGGCCCTCGAGCCCGGGGAGAAGCCCTATGC TTGTCCGGAATGTGGTAAGTCCTTCAGCCAGAGCAGCAACC TGGTGCGCCACCAGCGTACCCACACGGGTGAAAAACCGTAT AAATGCCCAGAGTGCGGCAAATCTTTTAGCCAGAGCAGCTC CCTGGTGCGCCATCAACGCACTCATACTGGCGAGAAGCCAT ACAAATGTCCAGAATGTGGCAAGTCTTTCAGTCGCTCCGAT AAACTGGTGCGCCACCAACGTACTCACACCGGTAAAAAAAC TAGTGGCCAGGCCGGCCGCCGAAATGAAATGGGTGCTTCAG GAGACATGAGGGCTGCCAACCTTTGGCCAAGCCCTCTTGTG ATTAAGCACACTAAGAAGAATAGCCCTGCCTTGTCCTTGAC AGCTGACCAGATGGTCAGTGCCTTGTTGGATGCTGAACCGC CCATGATCTATTCTGAATATGATCCTTCTAGACCCTTCAGTG AAGCCTCAATGATGGGCTTATTGACCAACCTAGCAGATAGG GAGCTGGTTCATATGATCAACTGGGCAAAGAGAGTGCCAGG CTTTGGGGACTTGAATCTCCATGATCAGGTCCACCTTCTCGA GTGTGCCTGGCTGGAGATTCTGATGATTGGTCTCGTCTGGCG CTCCATGGAACACCCGGGGAAGCTCCTGTTTGCTCCTAACTT GCTCCTGGACAGGAATCAAGGTAAATGTGTGGAAGGCATGG TGGAGATCTTTGACATGTTGCTTGCTACGTCAAGTCGGTTCC GCATGATGAACCTGCAGGGTGAAGAGTTTGTGTGCCTCAAA TCCATCATTTTGCTTAATTCCGGAGTGTACACGTTTCTGTCC AGCACCTTGAAGTCTCTGGAAGAGAAGGACCACATCCACCG TGTCCTGGACAAGATCACAGACACTTTGATCCACCTGATGG CCAAAGCTGGCCTGACTCTGCAGCAGCAGCATCGCCGCCTA GCTCAGCTCCTTCTCATTCTTTCCCATATCCGGCACATGAGT AACAAAGGCATGGAGCATCTCTACAACATGAAATGCAAGA ACGTTGTGCCCCTCTATGACCTGCTCCTGGAGATGTTGGATG CCCACCGCCTTCATGCCCCAGCCAGTCGCATGGGAGTGCCC CCAGAGGAGCCCAGCCAGACCCAGCTGGCCACCACCAGCTC CACTTCAGCACATTCCTTACAAACCTACTACATACCCCCGGA AGCAGAGGGCTTCCCCAACACGATCGGGCGCGCCGACGCGC TGGACGATTTCGATCTCGACATGCTGGGTTCTGATGCCCTCG ATGACTTTGACCTGGATATGTTGGGAAGCGACGCATTGGAT GACTTTGATCTGGACATGCTCGGCTCCGATGCTCTGGACGAT TTCGATCTCGATATGTTAATTAACTACCCGTACGACGTTCCG GACTACGCTTCTTGA

LhGR	Transcription Factor	ATGGCTAGTGAAGCTCGAAAAACAAAGAAAAAAATCAAAG GGATTCAGCAAGCCACTGCAGGAGTCTCACAAGACACTTCG GAAAATCCTAACAAAACAATAGTTCCTGCAGCATTACCACA GCTCACCCCTACCTTGGTGTCACTGCTGGAGGTGATTGAACC CGAGGTGTTGTATGCAGGATATGATAGCTCTGTTCCAGATTC AGCATGGAGAATTATGACCACACTCAACATGTTAGGTGGGC GTCAAGTGATTGCAGCAGTGAAATGGGCAAAGGCGATACCA GGCTTCAGAAACTTACACCTGGATGACCAAATGACCCTGCT ACAGTACTCATGGATGTTTCTCATGGCATTTGCCCTGGGTTG GAGATCATACAGACAATCAAGTGGAAACCTGCTCTGCTTTG CTCCTGATCTGATTATTAATGAGCAGAGAATGTCTCTACCCT GCATGTATGACCAATGTAAACACATGCTGTTTGTCTCCTCTG AATTACAAAGATTGCAGGTATCCTATGAAGAGTATCTCTGT ATGAAAACCTTACTGCTTCTCTCCTCAGTTCCTAAGGAAGGT CTGAAGAGCCAAGAGTTATTTGATGAGATTCGAATGACTTA TATCAAAGAGCTAGGAAAAGCCATCGTCAAAAGGGAAGGG AACTCCAGTCAGAACTGGCAACGGTTTTACCAACTGACAAA GCTTCTGGACTCCATGCATGAGGTGGTTGAGAATCTCCTTAC CTACTGCTTCCAGACATTTTTGGATAAGACCATGAGTATTGA ATTCCCAGAGATGTTAGCTGAAATCATCACTAATCAGATAC CAAAATATTCAAATGGAAATATCAAAAAGCTTCTGTTTCAT CAAAAATCTACTAGCAAACCGGTAACGTTATACGACGTCGC TGAATACGCCGGCGTTTCTCATCAAACCGTTTCTAGAGTGGT TAACCAGGCTTCACATGTTAGCGCTAAAACCCGGGAAAAAG TTGAAGCTGCCATGGCTGAGCTCAACTACATCCCGAACCGT GTTGCGCAGCAGCTGGCTGGTAAACAAAGCTTGCTGATCGG TGTCGCGACCTCGAGCTTGGCCCTGCACGCGCCGTCGCAAA TTGTCGCGGCGATTAAATCTCGCGCCGATCAACTGGGTGCC AGCGTGGTGGTGTCGATGGTAGAACGAAGCGGCGTCGAAGC CTGTAAAGCGGCGGTGCACAATCTTCTCGCGCAACGCGTCA GTGGGCTGATCATTAACTATCCGCTGGATGACCAGGATGCC ATTGCTGTGGAAGCTGCCTGCACTAATGTTCCGGCGTTATTT CTTGATGTCTCTGACCAGACACCCATCAACAGTATTATTTTC TCCCATGAAGACGGTACGCGACTGGGCGTGGAGCATCTGGT CGCATTGGGTCACCAGCAAATCGCGCTGTTAGCGGGCCCAT TAAGTTCTGTCTCGGCGCGTCTGCGTCTGGCTGGCTGGCATA AATATCTCACTCGCAATCAAATTCAGCCGATAGCGGAACGG GAAGGCGACTGGAGTGCCATGTCCGGTTTTCAACAAACCAT GCAAATGCTGAATGAGGGCATCGTTCCCACTGCGATGCTGG TTGCCAACGATCAGATGGCGCTGGGCGCAATGCGCGCCATT ACCGAGTCCGGGCTGCGCGTTGGTGCGGATATCTCGGTAGT GGGATACGACGATACCGAAGACAGCTCATGTTATATCCCGC CGTTAACCACCATCAAACAGGATTTTCGCCTGCTGGGGCAA ACCAGCGTGGACCGCTTGCTGCAACTCTCTCAGGGCCAGGC GGTGAAGGGCAATCAGCTGTTGCCCGTCTCACTGGTGAAAA GAAAAACCACTAGTGGATCGGAATTCGCTAACTTCAACCAG TCCGGAAACATCGCTGATTCTTCCTTGAGCTTCACTTTCACT AACTCTTCTAACGGACCTAACCTTATCACCACTCAGACCAAC TCTCAGGCTCTTAGCCAGCCAATCGCTAGCTCTAACGTGCAC GACAACTTCATGAACAACGAGATCACTGCTAGCAAGATCGA TGATGGTAACAATTCTAAGCCTCTTAGCCCAGGATGGACTG

ATCAGACTGCTTACAACGCATTCGGTATCACTACCGGTATGT
TCAACACCACTACCATGGACGATGTGTACAACTACCTCTTCG
ACGATGAGGATACTCCACCTAACCCTAAGAAGGAGTGA

8.3.2 Primers used for TAIL PCR

Table S3.2. AD Primers used for TAIL PCR. W = A or T, S = G or C, N = A or T or G or C.

Primer Name	Primer Sequence (5'-3')	Length	Degeneracy
AD1	NGTCGASWGANAWGAA	16	128
AD2	TGWGNAGSANCASAGA	16	128
AD3	AGWGNAGWANCAWAGG	16	128
AD4	STTGNTASTNCTNTGC	16	256
AD5	NTCGASTWTSGWGTT	15	64
AD6	WGTGNAGWANCANAGA	16	256

Table S3.3. T-DNA left border Primer sequences for pGREENII0229 vector.

Primer Name	Primer Sequence (5'-3')	Length
LB1	TGGCATGACGTGGGTTTCTGGCAGCTGGACTTC	33
LB2	ACAGGGCTTCAAGAGCGTGGTCGCTGTCATC	31
LB3	TACATCGAGACAAGCACGGTCAACTTCCGTA	31

8.3.3 Two-sample t-tests on fold changes

Table S3.4. The p-values of 2-sample two-sided t-test between fold changes of different treatments of Toggle 1.0 shoots (See **Section 3.2** Online Methods for plant numbers). Red color labels p-values larger than 0.05, thus not statistically significant differences. Mem is short for Memory. The difference in fold change between High Mem and High-Low is not statistically significant.

	Low Mem	Low-High	Low-Low	Control	High Mem	High-High	High-Low
Low Mem	-	0.0062	0.5565	0.0300	0.0004	0.0048	0.0007
Low-High	-	-	0.0020	0.0004	0.0001	0.0002	0.0001
Low-Low	-	-	-	0.0210	0.0001	0.0018	0.0004
Control	-	-	-	-	0.0010	0.0695	0.0022
High Mem	-	-	-	-	-	0.0062	0.7411
High-High	-	-	-	-	-	-	0.0109
High-Low	-	-	-	-	-	-	-

Table S3.5. The p-values of 2-sample two-sided t-test between fold changes of different treatments of Toggle 1.0 roots (See **Section 3.2** Online Methods for plant numbers). Red color labels p-values larger than 0.05, thus not statistically significant differences. Mem is short for Memory. The difference in fold change between High Mem and High-Low is not statistically significant.

	Low Mem	Low-High	Low-Low	Control	High Mem	High-High	High-Low
Low Mem	-	0.0000	0.1598	0.0237	0.0000	0.0012	0.0000
Low-High	-	-	0.0000	0.0000	0.0000	0.0000	0.0000
Low-Low	-	-	-	0.0615	0.0000	0.0008	0.0000
Control	-	-	-	-	0.0000	0.0017	0.0000
High Mem	-	-	-	-	-	0.0001	0.2379
High-High	-	-	-	-	-	-	0.0000
High-Low	-	-	-	-	-	-	-

Table S3.6. The p-values of 2-sample two-sided t-test between fold changes of different treatments of Toggle 2.0 shoots (See **Section 3.2** Online Methods for plant numbers). Red color labels p-values larger than 0.05, thus not statistically significant differences. Mem is short for Memory. The difference in fold change between High Mem and High-Low is not statistically significant.

	Low Mem	Low-High	Low-Low	Control	High Mem	High-High	High-Low
Low Mem	-	0.0000	0.0278	0.0470	0.0204	0.7834	0.0070
Low-High	-	-	0.0000	0.0000	0.0002	0.0001	0.0000
Low-Low	-	-	-	0.0037	0.0096	0.1386	0.0014
Control	-	-	-	-	0.0590	0.2208	0.0676
High Mem	-	-	-	-	-	0.0330	0.2349
High-High	-	-	-	-	-	-	0.0337
High-Low	-	-	-	-	-	-	-

Table S3.7. The p-values of 2-sample two-sided t-test between fold changes of different treatments of Toggle 2.0 roots (See **Section 3.2** Online Methods for plant numbers). Red color labels p-values larger than 0.05, thus not statistically significant differences. Mem is short for Memory. The difference in fold change between the High Mem and High-Low is not statistically significant.

	Low Mem	Low-High	Low-Low	Control	High Mem	High-High	High-Low
Low Mem	-	0.0000	0.0643	0.3049	0.0000	0.9208	0.0000
Low-High	-	-	0.0000	0.0000	0.0000	0.0000	0.0000
Low-Low	-	-	-	0.0068	0.0000	0.4391	0.0000
Control	-	-	-	-	0.0000	0.6534	0.0000
High Mem	-	-	-	-	-	0.0001	0.1070
High-High	-	-	-	-	-	-	0.0001
High-Low	-	-	-	-	-	-	-

Table S3.8. The p-values of 2-sample two-sided t-test between fold changes of different treatments of Toggle 2.1 shoots (See **Section 3.2** Online Methods for plant numbers). Red color labels p-values larger than 0.05, thus not statistically significant differences. Mem is short for Memory. The difference in fold change between the High Memory and High-Low is statistically significant.

	Low Mem	Low-High	Low-Low	Control	High Mem	High-High	High-Low
Low Mem	-	0.0000	0.8914	0.0777	0.0003	0.8806	0.0023
Low-High	-	-	0.0003	0.0000	0.0000	0.0001	0.0001
Low-Low	-	-	-	0.5699	0.0109	0.8462	0.0053
Control	-	-	-	-	0.0011	0.2137	0.0034
High Mem	-	-	-	-	-	0.0015	0.0356
High-High	-	-	-	-	-	-	0.0028
High-Low	-	-	-	-	-	-	-

Table S3.9. The p-values of 2-sample two-sided t-test between fold changes of different treatments of Toggle 2.1 roots (See **Section 3.2** Online Methods for plant numbers). Red color labels p-values larger than 0.05, thus not statistically significant differences. Mem is short for Memory. The difference in fold change between the High Mem and High-Low is not statistically significant.

	Low Mem	Low-High	Low-Low	Control	High Mem	High-High	High-Low
Low Mem	-	0.0002	0.3041	0.3898	0.0002	0.0031	0.0002
Low-High	-	-	0.0003	0.0001	0.0000	0.0000	0.0000
Low-Low	-	-	-	0.5220	0.0005	0.0235	0.0004
Control	-	-	-	-	0.0001	0.0018	0.0002
High Mem	-	-	-	-	-	0.0010	0.1251
High-High	-	-	-	-	-	-	0.0007
High-Low	-	-	-	-	-	-	-

8.3.4 Estimated parameter values from protoplast assay

Table S3.10. Parameter values used for choice of Toggle 1.0 and Toggle 2.0 components. These parameter values were estimated from the protoplast assays using **Equation S3.4.** Fold change indicates the ratio of the maximal expression level with no inducer to the lowest expression level achieved at the maximal inducer level. B, H and n are parameters characterizing the response functions of promoter-repressor pairs (defined in **Equation S3.4**). The parameter b is the dimensionless maximum expression level as defined in **Equation S3.3**, and 2b is the dimensionless maximum expression level of two copies of the LexA-based promoter to balance the stronger Gal4-based promoter. The choice of these combinations was based on the data from the best performing replicate, which are shown here.

	Construct Name	Fold Change	B (10^8)	H (10^8)	b	2b	n
Toggle 1.0	NOS_{2xGal4}.EAR	2.53	3.61	0.95	1.40	N.A.	3.03
	$35S_{2xLexA}$.EAR	5.99	0.66	2.57	0.69	1.38	2.56
Toggle 2.0	NOS_{2xGal4}.EAR	2.53	3.61	0.95	3.57	N.A.	3.03
	$35S_{4xLexA}$TATA.OFPx	4.31	0.48	1.01	0.51	1.02	3.31

Table S3.11. Parameter values estimated from the protoplast assays using **Equation S3.5** with estimated Hill coefficient less than 6. Fold change indicates the ratio of the maximal expression level with no inducer to the lowest expression level achieved at the maximal inducer level. A, B, H and n are parameters characterizing the response functions of promoter-repressor pairs (**Equation S3.5**).

Constructs	Replicate Index	Fold Change	A (10^8)	B (10^8)	H (10^8)	n
NOS_{2xGal4}.EAR	3	2.53	1.704	3.264	1.279	2.615
NOS_{2xGal4}.EAR	4	2.04	0.7942	1.172	0.7805	1.783
$35S_{2xLexA}$.EAR	2	4.68	0.3856	1.914	1.203	3.406
$35S_{2xLexA}$.EAR	3	5.99	0.107	0.5607	1.543	3.678
$35S_{4xLexA}$TATA.OFPX	1	4.31	0.0733	0.3932	0.833	4.852

8.4 Supplementary Notes

8.4.1 Designing principles of a bi-stable toggle switch

In order to model and simulate the plant toggle switch circuit, composed of two mutually repressing promoter-repressor pairs, we used a dimensionless system of ordinary differential equations (ODEs) as described in Gardner et al. [4]. The initial dimensional ODE equations can be written as follows. The rate of production of the repressor protein (X or Y) is determined by the concentration of its opposing repressor (Y or X) through a repressing Hill function, and its rate of degradation. Degradation is modeled as a first order process, yielding the following equations.

$$\frac{dX}{dT} = \frac{b_x}{1 + \left(\frac{Y}{K_x}\right)^{n_x}} - d_x X$$

$$\frac{dY}{dT} = \frac{b_y}{1 + \left(\frac{X}{K_y}\right)^{n_y}} - d_y Y \qquad \textbf{Eqn. S3.2}$$

Here, X and Y are the concentrations of the two repressors that are mutually repressing each other in the toggle switch design; b_x and b_y are the maximum expression levels of the promoters producing X and Y respectively. K_x and K_y are the concentrations of X and Y that repress the promoter expression to its half-maximal level and n_x and n_y are Hill coefficients. The parameters d_x and d_y are the first-order degradation rate constants of X and Y, respectively.

We de-dimensionalized these two ODEs into the form shown in **Equation S3.3** to reduce the dimensionality of parameter space.

$$\frac{dx}{dt} = \frac{\tilde{b}_x}{1 + (y)^{n_x}} - x \qquad \textbf{Eqn. S3.3}$$

$$\frac{dy}{dt} = \frac{\tilde{b}_y}{1 + (x)^{n_y}} - d_r y$$

Where:

$x=\frac{X}{K_y}$ and $y=\frac{Y}{K_x}$ are dimensionless concentrations of the two repressors X and Y;

$\tilde{b}_x= \frac{b_x}{K_y d_x}$ and $\tilde{b}_y= \frac{b_y}{K_x d_x}$ are the dimensionless maximum expression levels of the promoters producing X and Y respectively;

n_x and n_y are still the Hill coefficient of the promoters producing X and Y, respectively;

$d_r=\frac{d_y}{d_x}$ is the ratio between the degradation rate constant of X and Y, respectively. Time is de-dimensionalized by tdx.

We also assumed the degradation rate constants to be the same, thus $d_r = 1$. Therefore, the **Equation S3.3** is equivalent to the dimensionless ODE model used by Gardner et al. [4]. For simplicity, we relabel $\tilde{b}_x$ as b_x and $\tilde{b}_y$ as b_y in the remainder of the Supplementary Information. The resulting system of equations can be used to simulate and gain insights on the behaviors of toggle switch circuits. XPPaut (a tool to solve differential equations, http://www.math.pitt.edu/~bard/xpp/xpp.html) was used to generate the 2D phase diagrams of b_x and b_y at pre-determined values of Hill coefficients (**Fig. S3.5**).

From these 2D phase diagrams we can identify two principles for successful design of a toggle switch, which are the same as previously identified by Gardner et al. [4] These are: 1) a sigmoidal repressor response with a high Hill coefficient, and 2) large and balanced values of the dimensionless maximum expression levels, as defined above in **Equation S3.3**.

These two principles can be understood by referring to **Fig. S3.5**. As can be seen in the figure, if the value of the Hill coefficients, which measure the sigmoidal response, is larger, the bi-stable region is also larger. Secondly, larger and balanced values of the promoter strength, b_x and b_y, are more likely to lie near the center of the bistable region, whereas smaller or unbalanced values are more likely, other things remaining constant, to lie outside, or near the edge of, the bistable region. Therefore, large and balanced b_x and b_y is another key principle for bi-stability.

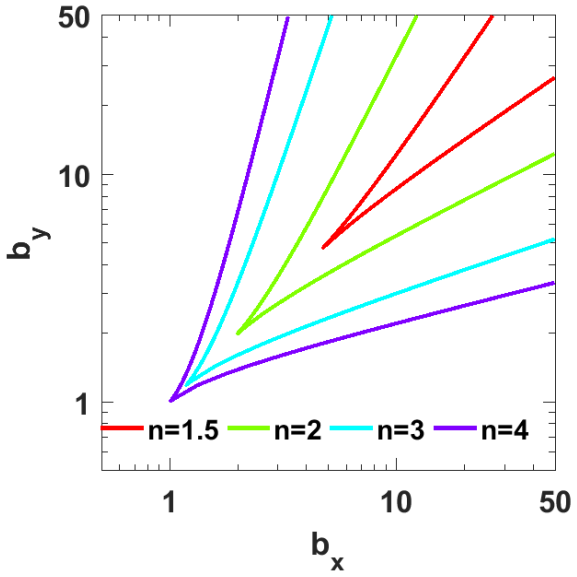

Figure S3.5. The phase diagram of the Toggle switch evaluated at different Hill coefficients. The axes b_x and b_y are dimensionless maximal expression levels of the repressible promoters. The bi-stable region is the region between the colored lines, for each choice of the Hill coefficient (n). The Hill coefficients (n) for both sides of the toggle were kept equal. Note that with larger n values, the bi-stable region gets larger.

8.4.2 Parameter Estimation from Protoplast Assays

In a previously published work, we have developed a method to quantitatively characterize repressible promoters using high throughput protoplast assays [2]. We developed a statistical model to remove intrinsic experimental variability, and quantitative promoter values were characterized for over 120 promoter-repressor pairs in *Arabidopsis* and over 100 pairs in

sorghum. For the purpose of this study, the promoter-repressor pairs in *Arabidopsis* are of interest. The performance of the repressible promoter was quantified by fitting the data to a Hill function as shown in **Equation S3.4**.

$$L_i = \frac{B_i}{1 + \left(\frac{F_i}{H_i}\right)^{n_i}} \qquad \textbf{Eqn. S3.4}$$

Here L_i is the output of the repressible promoter, measured in units of molecular concentration, and F_i is the molecular concentration of the repressor protein. The subscript i indicates the ith promoter-repressor in the library. Molecular concentration of L_i were calculated from luciferase luminescence values, converted into concentrations by using a calibrated standard curve between concentration and luminescence [4]. As typical for repressing Hill functions [6] the parameter B_i represents the maximum promoter strength, the parameter H_i is the repressor concentration at half-maximal expression and the parameter n_i (Hill coefficient) represents the sigmoidality of the response curve.

The raw data generated by protoplast assays were processed and normalized following the procedures described in Schaumberg et al. [4]. The normalized data were thereafter fitted to **Equation S3.4** using a nonlinear least-squares package in Matlab (Mathworks).

8.4.3 Comparison of parameters estimated from protoplast assays and whole plant luminescence data

As detailed in **Section 8.1.4**, a simple ODE system (**Equation S3.1**) was developed to describe the experimental results of the stably transformed toggle switch constructs and quantitative parameter values can be estimated by maximizing a log-likelihood using a MCMC scheme. These parameter values were then fed into the **Equation S3.4** without the inducible terms to evaluate their bistability (**Sections 8.1.4**, **8.2.4**, **8.2.6** and **8.2.8**). Such parameterized

models can also be used to test out different strategies to modify the design of Toggle 2.0 (**Section 8.2.7**). In addition, it is also possible to compare these parameter values to the ones previously estimated from the protoplast assays characterizing the repressor-promoter combinations. Such comparisons will help us to evaluate the accuracy of the transient expression in the protoplast assays as an approximation to the stable transformations.

To make the parameter values estimated from the two sources comparable, the method described in **Section 8.4.2** needs some modifications. First, one term characterizing leaky expression was added into **Equation S3.4**.

$$L_i = A_i + \frac{B_i}{1 + \left(\frac{F_i}{H_i}\right)^{n_i}} \qquad \textbf{Eqn. S3.5}$$

where A_i represents the relative leaky expression of the ith promoter and all the other variables are defined as in **Section 8.4.2**. Each of these parameters quantitatively characterizes how the promoter repressor pair behaves.

The raw data generated by protoplast assays were processed and normalized following the same procedures described in Schaumberg et al., [4]. The normalized data were then fitted to **Equation S3.5** using a nonlinear least-squares package in Matlab (Mathworks). Specifically, a Robust option of Least Absolute Residuals (LAR) and the Trust-Region algorithm were used. Parameter values were constrained to positive values for fitting. A good fit was defined to have an estimated value of Hill coefficient no larger than 6, which is assumed to be biologically relevant in this study. Out of the replicates of the NOS_{2xGal4}.EAR, $35S_{2xLexA}$.EAR and $35S_{4xLexA}$TATA.OFPx, the estimated parameter values of good fits are listed in **Table S3.11**.

To directly compare the parameter values estimated from the protoplast assays with the whole plant luminescence data, we used de-dimensionalized parameter values by normalizing A

and B by their corresponding H of the same promoter-repressor combination. For a brief proof that these are equivalent and comparable, please refer to **Section 8.4.4**. As shown in **Fig. S3.6**, the parameter values estimated from the protoplast assays generally overlap with the distribution of dimensionless parameter values estimated from the whole plant luminescence data. While this result supports the use of protoplasts for quantitative characterization of plant plants for synthetic biology, the possible quantitative differences between the protoplast estimates and those in a plant can be quite high, as seen in the figure. Therefore, quantitative predictions, for example of bistability properties, based on protoplast data are still subject to significant error. Allowing for these margins of error and using protoplast data for qualitative and semi-quantitative predictions however, allowed us to overcome these limitations and construct the first genetic toggle switch in a plant.

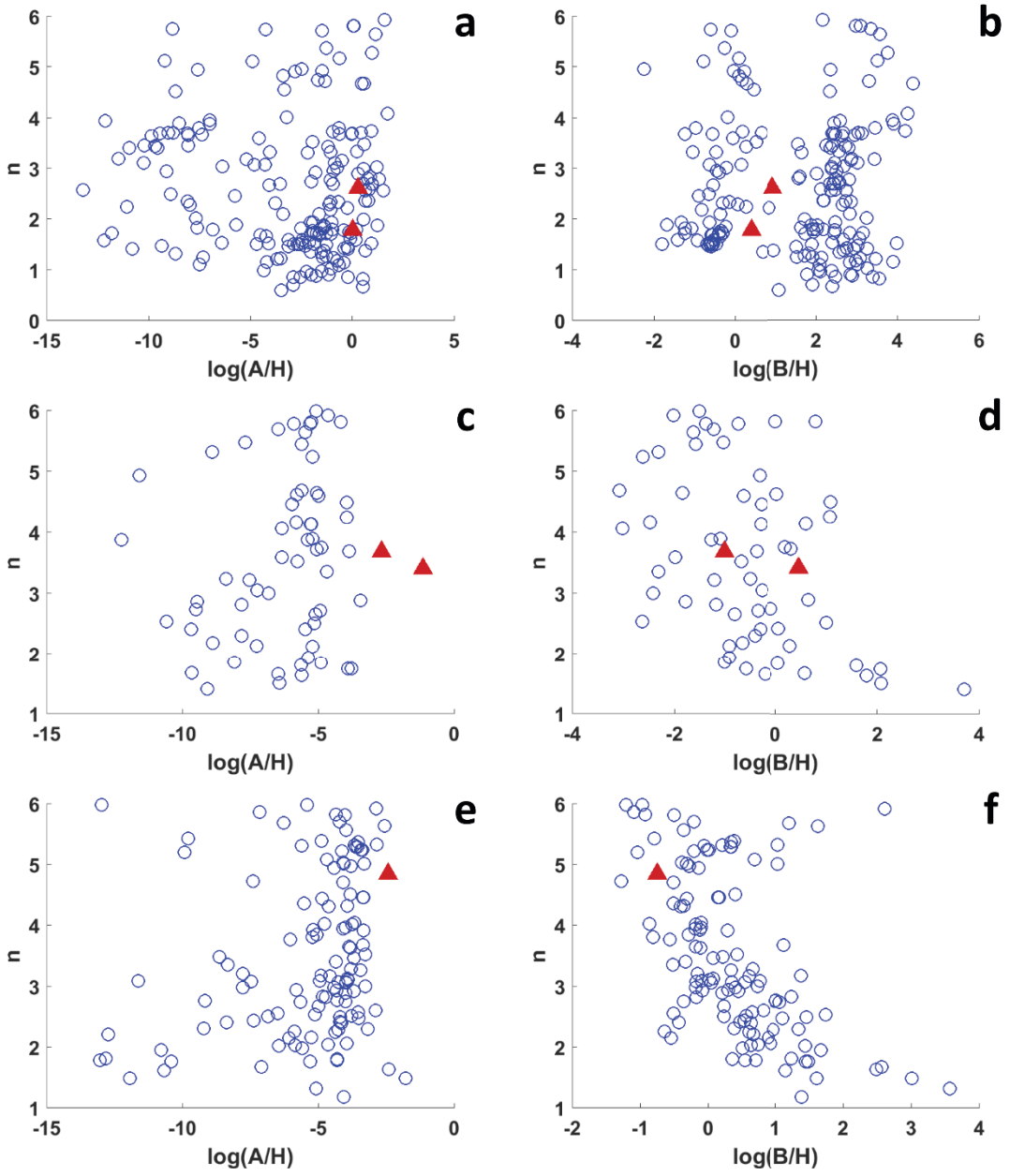

Figure S3.6. Comparisons between dimensionless parameter values estimated from protoplast assays and whole plant luminescence data.
The x-axis is the natural logarithm of the dimensionless variables A/H or B/H, as defined in **Eqn. S3.5**. **Section 8.4.4** explains the rationale behind using these parameters for comparison of the results of the protoplast with whole plant data. The y-axis represents the values of Hill coefficients. The empty blue circles are parameter value combinations estimated from the whole plant luminescence data and the filled red triangles the parameter values from protoplast assays. **a-b**, NOS_{2xGal4}.EAR; **c-d**, $35S_{2xLexA}$.EAR; **e-f**, $35S_{4xLexA}$TATA.OFPx.

8.4.4 Proof of the comparability of de-dimensionalized parameter values estimated from protoplast assays and whole plant luminescence data

In Schaumberg et al. [4], we developed a quantitative model of the parameters estimated from the protoplast assays in terms of the response function at the single-plasmid level, and mathematical expressions connecting the single-plasmid level and the experimental observables. Using variables as defined in **Equation S3.4**, the fitting results can be represented as:

$$B_i = C_2 \langle N_{ij} \rangle_j \alpha_i \beta_i$$

$$H_i = C_1 \tilde{C} \langle N_{ij} \rangle_j \alpha_i K_i$$

The meaning of each parameter is described briefly here for the reader's convenience. Please refer to Schaumberg et al. [4] for more details.

β_i represents the maximal expression of the R-luciferase (Rluc) protein with no repressor in a single plasmid (i.e. promoter strength);

K_i is the repressor concentration required for half-maximal expression of Rluc in a single plasmid (i.e. repressibility);

α_i represents the batch variability factor;

N_{ij} represents the total number of plasmids in the j-th well of the i-th plasmid;

Therefore, $\alpha_i N_{ij}$ describes the plasmid copy number in viable protoplasts in the j-th well of the i-th plasmid.

C_1 is the concentration - luminescence proportionality factor of F-Luciferase (Fluc);

C_2 is the concentration - luminescence proportionality factor of RLuc;

$\tilde{C}$ is a proportionality factor between the concentrations of repressor and FLuc (both of which are controlled by the same promoter).

A similar representation can be derived for the leaky expression level A due to its similarity to B_i.

$$A_i = C_2\langle N_{ij}\rangle_j \alpha_i a_i$$

Note that a_i is the leaky expression level in single-plasmid level, while α_i (alpha) is the batch variability factor. The mathematical representations of these parameters indicate an intuitive method to de-dimensionalize these parameters by simply dividing A_i and B_i by H_i.

$$\frac{A_i}{H_i} = \frac{C_2 a_i}{C_1 \tilde{C} K_i}$$

$$\frac{B_i}{H_i} = \frac{C_2 \beta_i}{C_1 \tilde{C} K_i}$$

As described in Schaumberg et al.[7], C_1 and C_2 can be estimated from the experimental standard curve relating the luminescence levels and the molecular numbers of the two types of luciferase. C_1 and C_2 were first estimated from standard curves measured experimentally. Then, their values were used to convert the experimental data from luminescence level to molecular numbers, after which the nonlinear least square fitting was carried out. Therefore, A_i, B_i and H_i are already in the unit of molecular numbers and the C_1 and C_2 in the dimensionless representation can be discarded. We can reasonably assume $\tilde{C} = 1$, meaning a 1:1 ratio between the molecular numbers of FLuc and repressor, because they are driven by the same promoter. Therefore, we have:

$$\frac{A_i}{H_i} = \frac{a_i}{K_i}$$

$$\frac{B_i}{H_i} = \frac{\beta_i}{K_i}$$

Following a similar logic, we can also develop a quantitative model of the parameters estimated from the whole plant luminescence data. Firstly, the mean luminescence emitted from a single pixel can be represented as:

$$\langle F_i \rangle = C_1 \tilde{C} \langle N_i \rangle R_i$$

where the meaning of each variable is similar to the protoplast assay but modified accordingly.

F_i represents the luminescence emitted from a single pixel and the square brackets indicate population mean across all pixels included to quantify the luminescence.

R_i represents the total number of repressors in a single cell;

$\mathrm{N_i}$ represents the total number of plant cells in one pixel;

$\mathrm{C_1}$ is the concentration - luminescence proportionality factor of FLuc;

$\tilde{\mathrm{C}}$ is a proportionality factor between the repressor concentration and FLuc concentration (both of which are controlled by the same promoter), which we assume equals 1, as explained above.

Because FLuc was the only reporter of the toggle switch assembled and tested in the whole plant, and population mean luminescence per pixel was used for the nonlinear least-square fitting, the ODE system formulated in **Equation S3.1** can be rescaled and the fitted parameters can be represented by:

$$A_i = C_1 \tilde{C} \langle N_i \rangle a_i$$

$$B_i = C_1 \tilde{C} \langle N_i \rangle \beta_i$$

$$H_i = C_1 \tilde{C} \langle N_i \rangle K_i$$

We can now de-dimensionalize the parameters in the same way.

$$\frac{A_i}{H_i} = \frac{a_i}{K_i}$$

$$\frac{B_i}{H_i} = \frac{\beta_i}{K_i}$$

Therefore, the de-dimensionalized parameter values estimated from the protoplast assay and the whole plant luminescence data are directly comparable.

8.4.5 Testing the MCMC Algorithm Using Simulated Experimental Data

We tested the reliability of the MCMC algorithm using a simulated dataset. We first picked a parameter set of the ODE model representing a bistable toggle switch, then simulated different treatments as applied in the experiments and sampled several discrete time points with a constant time step from the numerical solutions as in the experimental setup. In particular, only one side of the toggle switch was sampled and used for the MCMC, as only one side of the toggle switch is labeled with the luciferase gene reporter in the experiments.

The simulated data are shown as red dots in **Fig. S3.7a.** With the MCMC algorithm run as described in the **Section 8.1**, the true parameter values were recovered reliably (**Fig. S3.7b)**. Out of 100 runs, 92 runs were found to meet the preset threshold for log likelihood and all of them predict the bistability property of the toggle switch using the method described above.

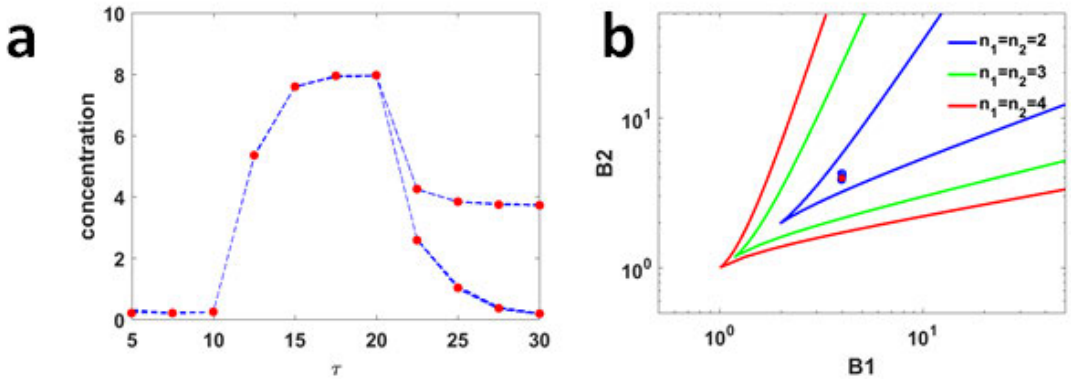

Figure S3.7. Reliability of the MCMC algorithm tested by simulated experimental data. **a**, Simulated data and MCMC fits. Numerical solutions of High memory and High to low as shown in red dots. MCMC fits are shown in blue dashed lines. **b**, Simulated data and MCMC fits in 2D phase diagram. True parameter value is shown by the red dot and the MCMC fits are the blue circles (n = 92).

REFERENCES

1. Padidam M, Cao Y. Elimination of transcriptional interference between tandem genes in plant cells. *Biotechniques.* 2001;31: 328–334.

2. Schaumberg KA, Antunes MS, Kassaw TK, Xu W, Zalewski CS, Medford JI, et al. Quantitative characterization of genetic parts and circuits for plant synthetic biology. *Nat Meth.* 2016;13: 94–100. doi: nmeth.3659

3. Press, W. H., Teukolsky, S. A., Vetterling, W. T. & Flannery BP. *Numerical Recipes: The Art of Scientific Computing.* 3rd edition. Cambridge University Press; 2007.

4. Gardner TS, Cantor CR, Collins JJ. Construction of a genetic toggle switch in Escherichia coli. *Nature.* 2000;403: 339–42. doi:10.1038/35002131

5. Singer T, Burke E. *Plant Functional Genomics.* In: Grotewold E, editor. *Methods in Molecular Biology.* Humana Press; 2003. pp. 241–271.

6. Alon U. *An Introduction to Systems Biology: Design Principles of Biological Circuits.* 1st edition. Taylor & Francis; 2006.

9.1 Supplementary figures

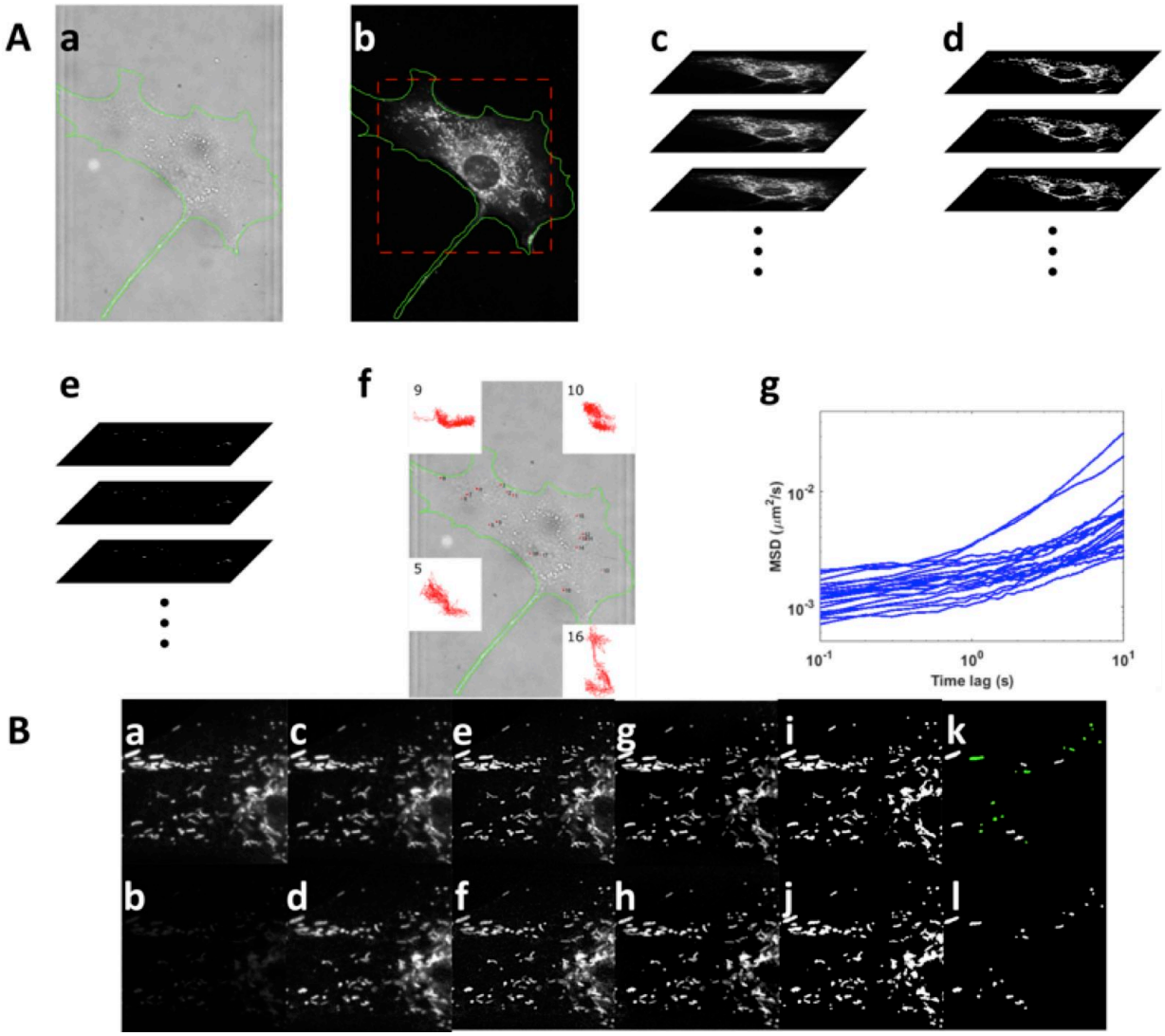

Figure S4.1: (A) Experimental flow chart of this study. (a) One isolated 10T1/2 cell imaged in bright-field (DICC channel). Green solid line indicates the cell boundary traced manually. (b) The same cell stained with MitoTracker Green FM and imaged under 488 nm. Red dashed line indicates the imaging window used to take time-lapse images. (c) A time-lapse image is taken for 100 s at a temporal resolution of 10 frames per second. (d) Image processing of the time-lapse images. (e) Punctate mitochondria spanning 100 seconds and without interaction with other mitochondria is selected. (f) The 2D centroids weighted by intensities of mitochondria are tracked to extract their trajectories. The insets at the four corners are examples of resulting mitochondrial trajectories. (g) Mean square displacement measured for each mitochondrion tracked. **(B) Image processing protocol used for the time-lapse images of mitochondria.** The

first row shows the first frame and the second row the last frame of the time-lapse series. (a,b) Raw images. (c,d) Histogram matching to adjust intensity. (e,f) 2D deconvolution. (g,h) Bandpass filtering in the frequency domain. (i,j) Grayscale thresholding. (k,l) Punctate mitochondria selected. Green colored mitochondria in panel (k) indicate the ones passed the morphological filtering of solidity less than 1.1 and aspect ratio less than 2.

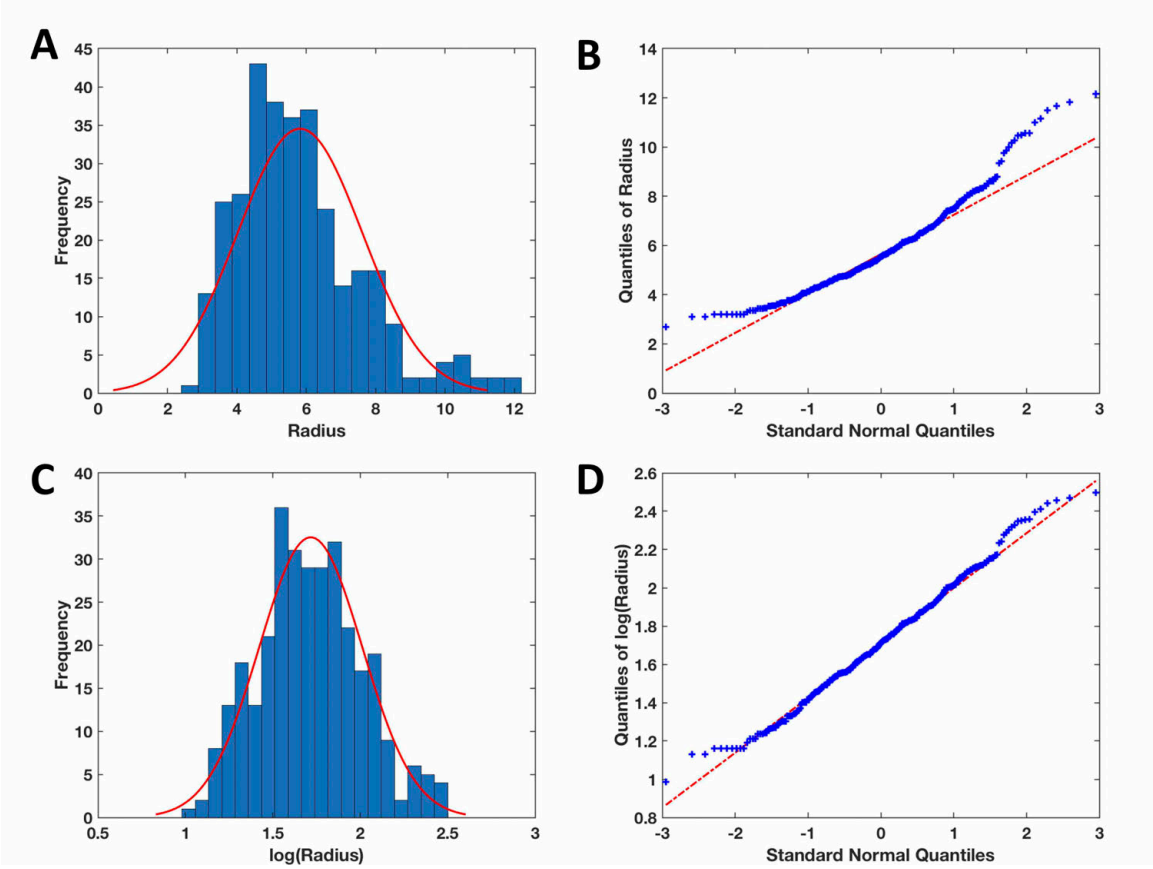

Figure S4.2. Distribution of hydrodynamic radii of mitochondria passing the morphological filtering is better described by a log-normal distribution than a Gaussian distribution. (A, C)
Histogram fitting of raw data and logarithmic transformed data of hydrodynamic radii respectively (n = 317). **(B, D)** Quantile-quantity plot of raw data and logarithmic transformed data of hydrodynamic radii respectively.

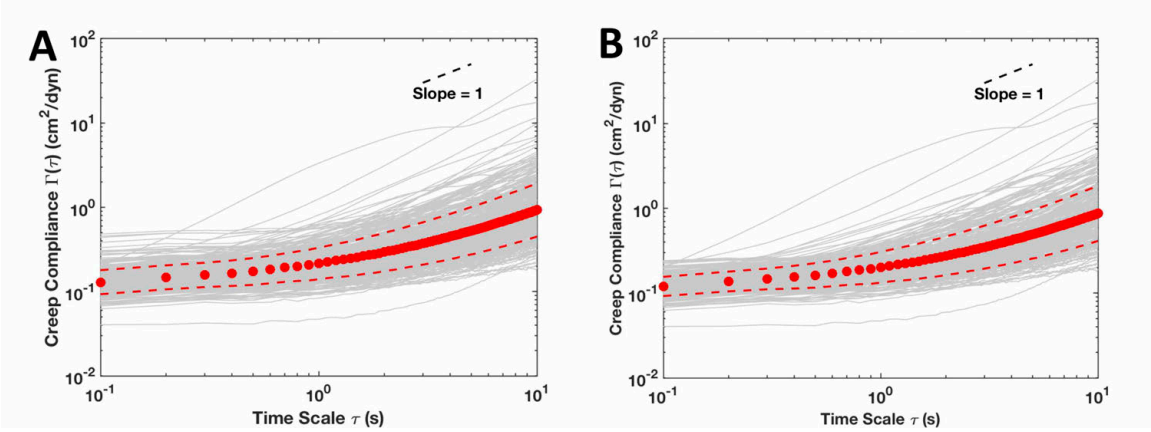

Figure S4.3. Morphological filtering reduces the variance in creep compliance.
Individual and population mean with standard deviations of creep compliance (**A**) without or (**B**) with morphological filtering respectively. Gray curves are individual mitochondria and red filled circles indicate population mean. Red dashed lines are standard deviations. Black dashed line is a visual guide of slope one.

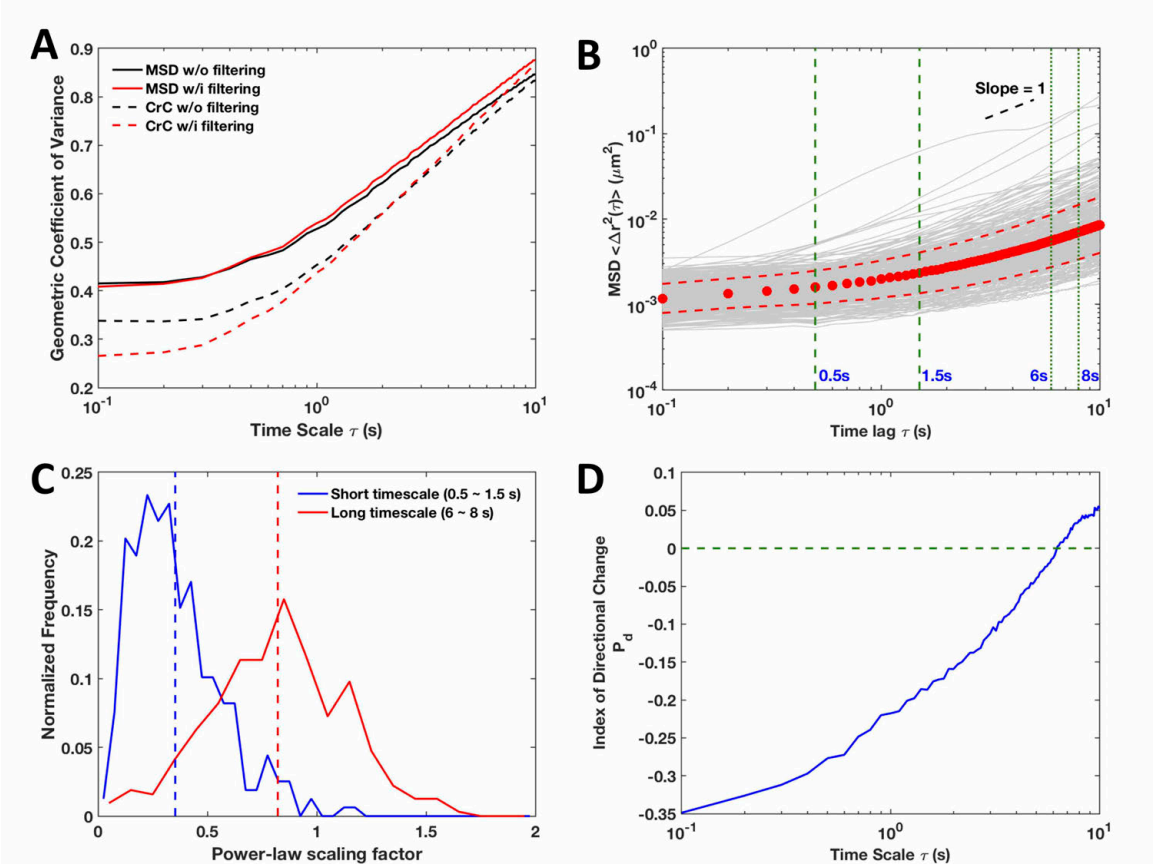

Figure S4.4. Measurements based on mitochondrial fluctuations (continued).
(**A**) The geometric coefficient of variance (GCV) of MSD and creep compliance (CrC) with and without morphological filtering. (**B**) Individual and population mean with standard deviations of MSDs (n=211). Gray curves are individual mitochondria and red filled circles indicate population mean. Red dashed lines are standard deviations. Vertical green dashed lines indicate the range of timescales where the two power-law scaling factors of different timescales were evaluated. Short timescale was evaluated between 0.5 and 1.5 s, while long timescale was between 6 and 8 s. Black dashed line is a visual guide of slope = 1. (**C**) Comparisons of the histograms of power-law scaling factor showing the different lag time dependence at short and long timescales evaluated. (**D**) Index of directional persistence, P_d, of control cells. Green dashed line indicates $P_d = 0$, which is characteristic of pure diffusion.

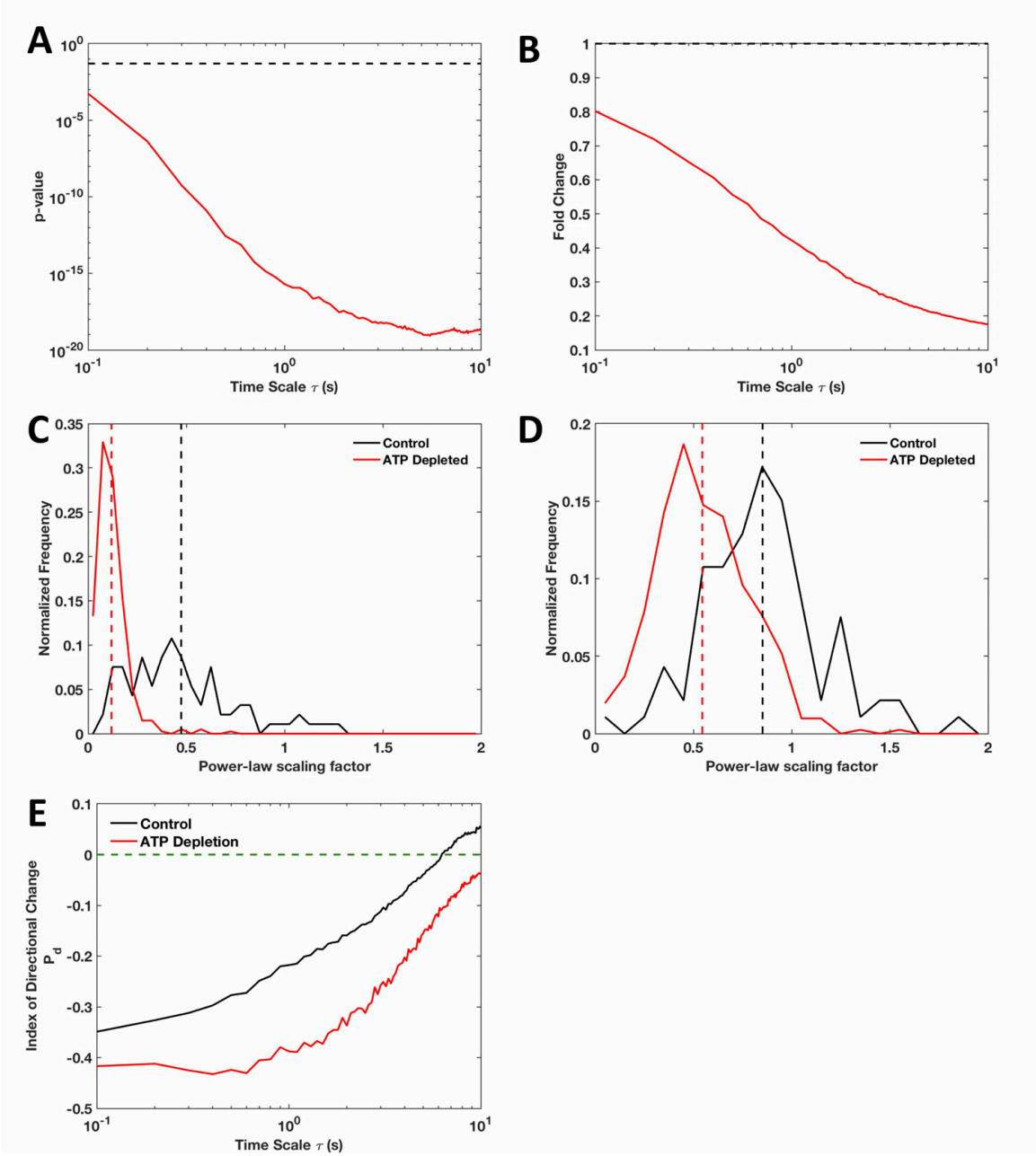

Figure S4.5. Mitochondrial fluctuations are ATP dependent (Continued).
(**A**) p-values of Wilcoxon rank sum test between ATP depleted cells and control cells on creep compliance. Black dashed line is a visual guide of p value equals to 0.05. The portion of the curve below 0.05 indicates that the change in mean is statistically significant, while being above that threshold is an indication of insignificant changes. (**B**) Fold change of creep compliances of ATP depleted cells compared to control cells. Black dashed line indicates a visual guide of fold change equals to one. (**C, D**) Comparisons between the control (black) and ATP depleted (red) cells in terms of the distributions of power-law scaling factor over short (0.5-1.5 s) and long (6-8 s) timescales respectively. Vertical dashed lines indicate the mean power-law scaling factor of the corresponding treatment as color-coded. The ATP depleted cells show a low mean power-law scaling factor of 0.12 compared to the control cells with a mean of 0.47 at the short timescale.

Although the slopes become closer at the long timescale, the mean power-law scaling factor of 0.55 of ATP depleted cells is still smaller than the control cells at 0.85. Black solid lines indicate control cells and red dashed lines are for ATP depleted cells. **E**) Indexes of directional persistence, P_d, of control and ATP depleted cells. Green dashed line indicates $P_d = 0$, which is characteristic of pure diffusion.

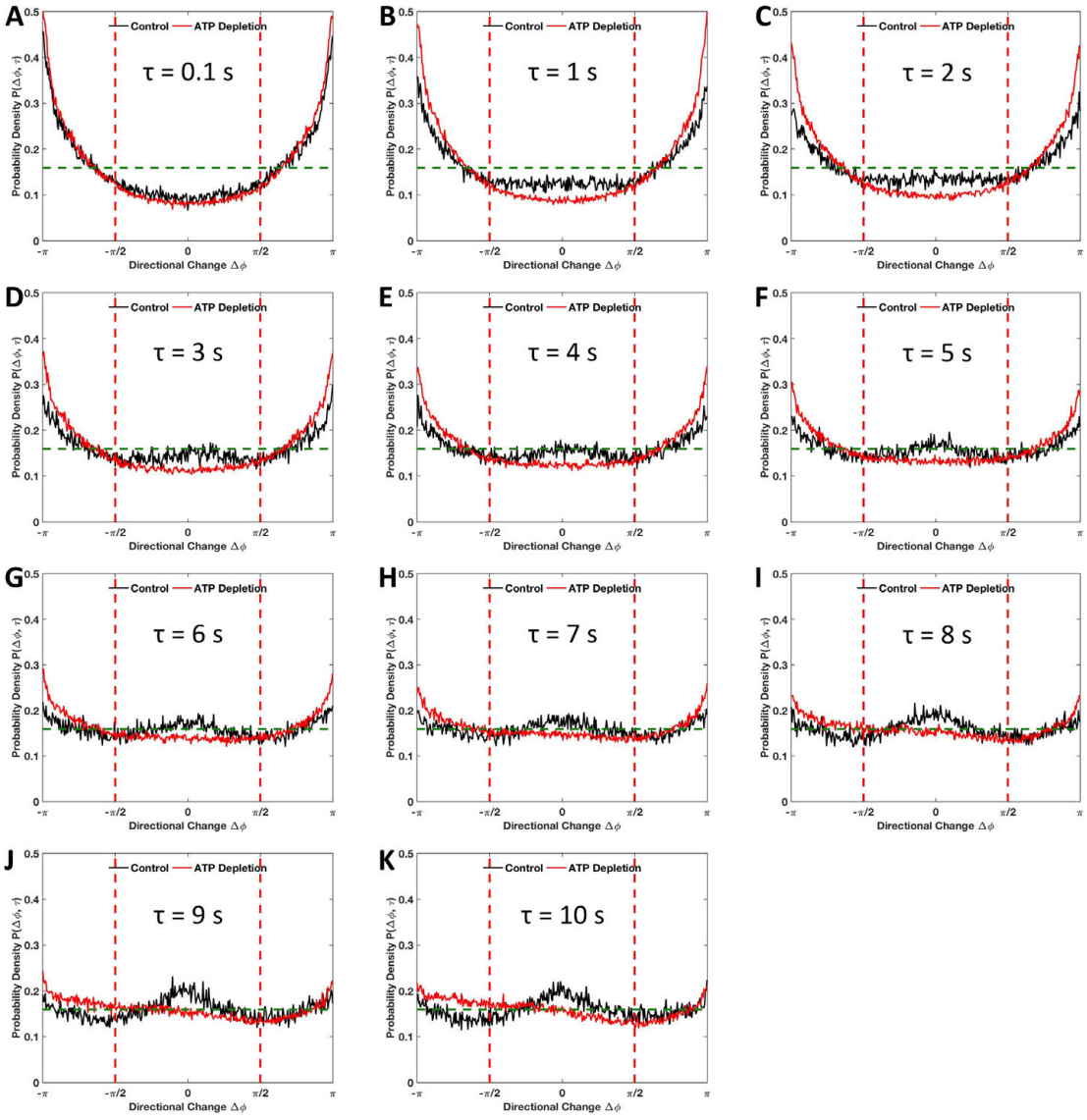

Figure S4.6. Distributions of directional change of control cells and ATP depleted cells as a function of lag times.

(**A-K**) Distributions of directional change of control cells and ATP depleted cells at different lag times. Green dashed line indicates a uniform distribution which is characteristic of pure diffusion.

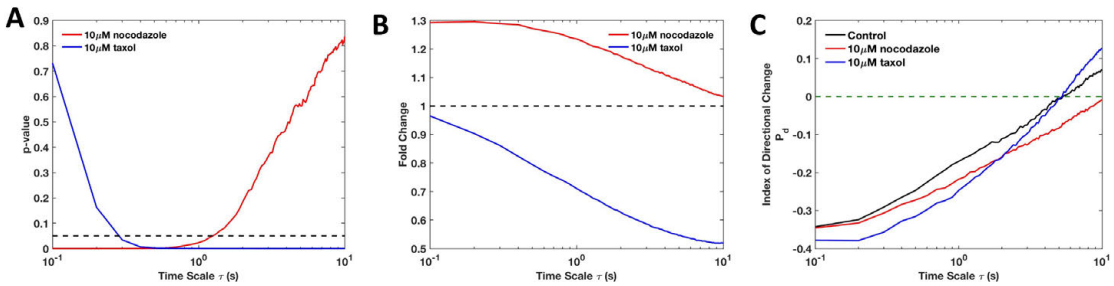

Figure S4.7. Microtubule network plays a significant role in mitochondrial fluctuations (continued).
(**A**) p-values of Wilcoxon rank sum test between chemical treated cells with taxol or nocodazole to control cells. Black dashed line is a visual guide of p-value equals to 0.05. (**B**) Fold change of the mean creep compliances of nocodazole or taxol treated cells compared to control cells. Black dashed line indicates a visual guide of fold change equals to one. (**C**) Directional persistence of control and nocodazole and taxol treated cells. Green dashed line indicates $P_d = 0$, which is characteristic of pure diffusion.

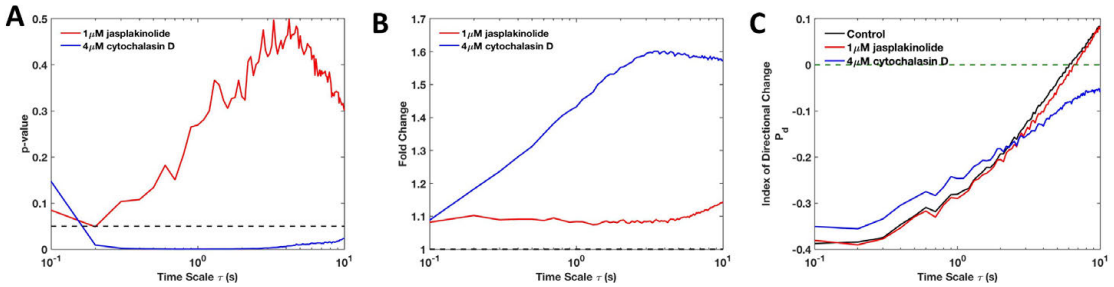

Figure S4.8. Actin network is required for active mitochondrial fluctuations. (continued).
(**A**) p values of Wilcoxon rank sum test between cells treated by jasplakinolide or cytochalasin D with control cells. Black dashed line is a visual guide of p-value equals to 0.05. (**B**) Fold change of the mean creep compliance of jasplakinolide or cytochalasin D treated cells compared to control cells. Black dashed line indicates a visual guide of fold change equals to one. (**C**) Directional persistence of control, jasplakinolide and cytochalasin D treated cells. Green dashed line indicates $P_d = 0$, which is characteristic of pure diffusion.

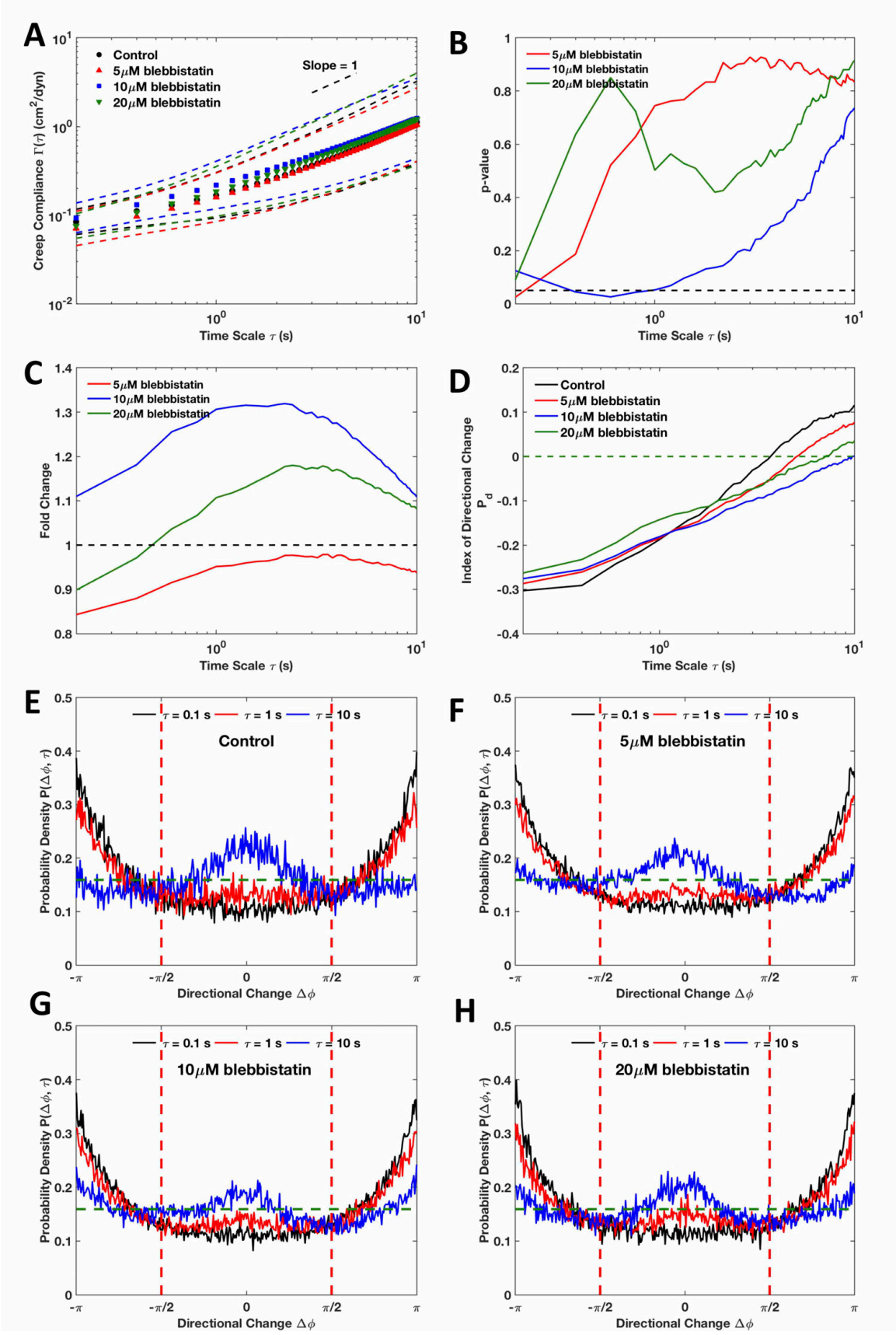
A
Control
5μM blebbistatin
10μM blebbistatin
20μM blebbistatin
Slope = 1
Creep Compliance Γ(τ) (cm²/dyn)
Time Scale τ (s)
B
5μM blebbistatin
10μM blebbistatin
20μM blebbistatin
p-value
Time Scale τ (s)
C
5μM blebbistatin
10μM blebbistatin
20μM blebbistatin
Fold Change
Time Scale τ (s)
D
Control
5μM blebbistatin
10μM blebbistatin
20μM blebbistatin
Index of Directional Change P_d
Time Scale τ (s)
E
τ = 0.1 s
τ = 1 s
τ = 10 s
Control
Probability Density P(Δφ, τ)
Directional Change Δφ
F
τ = 0.1 s
τ = 1 s
τ = 10 s
5μM blebbistatin
Probability Density P(Δφ, τ)
Directional Change Δφ
G
τ = 0.1 s
τ = 1 s
τ = 10 s
10μM blebbistatin
Probability Density P(Δφ, τ)
Directional Change Δφ
H
τ = 0.1 s
τ = 1 s
τ = 10 s
20μM blebbistatin
Probability Density P(Δφ, τ)
Directional Change Δφ

Figure S4.9. Mitochondrial fluctuations were not primarily driven by myosin II.
(**A**) Population mean creep compliances with standard deviations of control cells (n=38) and cells treated by 5μM (n=133), 10μM (n=67) and 20μM (n=85) blebbistatin. Markers of different shapes and colors indicate population means and dashed lines are standard deviations. Short black dashed line is a visual guide of slope one. (**B**) p-values of Wilcoxon rank sum test between each blebbistatin treated cells with different concentration to control cells. Black dashed line is a visual guide of p-value equals to 0.05. The portion of the curve below 0.05 indicates that the change in mean is statistically significant, while being above that threshold is an indication of insignificant change. (**C**) Fold changes of creep compliances of cells treated by blebbistatin of different concentrations compared to control cells. Dashed line indicates a visual guide of fold change equals to one. (**D**) Directional persistence of control cells and cells treated with blebbistatin of different concentrations. Green dashed line indicates $P_d = 0$, which is characteristic of pure diffusion. (**E-H**) Distribution of directional change at different lag times of control and cells treated with blebbistatin of different concentrations respectively. Green dashed horizontal line indicates a uniform distribution which is characteristic of pure diffusion.

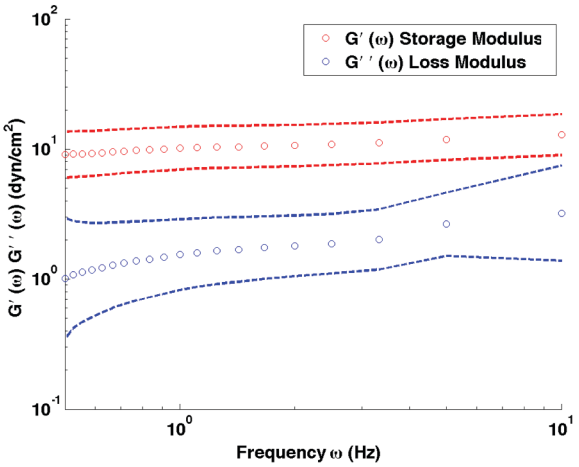

Figure S4.10. Storage modulus and loss modulus determined from ATP depleted cells using GSER.
Red curve shows the storage modulus and blue curve the loss modulus. Circles are population means and dashed lines are standard deviations.

9.2 Supplementary tables

Table S4.1. Chemical treatments

Target	Treatment/pharmacological agent name	Concentration	Reference
Actin	Jasplakinolide	1 μM	[1]
	Cytochalasin D	4 μM	[2,3]
Myosin II	Blebbistatin	5, 10, 20 μM	[4–6]
Microtubule	Nocodazole	10 μM	[7]
	Taxol	10 μM	[8–10]
All ATP dependent processes	ATP Depletion	2 mM NaN_3 + 2 mM Deoxy-glucose	[11,12]

Table S4.2. Comparisons of our results to previous studies.
PMR is short for passive microrheology and AMR is for active microrheology.

Reference	**Power-law exponent**	**Technique**	**Cell line**	**Mechanical property measured**
this work	0.12	PMR using ATP depletion	10T1/2-CH3	intracellular
[13]	0.16	AMR using optical tweezer	A7	intracellular
[14]	0.2	AMR using optical tweezer	mEF	intracellular
[15]	0.17	optical magnetic twisting cytometry (OMTC)	HASM	cortical
[16]	0.24	uniaxial stretching rheometer	C2-7	whole cell
[17]	0.2	Atomic Force Microscopy (AFM)	A549, BEAS-2B	cortical

9.3 Supplementary notes

9.3.1 Supplemental Note 4.1

Our image processing protocol includes the following processing steps (Fig. S1 B). 1) Histogram matching to adjust intensity (Fig. S4.1 B. c-d): Intensity histograms of all following frames in the time-lapse images are matched to that of the first frame to correct for the decrease in intensity due to photobleaching. 2) 2D deconvolution (Fig. S4.1 B. e-f): 2D deconvolution is carried out to sharpen the image using blind deconvolution for 25 iterations. This step reduces the blurriness of out-of-focus mitochondria. 3) Bandpass filtering in the frequency domain (Fig. S4.1 B. g-h): Each frame in the time-lapse series is first converted to a frequency-domain representation through Discrete Fourier Transform (DFT), then multiplied with a Gaussian bandpass filter of 2 to 200 pixels in the frequency domain to highlight the mitochondria with sizes within this range and then converted back to spatial domain via an inverse DFT. 4) Grayscale thresholding (Fig. S4.1 B. i-j): Otsu's method is applied to automatically approximate the binary threshold of each frame. 5) Mitochondria spanning the entire imaging period of 100 seconds and with no interaction with other mitochondria, were selected for further analysis (Fig. S4.1 B. k-l). A built-in Matlab function, bwconncomp(), was used to construct the three-dimensional connected objects from the binary time-lapse images generated in Step 4). No interaction with other mitochondria can thus be defined as no branch in the temporal axis of the three-dimensional connected objects.

9.3.2 Supplemental Note 4.2

The loss modulus G''(ω) measures the propensity to flow under random or applied forces, while the storage modulus G'(ω) measures its stretchiness, i.e. the ability to resist forces and store energy caused by deformation [18]. For systems at thermodynamic equilibrium, the

fluctuation dissipation theorem (FDT) is valid, and G'(ω) and G''(ω) can be determined based on the generalized Stokes-Einstein relationship (GSER), which is briefly recapitulated here:

$$\tilde{G}(s) = \frac{2k_BT}{3\pi as\langle \Delta r^2(s)\rangle} \quad [S1]$$

$\tilde{G}(s)$ is the shear modulus, s the Laplace frequency and $\langle \Delta r^2(s)\rangle$ the unilateral Laplace transform of $\langle \Delta r^2(t)\rangle$. However, truncation errors introduced by taking a numerical Laplace transform of $\langle \Delta r^2(t)\rangle$ can be significant [19]. To avoid this, following Ref. [19], an algebraic approximation can be carried out to replace $s\langle \Delta r^2(s)\rangle$ with the dominant component of its power-law expansion:

$$\tilde{G}(s) = \frac{2k_BT}{3\pi a\langle \Delta r^2(t)\rangle \Gamma(1+\alpha)} \quad [S2]$$

where $t = \frac{1}{s}$ is the lag time, $\alpha = \frac{\partial ln\langle \Delta r^2(t)\rangle}{\partial ln\, t}$ is the logarithmic slope of $\langle \Delta r^2(t)\rangle$, and Γ is the Gamma function. s can be substituted by $i\omega$ to obtain the complex shear modulus $G^*(\omega) = G'(\omega) + iG''(\omega)$. Applying Euler's formula, G'(ω) and G''(ω) can be calculated as:

$$G'(\omega) = |G^*(\omega)|\cos\left(\frac{\pi}{2}\alpha\right) \quad [S3]$$

$$G''(\omega) = |G^*(\omega)|\sin\left(\frac{\pi}{2}\alpha\right) \quad [S4]$$

where the α is the logarithmic slope of $\langle \Delta r^2(t)\rangle$ as in Eq. [S2].

9.3.3 Supplemental Note 4.3

To quantify the mitochondrial fluctuations from the tracking trajectories, mean square displacement (MSD) is widely used as the time-averaged and ensemble-averaged squared displacement between all possible time points for a given lag time as defined in Eq. 1. Similar to earlier works, there is also a high level of variance in our MSD results of individual mitochondrion (Fig. 4,1 A) [20]. We also found that the distributions of the MSDs at a single time lags can be better described by log-normal distributions than Gaussian distributions (Fig.

S4.11) [13,20]. In addition, algebraic means and standard deviations result in overestimations and poor behaviors in logarithmic scale for our cells (Fig. S4.12). Therefore, the mean of the logarithmic transformed data ($\bar{\mu}_{ln}$) is exponentiated to yield the mean values reported in this study. Similarly, the standard deviation of the logarithmic transformed data (s_{ln}) is exponentiated to generate the "multiplicative" log-normal standard deviations reported.

9.3.4 Supplemental Note 4.4

Fig. S4.13 shows the day-to-day variances of measurements carried out on control cells in three different days. We think these variances are mainly due to experimental batch-effects in preparing the cell samples while all the other factors are the same, such as subtle difference in doing the cell culture by different personnel and subtle differences in cell states. Such a batch effect was reported to be around 20% by other groups [21]. As can be observed in Fig. S4.13, the variance in our results appears to be on the similar level. To reduce this day-to-day variance due to the batch effect, we only compare among the measurements made on same days, although doing this actually increases the workload.

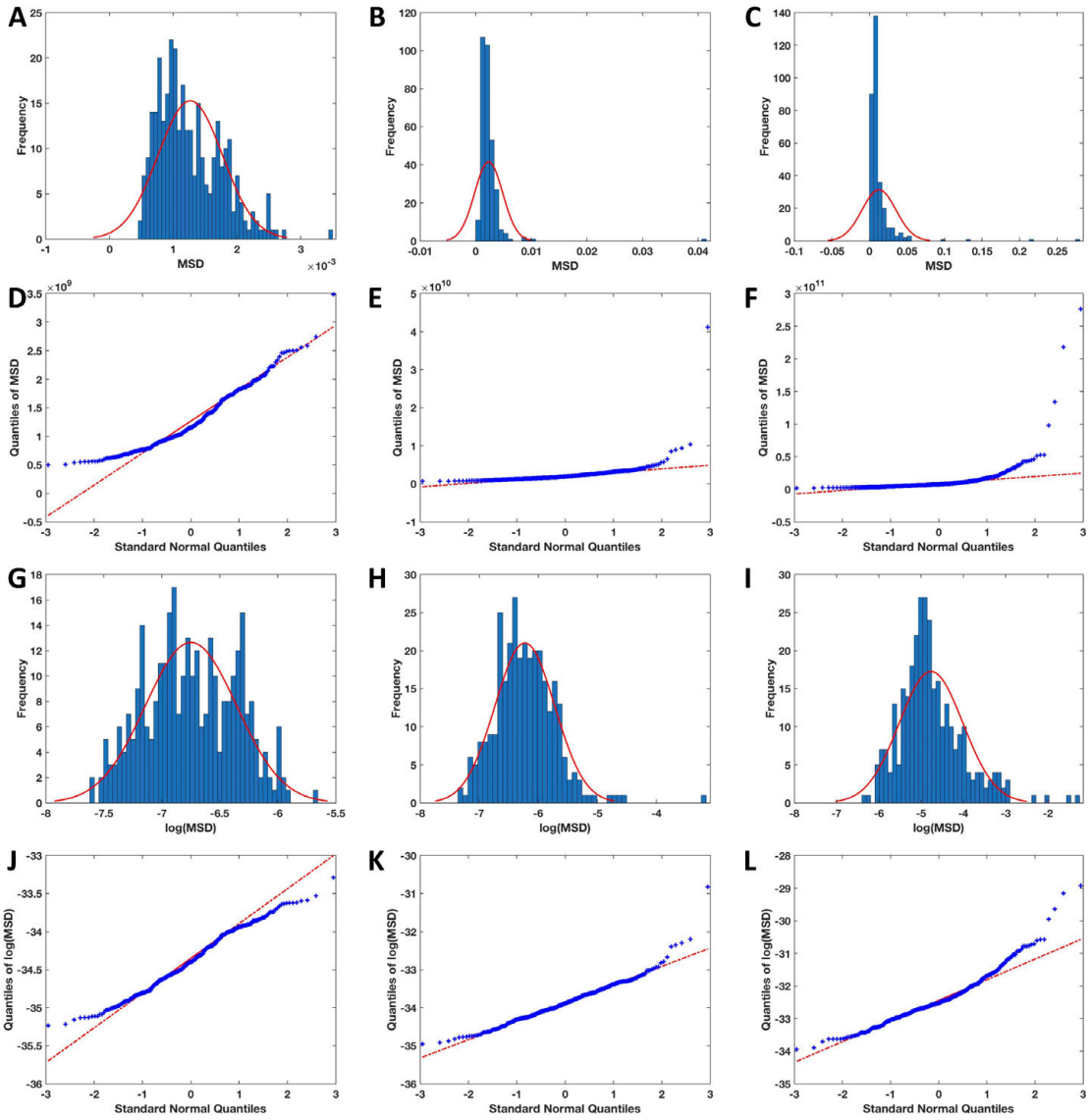

Figure S4.11. Distributions of MSD at single lag times are better described by log-normal distributions than Gaussian.
(**A-C**) Gaussian distribution fitting and (**D-F**) quantile-quantity plot of raw MSD at 0.1, 1 and 10 s respectively (n = 317). (**G-I**) Gaussian distribution fitting and (**J-L**) quantile-quantity plot of logarithmic transformed MSD at 0.1, 1 and 10 s respectively (n = 317).

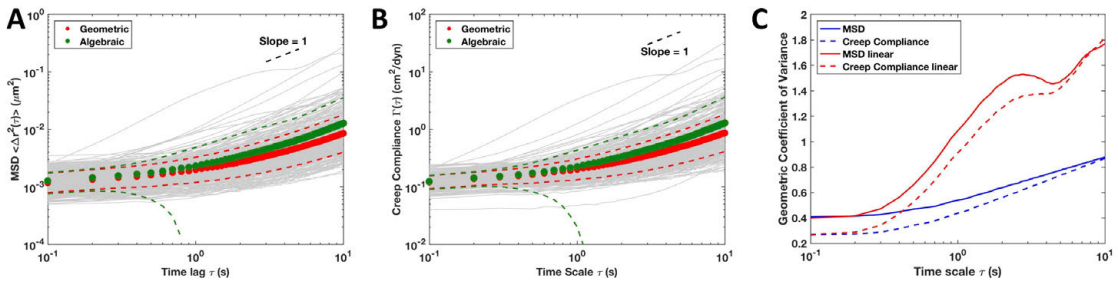

Figure S4.12. Comparisons between geometric statistics and algebraic statistics. Individual and population statistics of (**A**) MSDs and (**B**) creep compliance respectively (n = 317). Gray curves mark individual mitochondria. Filled circles indicate population means and dashed lines indicate standard deviations. Black dashed line is a visual guide of slope one. Algebraic statistics result in overestimation of population mean and standard deviations compared to geometric statistics. (**C**) Geometric coefficient of variance (GCV) of geometric statistics and algebraic statistics. The GCV results quantify the overestimation by algebraic standard deviations.

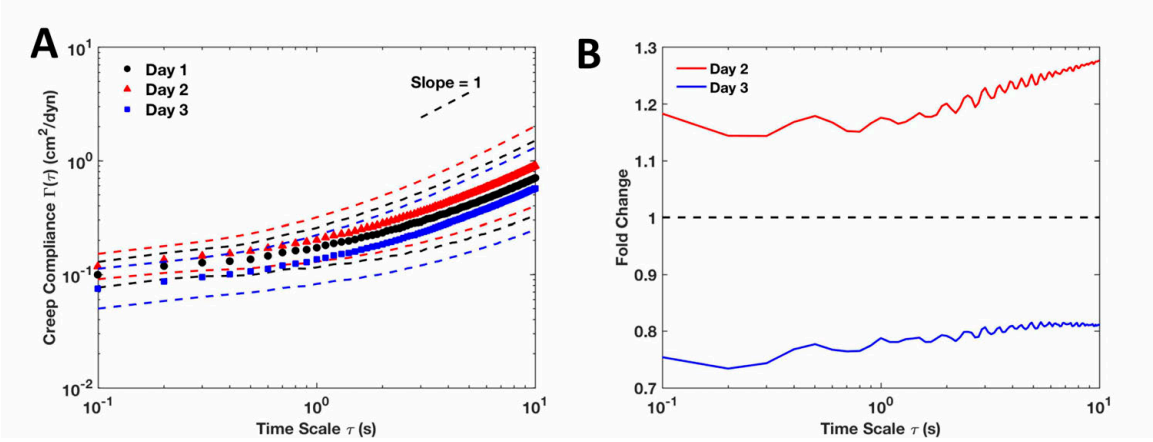

Figure S4.13. The day-to-day variances of measurements on control cells in three different days.
(A) Population means with standard deviations of creep compliances. Markers with different shapes and colors indicate population means and dashed lines in the same color are standard deviations. Black dashed line is a visual guide of slope one. **(B)** Fold changes of creep compliances of Day 2 and Day 3 compared to Day 1. Dashed line indicates a visual guide of fold change equals to one.

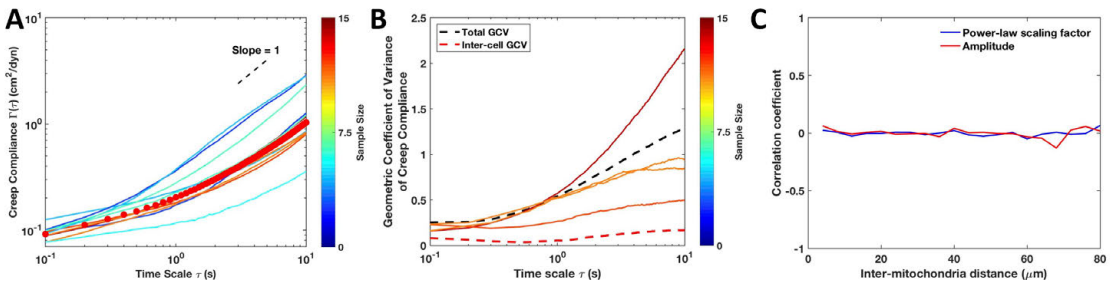

Figure S4.14. Viscoelastic microenvironment probed by mitochondria is highly heterogeneous.

(A) Cell-wise mean creep compliances compared to the population mean. The red filled circles indicate the population mean creep compliance. The solid lines indicate the cell-wise mean creep compliances, which are color-coded by the sample size of mitochondria tracked inside that cell in accordance to the colormap shown on the right. The cell-wise mean creep compliances converge towards the population mean as a function of the sample size of mitochondria inside one cell. The larger the sample size (labelled by warmer colors), the closer of the cell-wise mean to the population mean. **(B)** The heterogeneity in the creep compliance is dominated by intracellular sources, as measured by the geometric coefficient of variance (GCV). The population GCV is indicated by the black dashed line, the inter-cell GCV by the red dashed line and the intra-cell GCV of cells with large sample size (n >= 10) by the solid lines color-coded by the sample size as in **(A)**. **(C)** The viscoelasticity measured in the ATP depleted cells shows no obvious spatial correlation probably due to the high heterogeneity probed by mitochondria. The |G*| measurement of individual mitochondrion were fitted to a power-law model, so that the dimension of the data to be analyzed were reduced to the amplitude and the power-law scaling factor, which were binned based on the inter-mitochondria distance and the Pearson correlation coefficient calculated.

REFERENCES

1. Spector I, Braet F, Shochet NR, Bubb MR. New anti-actin drugs in the study of the organization and function of the actin cytoskeleton. *Microsc Res Tech.* 1999;47: 18–37. doi:10.1002/(SICI)1097-0029(19991001)47:1<18::AID-JEMT3>3.0.CO;2-E

2. Cooper JA. Effects of cytochalasins and phalloidin on actin. *J Cell Biol.* 1987;105:1473–1478.

3. Shoji K, Ohashi K, Sampei K, Oikawa M, Mizuno K. Cytochalasin D acts as an inhibitor of the actin-cofilin interaction. *Biochem Biophys Res Commun.* 2012;424: 52–57. doi:10.1016/j.bbrc.2012.06.063

4. Shu S, Liu X, Korn ED. Blebbistatin and blebbistatin-inactivated myosin II inhibit myosin II-independent processes in Dictyostelium. *Proc Natl Acad Sci*. 2005;102: 1472–1477. doi:10.1073/pnas.0409528102

5. Kovács M, Tóth J, Hetényi C, Málnási-Csizmadia A, Seller JR. Mechanism of blebbistatin inhibition of myosin II. *J Biol Chem.* 2004;279: 35557–35563. doi:10.1074/jbc.M405319200

6. Ramamurthy B, Yengo CM, Straight AF, Mitchison TJ, Sweeney HL. Kinetic mechanism of blebbistatin inhibition of nonmuscle myosin IIB. *Biochemistry.* 2004;43: 14832–14839. doi:10.1021/bi0490284

7. Vasquez RJ, Howell B, Yvon AM, Wadsworth P, Cassimeris L. Nanomolar concentrations of nocodazole alter microtubule dynamic instability in vivo and in vitro. *Mol Biol Cell.* 1997;8: 973–85.

8. Schiff PB, Fant J, Horwitz SB. Promotion of microtubule assembly in vitro by taxol. *Nature.* 1979;277: 665–667. doi:10.1038/277665a0

9. Horwitz SB. Taxol (paclitaxel): mechanisms of action. *Ann Oncol.* 1994;5 Suppl 6: S3-6.

10. Kingston DGI. Tubulin-interactive natural products as anticancer agents. *Journal of Natural Products.* 2009. pp. 507–515. doi:10.1021/np800568j

11. Ishikawa T, Bao-Li Z, Hitoshi M. Effect of sodium azide on the metabolic activity of cultured fetal cells. *Toxicol Ind Health.* 2006;22: 337–341.

12. Wick AN, Drury DR, Nakada HI, Wolfe JB. Localization of the primary metabolic block produced by 2-deoxyglucose. *J Biol Chem.* 1957;224: 963–969.

13. Guo M, Ehrlicher AJ, Jensen MH, Renz M, Moore JR, Goldman RD, et al. Probing the stochastic, motor-driven properties of the cytoplasm using force spectrum microscopy. *Cell.* 2014;158: 822–832. doi:10.1016/j.cell.2014.06.051

14. Guo M, Ehrlicher AJ, Mahammad S, Fabich H, Jensen MH, Moore JR, et al. The role of vimentin intermediate filaments in cortical and cytoplasmic mechanics. *Biophys J.* 2013;105: 1562–1568. doi:10.1016/j.bpj.2013.08.037

15. Fabry B, Maksym GN, Butler JP, Glogauer M, Navajas D, Fredberg JJ. Scaling the microrheology of living cells. *Phys Rev Lett.* 2001;87: 1–4. doi:10.1103/PhysRevLett.87.148102

16. Desprat N, Richert A, Simeon J, Asnacios A. Creep function of a single living cell.*Biophys J.* 2005;88: 2224–2233. doi:10.1529/biophysj.104.050278

17. Alcaraz J, Buscemi L, Grabulosa M, Trepat X, Fabry B, Farré R, et al. Microrheology of human lung epithelial cells measured by atomic force microscopy. *Biophys J.* 2003;84: 2071–2079. doi:10.1016/S0006-3495(03)75014-0

18. Wirtz D. Particle-tracking microrheology of living cells: principles and applications. *Annu Rev Biophys.* 2009;38: 301–26. doi:10.1146/annurev.biophys.050708.133724

19. Mason T, Ganesan K, van Zanten J, Wirtz D, Kuo S. Particle Tracking Microrheology of Complex Fluids. *Phys Rev Lett.* 1997;79: 3282–3285. doi:10.1103/PhysRevLett.79.3282

20. Hoffman BD, Massiera G, Van Citters KM, Crocker JC. The consensus mechanics of cultured mammalian cells. *Proc Natl Acad Sci.* 2006;103: 10259–10264. doi:10.1073/pnas.0510348103

21. Wu P-H, Hale CM, Chen W-C, Lee JSH, Tseng Y, Wirtz D. High-throughput ballistic injection nanorheology to measure cell mechanics. *Nat Protoc.* 2012;7: 155–170. doi:10.1038/nprot.2011.436

APPENDIX IV: SUPPLEMENTARY INFORMATION FOR CHAPTER 5

10.1 Supplementary figures

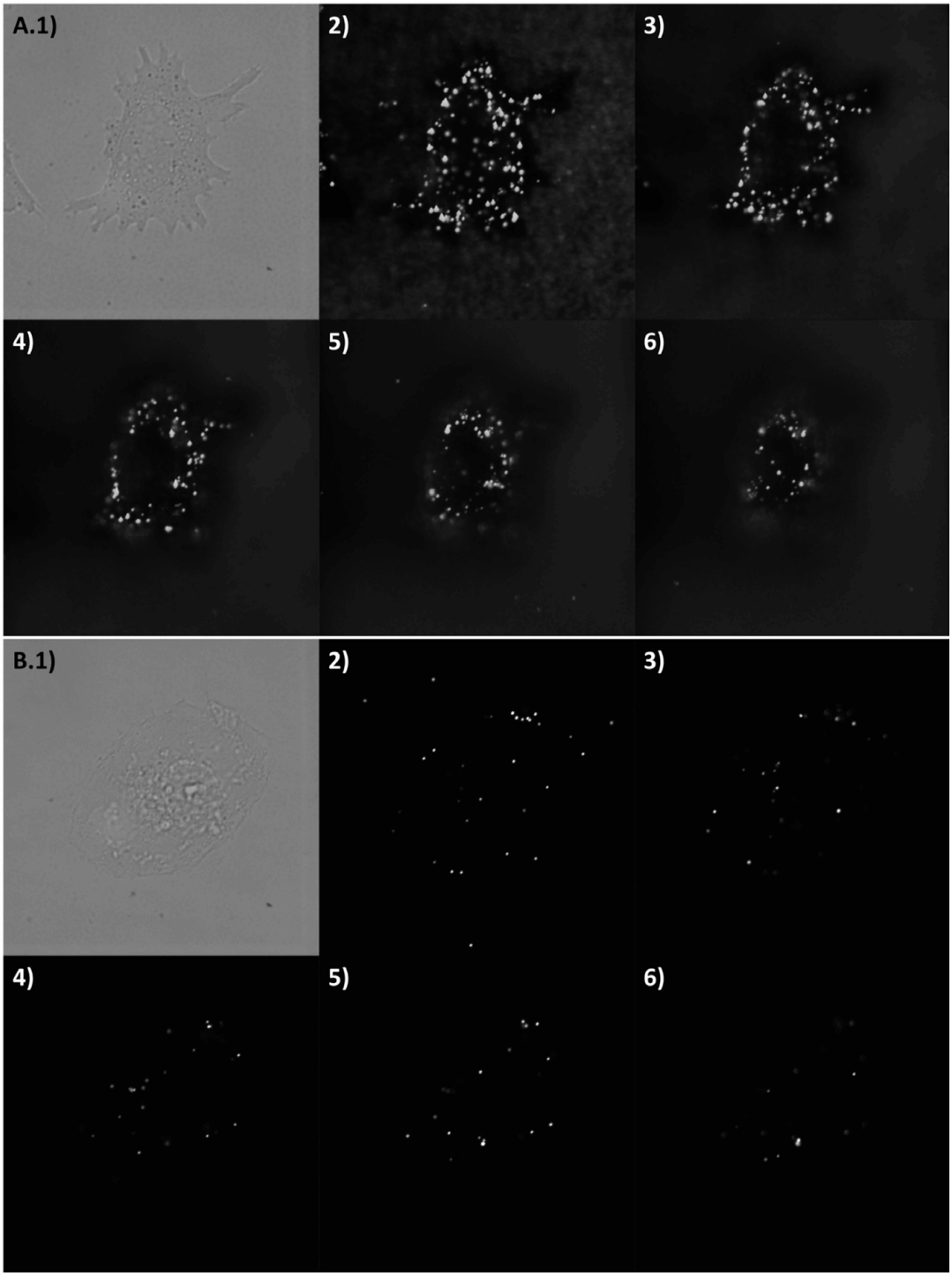

Figure S5.1. Glass beads load 100 nm fluorescent particles into cytoplasm of (A) MCF7 and (B) MDA-MB-231 cells under control condition.
1) Bright-field (DIC channel) image of MCF7 and MDA-MB-231 cells. **2-6)** Fluorescent (561 nm) images at different z-planes (from bottom to top with 1 μm apart) of MCF7 and MDA-MB-231 cells bead-loaded with 100nm fluorescent particles.

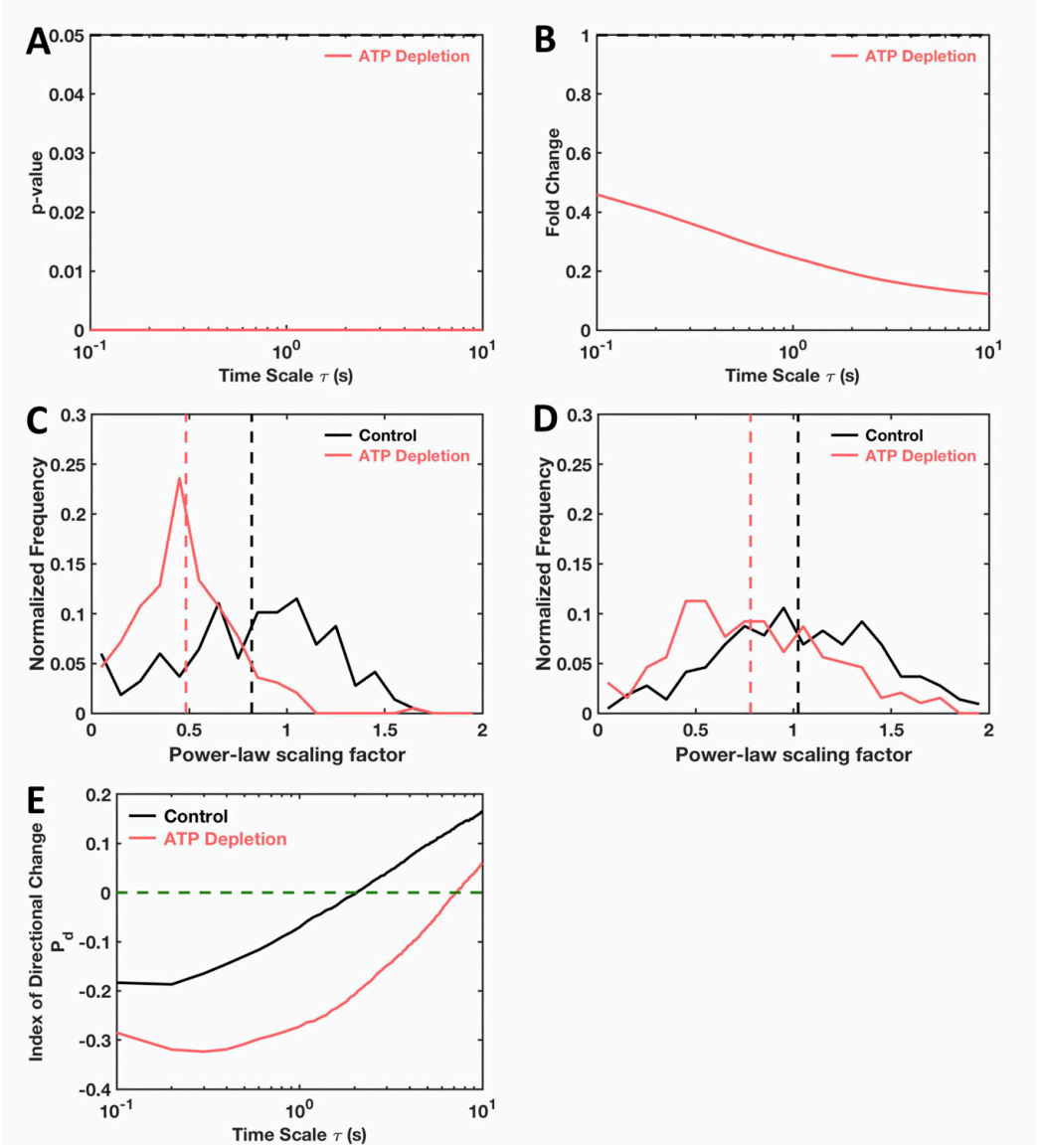

Figure S5.2. Fluctuations of fluorescent particles are ATP-dependent (continued).
(A) p-values of Wilcoxon rank sum test between MSDs of ATP depleted cells and control cells. Black dashed line is a visual guide of p value equals to 0.05. The portion of the curve below 0.05 indicates that the change in mean is statistically significant, while being above that threshold is an indication of insignificant changes. (**B**) Fold change of MSDs of ATP depleted cells compared to control cells. Black dashed line indicates a visual guide of fold change equals to one. (**C, D**) Comparisons between the control (black) and ATP depleted (red) cells in terms of the distributions of power-law scaling factor over short (0.5-1.5 s) and long (6-8 s) timescales respectively. Vertical dashed lines indicate the mean power-law scaling factor of the corresponding treatment as color-coded. **E**) Indexes of directional persistence, P_d, of control and ATP depleted cells. Green dashed line indicates $P_d = 0$, which is characteristic of pure diffusion.

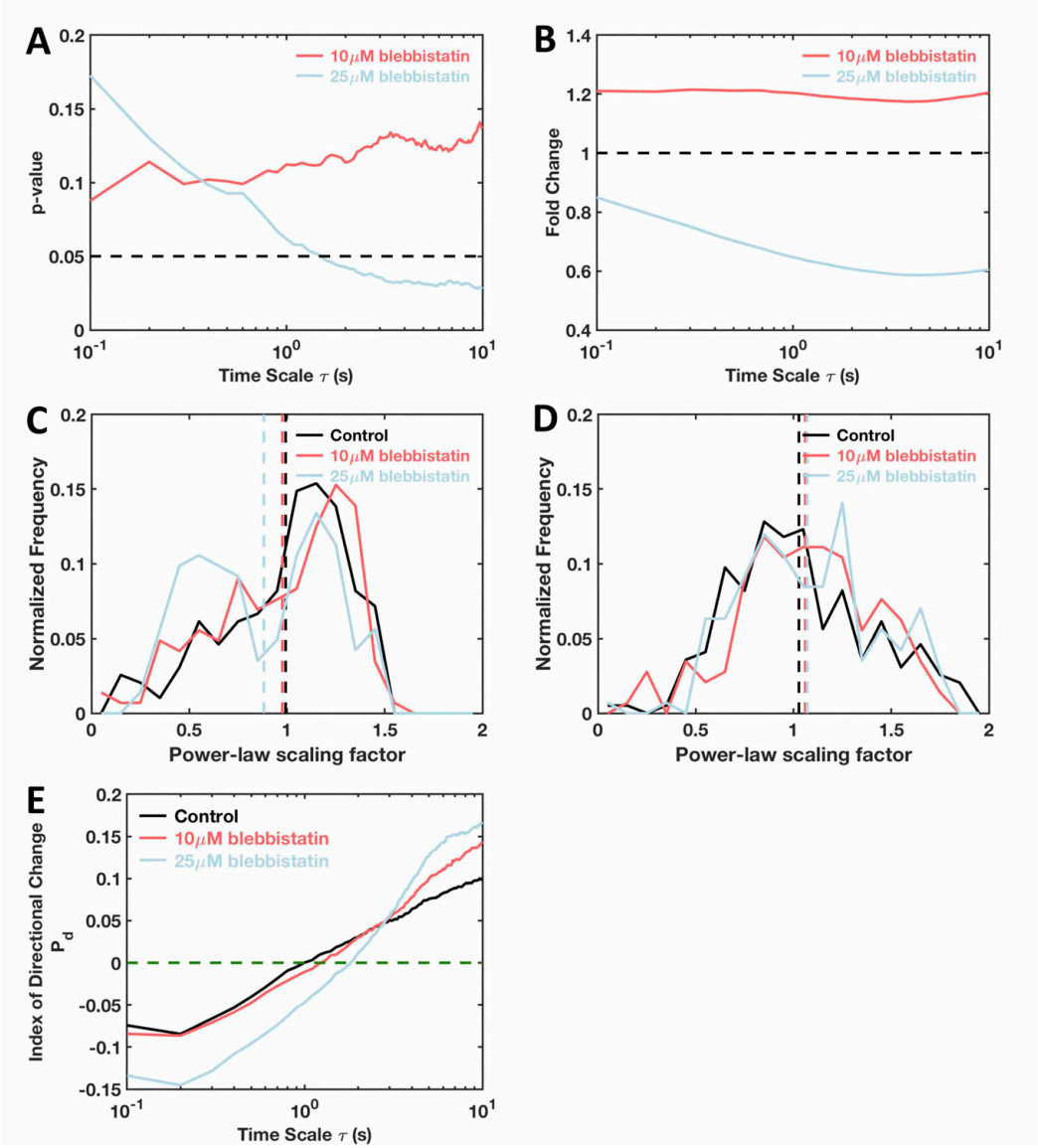

Figure S5.3. Myosin II plays a role in driving fluorescent particle fluctuations (continued). **(A) p-**values of Wilcoxon rank sum test between blebbistatin treated cells with different concentrations and control cells. Black dashed line is a visual guide of p value equals to 0.05. The portion of the curve below 0.05 indicates that the change in mean is statistically significant, while being above that threshold is an indication of insignificant changes. (**B**) Fold change of MSDs of blebbistatin treated cells with different concentrations compared to control cells. Black dashed line indicates a visual guide of fold change equals to one. (**C, D**) Comparisons between the control and blebbistatin treated cells with different concentrations in terms of the distributions of power-law scaling factor over short (0.5-1.5 s) and long (6-8 s) timescales respectively. Vertical dashed lines indicate the mean power-law scaling factor of the corresponding treatment as color-coded. **E**) Indexes of directional persistence, P_d, of control cells and blebbistatin treated cells with different concentrations. Green dashed line indicates $P_d = 0$, which is characteristic of pure diffusion.

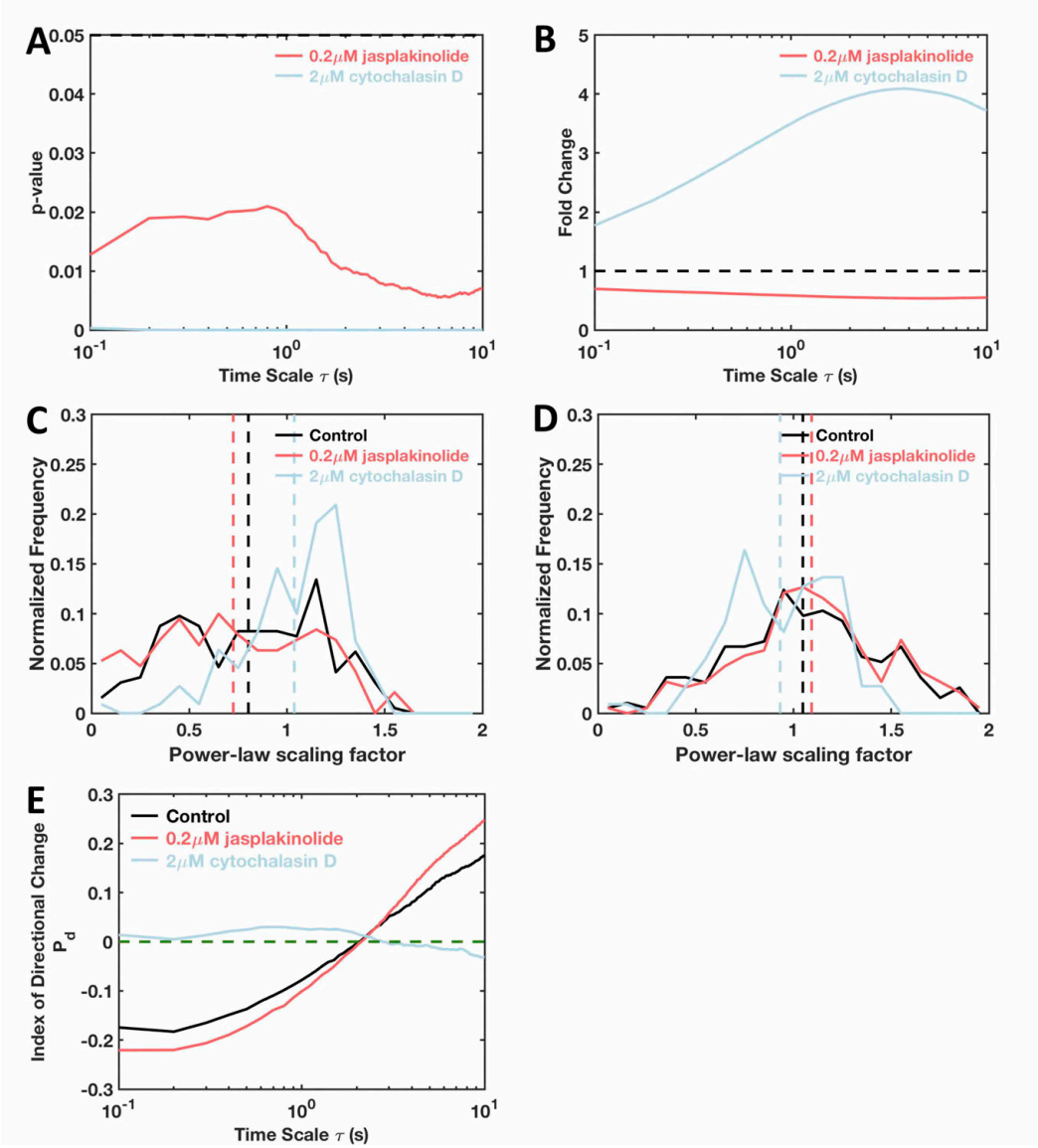

Figure S5.4. Actin network plays a major role in hindering fluctuations of fluorescent particle. (continued).

(**A**) p-values of Wilcoxon rank sum test between cells treated by jasplakinolide or cytochalasin D and control cells. Black dashed line is a visual guide of p value equals to 0.05. The portion of the curve below 0.05 indicates that the change in mean is statistically significant, while being above that threshold is an indication of insignificant changes. (**B**) Fold change of MSDs of cells treated by jasplakinolide or cytochalasin D compared to control cells. Black dashed line indicates a visual guide of fold change equals to one. (**C, D**) Comparisons between the control and cells treated by jasplakinolide or cytochalasin D in terms of the distributions of power-law scaling factor over short (0.5-1.5 s) and long (6-8 s) timescales respectively. Vertical dashed lines indicate the mean power-law scaling factor of the corresponding treatment as color-coded. **E**) Indexes of directional persistence, P_d, of control cells and cells treated by jasplakinolide or cytochalasin D. Green dashed line indicates $P_d = 0$, which is characteristic of pure diffusion.

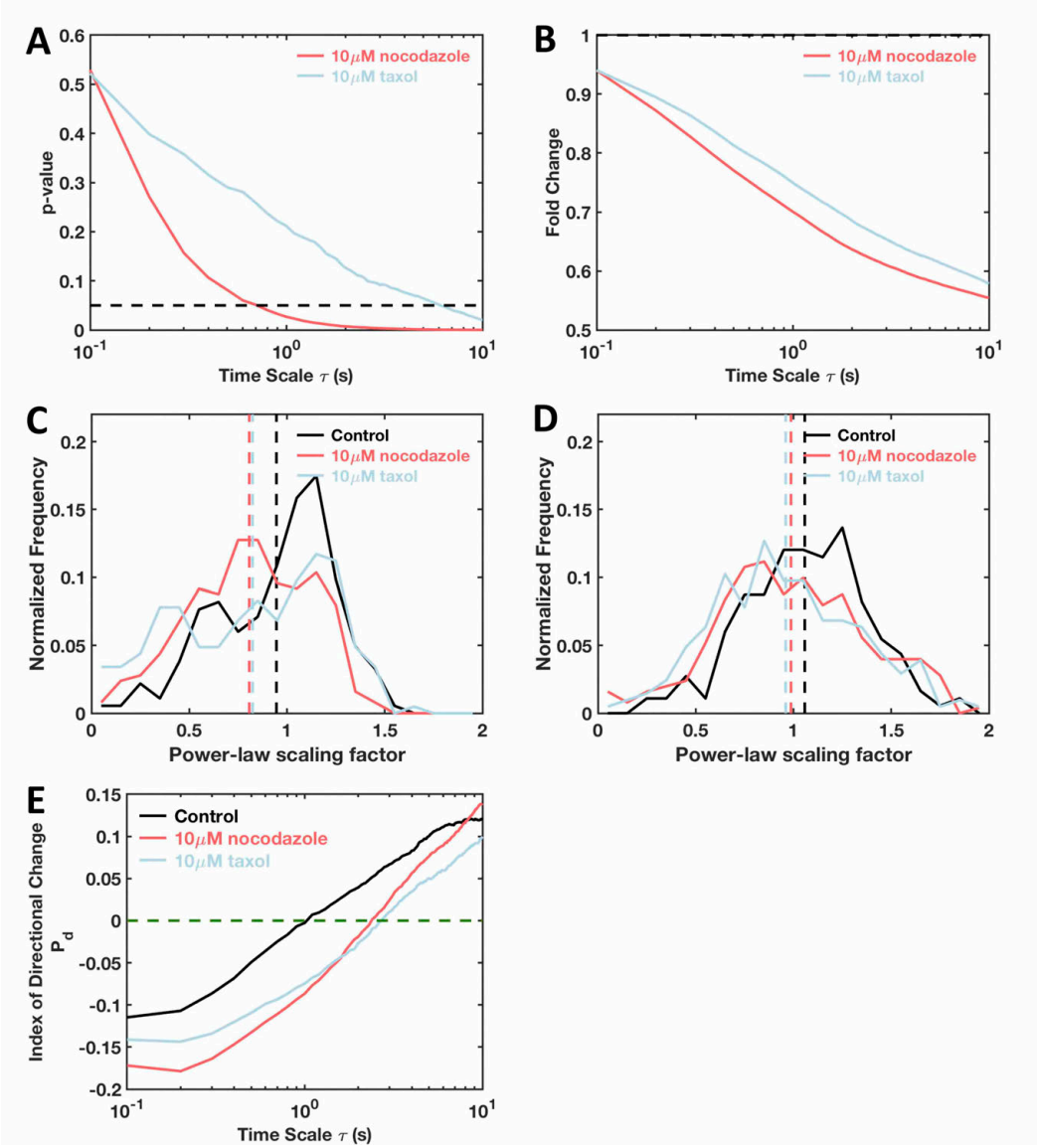

Figure S5.5. Microtubule network plays a minor role in determining fluctuations of fluorescent particle. (continued).

(**A**) p-values of Wilcoxon rank sum test between cells treated by nocodazole or taxol and control cells. Black dashed line is a visual guide of p value equals to 0.05. The portion of the curve below 0.05 indicates that the change in mean is statistically significant, while being above that threshold is an indication of insignificant changes. (**B**) Fold change of MSDs of cells treated by nocodazole or taxol compared to control cells. Black dashed line indicates a visual guide of fold change equals to one. (**C, D**) Comparisons between the control cells and cells treated by nocodazole or taxol in terms of the distributions of power-law scaling factor over short (0.5-1.5 s) and long (6-8 s) timescales respectively. Vertical dashed lines indicate the mean power-law scaling factor of the corresponding treatment as color-coded. **E**) Indexes of directional persistence, P_d, of control cells and cells treated by nocodazole or taxol. Green dashed line indicates $P_d = 0$, which is characteristic of pure diffusion.